Factorisation of beams in van der Meer scans and measurements of the ϕ^*_η distribution of $Z \to e^+e^-$ events in pp collisions at $\sqrt{s} = 8$ TeV with the ATLAS detector

A thesis submitted to the University of Manchester for the degree of Doctor of Philosophy in the Faculty of Engineering and Physical Sciences

Samuel Nathan Webb

School of Physics and Astronomy

2015

Contents

1 Introduction **9**

1.1 The Standard Model . . . 9
1.2 Particle colliders . . . 10
1.3 Units . . . 12
1.4 Outline of thesis . . . 12

2 The ATLAS detector **14**

2.1 Introduction . . . 14
2.2 The LHC . . . 14
2.3 ATLAS detector design . . . 16
2.3.1 The Inner Detector . . . 17
2.3.2 Calorimetry . . . 19
2.3.3 The Muon Spectrometer . . . 22
2.4 ATLAS detector operation . . . 23
2.4.1 Trigger system . . . 24

3 Luminosity **25**

3.1 Introduction to luminosity . . . 25
3.2 Luminosity measurement . . . 25
3.3 The van der Meer method . . . 26
3.4 ATLAS Luminosity measurement in 2012 . . . 28
3.4.1 Bunch-sensitive detectors and algorithms . . . 29
3.4.2 Bunch-integrating detectors . . . 32
3.4.3 Calibration . . . 32

4 Modelling bunch density profiles to estimate a correction to the luminosity for the assumption of beam-factorisation **35**

4.1 Introduction . . . 35
4.2 Beam spot information . . . 35

4.3 Calculating the evolution of the luminosity and the beam spot observables given single beam density profiles . . . 38
4.4 Beam profile choices . . . 39
4.4.1 Single Gaussian . . . 40
4.4.2 Double Gaussian . . . 41
4.4.3 Supergaussian . . . 42
4.5 Procedure for extracting single beam parameters . . . 43
4.5.1 Minimisation procedure . . . 43
4.5.2 Corrections . . . 44
4.6 Results . . . 56
4.6.1 Introduction . . . 56
4.6.2 April . . . 57
4.6.3 July . . . 64
4.6.4 November . . . 74
4.7 Systematic uncertainty evaluation . . . 80
4.7.1 Introduction . . . 80
4.7.2 Statistical uncertainties on individual beam parameters . . . 81
4.7.3 Systematic uncertainty due to beam spot resolution . . . 84
4.7.4 Uncertainty on the choice of beam parameterisation . . . 86
4.7.5 Conclusions . . . 87

5 Probing soft QCD using the ϕ^*_η angular observable 92
5.1 Quantum Chromodynamics . . . 92
5.2 The Drell-Yan process . . . 92
5.2.1 Description . . . 92
5.2.2 Boson transverse momentum distribution . . . 94
5.3 Monte Carlo event generators . . . 94
5.4 The ϕ^*_η observable . . . 96
5.4.1 Definition and motivation . . . 96
5.4.2 Final state radiation . . . 98
5.5 Measurements of ϕ^*_η at hadron colliders . . . 98

6 Measurements of the Z boson cross-section, differential in ϕ^*_η, in wide bins of boson mass and rapidity in the electron-positron channel with the ATLAS detector 101
6.1 Definition of the measurements . . . 101
6.2 Outline of analysis method . . . 103
6.3 Event selection . . . 104

6.3.1 Overview . . . 104
6.3.2 Additional details . . . 105
6.4 Electron selection . . . 106
6.4.1 Overview . . . 106
6.4.2 Additional details . . . 107
6.5 Truth event selection . . . 108
6.6 Binning choices . . . 110
6.7 Background estimation . . . 115
6.7.1 Monte Carlo backgrounds . . . 116
6.7.2 Multi-jet background . . . 118
6.7.3 Summary . . . 120
6.8 Data and model comparison . . . 120
6.8.1 Corrections for known disagreement . . . 123
6.8.2 Control distributions . . . 125
6.9 Obtaining the normalised differential cross-section . . . 129
6.10 Systematic uncertainties . . . 130
6.10.1 Introduction . . . 130
6.10.2 Modelling of the detector and beam-conditions . . . 131
6.10.3 Methodology of correction to truth level . . . 133
6.10.4 Modelling of the signal and background processes . . . 134
6.10.5 Summary . . . 136
6.11 Results . . . 138
6.11.1 Dressed level, di-electron channel . . . 138
6.11.2 Born level, combination with di-muon channel . . . 138
6.11.3 Comparison with theoretical predictions . . . 148
6.12 Conclusions . . . 153

A Luminosity **167**
A.1 Overlap integral of two moving beams modelled by the sum of multiple Gaussian distributions . . . 167

Word count: 33,236

Factorisation of beams in van der Meer scans and measurements of the ϕ^*_η distribution of $Z \to e^+e^-$ events in pp collisions at $\sqrt{s} = 8$ TeV with the ATLAS detector

A thesis submitted to the University of Manchester for the degree of Doctor of Philosophy in the Faculty of Engineering and Physical Sciences

Samuel Nathan Webb

School of Physics and Astronomy

2015

Abstract

Two analyses of data recorded in proton-proton collisions at the ATLAS detector in 2012 are presented in this thesis. The first pertains to the beam separation (van der Meer) scans required to calibrate the absolute luminosity. An estimate is made for the size of the correction needed to the standard van der Meer calibration method, which assumes that the proton bunch density profiles are factorisable. This is done by observing and modelling the evolution of various beam spot phenomena during the separation scans.

The second analysis described is a series of measurements of the Z/γ cross-section, differential in the ϕ^*_η observable, for different ranges of the boson invariant mass and absolute rapidity. In particular the events in which the boson decays to electron-positron pairs are considered. The ϕ^*_η observable is defined in terms of the well-measured lepton directions and enables a probe of initial state gluon radiation in the non-perturbative regime of QCD.

Declaration

No portion of the work referred to in the thesis has been submitted in support of an application for another degree or qualification of this or any other university or other institute of learning.

Copyright statement

1. The author of this thesis (including any appendices and/or schedules to this thesis) owns certain copyright or related rights in it (the "Copyright") and he has given The University of Manchester certain rights to use such Copyright, including for administrative purposes.

2. Copies of this thesis, either in full or in extracts and whether in hard or electronic copy, may be made **only** in accordance with the Copyright, Designs and Patents Act 1988 (as amended) and regulations issued under it or, where appropriate, in accordance with licensing agreements which the University has from time to time. This page must form part of any such copies made.

3. The ownership of certain Copyright, patents, designs, trade marks and other intellectual property (the "Intellectual Property") and any reproductions of copyright works in the thesis, for example graphs and tables ("Reproductions"), which may be described in this thesis, may not be owned by the author and may be owned by third parties. Such Intellectual Property and Reproductions cannot and must not be made available for use without the prior written permission of the owner(s) of the relevant Intellectual Property and/or Reproductions.

4. Further information on the conditions under which disclosure, publication and commercialisation of this thesis, the Copyright and any Intellectual Property and/or Reproductions described in it may take place is available in the University IP Policy[1], in any relevant Thesis restriction declarations deposited in the University Library, The University Librarys regulations[2] and in The Universitys policy on Presentation of Theses.

[1]see http://documents.manchester.ac.uk/DocuInfo.aspx?DocID=487
[2]see http://www.manchester.ac.uk/library/aboutus/regulations

Acknowledgements

I would firstly like to thank Terry Wyatt for his excellent supervision throughout my PhD, as well as at undergraduate level. I also thank Witold Kozanecki and Lee Tomlinson for their useful discussions, suggestions and guidance. In addition I thank all members of the Manchester Particle Physics Group for making the last three and a half years so enjoyable.

Finally I thank my parents, Andrew and Rosemary, and my siblings: Miriam, Jacob and Ethan.

Chapter 1

Introduction

1.1 The Standard Model

Particle physics is concerned with the identification of the fundamental constituents of the universe and their interactions. The theory which best describes these at present is called the Standard Model, which is a quantum field theory with a local SU(3) × SU(2) × U(1) gauge symmetry contructed from a series of experimental observations and theoretical insights [1]. The Standard Model has become one of the most thoroughly tested theories in physics and describes the operation of three of the four fundamental forces of nature, namely the electromagnetic, strong and weak forces with gravity being the exception. Forces in the theory are mediated by integer-spin particles (bosons); the photon, γ, and the gluon, g are the bosons responsible for mediating the electromagnetic and strong forces respectively whilst the W^+, W^- and Z bosons are responsible for mediating the weak force. The matter content is composed of half-integer spin particles (fermions), which can be divided into two categories: quarks, which interact via all three forces and leptons which only interact via the electromagnetic and/or weak interactions. Particles obtain mass via interactions with the Higgs field, excitations of which produce the only scalar (spin 0) particle in the model — the Higgs boson, H.

A summary of the fundamental particles in the Standard Model is given in Table 1.1 [1]. For each charged fermion there is a distinct anti-particle which has the same mass but opposite charge. The question of whether neutrinos, ν have a distinct anti-particle or constitute their own anti-particle is a topic of current research [2] [3].

Despite much success in describing the interactions between the known fundamental particles, the Standard Model is not able to explain all observed phenomena in nature — three of the most important are briefly described here. As already mentioned gravitational interactions between particles are not considered in the

Fermions			
Quarks	$\begin{pmatrix} u \\ d \end{pmatrix}$	$\begin{pmatrix} c \\ s \end{pmatrix}$	$\begin{pmatrix} t \\ b \end{pmatrix}$
Leptons	$\begin{pmatrix} e \\ \nu_e \end{pmatrix}$	$\begin{pmatrix} \mu \\ \nu_\mu \end{pmatrix}$	$\begin{pmatrix} \tau \\ \nu_\tau \end{pmatrix}$
Bosons			
γ, g, $W^{\pm}$, Z, H			

Table 1.1: A summary of the fundamental particles in the Standard Model [1].

Standard Model. For particles at everyday energies this is unimportant when making predictions as gravity is around 38 orders of magnitude weaker than the strong force [4]. However in order to describe the interaction of particles in the first 10^{-43} s of the universe, when particle energies were around 10^{20} times larger, a more complete theory is required [5]. The Standard Model is also inconsistent with two further issues relating to observations on very large length scales. The first is the abundance of matter over anti-matter in the universe. These are treated differently in the theory and given the reasonable assumption of an equal quantity of each at the beginning of the universe it is predicted that there should be residual matter left after a period of matter-anti-matter annihilation shortly afterwards. However the Standard Model predicts that there should be less matter remaining than is currently observed by several orders of magnitude [6].

The second issue concerns the astrophysical observations such as galaxy rotation speeds and galactic gravitational lensing which suggest the existence of a class of matter known as 'dark matter' which does not interact or only weakly interacts with the currently known fundamental particles. One extension to the Standard Model, which has been heavily studied, is named Supersymmetry and proposes a fermionic partner for each boson in the Standard Model and a bosonic partner for each fermion. Some of the additional particles could have the properties necessary to explain dark matter. However no direct experimental evidence for Supersymmetry has so far been seen [1].

1.2 Particle colliders

The discovery of new particles and the study of their behaviour is performed by initiating high-energy particle interactions and examining the properties of the resulting particles produced. Experiments which seek to do this can generally be divided into

two categories, those in which particles are fired into a stationary target (fixed-target experiments) and those in which two beams of particles are collided (high-energy colliders). Fixed target experiments have the advantage that a high percentage of incoming particles will collide with the target, however suffer from the fact that the invariant mass of the resultant particles must be lower than the energy of the incoming particle in order to conserve momentum. For this reason much of the research into very high-energy particles takes place at colliders. However fixed-target experiments are still contributing important results to certain research areas, for example, the NA62 experiment at CERN (The European Organisation for Nuclear Research, Geneva), measures the rate of the rare decay $K^+ \to \pi^+ \nu\bar{\nu}$ (where K^+ is a bound state of an up and an anti-strange quark) [7].

Most high-energy colliders collide bunches of particles to maximise the probability of an interaction. The bunches in the Large Hadron Collider (LHC) [8] at CERN contain around 10^{11} protons and yet there are only of order 20 interactions per collision (as of 2012). Circular colliders such as the LHC or the Tevatron [9], which operated at Fermilab near Chicago have the advantage that certain bunch pairs will collide thousands of times a second, increasing the number of useful interactions that can be gained for the initial outlay in time and energy of accelerating the particles in a bunch. Linear colliders such as the proposed International Linear Collider (ILC) do have some advantages over circular colliders, the main one being the near absence of energy loss from synchrotron radiation. It was this factor, which at the end of its lifetime in 2000, limited the energy of the particles in the Large Electron-Positron Collider (LEP) at CERN [10].

One of the most important considerations made when designing a high-energy collider is the type of particles being collided. Lepton colliders such as LEP allow the energy of the incoming particles to be known very precisely as the particles being accelerated are fundamental. This is in contrast to machines which collide composite particles formed of quarks (hadrons). The constituent quarks in a hadron have a distribution of momenta, which means the centre of mass energy of any one pair of incoming quarks is unknown and can only be determined by reconstructing the invariant mass of the particles produced in the collision. This is a particular disadvantage when there are out-going particles which do not interact with the detector, such as neutrinos. Particle kinematics in high-energy colliders are therefore generally described in terms of momentum transverse to the beam direction, p_{T}, which is assumed to be very small or zero in the system of the incoming particles.

A further advantage of lepton colliders is that leptons do not carry colour charge and therefore do not interact via the strong force. This means that there is no

gluon emission from the incoming particles which affords a cleaner experimental signature in which one can more easily identify the interesting particles produced in the interaction. The main advantage though of hadron colliders such as the LHC is that they accelerate heavier particles than lepton colliders — the proton is around 2000 times more massive than the electron — and therefore there is less synchrotron radiation which means higher collision energies can be achieved.

A third class of colliders are those which collide leptons with hadrons, such as the Hadron Elektron Ring Anlage (HERA) collider which ran at the Deutsches Elektronen-Synchrotron (DESY) research centre in Hamburg from 1992 until 2007 [11]. HERA collided either electrons or positrons with protons, which allowed the internal structure of the proton to be precisely measured.

Circular particle colliders generally have multiple interaction points around the machine. For example the LHC has four interaction points and at each is situated one large particle detector or experiment, which are named ATLAS (A Toroidal LHC Apparatus) [12], ALICE (A Large Ion Collider Experiment) [13], CMS (Compact Muon Solenoid) [14] and LHCb (LHC Beauty) [15]. There are also three smaller experiments located at or near the LHC interaction points, LHCf (LHC Forward) [16], TOTEM (TOTal Elastic and diffractive cross section Measurement) [17] and MOEDAL (Monopole and Exotics Detector at the LHC) [18]. The results presented in this thesis are obtained using data from the ATLAS experiment. A more detailed description about the LHC and ATLAS specifically is given in Chapter 2.

1.3 Units

Unless otherwise stated the system of units used in this thesis is the standard used in the field of high energy particle physics, sometimes called 'natural units'. That is, the speed of light, c, and the reduced Planck's constant, $\hbar$, are set equal to unity and energies are expressed in electron-volts, eV. One electron-volt is approximately equal to 1.6×10^{-19} J. In this system the mass of the proton is equal to 0.94 GeV.

1.4 Outline of thesis

Chapter 2 introduces the ATLAS experiment. The design and operation of its various sub-detectors are described as well as how the particles produced by the interactions in the LHC can be identified. Chapter 3 introduces the concept of the luminosity of an accelerator, which can be defined as the rate of a particular process divided by its cross-section. The luminosity is determined in ATLAS during

operations by measuring a quantity to which it is proportional. The calibration of the proportionality constant using beam separation scans is then also described. Chapter 4 then details a study undertaken to determine an important correction to the calibration method, namely for the assumption of beam-factorisation, and its associated systematic uncertainty.

Chapter 5 describes how in recent years tests of Quantum Chromodynamics (QCD), the quantum field theory description of the strong force, have been performed by measuring the angular distribution of lepton pairs in Z boson and photon decays. The specific angular variable of interest is named ϕ^*_η and measurements of this distribution for the Z boson decaying to electron-positron pairs are detailed in Chapter 6.

Chapter 2

The ATLAS detector

2.1 Introduction

The ATLAS experiment is a general purpose particle detector located at one of the four collision points of the Large Hadron Collider at CERN, 100 m underground. This chapter first provides an introduction to the LHC, describing its characteristics and how particles are brought into collision (Section 2.2). Section 2.3 describes the design of the ATLAS experiment and Section 2.4 then describes the operation of the detector during data taking and how interesting collisions are selected using a three-tiered trigger system.

2.2 The LHC

At 27 km in circumference the LHC is one of the largest particle colliders ever built as well as colliding particles with a record centre of mass energy ($\sqrt{s}$) of 8 TeV in 2012. The previous record-holder was the Tevatron, which by the end of its operations collided protons and anti-protons with $\sqrt{s}$ equal to 1.96 TeV. The LHC also has a higher particle collision rate (higher luminosity) than the Tevatron, where the luminosity was limited by the production rate of anti-protons.

For the majority of its running the LHC has collided bunches of protons with $\sqrt{s}$ of 7 TeV in 2010 and 2011 and 8 TeV in 2012. However the machine has also been used to collide bunches of lead ions with a centre of mass energy per nucleon pair ($\sqrt{s_{NN}}$) of 2.76 TeV and to collide lead ions with protons at $\sqrt{s_{NN}}$ equal to 5.02 TeV. During the majority of 2013 and 2014 the LHC was switched off to allow upgrades to the machine itself as well as to the various experiments around the collider. These improvements have allowed the maximum centre of mass energy to be increased to 13 TeV for collisions in 2015.

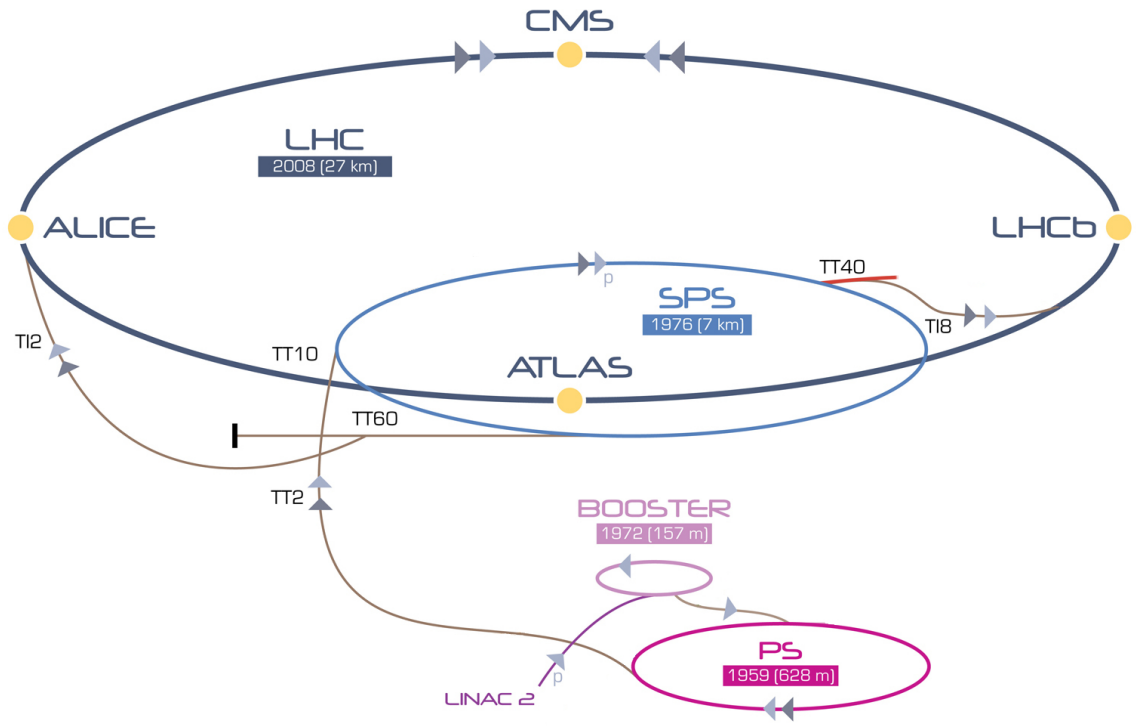

Figure 2.1: The LHC injection chain for protons [19].

A series of machines is required to be able to accelerate the protons (or lead ions) to collision energies. These are collectively named the LHC injection chain, a diagram of which is provided in Figure 2.1 [19].

Protons are obtained by removing electrons from hydrogen gas by passing it through an electric field. The protons are then accelerated to 50 MeV using the only linear accelerator in the chain named Linac 2. They then enter the Proton-Synchrotron (PS) Booster which accelerates them to 1.4 GeV in preparation for transfer to the PS itself. After reaching energies of 26 GeV the protons leave the PS via Transfer Tunnels (TT) TT2 and TT10. They then arrive in the Super Proton Synchrotron where they are accelerated to an energy of 450 GeV. The protons for the anti-clockwise LHC beam then proceed along TT40 and Injector Tunnel (TI) TI8 whereas those for the clockwise beam proceed along TT60 and TI2 into the LHC. The energy of the protons is then increased in the LHC until collision energy (4 TeV in 2012) is reached. The only difference in the lead ion injector chain is that the ions initially pass though a different linear accelerator, named Linac 3.

The SPS has been an important accelerator in its own right, most significantly when it acted as a proton-anti-proton collider from 1981 to 1984. This enabled the discoveries of the W and Z bosons in 1983 by the UA1 (Underground Area 1) and UA2 experiments, the two general purpose detectors located on the SPS.

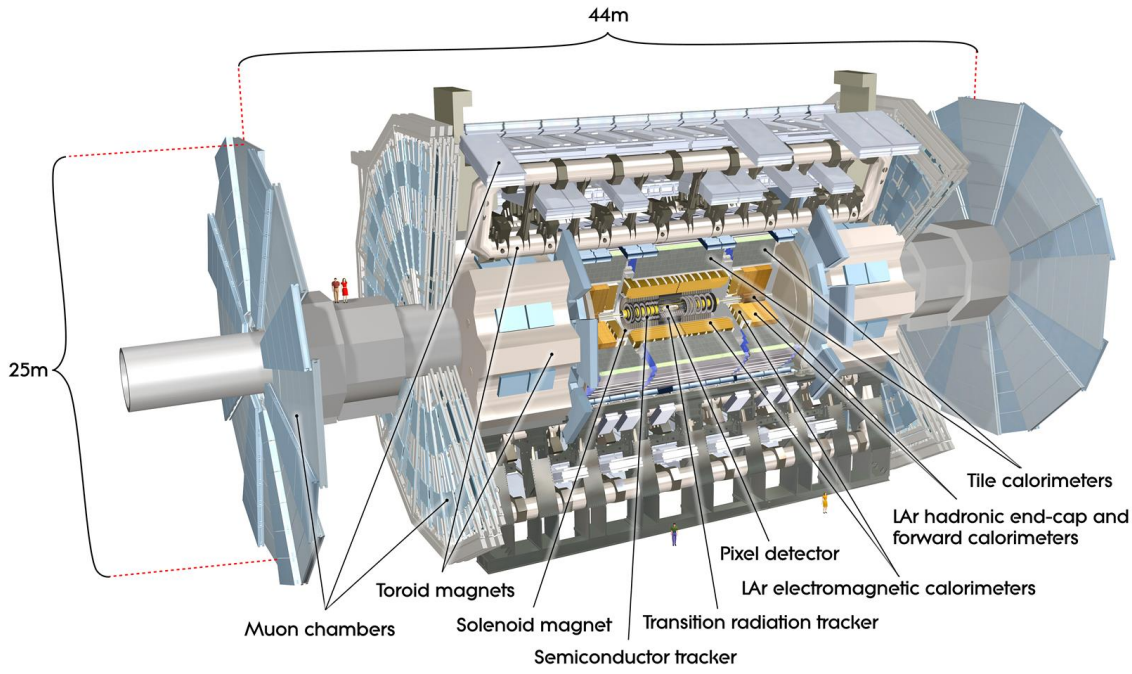

Figure 2.2: A diagram of the ATLAS detector in which the most important sub-detectors are labelled [12].

2.3 ATLAS detector design

The following section describes the design and layout of the ATLAS detector [12]. ATLAS is approximately cylindrical in shape and can be divided into three parts, a central section known as the barrel and two 'end-caps'. It measures around 44 m along its axis and its diameter is around 25 m. A diagram of the ATLAS detector is shown in Figure 2.2 [12].

The LHC beam travels along the axis of the cylinder, passing through both end-caps and defines the z-axis of the coordinate system used with the detector. The nominal interaction point in the centre of the cylinder is defined as the origin of the coordinate system. The direction pointing from the origin to the centre point of the LHC defines the positive x-axis whilst the positive y-axis is defined as pointing upwards. The detector is nominally symmetric about the x-y plane at $z = 0$. The shape of the detector suggests the use of polar coordinates to describe a particle's position. The azimuthal angle, ϕ, is measured around the beam axis and the polar angle, θ, is measured from the beam axis. One further useful quantity is the pseudorapidity, η, defined in Equation 2.1 such that differences in pseudorapidity are Lorentz invariant for boosts along the beam direction in the ultra-relativistic

limit.

$$\eta = -\ln \tan \frac{\theta}{2} \tag{2.1}$$

The ATLAS Inner Detector (ID) is the collective term for the three detector sub-systems which are closest to the beam line. These are the pixel detector, the Semi-Conductor Tracker (SCT) and the Transition Radiation Tracker (TRT). These are used in order to measure a particle's path or track to high precision and to distinguish between different types of particle. Each of the sub-systems are described in more detail in Section 2.3.1. The ID is immersed in a 2 T solenoidal magnetic field, which causes the bending of the paths of charged particles, the curvature of which is then used in the determination of a particle's momentum. Surrounding the ID is the electromagnetic (EM) calorimeter and then the hadronic calorimeters. The EM calorimeter is used to precisely measure the energies of electrons and photons whilst the hadronic calorimeters are suited to measuring the energies of jets, the cones of particles produced by the hadronisation of quarks and gluons. The calorimeters are described in further detail in Section 2.3.2. The outermost sub-detectors in ATLAS are dedicated to measuring the properties of high-energy muons and are collectively termed the Muon Spectrometer (MS). Within the MS are three large super-conducting air-core toroidal magnets, one in the barrel and one in each of the end-caps. Together these achieve a magnetic field of 0.5 T in the central region of the MS and 1 T in the end-cap regions. Further information on the MS is provided in Section 2.3.3.

2.3.1 The Inner Detector

During normal LHC operations there can be multiple proton-proton interactions per bunch crossing (pile-up) and in 2012 this number was typically between 15 and 30. Therefore the instrumentation closest to the beam, the ID, is required to have fine granularity in order to distinguish between the hundreds of particle tracks created every 50 ns.

The structure of the barrel region of the ID is shown in Figure 2.3 [12]. Three layers of silicon pixel modules form the elements of the ID closest to the beam pipe in both the barrel and end-cap regions. All of the 1744 pixel modules are identical and each module contains 47232 pixels. The size of around 90% of the pixels is 50 µm × 400 µm with the remainder being 50 µm × 600 µm. In addition to the requirement of a high spatial resolution the pixel layers must continue operating under sustained intense radiation.

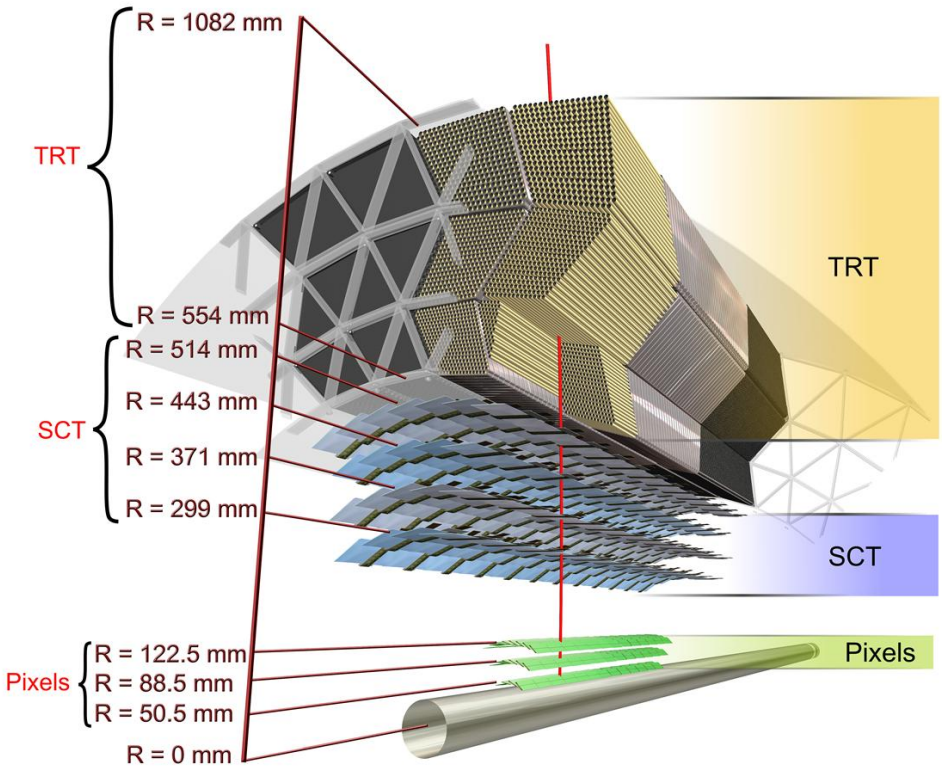

Figure 2.3: The ATLAS Inner Detector (barrel) [12]

Four cylindrical layers of silicon microstrip modules in the barrel and nine disk layers in each of the end-caps form the SCT sub-detector. These surround the pixel layers and provide additional and complementary measurements of a charged particle's track. The 2112 SCT modules in the barrel are identical and consist of four 770 strip sensors, two on each face. The strips on one of the faces are aligned parallel to the beam direction whilst those on the opposite face have a relative rotation of 40 mrad in order to provide information on a particle's z-coordinate [20]. The 1976 SCT modules in the end-caps have a wedge-shaped geometry and vary in size dependent on their location on an end-cap disk. The modules have a similar sensor layout to those in the barrel but here the strips on one of the faces are aligned radially and those on the opposite face again have a relative rotation of 40 mrad.

The outermost component of the ID, the TRT, is composed of 4 mm diameter straw tubes filled with a gas mixture of 70% xenon, 27% carbon dioxide and 3% oxygen [12]. In the barrel region there are 73 layers of straws, aligned with the beam axis and embedded in an array of polypropylene fibres. In each end-cap there are 160 layers of straws, arranged radially and interspersed with layers of polypropylene foils. In addition to providing extra particle tracking information the TRT is also used for distinguishing between electrons and pions [21]. As a relativistic particle enters a material of a different dielectric constant (in this case the polypropylene) it radiates photons. The total energy loss of an ultra-relativistic particle due to this transition radiation is proportional to its Lorentz factor, γ, and also depends on the properties of the material. Up to particle energies of 100 GeV only the low-mass electron produces enough photons with energy above the detection threshold (typically 6 keV).

2.3.2 Calorimetry

The electromagnetic sampling calorimeter consists of alternate layers of lead absorbers and kapton electrodes arranged in an accordion-shaped geometry and immersed in liquid argon (LAr) [22]. This design is used both in the barrel and the end-cap regions as illustrated in Figure 2.4 [23]. The barrel region covers a pseudo-rapidity range $|\eta| < 1.475$, an outer end-cap wheel covers $1.375 < |\eta| < 2.5$ and an inner end-cap wheel covers the range $2.5 < |\eta| < 3.2$. The entire EM calorimeter is completely symmetric in the azimuthal angle, ϕ, without any cracks. Both the barrel and end-cap EM calorimeters are housed in their own cryostat, which each have an operating temperature of 87 K. An end-cap cryostat also contains the LAr hadronic end-cap calorimeter (HEC) and forward calorimeter (FCal).

As an electron or photon passes through the layers of lead an electromagnetic

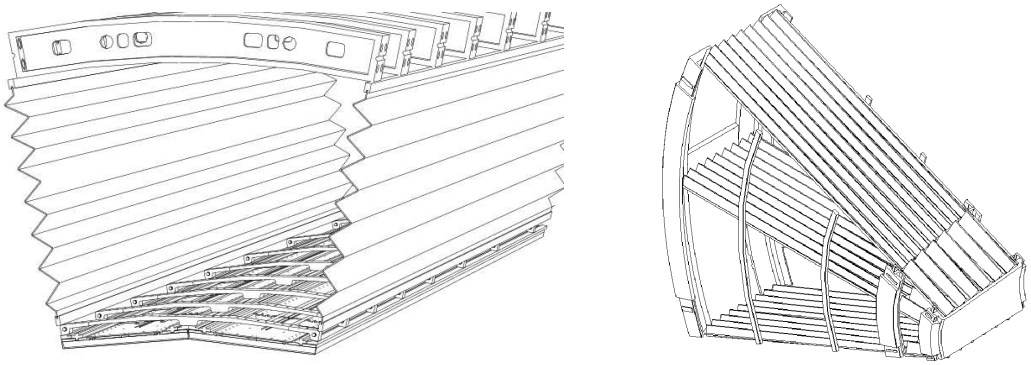

Figure 2.4: The left diagram depicts a barrel EM calorimeter module in which only the first and last of the 64 absorbers are shown. The right diagram depicts an end-cap module again in which only three of the (96 outer wheel, 32 inner wheel) absorbers are shown [23].

shower is induced via processes such as bremsstrahlung and pair-production, which cause ionisation of the liquid argon that is collected by the electrodes. The signal produced is proportional to the energy of the particle and the conversion factor is obtained using test-beam measurements and the behaviour of well-understood resonances such as $Z \rightarrow e^+e^-$ [24]. The EM calorimeter is designed to contain the electromagnetic showers of electrons and photons and as such is more than 22 radiation lengths thick in the barrel and more than 24 thick in the end-cap regions. The EM calorimeter has three active layers in depth in the range devoted to precision measurements, $|\eta| < 2.5$, and two layers in the range $2.5 < |\eta| < 3.2$. A diagram of a barrel module indicating the granularity in η and ϕ of each of the layers is given in Figure 2.5 [12]. The largest fraction of the energy from an electromagnetic shower is collected by the second layer. The energy resolution in the pseudorapidity range between 1.37 and 1.52 is worse due to the transition between the barrel and end-cap cryostats. This region is therefore not used in precision electron measurements such as the one described in Chapter 6.

The tile hadronic sampling calorimeter (TileCal) covers the pseudorapidity range $|\eta| < 1.7$ and is subdivided into a central barrel 5.8 m in length and two extended barrels, 2.6 m in length, each of which is split azimuthally into 64 wedge-shaped modules. A diagram showing the design of one of the modules is shown in Figure 2.6 [12]. Steel plates are used for the absorbing material and scintillating tiles as the sampling material. The ultraviolet light from the scintillators is converted to visible light by wavelength-shifting fibres which transmit the signal to photomultiplier tubes (PMTs). The total thickness of the detector up to and including the TileCal is 9.7 interaction lengths. This figure increases to 10 for the end-cap regions. This

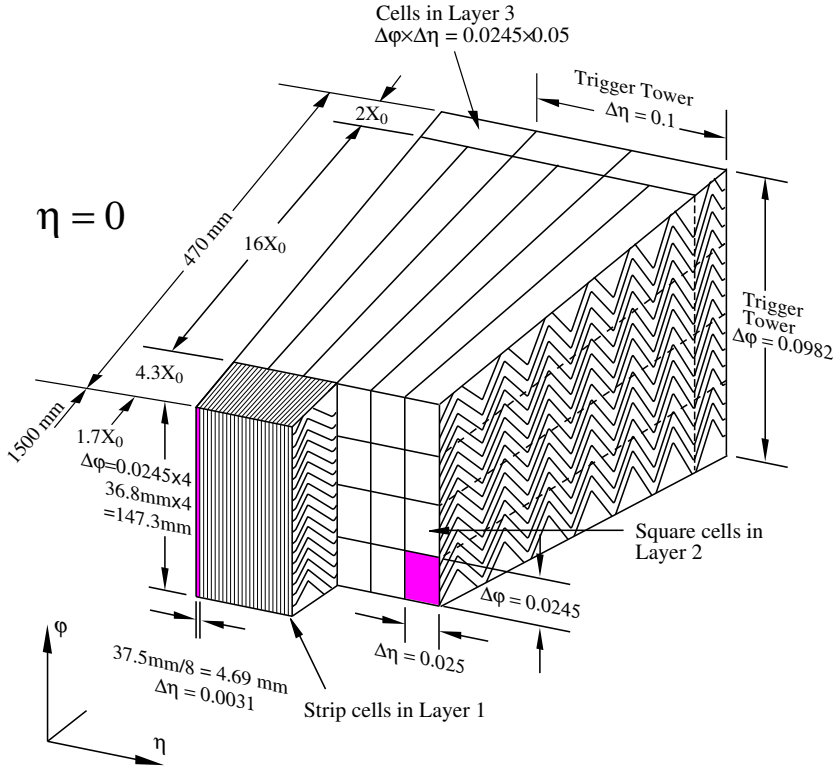

Figure 2.5: A diagram of a barrel EM calorimeter module indicating the granularity in η and ϕ in each of the three layers [12].

thickness combined with wide coverage of the calorimetry in pseudorapidity enables precise measurements of the missing transverse energy ($E_{\mathrm{T}}^{\mathrm{miss}}$) - the energy carried by particles which do not interact with the detector such as neutrinos.

The hadronic end-cap calorimeters (HEC) use copper as the absorbing material and liquid argon as the sampling material. The HEC covers the pseudorapidity range $1.5 < |\eta| < 3.2$ and consists of two independent wheels per end-cap, each of which are divided into 32 wedge-shaped modules. The range $3.1 < |\eta| < 4.9$ is covered by the forward calorimeter, FCal. Each forward calorimeter consists of three modules. The module closest to the interaction point uses copper rods as the absorbing material and is optimised for electromagnetic measurements. The other two modules use tungsten rods and are designed for hadronic energy measurements. The rods are centred within tubes which run parallel to the beam pipe. The gaps between the tubes and rods are filled with liquid argon, which is again used as the sampling material.

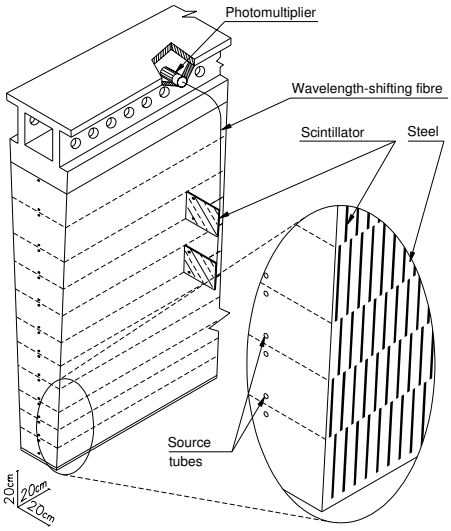

Figure 2.6: A diagram of a TileCal module showing the layout of the steel absorbing plates and scintillating tiles [12].

2.3.3 The Muon Spectrometer

According to the Bethe formula description of the mean rate of energy loss or 'stopping power' of particles in matter, muons of momenta typically produced in ATLAS (0.1 GeV to 1000 GeV) are approximately minimum ionising particles [1]. As such they are generally the only type of Standard Model particle to penetrate the calorimetry systems and interact with the detectors of the Muon Spectrometer (MS).

The most striking feature of the MS is three large air-core superconducting toroid magnets, one in the barrel region and one in each end-cap. The barrel toroid [25] is formed of eight racetrack shaped coils, each housed in its own cryostat, and has an axial length of 25.3 m, an inner diameter of 9.4 m and an outer diameter of 20.1 m [12]. The end-cap toroids are also both formed of eight coils all contained within one cryostat. They have an inner diameter of 1.65 m, an outer diameter of 10.7 m and an axial length of 5.0 m. The toroid magnetic field in the barrel is approximately 0.5 T, with this rising to approximately 1 T in the end-cap regions. The field is non-uniform and causes charged particles to bend in a plane containing the beam-axis.

The barrel region of the MS is formed of three concentric cylindrical layers, on either side of, and between the toroid coils as indicated in Figure 2.7 [26]. The end-cap regions consist of a series of large wheels perpendicular to the beam-axis. In the pseudorapidity range $0 < |\eta| < 2.7$ precision tracking is performed by Monitored Drift Tube (MDTs), complemented by Cathode-Strip Chambers (CSCs) at high

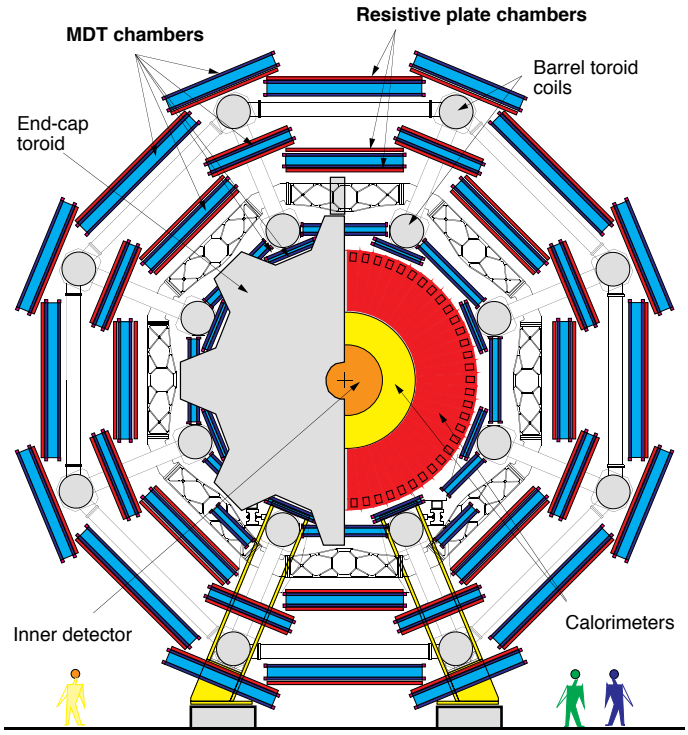

Figure 2.7: A view of the Muon Spectrometer in the transverse plane. One half of the end-cap toroid has been cut-away [26].

pseudorapidity, $2.0 < |\eta| < 2.7$, where the particle fluxes and track density is the highest. Fast determination of muon transverse momentum (p_{T}) and fast but coarse tracking information for use in the trigger system (see Section 2.4) is provided in the barrel region by Resistive Plate Chambers (RPCs) and in the end-cap regions by multi-wire proportional chambers named Thin Gap Chambers (TGCs).

2.4 ATLAS detector operation

The period in which proton bunches are circulating in the LHC is known as a fill, the average duration of which in 2012 was 6.1 hours [27]. Each period of ATLAS data taking is termed a run. A run generally corresponds to one LHC fill however they are independent - there may be multiple runs per fill or runs without any circulating beam.

The proton bunches in the LHC form a series of 'bunch trains' with a separation in time of 50 ns between bunches in a train. In 2012 this led to a maximum of 1380 bunch crossings per proton revolution, which equates to 1.6×10^7 crossings per second. Given the average number of proton-proton collisions per crossing, which was 20.7 in 2012 [28], this leads to an approximate collision rate of $3.2 \times 10^8\,\mathrm{s}^{-1}$. When a bunch crossing contains an interaction it is termed an event. The ATLAS

data taking system is designed to record 200 events per second for later analysis and therefore a three-tiered trigger system is used to select events which are considered interesting in the context of the ATLAS physics programme.

2.4.1 Trigger system

The primary selection of events is performed by the Level-1 (L1) trigger, which is implemented using custom-made electronics [12]. The trigger is run on each bunch crossing and is designed to select events which pass certain criteria defined on a 'trigger-menu'. These criteria consist of signatures for high-p_{T} electrons, photons, jets, hadronically decaying τ-leptons, and muons as well as for large missing and total transverse energy. Further menu items are formed from combinations of any of the above signatures. A decision on whether or not an event passes the selection is made within 2.5 µs and the events are passed to the Level-2 (L2) trigger for further refinement at a rate of 75 kHz.

For each event passing the L1 trigger one or more Regions-of-Interest (RoIs) are defined in η and ϕ, indicating in which parts of the detector the signatures were identified. The L2 trigger uses all of the available detector information within the RoIs to make a better informed decision on whether an event should be selected. This process takes approximately 40 ms and has an event output rate of 3.5 kHz. The entire detector readout for the events chosen by the L2 trigger is then used to assemble events into a single formatted data structure in a process known as event-building. The final tier of the trigger system, the Event Filter (EF), then uses modified versions of the offline-analysis procedures on these assembled events to reduce the event output rate to the 200 Hz required. The processing time for a single event by the EF is around four seconds.

Chapter 3

Luminosity

3.1 Introduction to luminosity

The absolute luminosity of a particle collider, $\mathscr{L}$, can most simply be expressed as the rate for a certain process, R, divided by the cross-section for that process, σ, (Equation 3.1).

$$\mathscr{L} = \frac{R}{\sigma} \tag{3.1}$$

For colliders with a bunched beam, such as the LHC, the luminosity of the machine, $\mathscr{L}$ is equal to the sum of the luminosity of each colliding bunch pair (BCID), $\mathscr{L}_b$. For BCIDs with zero crossing angle $\mathscr{L}_b$ can be written as in Equation 3.2 in terms of various parameters of the bunches, where f_r is the bunch revolution frequency, n_i is the number of particles (population) of bunch i, and $\hat{\rho}_i(x, y)$ is the normalised density profile of bunch i [29].

$$\mathscr{L}_b = f_r n_1 n_2 \int \hat{\rho}_1(x, y)\hat{\rho}_2(x, y)dxdy \tag{3.2}$$

3.2 Luminosity measurement

One can use Equation 3.1 to obtain the absolute luminosity (either on a bunch-by-bunch basis or for the whole machine) by counting the rate for a particular process and using prior knowledge of the associated cross-section. One may consider using a particle interaction for which the cross-section is well-known such as a Z boson decaying to two muons.

Alternatively one may use a detector and an associated algorithm to measure the observed, or visible, proton-proton interaction rate per bunch crossing, μ_{vis},

which has an initially unknown cross-section, σ_{vis}. The luminosity of a bunch is then given by Equation 3.3, where μ_{vis} and σ_{vis} depend on the particular detector and algorithm used. This is the method used for the default measurement of the luminosity in ATLAS.

$$\mathscr{L}_b = \frac{\mu_{\text{vis}} f_r}{\sigma_{\text{vis}}} \tag{3.3}$$

The value of σ_{vis} is calibrated by making a measurement of the absolute luminosity at a certain point in time using Equation 3.2. Without any prior knowledge of the (poorly understood) individual bunch density profiles, $\hat{\rho}$, one can make a measurement of the overlap integral $\int \hat{\rho}_1(x,y)\hat{\rho}_2(x,y)dxdy$ using a method pioneered by Simon van der Meer at the Intersecting Storage Rings (ISR) accelerator at CERN [30]. The technique is explained in Section 3.3.

3.3 The van der Meer method

Under the assumption that the bunch density profiles can be factorised into independent horizontal and vertical components (i.e., $\hat{\rho}_1(x,y) = \rho_{x1}(x)\rho_{y1}(y)$) one can rewrite Equation 3.2 as Equation 3.4. The extent to which this is a good assumption is the subject of Chapter 4.

$$\mathscr{L}_b = f_r n_1 n_2 \int \rho_{x1}(x)\rho_{x2}(x)dx \int \rho_{y1}(y)\rho_{y2}(y)dy \tag{3.4}$$

In order to obtain $\int \rho_{x1}(x)\rho_{x2}(x)dx$ van der Meer proposed measuring a quantity proportional to the luminosity (say μ_{vis}) as the two beams are separated in the horizontal (x) direction. This procedure is known as a 'beam separation scan' or more commonly a van der Meer (vdM) scan. Equation 3.5 gives an expression for μ_{vis} as a function of beam separation, h, where A is an unknown proportionality constant. Note that the convention in ATLAS vdM scans is that when the two beams are displaced symmetrically (as was always the case in 2012) the separation is defined as the position of beam 1 minus the position of beam 2.

$$\mu_{\text{vis}}(h) = A \int \rho_{x1}(x)\rho_{x2}(x+h)dx \tag{3.5}$$

By integrating Equation 3.5 with respect to separation (h) and dividing by the value of μ_{vis} at zero separation ($\mu_{\text{vis}}^{\text{MAX}}$) one obtains Equation 3.6.

$$\frac{\int \mu_{\text{vis}}(h)dh}{\mu_{\text{vis}}^{\text{MAX}}} = \frac{A \int \left(\int \rho_{x1}(x)\rho_{x2}(x+h)dx \right) dh}{A \int \rho_{x1}(x)\rho_{x2}(x)dx} \tag{3.6}$$

If it is assumed that the integrals in the numerator of the right hand side of Equation 3.6 are performed over the entire range where the integrands are non-zero then the substitution $x + h \rightarrow a$ and $dh \rightarrow da$ can be made (Equation 3.7). This is a reasonable assumption as the measured μ_{vis} becomes very small at large beam separations.

$$\frac{\int \mu_{\text{vis}}(h)dh}{\mu_{\text{vis}}^{\text{MAX}}} = \frac{\int \left(\int \rho_{x1}(x)\rho_{x2}(a)dx \right) da}{\int \rho_{x1}(x)\rho_{x2}(x)dx} \tag{3.7}$$

Using the fact that the bunch density profiles are normalised one obtains Equation 3.8, where the quantity Σ_x, the convolved bunch width, is defined.

$$\frac{\int \mu_{\text{vis}}(h)dh}{\mu_{\text{vis}}^{\text{MAX}}} = \frac{1}{\int \rho_{x1}(x)\rho_{x2}(x)dx} = \sqrt{2\pi}\Sigma_x \tag{3.8}$$

By performing a similar separation of the beams in the vertical (y) direction one obtains Σ_y. Equation 3.4 can then be written in terms of Σ_x and Σ_y to get an expression for the bunch luminosity which does not require knowledge of the bunch density profiles (Equation 3.9).

$$\mathscr{L}_b = \frac{f_r n_1 n_2}{2\pi\Sigma_x\Sigma_y} \tag{3.9}$$

A measurement of the absolute bunch luminosity at a certain time allows the calibration of σ_{vis} for each detector and algorithm using Equation 3.3, which is rewritten in terms of Σ_x, Σ_y and $\mu_{\text{vis}}^{\text{MAX}}$ in Equation 3.10.

$$\sigma_{\text{vis}} = \mu_{\text{vis}}^{\text{MAX}} \frac{2\pi\Sigma_x\Sigma_y}{n_1 n_2} \tag{3.10}$$

The value of $\mu_{\text{vis}}^{\text{MAX}}$ and the bunch population product $n_1 n_2$ can be different for each pair of colliding bunches. However the value of σ_{vis} is a property of the detector, and one should therefore measure the same value for each BCID. This enables a consistency check on the vdM scan procedure and any disagreement is a source of systematic uncertainty on μ_{vis} and therefore the luminosity.

In an ideal scenario μ_{vis} could be measured continuously as a function of beam separation allowing $\int \mu_{\text{vis}}(h)dh$ (and therefore Σ_x and Σ_y) to be determined exactly. However in order to obtain a precise measurement of μ_{vis} the beams are held for a period of around 45 seconds at a constant separation. Due to time constraints μ_{vis} is measured at a limited number of beam separation steps (generally 25 in the ATLAS 2012 vdM scans). The Σ values are therefore determined by performing a fit to the curve of μ_{vis} versus beam separation (Σ_x is obtained from the x-scan and Σ_y

from the y-scan). Example function choices for the fit are a Gaussian plus a constant background or the sum of two Gaussian functions (double Gaussian) plus a constant background. Any background term is subtracted from data before determining Σ. Note if the curve is fitted with a single Gaussian then Σ is equal to the width of that Gaussian. Note also that Equations 3.9 and 3.10 are still valid when the two beams have a non-zero crossing angle [29].

VdM scans were not employed at the Tevatron for use in luminosity calibration for the technical reason that the counter-rotating proton and anti-proton beams shared the same beam-pipe and were steered by the same magnets — as such they could not be magnetically separated [31]. Instead the measured rates in a particular luminosity detector were converted to an absolute luminosity using a measurement of the total $p\bar{p}$ inelastic cross-section (determined from an application of the optical theorem) and then using a Monte Carlo simulation to estimate the detector acceptance [31].

3.4 ATLAS Luminosity measurement in 2012

The luminosity in ATLAS is measured using a variety of detectors [29], each of which measure one or more observables. These can be divided into two main categories, bunch-sensitive and bunch-integrating detectors. Bunch-sensitive detectors can measure the luminosity of individual BCIDs, for which example observables are 'event counting' in which a particular BCID either passes or fails some criteria and 'hit counting' in which the number of detector channels with a signal above some value is counted per BCID. These are described in more detail in Section 3.4.1. Bunch-integrating detectors, described in Section 3.4.2, measure a time averaged quantity, such as the currents in a calorimeter, and therefore cannot distinguish between separate BCIDs.

The importance of multiple methods for measuring the luminosity is illustrated in Figure 3.1 [32]. This shows, as a function of time, the fractional deviation in the average number of interactions per BCID obtained using a selection of different methods with respect to the primary measure in 2012. In principle each method is measuring the same quantity, but the fact that there are a relative changes in the fractional deviation over time indicates that the efficiency of one of more methods to measure the luminosity is not constant. The extent to which the different methods agree over long time periods is termed 'long-term stability' and was in 2012 the dominant contribution (2%) to the total systematic uncertainty on the luminosity measurement.

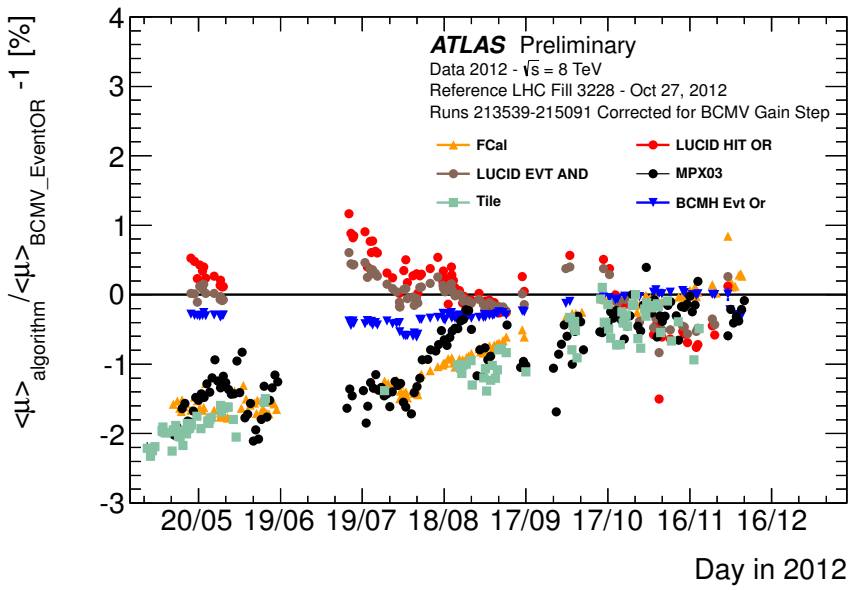

Figure 3.1: Fractional deviation in the number of interactions per BCID $\langle\mu\rangle$ (averaged over all colliding bunch pairs), obtained using different methods with respect to the primary measure in 2012 (BCMV EventOR) as a function of time in 2012. Each point shows the mean deviation for a single run compared to a reference run taken on October 27, 2012 [32].

3.4.1 Bunch-sensitive detectors and algorithms

The preferred measurement of the luminosity in 2012 was obtained from the Beam Conditions Monitor (BCM). The BCM is formed of a station of four modules either side of the interaction point at z = ±184 cm. The modules in a station are distributed in a cross-pattern around the beam-axis at $|\eta| = 4.2$, as shown in Figure 3.2 [33], and each module consists of two back-to-back diamond sensors, read out in parallel. Diamond was chosen for its radiation hardness and fast signal formation [34].

The BCM's primary purpose is to monitor beam particle loss, which could potentially cause detector damage, and to send a signal to the LHC to abort and dump the beam if this becomes too great. The fast response and readout time required of the BCM also enables a bunch-by-bunch measurement of the luminosity. The horizontal and vertical modules are read-out separately enabling two measurements of the luminosity, named BCMH and BCMV, which are treated as being two independent detectors.

Two event counting algorithms are used to obtain μ_{vis} (and therefore the luminosity): EventOR in which a bunch crossing is counted as having passed if there is at least one hit in the BCM station on either side of the interaction point (sides A

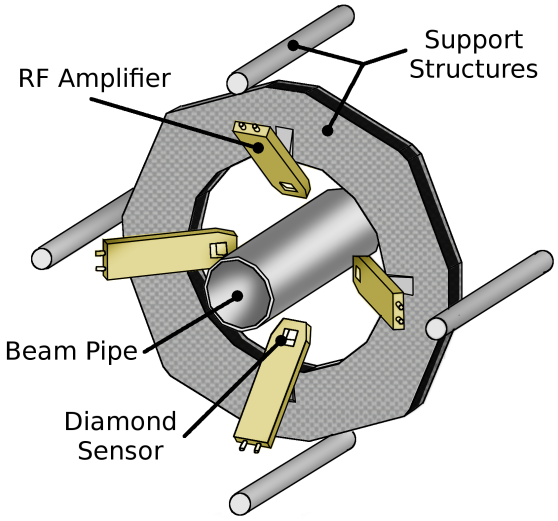

Figure 3.2: A diagram of one BCM station indicating the position of the four modules around the beam-pipe [33].

and C), and EventAND in which a bunch crossing passes only there is a hit in both BCM stations.

If one assumes that the number of interactions in a bunch crossing follows a Poisson distribution, the probability of a bunch crossing passing the EventOR algorithm (at least one hit) is equal to one minus the probability of observing zero hits. This is shown in Equation 3.11, where N_{EventOR} is the number of bunch crossings passing the EventOR algorithm in a given time interval and N_{BCID} is the total bunch crossings in that time [29].

$$P_{\text{EventOR}}\left(\mu_{\text{vis}}^{\text{OR}}\right) = 1 - e^{-\mu_{\text{vis}}^{\text{OR}}} = \frac{N_{\text{EventOR}}}{N_{\text{BCID}}} \tag{3.11}$$

One can rearrange Equation 3.11 in order to obtain an expression for $\mu_{\text{vis}}^{\text{OR}}$ as a function of the event counting rate as shown in Equation 3.12.

$$\mu_{\text{vis}}^{\text{OR}} = -\ln\left(1 - \frac{N_{\text{EventOR}}}{N_{\text{BCID}}}\right) \tag{3.12}$$

An expression for $\mu_{\text{vis}}^{\text{AND}}$ is derived in a similar fashion, but the calculation is slightly more involved. The probability of a bunch crossing pass the EventAND algorithm (at least one hit in both sides A and C) is equal to one minus the probability of there being no hit on at least one side [35]. This is expressed in Equation 3.13 as one minus the probability of no hits on side A, minus the probability of no hits on

side C, plus (to avoid double-counting) the probability of no hit either side.

$$P_{\text{EventAND}}\left(\mu_{\text{vis}}^{\text{AND}}\right) = 1 - e^{-\mu_{\text{vis}}^{\text{A}}} - e^{-\mu_{\text{vis}}^{\text{C}}} + e^{-\mu_{\text{vis}}^{\text{OR}}} = \frac{N_{\text{pass EventAND}}}{N_{\text{BCID}}} \tag{3.13}$$

Equation 3.13 can be simplified using the relation between the visible interaction rate for each algorithm, $\mu_{\text{vis}}^{\text{OR}} = \mu_{\text{vis}}^{\text{A}} + \mu_{\text{vis}}^{\text{C}} - \mu_{\text{vis}}^{\text{AND}}$, and by assuming that the acceptance for the detectors in sides A and C is approximately equal, that is, $\mu_{\text{vis}}^{\text{C}} \approx \mu_{\text{vis}}^{\text{A}}$. This is shown in Equation 3.14.

$$\frac{N_{\text{pass EventAND}}}{N_{\text{BCID}}} = 1 - 2e^{-\frac{\mu_{\text{vis}}^{\text{AND}} + \mu_{\text{vis}}^{\text{OR}}}{2}} + e^{-\mu_{\text{vis}}^{\text{OR}}} \tag{3.14}$$

Finally one can use Equation 3.3 to express Equation 3.14 in terms of $\mu_{\text{vis}}^{\text{AND}}$ and the visible cross-sections $\sigma_{\text{vis}}^{\text{OR}}$ and $\sigma_{\text{vis}}^{\text{AND}}$, which are determined in the vdM scans (Equation 3.15) [29].

$$\frac{N_{\text{pass EventAND}}}{N_{\text{BCID}}} = 1 - 2e^{-\left(1+\frac{\sigma_{\text{vis}}^{\text{OR}}}{\sigma_{\text{vis}}^{\text{AND}}}\right)\frac{\mu_{\text{vis}}^{\text{AND}}}{2}} + e^{-\left(\frac{\sigma_{\text{vis}}^{\text{OR}}}{\sigma_{\text{vis}}^{\text{AND}}}\right)\mu_{\text{vis}}^{\text{AND}}} \tag{3.15}$$

Unlike Equation 3.11, one cannot analytically invert Equation 3.15 to obtain an expression for $\mu_{\text{vis}}^{\text{AND}}$, so this is instead done numerically. The primary measure of the luminosity in 2012 was obtained from BCMV using the EventOR algorithm.

The other detector used to make a precise bunch-by-bunch measure of the luminosity is LUCID (LUminosity measurement using Cerenkov Integrating Detector) [29]. A LUCID detector is situated either side of the interaction point at $z = \pm 17\,\text{m}$ and consists of sixteen aluminium tubes. These cover the pseudorapidity range $5.6 < |\eta| < 6.0$ and are connected via quartz windows to photomultiplier tubes (PMTs). Charged particles travelling above the local speed of light in the quartz emit Cerenkov radiation, the signal from which is amplified by the PMTs. Note that at the start of LUCID operations, and for a small fraction of 2012 data-taking, the aluminium tubes were filled with C_4F_{10} gas, which induced a higher flux of Cerenkov radiation. This was removed in order to reduce the device sensitivity and allow measurements of a wider range of luminosities [36].

LUCID was designed with luminosity measurements as its primary purpose and as such can perform more sophisticated measurements than BCM. In addition to event counting, hit counting and particle counting algorithms can also be employed [29].

Two further methods for measuring the luminosity involve counting the number of tracks or vertices (interaction points) reconstructed by ATLAS software. Whilst

bunch-sensitive luminosity measurements can be made with these methods, an extended time-period is required to accumulate enough events due to the limited read-out rate of the triggers used. In the case of vertex-counting μ_{vis} is found by determining the average number of vertices per events satisfying some criteria and then applying corrections for known non-linear behaviour with increasing pile-up [29]. For track counting μ_{vis} is simply the average number of tracks per event.

3.4.2 Bunch-integrating detectors

Both the hadronic tile calorimeter (TileCal) and the forward calorimeter (FCal) are used to estimate the luminosity. In the case of TileCal, PMT currents in a selection of cells with a pseudorapidity range $|\eta| \approx 1.25$ are measured, whilst for FCal the currents on the high-voltage lines supplying the liquid argon modules are measured [37]. After performing corrections for pedestals and non-collision backgrounds the currents measured are assumed to be proportional to the luminosity [29].

Neither of these calorimetry methods are able to distinguish the luminosity of individual BCIDs and also not all of the calorimeter cells used are sensitive to the low luminosity in vdM scans. As such an independent calibration of the luminosity of TileCal and FCal cannot be performed and instead σ_{vis} is obtained by comparing the measured currents to the luminosity from LUCID or BCM: either at the peak of a vdM scan (TileCal) or in a particular reference run (FCal).

The luminosity is also measured using a series of thirteen Medipix (MPX) pixel detectors distributed throughout the ATLAS detector and read-out independently [38]. These detectors measure a bunch-integrated luminosity by counting the number of pixel-hits in a certain time window (which depends on the detector in question). As for the TileCal and FCal measurements the MPX detectors cannot provide an independent luminosity calibration. However changes in the MPX luminosity over time with respect to BCM (as in Figure 3.1) contribute towards an estimate of the uncertainty on long-term stability.

3.4.3 Calibration

A total of fifteen pairs of horizontal (x) and vertical (y) van der Meer scans were performed over three calibration sessions in April, July and November 2012. Multiple measurements of σ_{vis} are therefore made close together in time to check the consistency of the vdM method and also several months apart to check the long-term stability of a detector. VdM scans may either be performed with zero beam-separation in the direction transverse to the scan (centred scans), or performed with

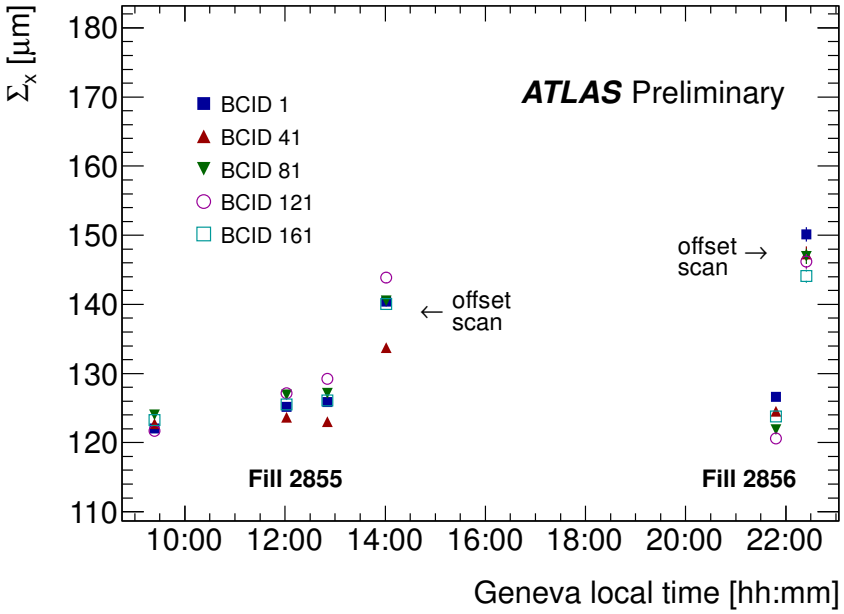

Figure 3.3: Time evolution of Σ_x for five different BCIDs, measured using the LUCID_EventOR luminosity algorithm during the van der Meer scan session of July 19, 2012. The beams remained vertically centred on each other during the first three scans of LHC fill 2855 and the first scan of fill 2856, and were separated vertically by 344 μm during the last scan in each fill [32].

a constant transverse separation (offset scans). Two of the scan pairs in each of the July and November sessions were offset scans, the remainder were centred scans.

Figure 3.3 shows the measured value of Σ_x for a series of 5 BCIDs in each of the vdM x-scans in the July session [32]. The results in the figure were obtained using the LUCID detector with the EventOR algorithm. The first three and the fifth point are from centred x-scans and the other two points (labelled as offset scans) are from x-scans in which there was a separation in y.

The bunch widths and therefore Σ_x and Σ_y are expected to gradually increase over time due to emittance[1] growth [39], which also causes a corresponding decrease in $\mu_{\text{vis}}^{\text{MAX}}$ in Equation 3.10 such that in principle σ_{vis} remains constant [29]. If the assumption of beam-factorisation held ($\hat{\rho}_1(x,y) = \rho_{x1}(x)\rho_{y1}(y)$) then the value of Σ_x measured would not depend on how separated the beams were in the y-direction. That is, one should not see the 10 to 20 percent increase in Σ_x (depending on the BCID) observed in the offset scans with respect to the centred scans.

It is clear from Figure 3.3 that the factorisation assumption only approximately holds and therefore a correction should be applied to Equation 3.10. A method for

[1]The emittance of a bunch is a measure of the constituent particles' location in position and momentum space [1].

estimating the size of this correction by forming a better understanding of the bunch density profiles is the subject of Chapter 4.

Chapter 4

Modelling bunch density profiles to estimate a correction to the luminosity for the assumption of beam-factorisation

4.1 Introduction

In order to test for and if necessary correct for the assumption of beam factorisation in the vdM method one needs knowledge of the shape of the bunch density profiles. These can be parameterised using information on the evolution of the position and size of the beam spot (or luminous region) during a vdM scan, alongside constraints from the evolution of μ_{vis}.

4.2 Beam spot information

The beam spot is defined by performing an unbinned maximum-likelihood fit of a three-dimensional (3D) Gaussian to the distribution of vertices (interaction points) collected over a certain time period. In the case of a vdM scan this period corresponds to the length of a scan step. The beam spot position in x, y and z is defined as the mean of the fitted Gaussian and the vertex-resolution corrected beam spot width in x, y and z is defined by the width of the fitted Gaussian in each of those dimensions respectively. The beam spot z-width is also alternatively referred to as the luminous length. A more detailed explanation of the fitting procedure is given in [40]. Note that the beam spot fit can either be performed using the vertices from each BCID individually or using the vertices from all BCIDs together,

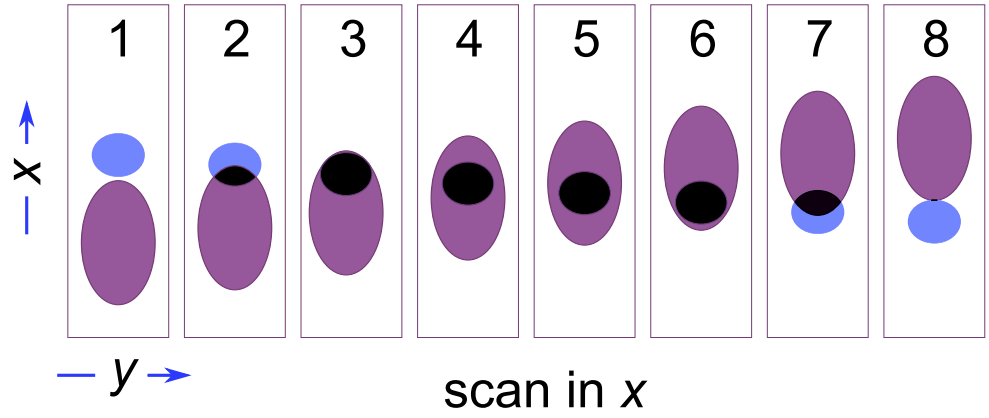

Figure 4.1: This diagram shows eight scan steps of a centred x-scan. Beam 1 in purple moves from negative x to positive x over the course of the scan and beam 2 in blue moves in the opposite direction. The overlap of the two beams in black moves in the negative x-direction.

known as 'BCID blind'. The former is the definition used in the following analysis (due to significant variations in the shape of the bunch density profiles) and as such descriptions of beam properties are assumed to refer to a particular bunch in the beam.

Qualitatively Figures 4.1, 4.2 and 4.3 show how certain qualities of the beams can result in beam spot movement in both the direction of the scan and the transverse direction. Figure 4.1 shows eight scan steps in a centred x-scan. Beam 1 in purple moves from negative x to positive x over the course of the scan whilst beam 2 in blue moves in the opposite direction. The two beams have the same y-width but beam 1 has a larger x-width. For this simplified diagram the beam spot is indicated by the area of the overlap of beams 1 and 2, coloured in black. Over the course of the scan the overlap region moves in the negative x-direction, which is the same sense as the narrower of the two beams.

Figure 4.2 shows six scan steps of a centred x-scan. In this diagram the two beams have the same x and y widths, but opposite x-y correlation. Over the course of the scan the overlap region moves in the positive y direction, transverse to the movement of the beams.

The features seen in these two figures correspond most closely to the single Gaussian beam profile in which the overlap has only one maximum (see Section 4.4.1). For more complicated beam profiles such as the double Gaussian for which there might be multiple maxima, the idea that the beam spot position follows the motion of the 'narrower' (for some definition) beam is still a good approximation but the rate of change of the movement and behaviour at large separation may vary. Note that for single Gaussian beams the transverse movement of the beam spot during

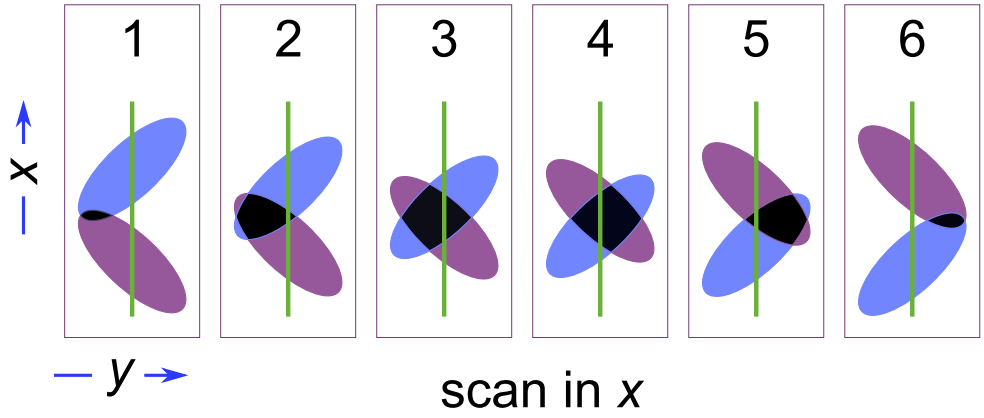

Figure 4.2: This diagram shows six scan steps of a centred x-scan. Beam 1 in purple moves from negative x to positive x over the course of the scan and beam 2 in blue moves in the opposite direction. The overlap of the two beams in black moves in the positive y-direction.

a scan does not alone fully constrain the value of the x-y correlation term of each beam [41]. A further constraint is obtained from the value of μ_{vis} as a function of separation, but one must also examine the evolution of the x-y correlation of the beam spot itself over the course of the scan.

Figure 4.3 shows six scan steps of a one-dimensional x-scan in which the beams are modelled as double Gaussian. The top set of diagrams show beam 1 moving from zero separation to positive x over the course of the scan. The contributions to the density profile from the two single Gaussians ('narrow' and 'broad') are highlighted in different shades of purple. The corresponding set of diagrams for beam 2, moving from zero separation to negative x, are show in the middle row. The bottom row shows the overlap of the two beams at each scan step, which in one dimension is the product of the density profiles of the two beams. Note that the scale on the vertical axis is not the same at each scan step.

At small beam separation the largest contribution to the overlap is from the two narrow Gaussians and the width of the overlap is narrow as well. At larger separations there are contributions to the overlap from the narrow Gaussian of each beam with the broad Gaussian of the other. This results in a double peaked structure and causes the overall width of the overlap region to increase. At the largest separations the dominant contribution is from the product of the two broad Gaussians and the overall width begins to decrease.

An analysis of beam spot data to parameterise the beam density profiles using a single Gaussian model has already been performed [42]. The analysis in this thesis extends and expands on that work to include other models and to consider further information (for example, the evolution of beam spot width).

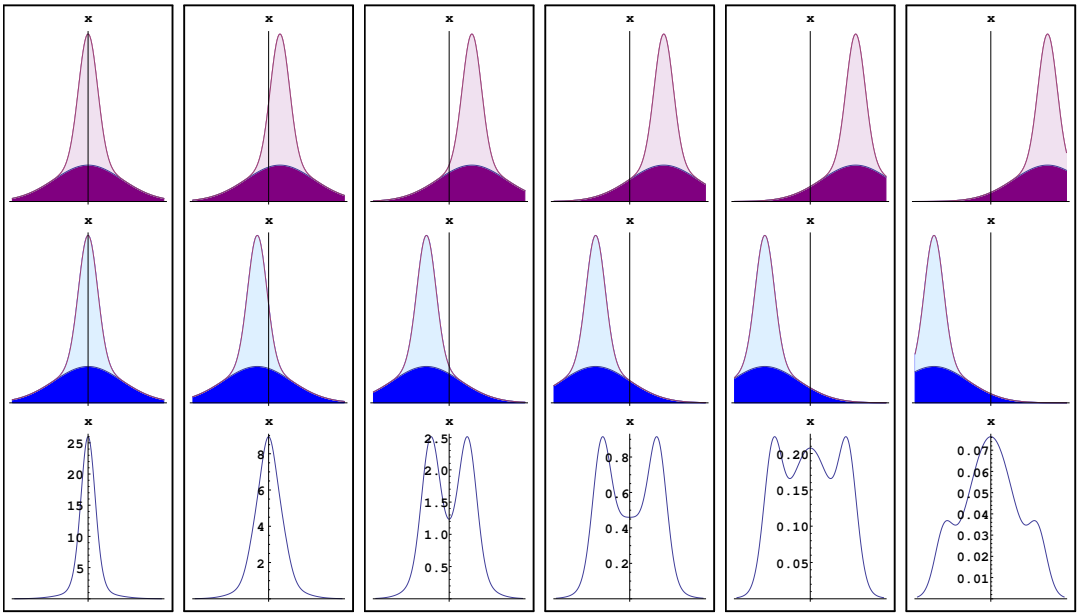

(a) 1 (b) 2 (c) 3 (d) 4 (e) 5 (f) 6

Figure 4.3: This diagram shows six scan steps of a one-dimensional scan in which the beams are modelled as double Gaussian. Beam 1 in purple (top set of diagrams) moves from zero separation to positive x over the course of the scan and beam 2 in blue (middle set of diagrams) moves in the opposite direction. The overlap of the two beams (bottom set of diagrams) changes shape during the course of the scan.

4.3 Calculating the evolution of the luminosity and the beam spot observables given single beam density profiles

The distribution of vertices or the luminosity density, $\mathcal{L}$, as a function of 3D position ($\mathbf{x}$) and at beam separation $(\delta x, \delta y)$ is proportional to the time integral of the product of the two beam density profiles, $\rho_1(\mathbf{x}, t)$ and $\rho_2(\mathbf{x}, t)$ [42] (Equation 4.1).

$$\mathcal{L}(\mathbf{x}, \delta x, \delta y) \propto \int \rho_1(\mathbf{x}, t, \delta x, \delta y)\rho_2(\mathbf{x}, t, \delta x, \delta y)dt \tag{4.1}$$

The luminosity, $\mathscr{L}$, is then defined as the integral of $\mathcal{L}$ over space, $\mathbf{x}$ [39]. The analytic definition of the beam spot position, $\langle \mathbf{x} \rangle$, which approximates best to a 3D single Gaussian fit to the luminosity density is the expectation value, Equation 4.2.

$$\langle \mathbf{x} \rangle (\delta x, \delta y) = \frac{\iint \mathbf{x}\rho_1(\mathbf{x}, t, \delta x, \delta y)\rho_2(\mathbf{x}, t, \delta x, \delta y)d\mathbf{x}dt}{\mathscr{L}} \tag{4.2}$$

Correspondingly the beam spot width can be very well approximated by the

standard deviation of the luminosity density, defined in Equation 4.3.

$$\sigma_{\mathcal{L}}(\delta x, \delta y) = \sqrt{\frac{\iint \mathbf{x}^2 \rho_1(\mathbf{x}, t, \delta x, \delta y)\rho_2(\mathbf{x}, t, \delta x, \delta y) d\mathbf{x} dt}{\mathscr{L}} - \langle \mathbf{x} \rangle^2 (\delta x, \delta y)} \tag{4.3}$$

Given a particular beam model and parameterisation one can determine (or 'simulate') the evolution of beam spot position and width during a scan and compare the result to data. This is the basis of the technique used to estimate the shape of the beams in this analysis. A range of observables is simulated for a given parameter set and the agreement with data is estimated using a χ^2 method. A minimisation routine is then used to modify these parameters in order to minimise the χ^2. Further details on the χ^2 minimisation are given in Section 4.5.

It can be shown that for Gaussian beam profiles the beam spot movement during a scan is linear [42]. Any departure from this behaviour in data is evidence for non-Gaussian beams and furthermore if observed in the plane transverse to the scan direction is an indication of non-factorisation.

4.4 Beam profile choices

One may choose any beam profile function to use in calculating the luminosity and beam spot variables. However functions based on the Gaussian distribution are more physically motivated from the central limit theorem of probability [1]. Three function choices are now discussed, the single Gaussian distribution, the sum of multiple Gaussian distributions (specifically the double Gaussian) and the (double) supergaussian distribution [43]. The advantage of describing a beam density profile by the sum of multiple Gaussian distributions (including the single Gaussian) is that the integral of the product of two beam density profiles can be calculated analytically, increasing the speed at which the χ^2 minimisation can be performed.

The equations in the following subsections are for two-dimensional beams and do not include the possibility for the beams to be moving in time. However the 3D time integral of the overlap of two moving 3D beams modelled as the sum of multiple Gaussians is given in Appendix A.1. That derivation also allows for the beams to have a crossing angle. However the characteristic evolution of the luminosity, beam spot width and position during a scan for the various beam profile functions discussed in this section remain valid in 3D.

4.4.1 Single Gaussian

The single Gaussian distribution, G (in two dimensions), is defined in Equation 4.4 as a function of coordinate $\mathbf{x}$, with a mean denoted by the vector $\boldsymbol{\mu}$ and with a covariance matrix denoted by $\boldsymbol{\sigma}$.

$$G(\mathbf{x}, \boldsymbol{\mu}, \boldsymbol{\sigma}) = \frac{1}{(2\pi)|\boldsymbol{\sigma}|^{\frac{1}{2}}} \exp\left(-\frac{1}{2}(\mathbf{x}-\boldsymbol{\mu})^{\mathsf{T}}\boldsymbol{\sigma}^{-1}(\mathbf{x}-\boldsymbol{\mu})\right) \tag{4.4}$$

The product of two two-dimensional Gaussian distributions, $G(\mathbf{x}, \boldsymbol{\mu}, \boldsymbol{\sigma})$ and $G(\mathbf{x}, \boldsymbol{\nu}, \mathbf{s})$ is also a Gaussian distribution $A \times G(\mathbf{x}, \boldsymbol{\alpha}, K)$, where K is given in Equation 4.5, $\boldsymbol{\alpha}$ is given in Equation 4.6, and A is given in Equation 4.7. This is the 2D luminous region.

$$K^{-1} = \boldsymbol{\sigma}^{-1} + \mathbf{s}^{-1} \tag{4.5}$$

$$\boldsymbol{\alpha} = K\left(\boldsymbol{\sigma}^{-1}\boldsymbol{\mu} + \mathbf{s}^{-1}\boldsymbol{\nu}\right) \tag{4.6}$$

$$A = \frac{\exp\left(-\frac{1}{2}\left(\boldsymbol{\mu}^{\mathsf{T}}\boldsymbol{\sigma}^{-1}\boldsymbol{\mu} + \boldsymbol{\nu}^{\mathsf{T}}\mathbf{s}^{-1}\boldsymbol{\nu} - \boldsymbol{\alpha}^{\mathsf{T}}K^{-1}\boldsymbol{\alpha}\right)\right)}{(2\pi)} \frac{|K|^{\frac{1}{2}}}{|\boldsymbol{\sigma}|^{\frac{1}{2}}|\mathbf{s}|^{\frac{1}{2}}} \tag{4.7}$$

In the case of a single Gaussian luminous region the beam spot position is just $\boldsymbol{\alpha}$ and the beam spot widths can be read from the covariance matrix K. It can be seen from Equation 4.5 that the covariance matrix is not a function of the individual beam positions (i.e., not a function of separation). This is to say that the beam spot width does not change as a function of separation when the beams are single Gaussian. Furthermore as $\boldsymbol{\alpha}$ is a linear function of $\boldsymbol{\mu}$ and $\boldsymbol{\nu}$ the beam spot movement is linear as a function of separation (in the situation where the beams are moved in equal and opposite steps as in a vdM scan).

The luminosity is given by the integral over space of the luminous region, Equation 4.8, which is just A since $G(\mathbf{x}, \boldsymbol{\alpha}, K)$ is normalised.

$$\mathscr{L} = \int A \times G(\mathbf{x}, \boldsymbol{\alpha}, K) d\mathbf{x} = A \tag{4.8}$$

Note that, in the case of two arbitrary single Gaussian beams the luminous region (itself a single Gaussian) can still be factorised. However this Gaussian may be rotated with respect to the scan plane causing Σ_x and Σ_y to be underestimated [29]. For a detailed beam spot analysis using single Gaussian beams see references [41] and [42].

4.4.2 Double Gaussian

A simple extension to the single Gaussian distribution is the weighted sum of two normalised single Gaussian distributions named the double Gaussian distribution (Equation 4.9).

$$G(\mathbf{x}, \boldsymbol{\mu}, \boldsymbol{\sigma}_1, \boldsymbol{\sigma}_2, w) = w \times G(\mathbf{x}, \boldsymbol{\mu}, \boldsymbol{\sigma}_1) + (1 - w) \times G(\mathbf{x}, \boldsymbol{\mu}, \boldsymbol{\sigma}_2) \tag{4.9}$$

The product of two double Gaussian distributions has four terms, each of which is the product of two single Gaussian distributions. Since the product of two single Gaussian distributions is also Gaussian the product of two double Gaussian distributions is just the sum of four single Gaussian distributions, each of which can be integrated analytically (using the method in Section 4.4.1).

Each of these single Gaussians has the form $A \times G(\mathbf{x}, \boldsymbol{\alpha}, K)$ (see Equations 4.5, 4.6 and 4.7). The luminosity of each of these Gaussians is given by Equation 4.8 therefore the total luminosity is the sum of the A value corresponding to each Gaussian (Equation 4.10). Here the weight factors are absorbed into the definition of A.

$$\mathscr{L} = \sum_{i=1}^{4} \int A_i \times G(\mathbf{x}, \boldsymbol{\alpha}_i, K_i) d\mathbf{x} = \sum_{i=1}^{4} A_i \tag{4.10}$$

The beam spot position (using the definition in Equation 4.2) is given by Equation 4.11.

$$< \mathbf{x} >= \frac{\sum_{i=1}^{4} A_i \boldsymbol{\alpha}_i}{\sum_{i=1}^{4} A_i} \tag{4.11}$$

Then the beam spot covariance matrix, $\boldsymbol{\Sigma}$, (in order to determine the beam spot width in each dimension using the definition in Equation 4.3) is given by Equation 4.12.

$$\boldsymbol{\Sigma} = \frac{\sum_{i=1}^{4} A_i \left(K_i + \boldsymbol{\alpha}_i \boldsymbol{\alpha}_i^{\mathsf{T}}\right)}{\sum_{i=1}^{4} A_i} - \frac{\left(\sum_{i=1}^{4} A_i \boldsymbol{\alpha}_i\right) \left(\sum_{i=1}^{4} A_i \boldsymbol{\alpha}_i\right)^{\mathsf{T}}}{\left(\sum_{i=1}^{4} A_i\right)^2} \tag{4.12}$$

There is now the possibility for non-linear movements of the beam spot position and for the beam spot width to vary during a scan. This description of the double Gaussian distribution could further be extended to the weighted sum of a larger number of single Gaussian distributions, for example the triple Gaussian or the quadruple Gaussian, etc. These are however not considered in this thesis.

4.4.3 Supergaussian

Certain features observed in the evolution of beam spot position and width in the November vdM scan session (see Section 4.6.4) could not be produced if the beam profiles were described by the sum of multiple single Gaussian distributions. Therefore the supergaussian distribution [43] is used as an alternative. The normalised supergaussian distribution in one dimension is shown in Equation 4.13, where Γ is the gamma function. The form of the supergaussian reduces to that of the single Gaussian when the parameter ϵ is zero.

$$G_{SG}(x,\mu,\sigma,\epsilon) = \frac{2^{-\frac{3+\epsilon}{2+\epsilon}}}{\sigma\Gamma\left[1+\frac{1}{2+\epsilon}\right]} \exp\left(-\frac{1}{2}\left(\frac{|x-\mu|}{\sigma}\right)^{2+\epsilon}\right) \tag{4.13}$$

Unlike for a single Gaussian there is no obvious way to generalise this form to two or three dimensions using vectors and matrices. Therefore three one-dimensional supergaussian distributions are multiplied together to form the three-dimensional supergaussian. The procedure does not allow for any x-y correlation in the beams and therefore (assuming there is not a beam crossing angle in both the x-z and y-z planes) does not allow for any transverse movement of the beam spot during a scan (see Figure 4.2).

For the case of the single Gaussian introducing x-y correlation, κ, is the same as scaling the widths of the beams in x and y and rotating around the individual beams' z-axis by an angle θ_{xy} (Equations 4.14 to 4.16).

$$\sigma_x \to \frac{1}{\sqrt{2}}\sqrt{\sigma_x^2+\sigma_y^2+\sqrt{\sigma_x^4+2\left(2\kappa^2-1\right)\sigma_x^2\sigma_y^2+\sigma_y^4}} \tag{4.14}$$

$$\sigma_y \to \frac{1}{\sqrt{2}}\sqrt{\sigma_x^2+\sigma_y^2-\sqrt{\sigma_x^4+2\left(2\kappa^2-1\right)\sigma_x^2\sigma_y^2+\sigma_y^4}} \tag{4.15}$$

$$\theta_{xy} = \arctan\left(\frac{-2\kappa\sigma_x\sigma_y}{\sigma_x^2-\sigma_y^2-\sqrt{\sigma_x^4+2\left(2\kappa^2-1\right)\sigma_x^2\sigma_y^2+\sigma_y^4}}\right) \tag{4.16}$$

The same transformation can be applied to the three-dimensional supergaussian in order to introduce x-y correlation. If κ is zero then no transformation is applied. The x-y correlation in this thesis is always given in terms of κ. For the case of zero ϵ, κ has exactly the same meaning as in the single Gaussian distribution.

As for the single Gaussian distribution (Equation 4.9) one can form a double supergaussian distribution from the weighted sum of two normalised single supergaussian distributions. Note that a form of the analytic integral of the product of

two supergaussian distributions (double or single) has not been found and therefore this is integrated numerically in this analysis.

4.5 Procedure for extracting single beam parameters

This section describes how the bunch density profiles are parameterised by minimising a χ^2 value which characterises the agreement between data and a model for the luminosity, beam spot position and width observables during a vdM scan. Section 4.5.1 provides an outline of the analysis procedure and how the minimisation is performed. Then Section 4.5.2 details the various corrections that must be applied to the model to more accurately compare to data.

4.5.1 Minimisation procedure

The χ^2 minimisation is performed using Minuit 2 [44] separately for each scan and BCID combination and for each bunch density profile model considered. For a given initial choice of parameters the luminosity, beam spot position, beam spot width and beam spot x-y correlation are then calculated at each scan step using the 'true' beam separations (the nominal separations corrected for the various effects described in Section 4.5.2). The agreement of the model with data is characterised by the χ^2 value defined in Equation 4.17, where data_i and model_i are the values of the data and model evaluated at position i, where i runs over each scan step in both the horizontal and vertical directions and over all observables, and $\sigma_{\text{data},i}$ is the uncertainty on the value of data_i.

$$\chi^2 = \sum_i \left(\frac{\text{data}_i - \text{model}_i}{\sigma_{\text{data},i}} \right)^2 \tag{4.17}$$

The observables of the model are calculated using a 3D time overlap integral. This is either done analytically in the case of double Gaussian beam profiles (see Appendix A.1 for the calculation) or numerically in the case of double supergaussian beam profiles.

In order to compare the luminosity from the model (which is the absolute luminosity) to μ_{vis} from the data (which is proportional to the absolute luminosity) the luminosity from the simulation is normalised to data. This is done by multiplying each simulated point in the luminosity curve in both the x and y-scans by a constant, which is included as one of the free variables in the minimisation routine.

At each scan point the beam widths of the simulation are modified slightly to correct for the dynamic-β effect. The size of the modification depends on amongst other things the beam separation and the values of Σ_x and Σ_y. This procedure is documented more fully in Section 4.5.2.5.

At very large beam separations the number of vertices measured during a scan step which pass certain selection criteria can be very low or zero. This means that a measurement of the beam spot position and width cannot be made. The beam separations in which there is no information on these quantities are not considered in the minimisation routine.

Plots showing the comparison between data and the model (calculated using the parameter set corresponding to the minimum χ^2 value) for each of the different observables for an example scan/BCID in each scan session are shown in Section 4.6.

Note that the coordinate systems of the ATLAS experiment and of the LHC are both right-handed systems with parallel z-axes pointing in opposite directions. This means that the sign of both the z and the x coordinates is reversed when transforming between the two systems. In the results presented, all of the beam separations are given in the LHC coordinate system and all observables are given in the ATLAS coordinate system. This means that the sign of the beam spot x and z positions and of the beam spot x-y correlation must be reversed in the simulation to correctly compare to data.

4.5.2 Corrections

The following sections describe the various corrections that are applied in the analysis. The philosophy of the corrections is that measured quantities (such as μ_{vis}, beam spot position and beam spot width) should remain unchanged (the one exception is the luminosity background subtraction), whilst corrections are applied either to the simulation beam parameters during a scan (for example, the dynamic-β correction) or to the nominal separations (for example, the orbit drift correction). The corrections are introduced in the order in which they are applied.

4.5.2.1 Luminosity background subtraction

Particles which do not originate directly from the interaction of the two bunches considered can still be detected and cause various of the luminosity algorithms to pass. The increase of μ_{vis} due to these particles is not due to an increase in absolute luminosity and therefore their contribution must be subtracted in order to compare to the simulation, which only considers the luminosity from the two colliding

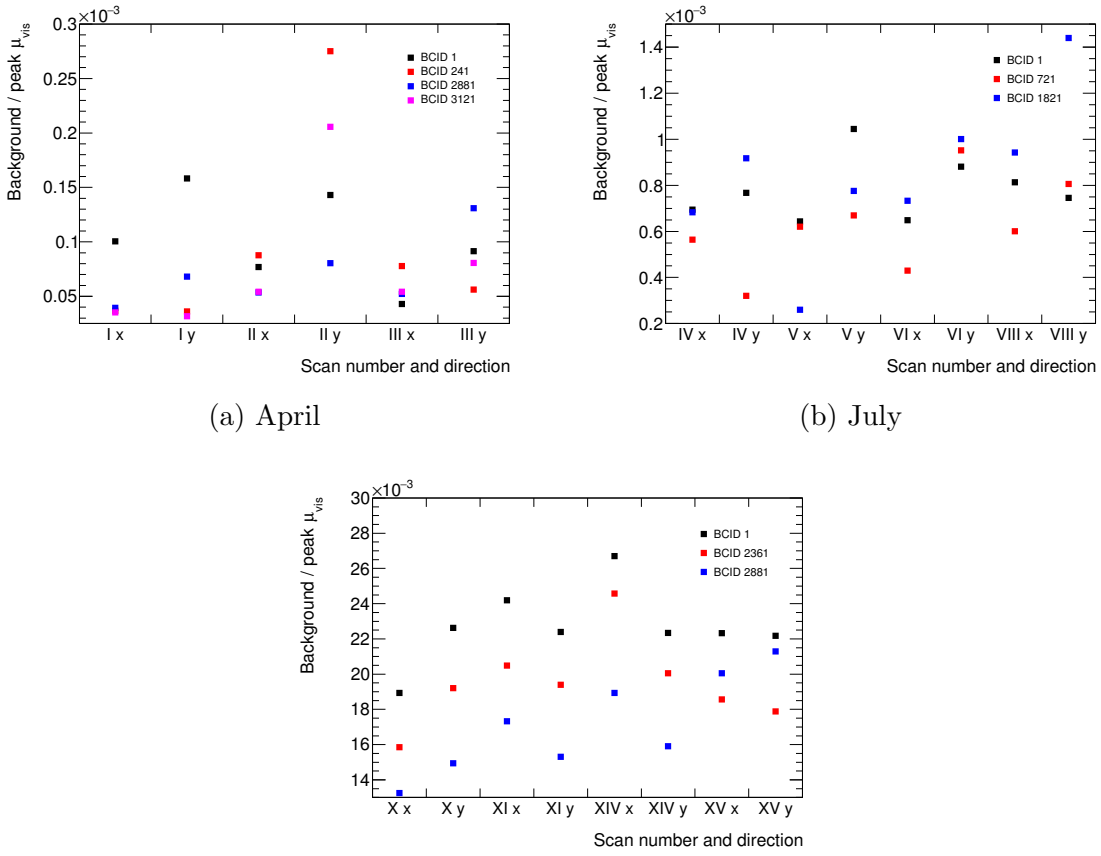

(a) April

(b) July

(c) November

Figure 4.4: The ratio of the background term to the peak μ_{vis} value as a function of scan number/direction. The ratio is shown for each BCID considered in this analysis and for each of the three scan sessions in 2012.

bunches.

The level of background to be subtracted is determined by fitting the curve of μ_{vis} against separation with either a Gaussian plus a constant term (for the November scan session) or a double Gaussian plus a constant term (for the April and July scan sessions). This constant term is assumed to be entirely background and is subtracted from the data for the comparisons with the simulation. The μ_{vis} data are taken from the BCMV detector using the EventOR algorithm.

The ratio of the background term to the peak μ_{vis} value in each scan and for each BCID is shown in Figure 4.4a for the April session, Figure 4.4b for the July session and Figure 4.4c for the November session. Note that the ratio is considerably larger in November compared to April and July as the November vdM scans took place during a period when the BCM detector was experiencing high levels of noise, the cause of which remains unexplained.

Scan number	Correction in x after x-scan (µm)	Correction in y after y-scan (µm)
V	13.4	0
X	-9.6	-13
XI	-26.6	0
XII	-16	0

Table 4.1: A summary of the in-plane corrections to beam separation made after each vdM scan.

4.5.2.2 Beam centring

A very accurate measure of the difference between the true and nominal separation in the dimension of the scan-direction (in-plane) is given by the position of the peak of the fit to μ_{vis} versus separation (with a double Gaussian plus a constant for example). A shift is applied to the in-plane nominal separations such that the peak of the scan curve is at zero separation. The transverse beam separations in the other scan direction (which are nominally zero) are also shifted by the same amount. This procedure is called the 'centring correction'.

If this correction had been observed to be large at the time the scan was performed then the beams were sometimes physically corrected by a certain amount. In the 2012 scan sessions the x-scans always precede the y-scans. This means that a physical centring correction made after the x-scan affects the transverse beam separation during a y-scan. Therefore the size of the transverse beam separation as determined by fitting the x-scan curve must be reduced by the size of the physical correction.

Table 4.1 documents the size of the physical correction applied after each scan for which it is non-zero. As detailed in Section 4.5.2.3, at the scan peak there is no additional in-plane orbit drift correction.

4.5.2.3 Orbit drift

As the scan session progresses the position of the beam at the interaction point (IP), as extrapolated from the left and right-sided Beam Position Monitors (BPMs) can change; this is known as orbit drift. The BPMs are outside the vdM bumps[1], which means that excluding other effects such as beam-beam deflection (Section 4.5.2.4) they have no knowledge of the separation of the beams during a vdM scan. Therefore if there were no orbit drift the extrapolated position of the beam at the IP would

[1]Two pairs of steering dipole magnets positioned either side of the interaction point are used to create local distortions in the beam orbit, known as 'bumps'.

remain constant throughout a scan session. The exact method of how the position of the beam at the IP is determined using a three parameter betatron oscillation fit to the BPM readings is described in [45].

If it is known by how much the beam drifts during the scan session then one can determine what the corrected or true separation of the beams was at a given nominal separation. The separation of the beams in the simulation in both x and y is set to the true separation at each scan point. The beam separations for the data are also corrected to the true separations.

The position of each beam at the IP is provided in tabular format in regular time intervals (60 seconds or less) as extrapolated from the left and from the right-sided BPMs. The consistency of the two measurements for each beam is checked and for subsequent calculations the average is used. Figure 4.5 shows the evolution of the extrapolated beam spot positions during and between April scans I and II and Figures 4.6 and 4.7 show the same thing for July scans IV, V and VI and November scans XI and XIV respectively.

It can be seen from Figure 4.5 that the extrapolated beam positions are only consistent on the order of one micron, around 10 percent of a separation step in April. Similarly in July and November (Figures 4.6 and 4.7) the consistency is on the order of five microns or less, also around 10 percent of the separation step in July and November. Therefore there could have been some additional transverse offset during one or more of these scans which is hidden by this inconsistency.

Due to the effects of beam-beam deflection the extrapolated beam positions during a scan are sensitive to the movement of the beams inside the vdM bumps. Secondly and more importantly 'knob leakage', the principle that the beam orbits may be perturbed by non-perfect closure of the vdM bumps, can also influence the extrapolated beam positions during a scan. It is difficult to decouple these effects from genuine orbit drift outside the vdM bump and so the beams are assumed to have moved linearly between the beam positions immediately before and immediately after the scan. This assumption is made both for in-plane beam movement and the beam movement in the transverse direction. The absolute extrapolated positions of the beams at the IP as determined by the orbit fit is not relevant: rather the change in these positions during a scan session. Therefore one is able to set the in-plane position for a beam at the scan peak (zero true separation) to be zero by adding a constant offset.

A summary of the corrections applied to the individual beam positions are documented below, where the nominal positions of beam 1 are equal to the corresponding nominal separations divided by two and the nominal positions of beam 2 are equal to

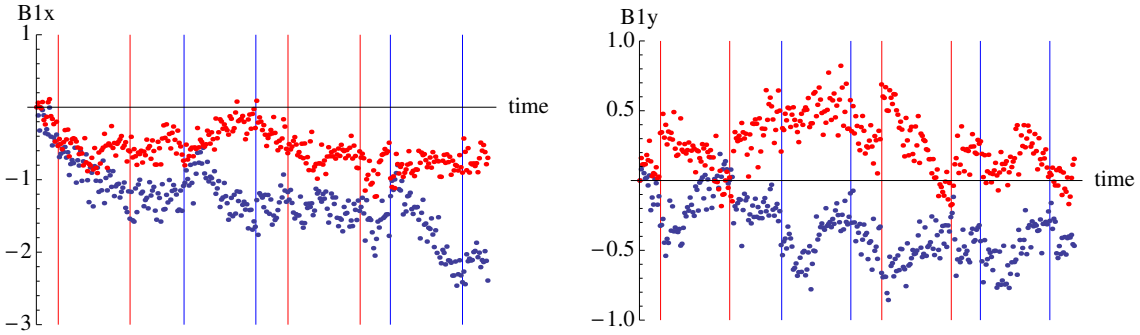

(a) Beam 1 x

(b) Beam 1 y

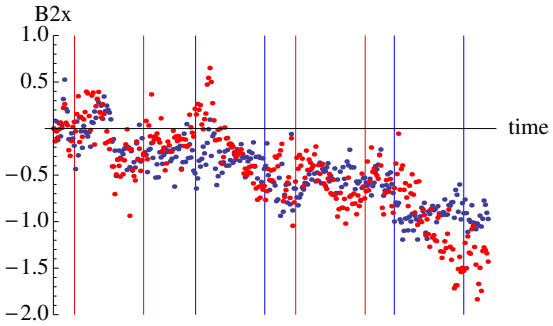

(c) Beam 2 x

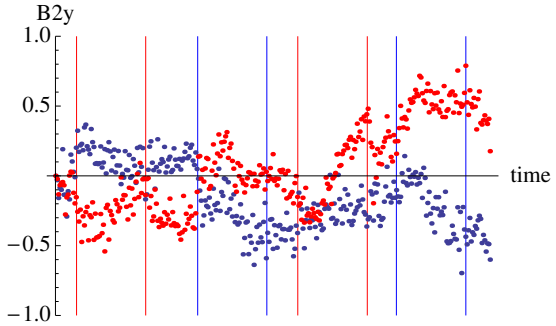

(d) Beam 2 y

Figure 4.5: The evolution of the extrapolated beam spot positions at the IP from the left (blue points) and from the right (red points) as a function of time during and between scans I and II. The x-scans take place between the red vertical lines and the y-scans between the blue vertical lines. Figures 4.5a and 4.5c show the evolution of the horizontal positions of beams 1 and 2 respectively and Figures 4.5b and 4.5d show the evolution of their vertical positions. The separations are given in microns.

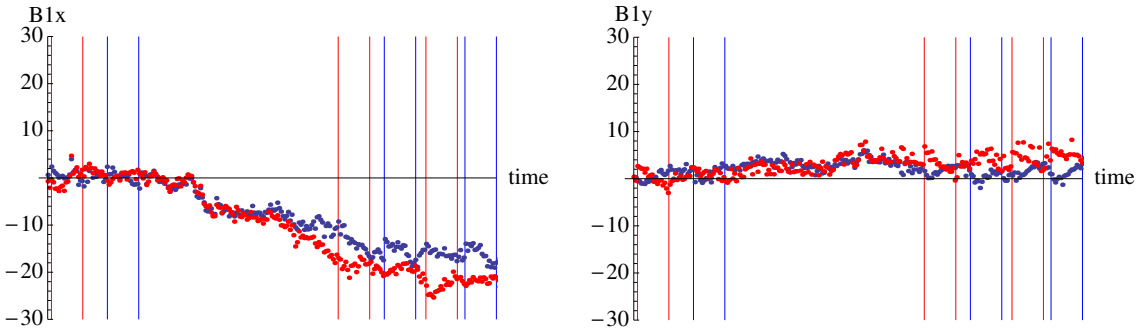

(a) Beam 1 x

(b) Beam 1 y

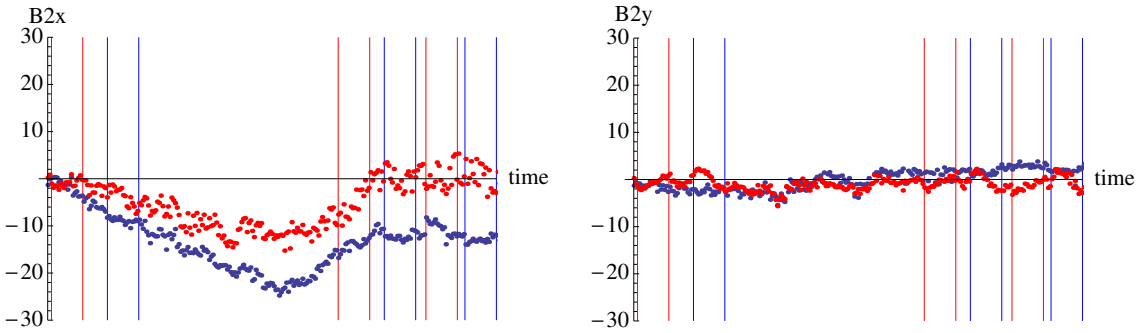

(c) Beam 2 x

(d) Beam 2 y

Figure 4.6: The evolution of extrapolated beam spot positions at the IP from the left (blue points) and from the right (red points) as a function of time during and between scans IV, V and VI. The x-scans take place between the red vertical lines and the y-scans between the blue vertical lines. Figures 4.6a and 4.6c show the evolution of the horizontal positions of beams 1 and 2 respectively and Figures 4.6b and 4.6d show the evolution of their vertical positions. The separations are given in microns.

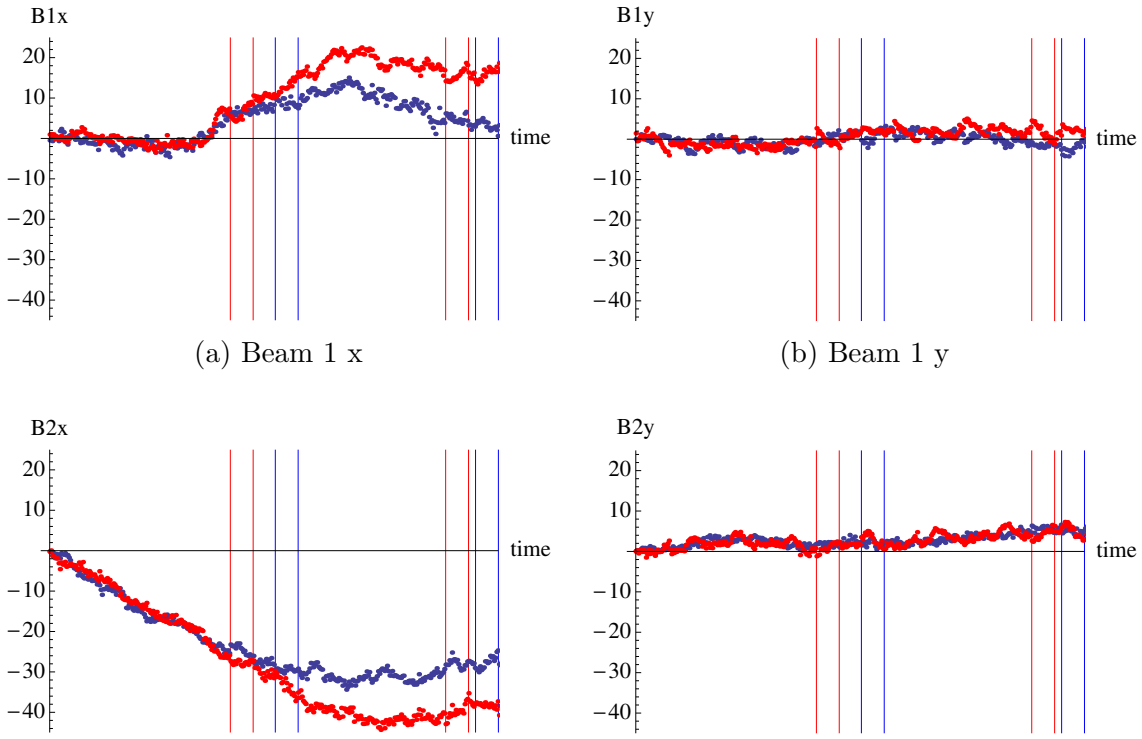

(a) Beam 1 x

(b) Beam 1 y

(c) Beam 2 x

(d) Beam 2 y

Figure 4.7: The evolution of extrapolated beam spot positions at the IP from the left (blue points) and from the right (red points) as a function of time during and between scans XI, and XIV. The x centred scans take place between the red vertical lines and the y centred scans between the blue vertical lines. Figures 4.7a and 4.7c show the evolution of the horizontal positions of beams 1 and 2 respectively and Figures 4.7b and 4.7d show the evolution of their vertical positions. The separations are given in microns. Note that offset scans XII and XIII take place between the centred scans indicated.

the negative of the corresponding nominal separations divided by two. The nominal separations have at this stage already had the centring correction applied.

The correction is applied to the individual nominal beam positions, rather than the nominal separation in order to correctly treat the variation in absolute beam spot position. If the two beams were to drift in the same direction during a scan then the correction to the nominal separation may remain small. However the absolute position of the beam spot would change relative to some zero value. The zero values in the x and y directions are included as fit parameters and are determined independently for each scan pair and BCID.

In the x-direction during an x-scan each beam position is orbit corrected by an amount determined by linearly interpolating between the positions at the times immediately before and immediately after the x-scan and by adding a constant value, which forces the correction to zero at the scan peak. In the x-direction during a y-scan each beam position is orbit corrected by an amount determined by linearly interpolating between the positions at the times immediately before and immediately after the y-scan and adding the same constant value used for the x-scan.

The corrections in the y-direction mirror those in the x-direction and are documented here for completeness. In the y-direction during an y-scan each beam position is orbit corrected by an amount determined by linearly interpolating between the positions at the times immediately before and immediately after the y-scan and by adding a constant value, which forces the correction to zero at the scan peak. In the y-direction during a x-scan each beam position is orbit corrected by an amount determined by linearly interpolating between the positions at the times immediately before and immediately after the x-scan and adding the same constant value used for the y-scan.

4.5.2.4 Beam-beam deflection

When the two beams are separated as in a vdM scan each beam receives an angular kick from the other causing an orbit shift. This effect is called beam-beam deflection. The size of the angular kick for a chosen beam depends upon the beam energy, the charge of the opposing bunch, Σ_x, Σ_y and the separation of the two beams. The size of the associated orbit shift then depends on the size of the angular kick, β^* (a measure of beam focussing at the interaction point) and the beam tune.

The consequence of beam-beam deflection is similar to that of orbit drift: to modify the nominal separation of the beams. The size of the orbit shift is calculated analytically using the Bassetti-Erskine formula [46] applied to Gaussian untilted elliptical beams. The separation of the beams in the simulation is then modified

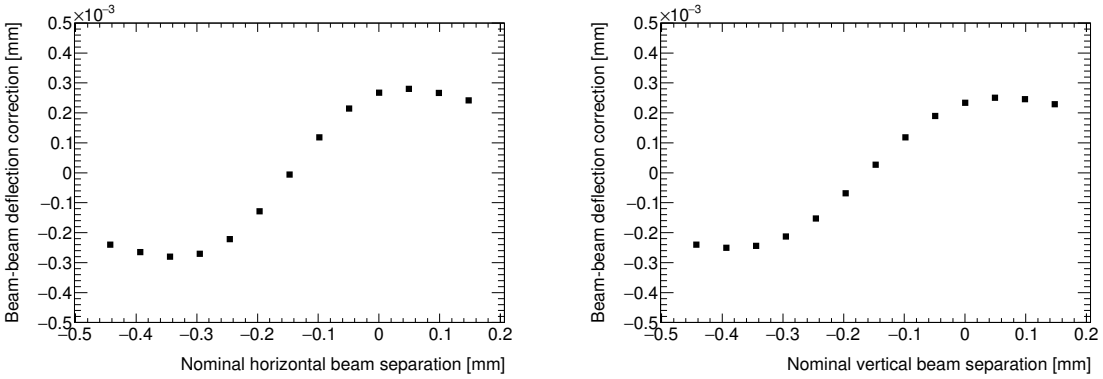

(a) x-scan (b) y-scan

Figure 4.8: The size of the in-plane beam-beam deflection correction as a function of nominal separation for scan III BCID 1.

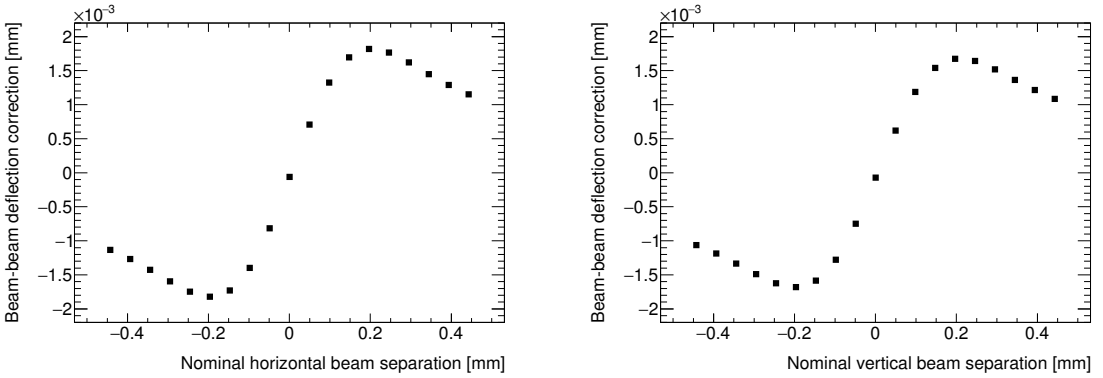

(a) x-scan (b) y-scan

Figure 4.9: The size of the in-plane beam-beam deflection correction as a function of nominal separation for scan VI BCID 1.

at each scan point (in both the in-plane and transverse directions) by the amount determined. The beam separations for the data are also corrected for this effect. Note that the separations have already had the centring correction and orbit drift correction applied before the beam-beam deflection correction is applied.

The size of the beam-beam deflection correction as a function of separation is very similar for all of the scans and BCIDs in July and November as the quantities Σ_x, Σ_y and the bunch charge have similar magnitudes and all of the other quantities are the same. The value of β^* is less in April (0.6 m) than in July or November (11 m) and the typical values of Σ are also smaller. Figure 4.8 shows the size of the in-plane beam-beam deflection correction (in both the x and y-scans) as a function of nominal separation for scan III BCID 1 and Figure 4.9 shows the same thing for scan VI BCID 1 to provide an example of the typical correction size in April and July/November respectively.

4.5.2.5 Dynamic-β

The dynamic-β effect refers to the focussing and defocussing of the particles in the bunch of one beam by the bunch of the second beam and vice versa. This causes a modification to the beam optics and therefore an enhancement or a reduction of the beam size and therefore the luminosity that is a function of separation [47].

A correction to the beam widths of the simulation (in x and y and for both Gaussians if the density profile is double Gaussian) is applied at each scan step, whilst the data are not modified. This correction is calculated using a lookup table which provides the evolution of $\Delta\beta_x/\beta^*_{x,0}$ and $\Delta\beta_y/\beta^*_{y,0}$ as a function of separation (in units of single beam sizes) in both the x and y-scans. The value $\Delta\beta$ is the change in the IP β-function due to the dynamic-β effect and β^*_0 is the assumed unperturbed value of β^* at the IP [48]. β^*_0 was 0.6 m in April and 11 m in July and November.

The values in the lookup table are calculated for particular emittance, bunch charge and β^*_0 and are simulated using the program MAD-X [49]. The dynamic-β correction scales linearly with the average bunch charge of the two beams and β^*. In addition the correction in a x-scan scales linearly with $1/\left(\sqrt{\epsilon_x}\left(\sqrt{\epsilon_x}+\sqrt{\epsilon_y}\right)\right)$ and in a y-scan with $1/\left(\sqrt{\epsilon_y}\left(\sqrt{\epsilon_y}+\sqrt{\epsilon_x}\right)\right)$, where ϵ_x and ϵ_y are the measured emittances in x and y respectively.

The following method for calculating the effect on the beam sizes due to dynamic-β is taken from reference [48] and is reproduced here for convenience. The values of ϵ_x and ϵ_y are estimated using the formulae given in Equations 4.18 and 4.19, where γ is the relativistic γ-function of the beam, which for beams of energy 4 TeV is 4263.

$$\epsilon_x = \frac{\gamma}{2\beta^*_{x,0}}\Sigma_x^2 \tag{4.18}$$

$$\epsilon_y = \frac{\gamma}{2\beta^*_{y,0}}\Sigma_y^2 \tag{4.19}$$

The values of $\Delta\beta_x/\beta^*_{x,0}$ for both scan directions are scaled by the quantity in Equation 4.20 and the values of $\Delta\beta_y/\beta^*_{y,0}$ for both scan directions are scaled by the quantity in Equation 4.21, where N is the average of the bunch population of each beam and the subscript 'sim' refers to the values of the quantities that the lookup table was simulated using.

$$\frac{N}{N_{\text{sim}}}\frac{\sqrt{\epsilon_{x,\,\text{sim}}}\left(\sqrt{\epsilon_{x,\,\text{sim}}}+\sqrt{\epsilon_{y,\,\text{sim}}}\right)}{\sqrt{\epsilon_x}\left(\sqrt{\epsilon_x}+\sqrt{\epsilon_y}\right)} \tag{4.20}$$

$$\frac{N}{N_{\text{sim}}}\frac{\sqrt{\epsilon_{y,\,\text{sim}}}\left(\sqrt{\epsilon_{y,\,\text{sim}}}+\sqrt{\epsilon_{x,\,\text{sim}}}\right)}{\sqrt{\epsilon_y}\left(\sqrt{\epsilon_y}+\sqrt{\epsilon_x}\right)} \tag{4.21}$$

An auxiliary lookup table is then constructed to obtain the quantities given in Equations 4.22 and 4.23 for both the y and the x-scans, where $\delta_{x/y}$ is the beam separation in x or y given in units of single-beam size and is related to the true separation, $\Delta_{x/y}$ (i.e., already corrected for orbit drift and beam-beam deflection) by the relation in Equation 4.24.

$$\frac{\beta^*_{x,\,\mathrm{dynamic}}\left(\delta_{x/y}\right)}{\beta^*_{x,0}} = 1 + \frac{\Delta\beta_x}{\beta^*_{x,0}}\left(\delta_{x/y}\right) \tag{4.22}$$

$$\frac{\beta^*_{y,\,\mathrm{dynamic}}\left(\delta_{x/y}\right)}{\beta^*_{y,0}} = 1 + \frac{\Delta\beta_y}{\beta^*_{y,0}}\left(\delta_{x/y}\right) \tag{4.23}$$

$$\delta_{x/y} = \sqrt{2}\,\frac{|\Delta_{x/y}|}{\Sigma_{x/y}} \tag{4.24}$$

As the lookup table only provides values in discrete steps of $\delta_{x/y}$ a linear interpolation between the two closest values to the actual separation is performed to obtain the required correction. The values of the simulated x-widths corrected for dynamic-β at a particular true separation are obtained by multiplying the uncorrected x-widths by the square root of the quantity in Equation 4.22 (Equation 4.25). Similarly the corrected y-widths are obtained by multiplying the uncorrected y-widths by the square root of the quantity in Equation 4.23 (Equation 4.26).

$$\sigma_{x,\,\mathrm{corrected}}\left(\Delta_{x/y}\right) = \sqrt{\frac{\beta^*_{x,\,\mathrm{dynamic}}\left(\delta_{x/y}\right)}{\beta^*_{x,0}}}\,\sigma_x\left(\Delta_{x/y}\right) \tag{4.25}$$

$$\sigma_{y,\,\mathrm{corrected}}\left(\Delta_{x/y}\right) = \sqrt{\frac{\beta^*_{y,\,\mathrm{dynamic}}\left(\delta_{x/y}\right)}{\beta^*_{y,0}}}\,\sigma_y\left(\Delta_{x/y}\right) \tag{4.26}$$

Figure 4.10a shows the value of the factor multiplying the x-widths (black) and multiplying the y-widths (red) as a function of nominal separation for the x-scan of scan III BCID 1 and Figure 4.10b shows the same thing for the y-scan of scan III BCID 1. The size of the factor at a particular separation is similar for all scans and BCIDs in April. Figure 4.11 shows the corresponding plots for scan VI BCID 1. The size of the factor at a particular separation is similar for all scans and BCIDs in July and November.

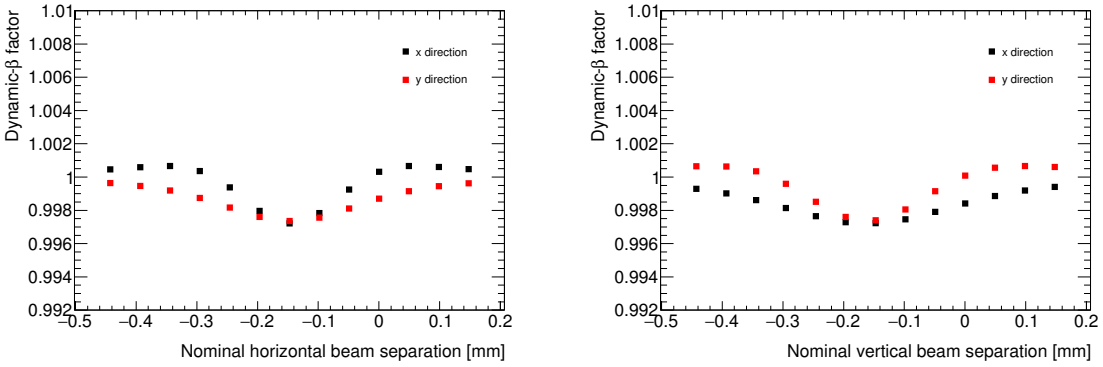

(a) x-scan

(b) y-scan

Figure 4.10: The size of the factor multiplying the x-widths (black) and multiplying the y-widths (red) as a function of nominal separation for the x-scan (Figure 4.10a) and for the y-scan (Figure 4.10b) of scan III BCID 1.

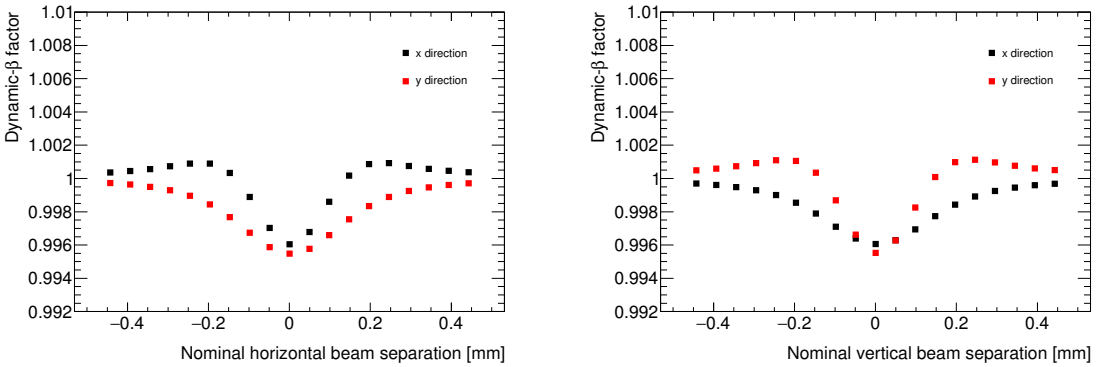

(a) x-scan

(b) y-scan

Figure 4.11: The size of the factor multiplying the x-widths (black) and multiplying the y-widths (red) as a function of nominal separation for the x-scan (Figure 4.11a) and for the y-scan (Figure 4.11b) of scan VI BCID 1.

Parameter	April	July	November
Emittance [µm]	3	3-4	2.5-3.2
β^* [m]	0.6	11	11
Number of colliding bunches	35	35	29
Approximate number of protons per bunch ($\times 10^{10}$)	7	8	9

Table 4.2: A summary of the key parameters of each vdM session in 2012.

4.6 Results

4.6.1 Introduction

This section presents the results of the analysis. Three vdM scan sessions are examined, April, July and November 2012. A summary of the key parameters of each session is provided in Table 4.2.

For each scan session plots of the evolution of luminosity, beam spot position, beam spot width and beam spot x-y correlation with separation for a particular vdM scan and BCID are shown. These compare the data and the model, which is calculated using the set of beam parameters that minimised the χ^2 between the two. That set of parameters is also given alongside the χ^2 value. Note that the uncertainties on the data are statistical in nature only.

Then the extent to which the factorisation assumption holds in each centred scan is estimated using the best fit model. Firstly the luminosity at zero separation is calculated exactly using the formulae in Appendix A.1 and this is denoted the true luminosity. This calculation makes no assumption of the level of factorisation of the beams.

Then the ratio is taken of the true luminosity to the luminosity of the same model but estimated using the vdM method [29] which assumes factorisation. This is denoted the vdM luminosity. Since the quantities n_b, n_f, n_1 and n_2 cancel in this ratio the relevant expression for the luminosity assuming factorisation is given in Equation 4.27.

$$\mathscr{L} = \frac{1}{2\pi\Sigma_x\Sigma_y} \tag{4.27}$$

Two techniques to obtain the vdM luminosity were investigated. In the first technique the vdM luminosity is calculated exactly using a numerical integral of a smooth luminosity curve at zero transverse separation. In this case the ratio of the true luminosity to the vdM luminosity is denoted R. In the second technique the

vdM luminosity is calculated by simulating the scan curve at the same separations as in data (and zero separation in the transverse plane) and then fitting the curve with the same function as used in the analysis of the corresponding data (other than a possible constant term). In this case the ratio of the true luminosity to the vdM luminosity is denoted R_{vdM}.

It was found that R_{vdM} was a less suitable variable than R to characterise the level of non-factorisation because it suffers from an additional uncertainty due to the choice of fit-function and was therefore dropped from further consideration.

The ratio R is interpreted as the factor by which the measured absolute luminosity should be multiplied (and therefore by which the measured σ_{vis} must be divided) in order to correct for the vdM factorisation assumption.

4.6.2 April

The April scan session consisted of three centred scans (I, II, and III) and took place on 16th April 2012. All scans were completed in LHC Fill 2520 and ATLAS run number 201351. There were 35 colliding bunches, of which four (1, 241, 2881 and 3121) have associated beam spot evolution data. The nominal β^* was 0.6 m.

The function which was found to best describe the bunch density profiles in the April sessions is the double Gaussian. A comparison between data from scan I, BCID I (black points) and the best-fit model (red line) for various observables is presented in Figures 4.13 (x, or horizontal scan) and 4.14 (y, or vertical scan). The level of agreement between the data and model is representative of that for the other scan and BCID combinations in the April session (see Table 4.4).

Figure 4.13a shows the specific μ_{vis} (μ_{vis} divided by $n_1 n_2$) as a function of separation for the BCMV detector and EventOR algorithm. As described in Section 4.5.1 the luminosity of the model is normalised to the data by multiplying each model point in the luminosity curve by a constant which is a free variable in the minimisation routine. Figures 4.13b, 4.13c and 4.13d then show the evolution of the x, y and z beam spot positions respectively with separation. Figures 4.13e, 4.13f and 4.13g then show the evolution of the x, y and z beam spot widths respectively with separation. Finally Figure 4.13h shows the evolution of the beam spot x-y correlation with separation. The same series of plots for the y-scan is then shown in Figure 4.14. Underneath each plot is displayed a residual plot on which is plotted for each scan point the value of the data minus the value of the model divided by the uncertainty on the data.

Then Table 4.3 displays the set of model beam parameters that minimised the χ^2 value between data and model. The double Gaussian beam parameters comprise

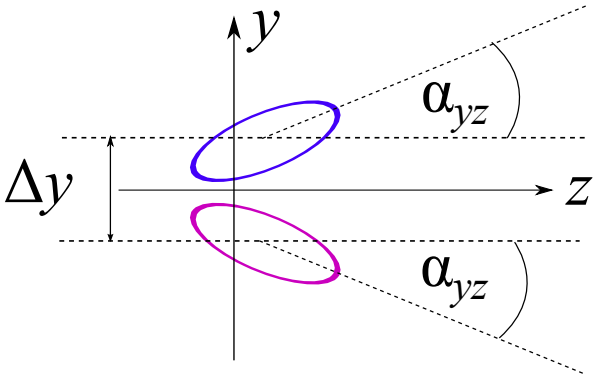

Figure 4.12: This diagram illustrates the definition of the half-crossing angle in the y-z plane, α_{yz}. The situation of non-zero beam separation in the y-direction is depicted. The half-crossing angle in the x-z plane, α_{xz} is defined analogically.

(for each beam) the widths of Gaussian 'a' and Gaussian 'b' in each dimension ($\sigma_{x,a}$, $\sigma_{x,b}$, $\sigma_{y,a}$, $\sigma_{y,b}$, $\sigma_{z,a}$, $\sigma_{z,b}$), the x-y correlation for Gaussian 'a' and Gaussian 'b' (κ_a, κ_b) and the weight of Gaussian 'a' (w). The half-crossing angle in the x-z and y-z planes is also provided (α_{xz} and α_{yz}), the definition of which is illustrated by Figure 4.12. Then the χ^2 and χ^2 per number of degrees of freedom (NDF) is given along with the correction ratio R defined in Section 4.6.1.

The use of double Gaussian beam profiles allows the data observables to be described reasonably well, but the χ^2/NDF is not as low as for the July and November scans. The plots which give a large contribution to the χ^2 are the vertical and longitudinal beam spot positions in both the x and y-scans (Figures 4.13c, 4.13d, 4.14c and 4.14d). Two possible contributing factors for this are provided below.

Unlike the July and November scans the April scans were conducted with a non-zero nominal beam crossing angle in the y-z plane. The vertical beam spot position depends on this angle and on the z-widths of the beams. However the angle can vary between the x-scan and the y-scan by a few µrad therefore there can be a discrepancy in absolute vertical beam spot position between the x and y-scans if it is assumed that the crossing angle is constant. One observes that the data are systematically above the simulation in the x-scan (Figure 4.13c) and systematically below it in the y-scan (Figure 4.14c).

Secondly the longitudinal beam spot position (at zero beam separation) is observed to drift throughout a scan session by 2 or 3 microns. A similar effect is also observed in standard LHC physics runs. This could account for the discrepancy between Figures 4.13d and 4.14d in which the data are systematically below the simulation in the x-scan and systematically above it in the y-scan. This effect, coupled with a drifting crossing angle could also in part account for the model to not fully

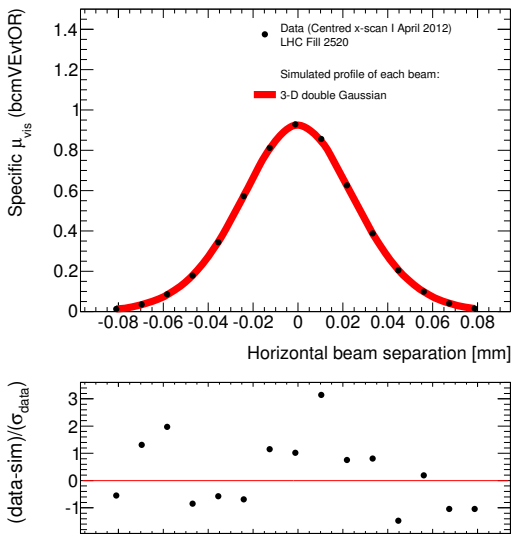

(a) Specific μ_{vis} as a function of horizontal separation

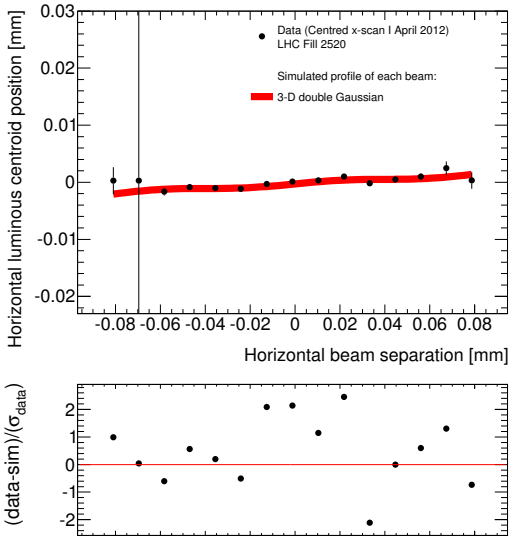

(b) Beam spot horizontal position as a function of horizontal separation

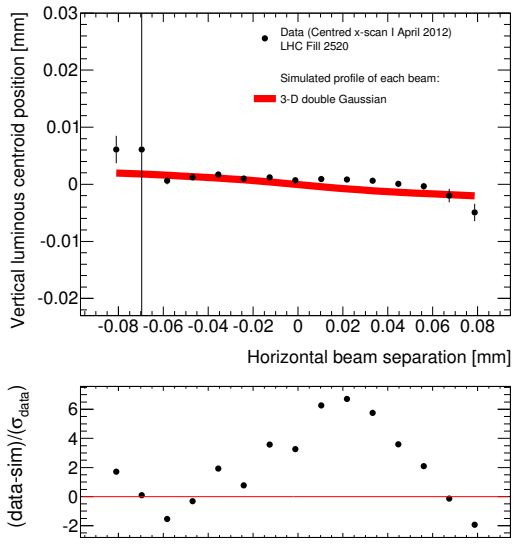

(c) Beam spot vertical position as a function of horizontal separation

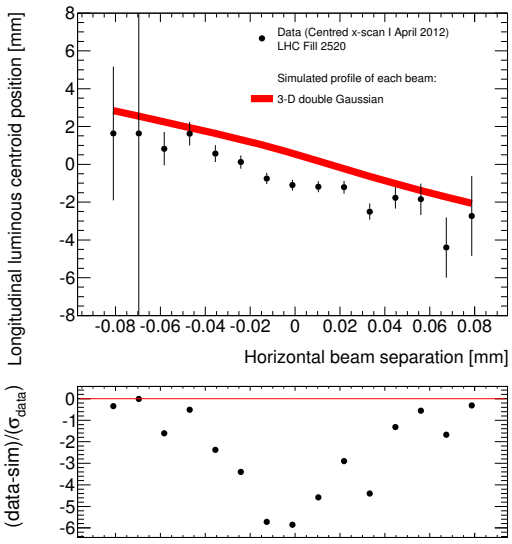

(d) Beam spot longitudinal position as a function of horizontal separation

Figure 4.13: Scan I, BCID 1, x-scan

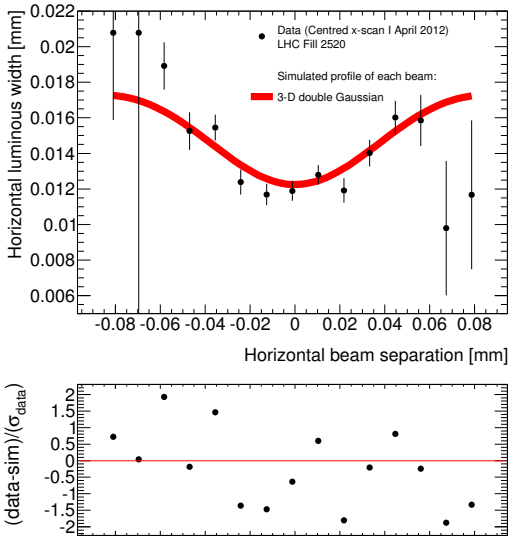

(e) Beam spot horizontal width as a function of horizontal separation

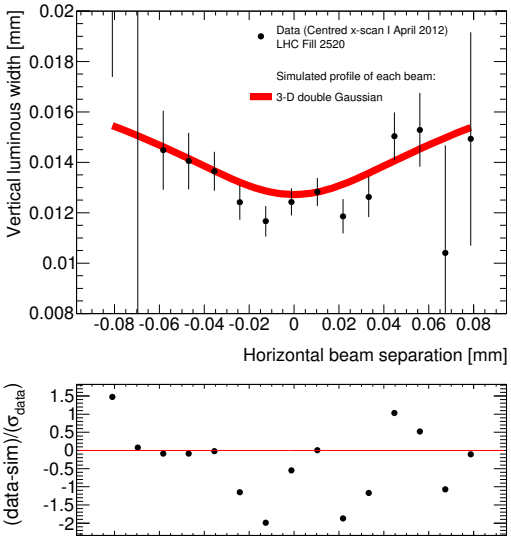

(f) Beam spot vertical width as a function of horizontal separation

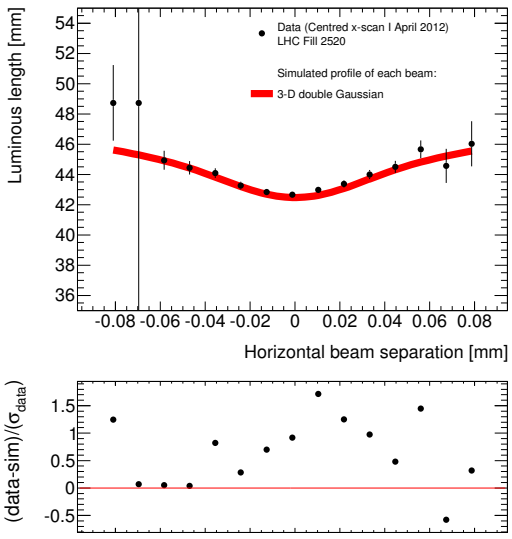

(g) Beam spot luminous length (z-width) as a function of horizontal separation

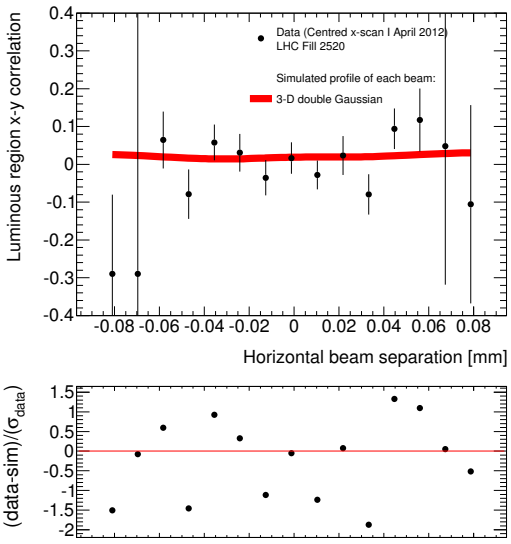

(h) Beam spot x-y correlation as a function of horizontal separation

Figure 4.13: Scan I, BCID 1, x-scan

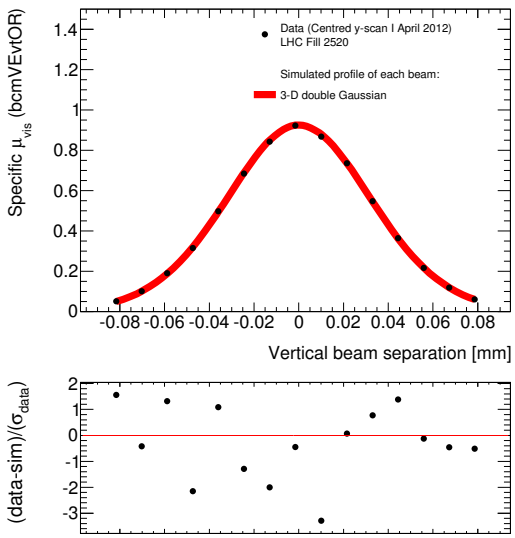

(a) Specific μ_{vis} as a function of vertical separation

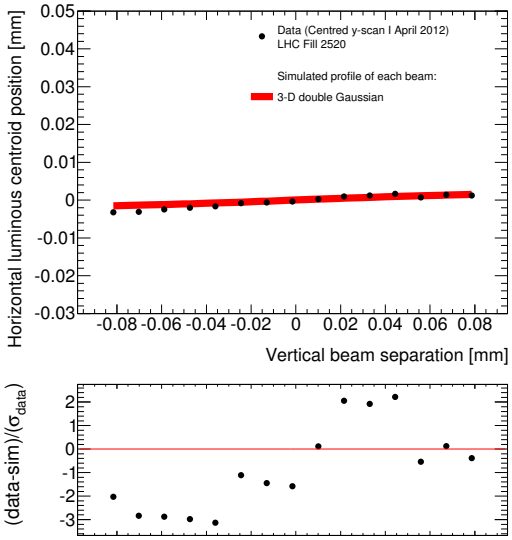

(b) Beam spot horizontal position as a function of vertical separation

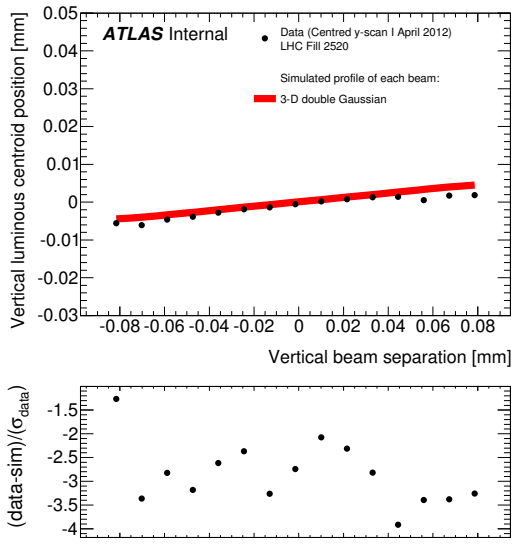

(c) Beam spot vertical position as a function of vertical separation

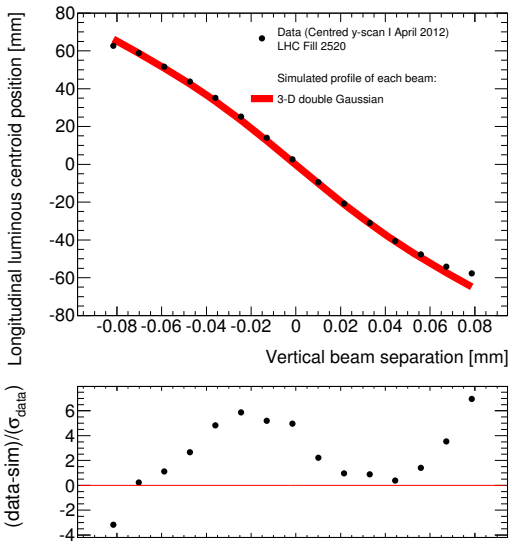

(d) Beam spot longitudinal position as a function of vertical separation

Figure 4.14: Scan I, BCID 1, y-scan

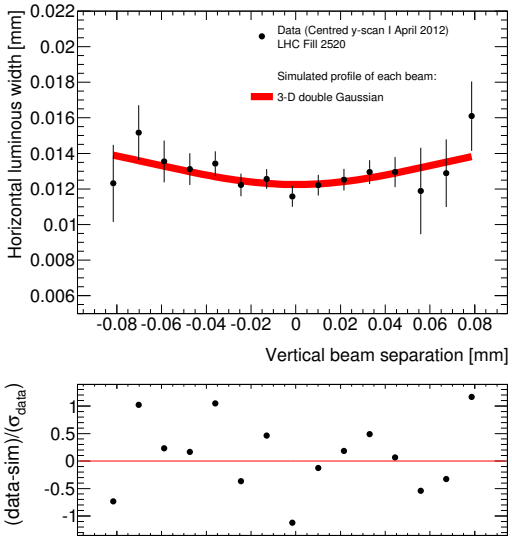

(e) Beam spot horizontal width as a function of vertical separation

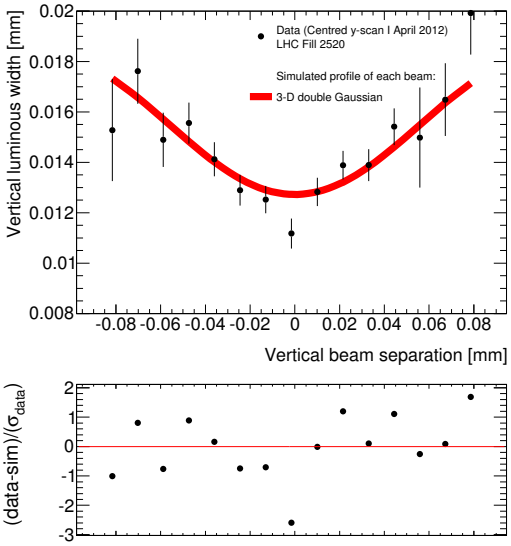

(f) Beam spot vertical width as a function of vertical separation

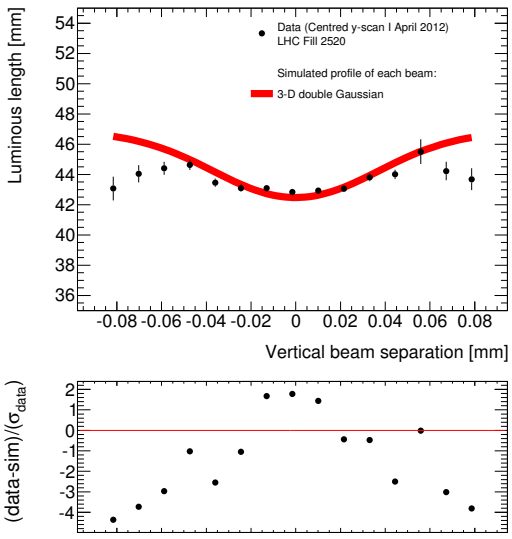

(g) Beam spot luminous length (z-width) as a function of vertical separation

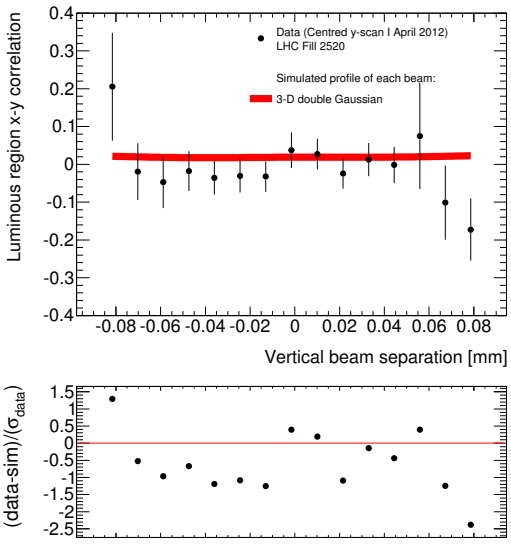

(h) Beam spot x-y correlation as a function of vertical separation

Figure 4.14: Scan I, BCID 1, y-scan

Parameter	Beam 1	Beam 2
$\sigma_{x,a}$	0.0228	0.0211
$\sigma_{x,b}$	0.0147	0.0108
$\sigma_{y,a}$	0.0225	0.0243
$\sigma_{y,b}$	0.0114	0.013
$\sigma_{z,a}$	76.1	76.1
$\sigma_{z,b}$	73.2	72.4
κ_a	0.0163	-0.0684
κ_b	0.116	-0.178
w	0.567	0.737
α_{xz}	$2.3\,\mu\text{rad}$	
α_{yz}	$-180\,\mu\text{rad}$	
χ^2/NDF	968 / 216 = 4.48	
R	184.3 / 188.9 = 0.976	

Table 4.3: The beam parameter set which minimises the χ^2 for a 3D double Gaussian beam density model in scan I, BCID 1. The units of the beam widths are mm. R is the ratio of the true luminosity (not assuming factorisation) to the vdM luminosity (assuming factorisation) in which the vdM luminosity is calculated by numerically integrating a smooth luminosity curve and is the value by which σ_{vis} must be divided in order to correct for the factorisation assumption.

describe the shape of the data in Figure 4.14d. Note that the above discrepancies are observed in scans I and II but not in scan III.

If the crossing angle were exactly zero then the calculation of the absolute luminosity would become a 2D problem as the z-components of the beam spot would be decoupled from the x and y-components. Therefore a good description of the evolution of the z-components of the beam spot in the case when the crossing angle is non-zero is not as important as the description of the evolution of the x and y-components and of the luminosity, which are generally good.

A summary of the ratio R and of the χ^2 per degree of freedom obtained from the fit, for each scan and BCID analysed in April is given in Table 4.4. A plot of R as a function of scan number in April is shown in Figure 4.15 along with the associated statistical uncertainties (see Section 4.7.2).

The value of R for each BCID is initially several percent below 1 in scan I, indicating high levels of non-factorisation, however its value increases throughout the remainder of the session.

	Scan number		
	I	II	III
BCID 1	4.48 - 0.976	3.98 - 0.981	2.15 - 0.992
BCID 241	4.18 - 0.975	3.46 - 0.980	2.09 - 0.989
BCID 2881	5.94 - 0.972	5.19 - 0.976	1.96 - 0.991
BCID 3121	5.31 - 0.970	4.29 - 0.979	2.13 - 0.992

Table 4.4: The χ^2 per degree of freedom and the value of R for each scan and BCID studied in April.

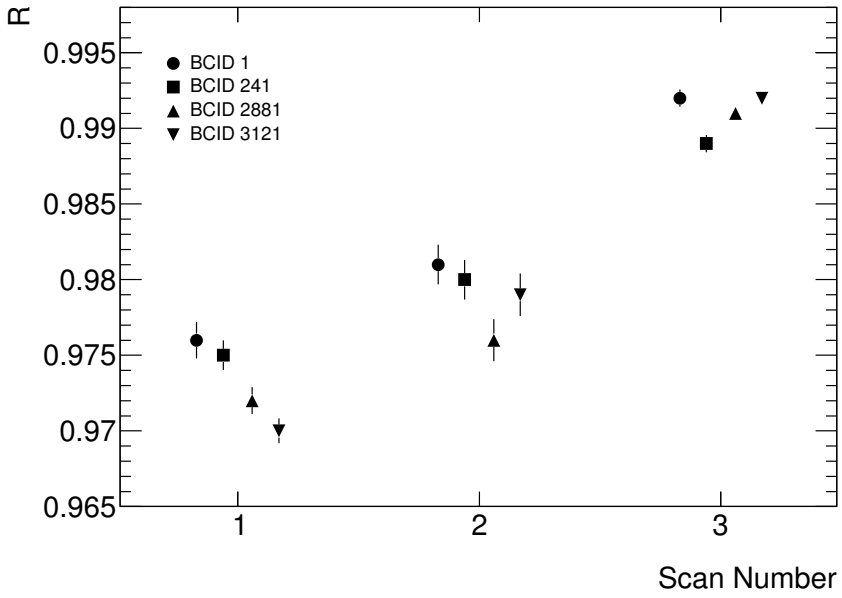

Figure 4.15: R as a function of scan number for each BCID considered during the April scan session.

4.6.3 July

The July scan session consisted of four centred scans (IV, V, VI and VIII) and two offset scans (VII and IX) and took place on 19th July 2012. Scans IV, V, VI and VII were completed in LHC Fill 2855 and ATLAS run number 207216. Scans VIII and IX were completed in LHC Fill 2856 and ATLAS run number 207219. There were 35 colliding bunches, of which three (1, 721 and 1821) have associated beam spot evolution data. The nominal β^* was 11 m. An estimation for R was only obtained for the centred scans IV, V, VI and VIII.

The function which was found to best describe the bunch density profiles in the July sessions was again the double Gaussian. A comparison between data from scan IV, BCID I and the best-fit model for various observables is presented in Figures 4.16 (x, or horizontal scan) and 4.17 (y or vertical scan) in the same fashion as for the

Parameter	Beam 1	Beam 2
$\sigma_{x,a}$	0.0674	0.0686
$\sigma_{x,b}$	0.107	0.108
$\sigma_{y,a}$	0.0579	0.0641
$\sigma_{y,b}$	0.115	0.122
$\sigma_{z,a}$	84.9	84.5
$\sigma_{z,b}$	81	81.2
κ_a	0.0344	-0.0055
κ_b	-0.00114	-0.000881
w	0.366	0.445
α_{xz}	$5.9\,\mu\text{rad}$	
α_{yz}	$-8.2\,\mu\text{rad}$	
χ^2/NDF	354 / 280 = 1.27	
R	9.888 / 10.28 = 0.962	

Table 4.5: The beam parameter set which minimises the χ^2 for a 3D double Gaussian beam density model in scan IV, BCID 1. The units of the beam widths are mm. R is the ratio of the true luminosity (not assuming factorisation) to the vdM luminosity (assuming factorisation) in which the vdM luminosity is calculated by numerically integrating a smooth luminosity curve and is the value by which σ_{vis} must be divided in order to correct for the factorisation assumption.

April scans. The level of agreement between the data and model is representative of that for the remaining centred scans and BCIDs in the July session (see Table 4.6). Table 4.5 then displays the set of model beam parameters that minimised the χ^2 value between data and model.

As a cross-check of the method offset scan VII BCID 1 was simulated using the best fit bunch parameters from scan VI, the closest centred scan in time. A comparison between the data and the model for the standard set of observables is shown in Figures 4.18 (x-scan) and 4.19 (y-scan). The luminosity normalisation used in Figures 4.18a and 4.19a is the same as was used in scan VI and of the corrections described in Section 4.5.2 only an overall centring correction (in both x and y) is applied to the offset scan separations. The model does a reasonable job of describing the data in the offset scan which suggests that the double Gaussian function is a good description of the bunch density profiles even towards the bunch extremities.

A summary of the ratio R and of the χ^2 per degree of freedom obtained from the fit, for each scan and BCID analysed in July is given in Table 4.6. A plot of R as a function of scan number in July is shown in Figure 4.20 along with the associated statistical uncertainties (see Section 4.7.2).

The value of R varies between around 0.955 and 0.975 depending on the scan

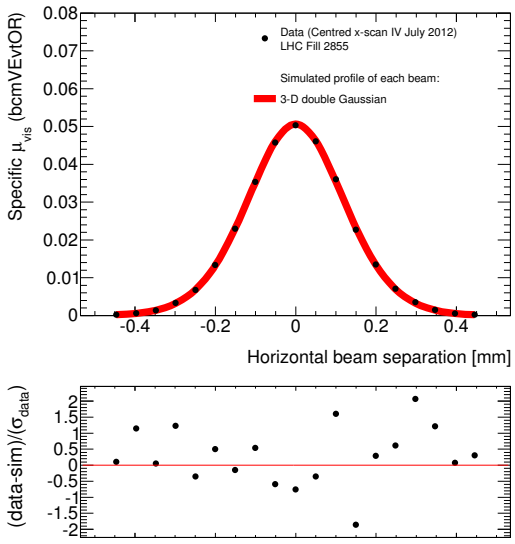

(a) Specific μ_{vis} as a function of horizontal separation

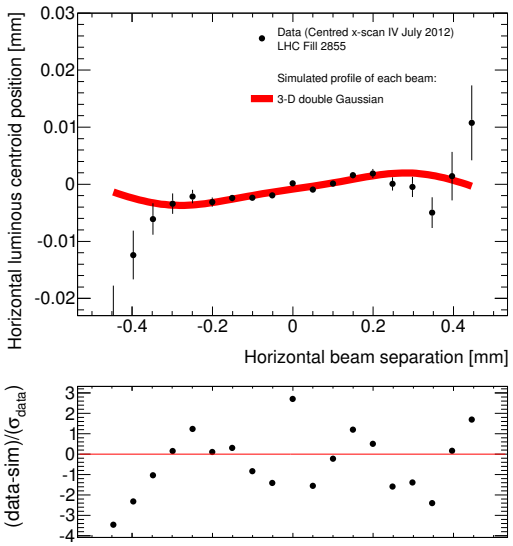

(b) Beam spot horizontal position as a function of horizontal separation

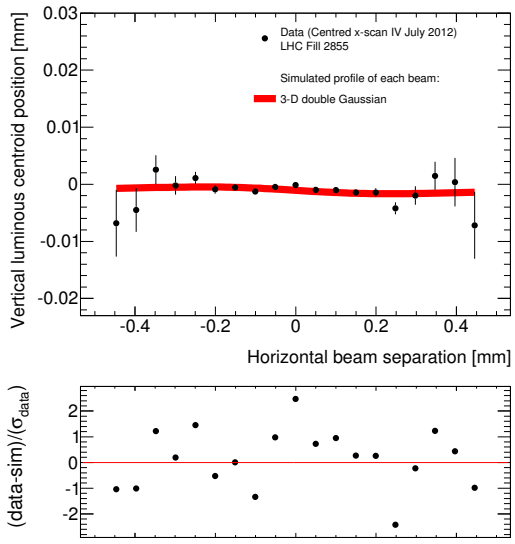

(c) Beam spot vertical position as a function of horizontal separation

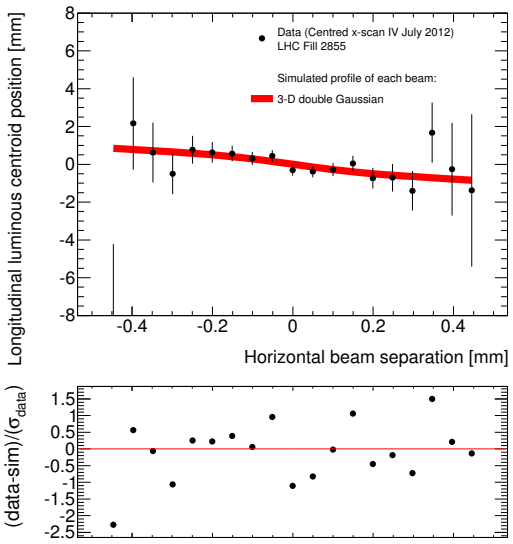

(d) Beam spot longitudinal position as a function of horizontal separation

Figure 4.16: Scan IV, BCID 1, x-scan

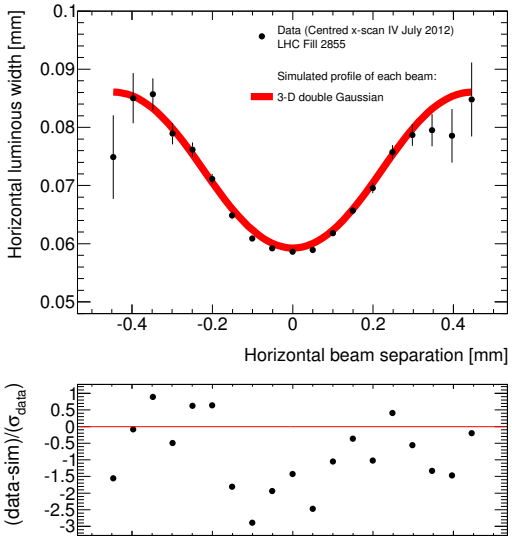

(e) Beam spot horizontal width as a function of horizontal separation

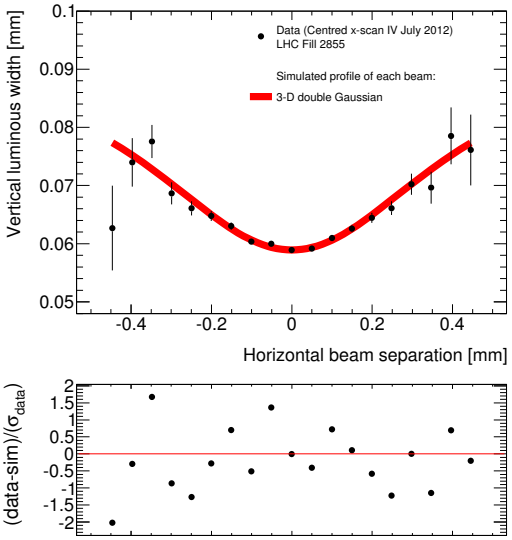

(f) Beam spot vertical width as a function of horizontal separation

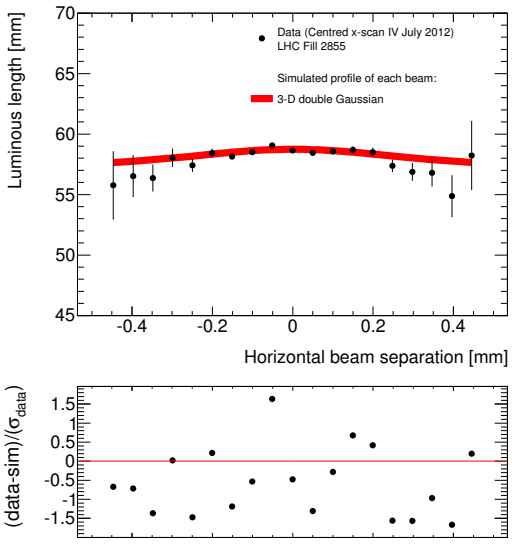

(g) Beam spot luminous length (z-width) as a function of horizontal separation

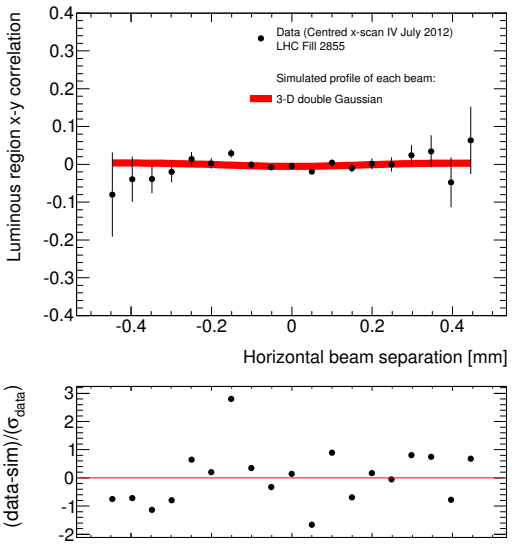

(h) Beam spot x-y correlation as a function of horizontal separation

Figure 4.16: Scan IV, BCID 1, x-scan

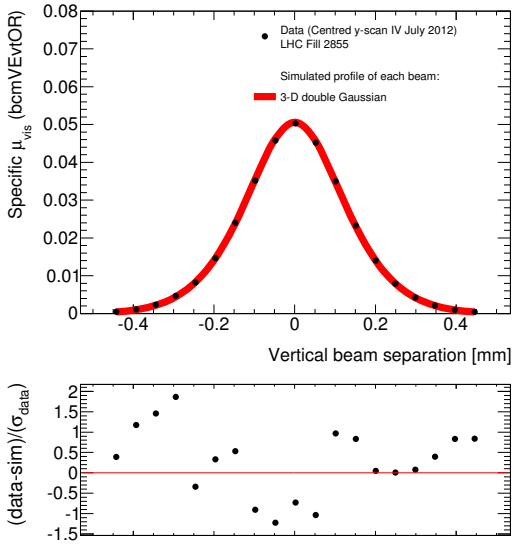

(a) Specific μ_{vis} as a function of vertical separation

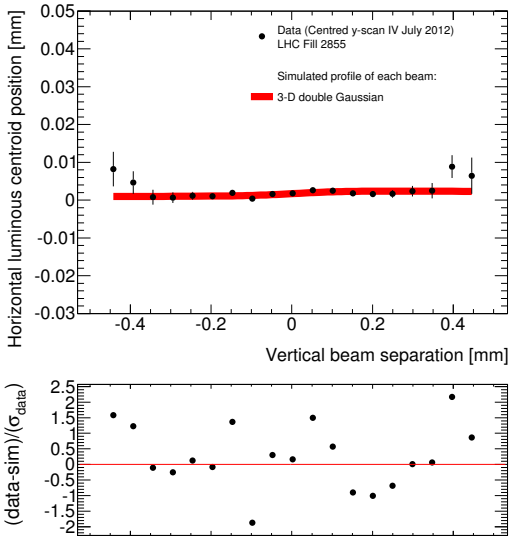

(b) Beam spot horizontal position as a function of vertical separation

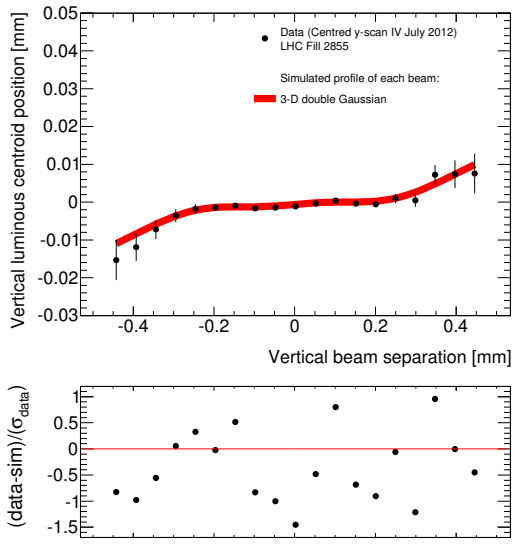

(c) Beam spot vertical position as a function of vertical separation

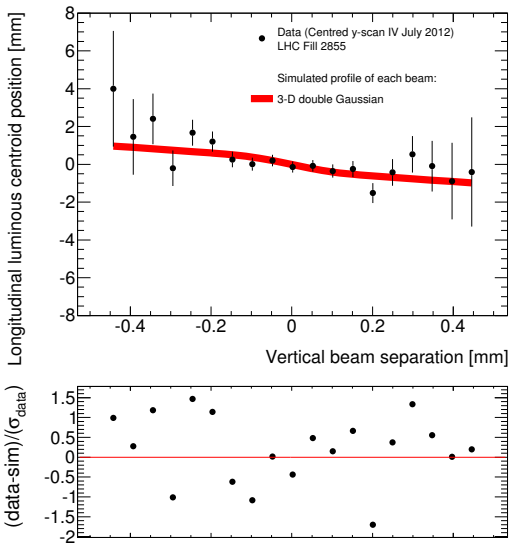

(d) Beam spot longitudinal position as a function of vertical separation

Figure 4.17: Scan IV, BCID 1, y-scan

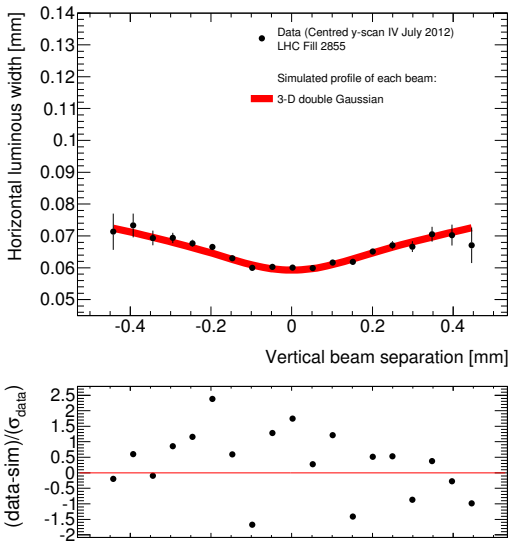

(e) Beam spot horizontal width as a function of vertical separation

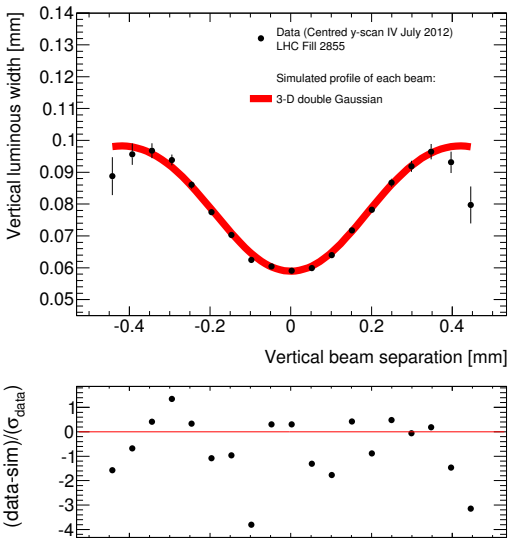

(f) Beam spot vertical width as a function of vertical separation

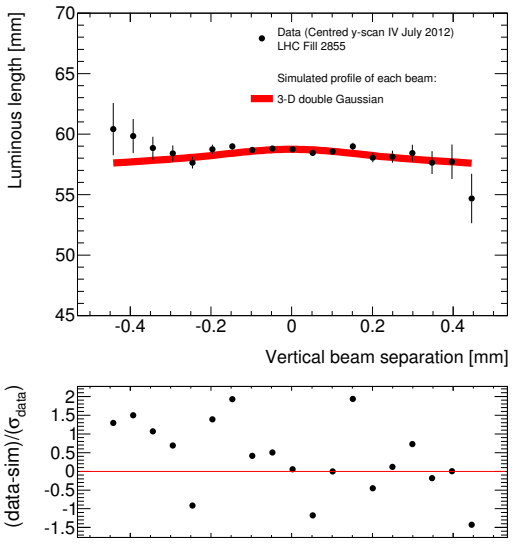

(g) Beam spot luminous length (z-width) as a function of vertical separation

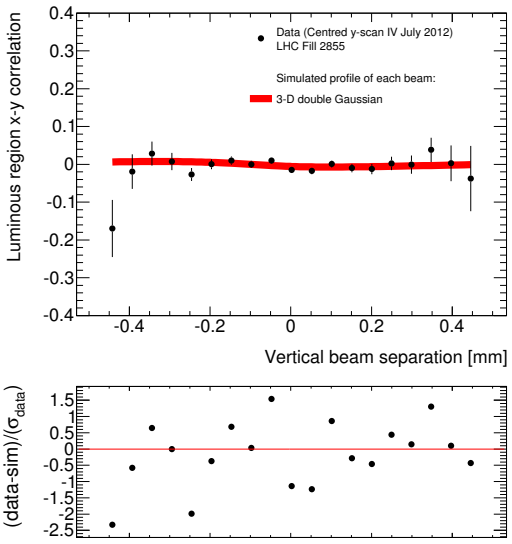

(h) Beam spot x-y correlation as a function of vertical separation

Figure 4.17: Scan IV, BCID 1, y-scan

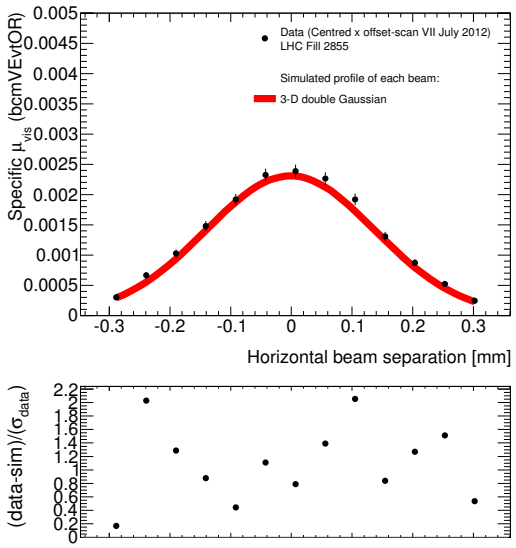

(a) Specific μ_{vis} as a function of horizontal separation

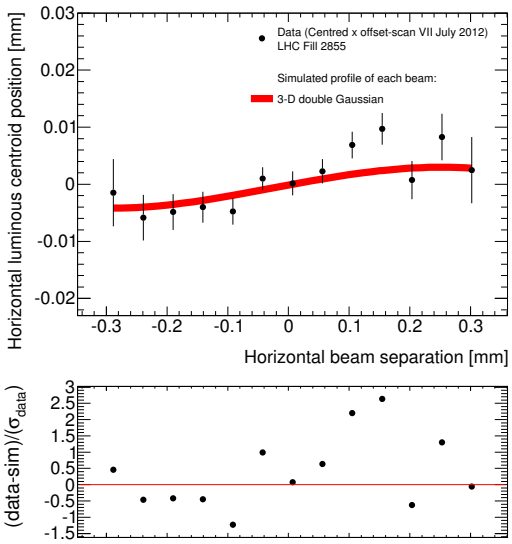

(b) Beam spot horizontal position as a function of horizontal separation

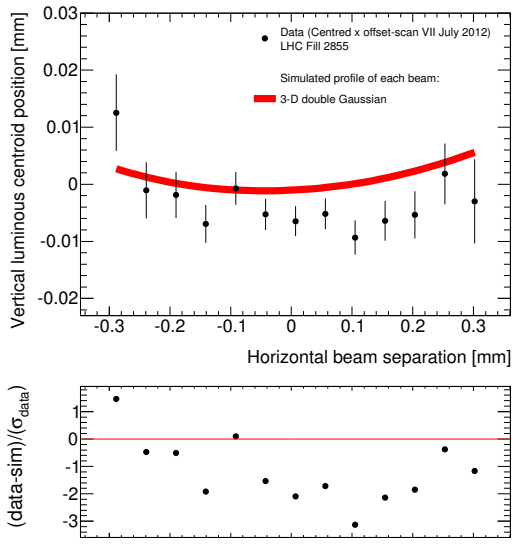

(c) Beam spot vertical position as a function of horizontal separation

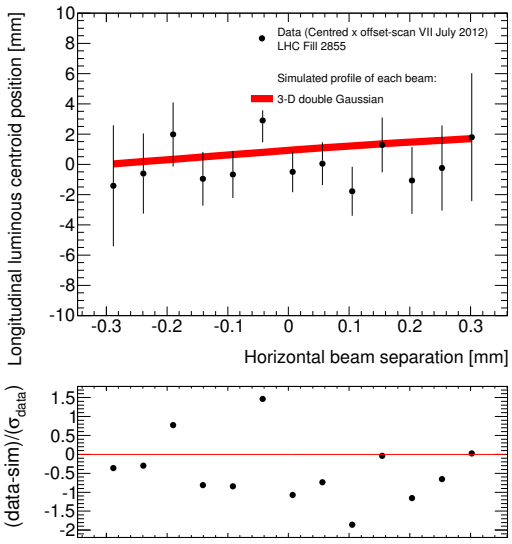

(d) Beam spot longitudinal position as a function of horizontal separation

Figure 4.18: Scan VII, BCID 1, x-scan

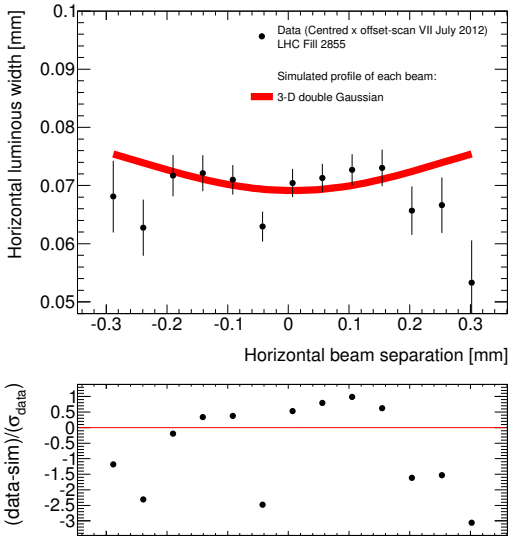

(e) Beam spot horizontal width as a function of horizontal separation

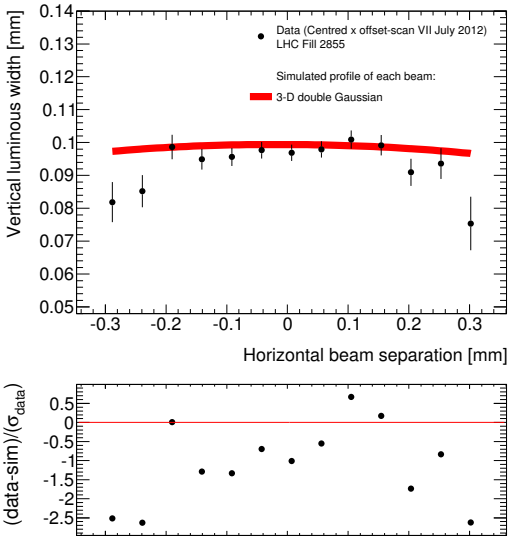

(f) Beam spot vertical width as a function of horizontal separation

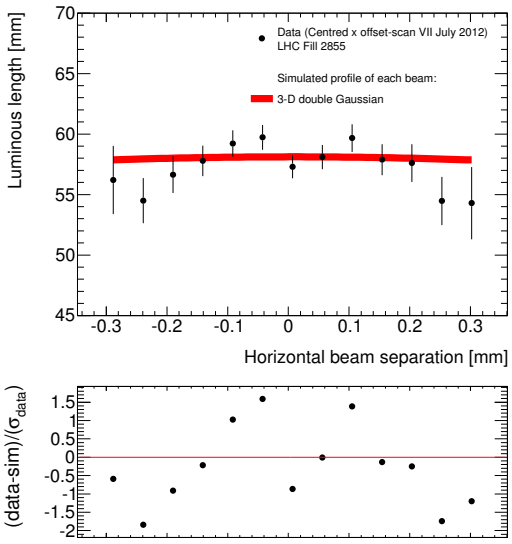

(g) Beam spot luminous length (z-width) as a function of horizontal separation

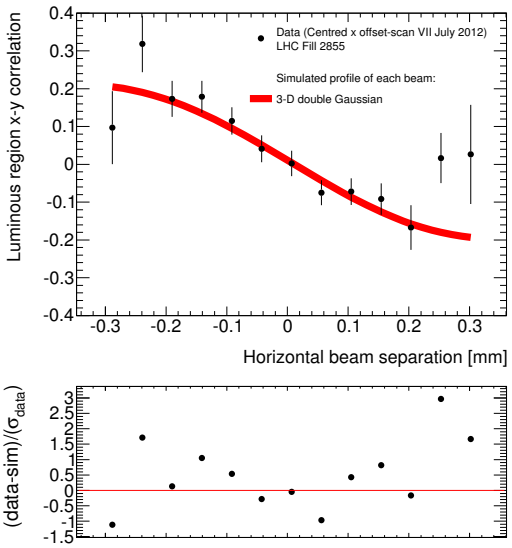

(h) Beam spot x-y correlation as a function of horizontal separation

Figure 4.18: Scan VII, BCID 1, x-scan

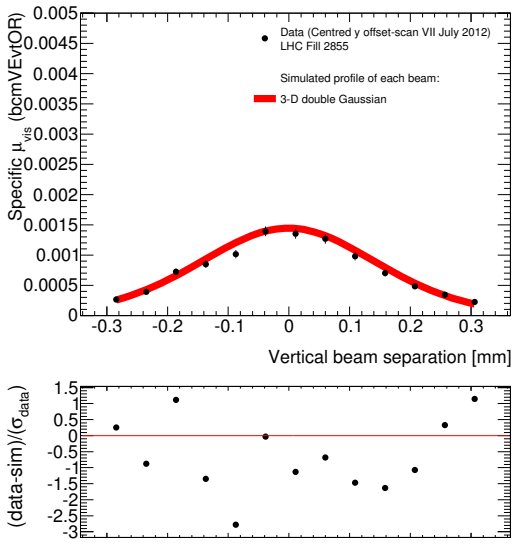

(a) Specific μ_{vis} as a function of vertical separation

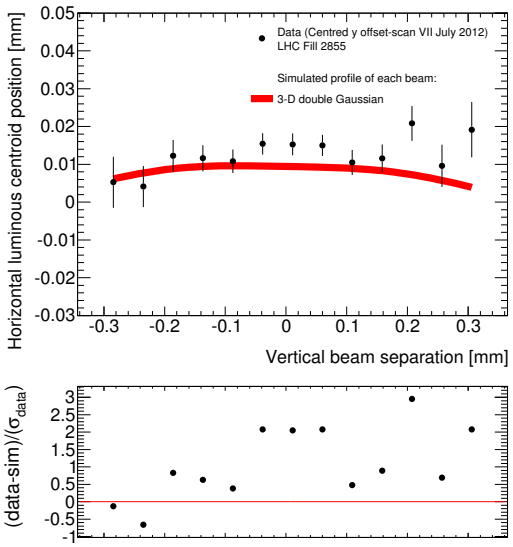

(b) Beam spot horizontal position as a function of vertical separation

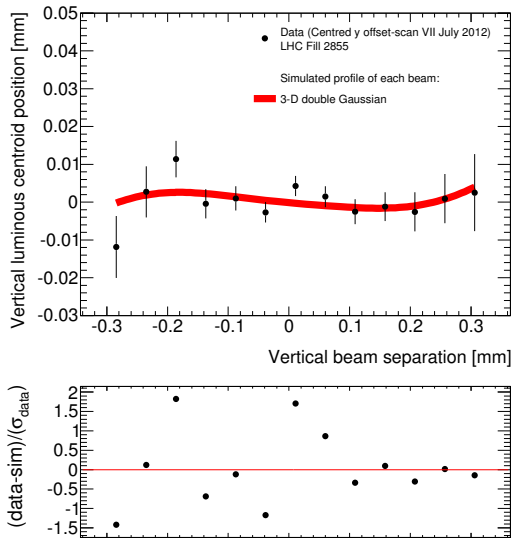

(c) Beam spot vertical position as a function of vertical separation

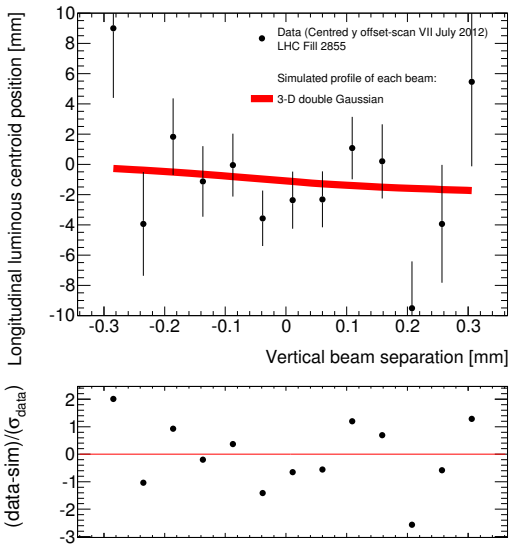

(d) Beam spot longitudinal position as a function of vertical separation

Figure 4.19: Scan VII, BCID 1, y-scan

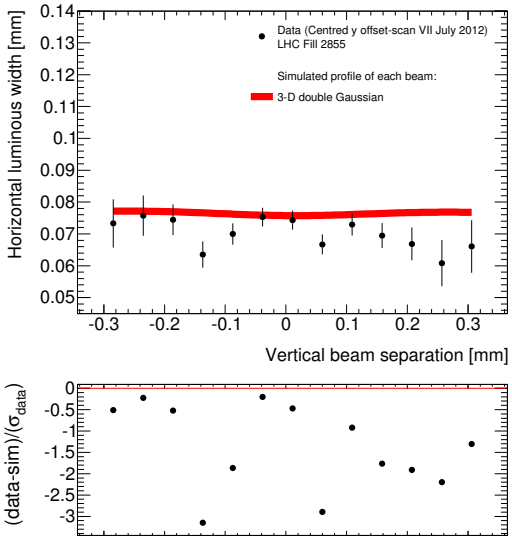

(e) Beam spot horizontal width as a function of vertical separation

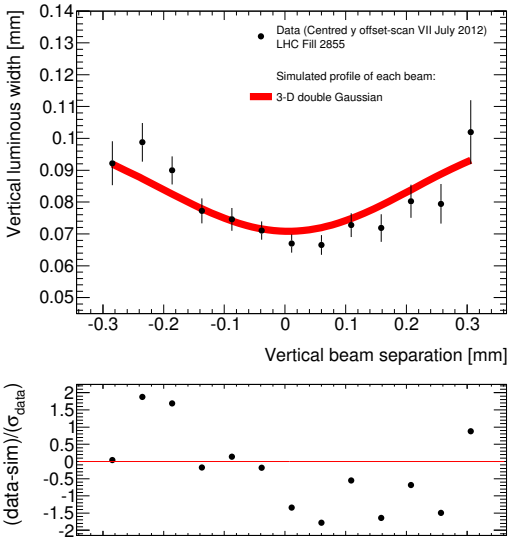

(f) Beam spot vertical width as a function of vertical separation

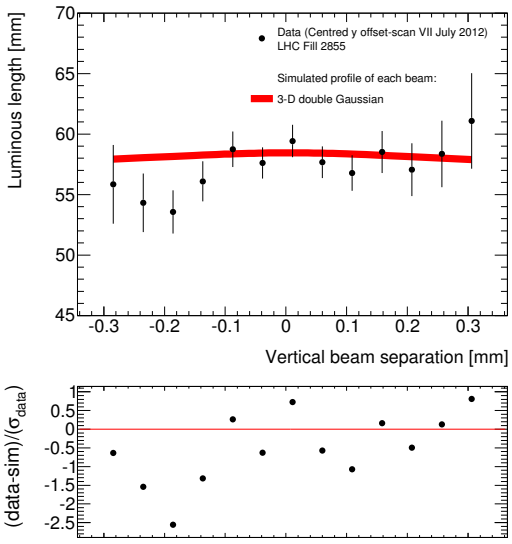

(g) Beam spot luminous length (z-width) as a function of vertical separation

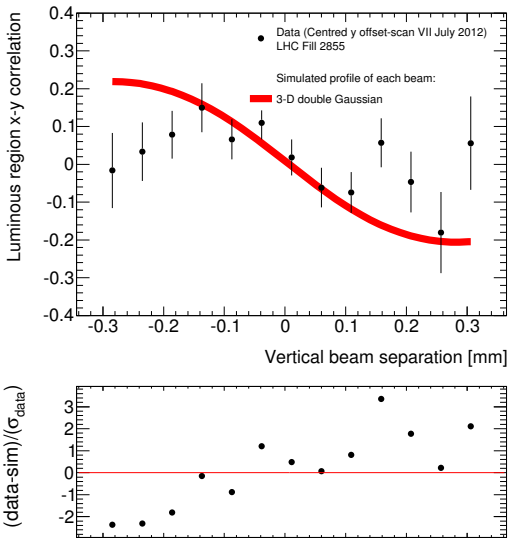

(h) Beam spot x-y correlation as a function of vertical separation

Figure 4.19: Scan VII, BCID 1, y-scan

	Scan number			
	IV	V	VI	VIII
BCID 1	1.27 - 0.962	1.28 - 0.974	1.25 - 0.975	1.11 - 0.970
BCID 721	1.92 - 0.959	1.39 - 0.974	1.71 - 0.977	1.4 - 0.969
BCID 1821	1.51 - 0.956	1.49 - 0.970	1.59 - 0.972	1.29 - 0.962

Table 4.6: The χ^2 per degree of freedom and the value of R for each scan and BCID studied in July.

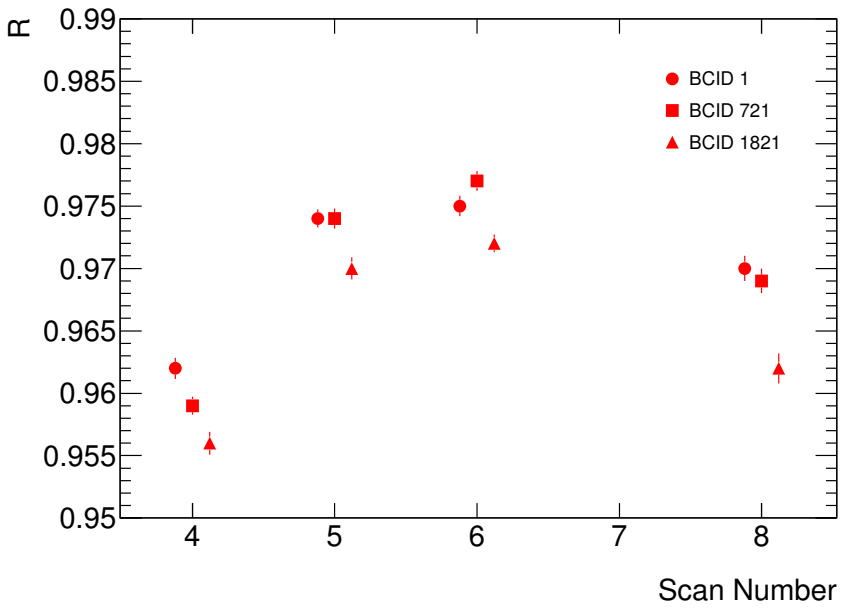

Figure 4.20: R as a function of scan number for each BCID considered during the July scan session.

and BCID indicating high levels of non-factorisation in the beams.

4.6.4 November

The November scan session consisted of four centred scans (X, XI, XIV and XV) and two offset scans (XII and XIII) and took place on the 22nd and 23rd November 2012. Scans X, XI, XII, XIII and XIV were completed in LHC Fill 3311 and ATLAS run number 214984. Scan XV was completed in LHC Fill 3316 and ATLAS run number 215021. There were 29 colliding bunches, of which three (1, 2361 and 2881) have associated beam spot evolution data. The nominal β^* was 11 m. An estimation for R was only obtained for the centred scans X, XI, XIV and XV.

The function which was found to best describe the bunch density profiles in the November sessions was the double supergaussian. A comparison between data

from scan XI, BCID I and the best-fit model for various observables is presented in Figures 4.21 (x, or horizontal scan) and 4.22 (y or vertical scan) in the same fashion as for the April and July scans. The level of agreement between the data and model is representative of that for the remaining centred scans and BCIDs in the November session (see Table 4.8).

The motivation for using a double supergaussian instead of the double Gaussian in November comes from the observation that the beam spot width in the same dimension as the scan direction decreases as beam separation is increased from zero (for example, Figure 4.21e). This effect was not possible to produce using double Gaussian beam profiles (assuming that the weights of both Gaussians are positive). Since there is no requirement to reproduce such an effect in the z-direction (i.e., no z-scan is performed) and to reduce the time taken for the minimisation, the four epsilon parameters in z are set to zero.

A point to note is that despite the double supergaussian model being an improvement over the double Gaussian in some cases (as in Figure 4.21e) it still is not able to qualitatively describe all the features of the November data as well as the double Gaussian model describes the features of the July data — resulting in higher values of the χ^2 per degree of freedom. This may be because the double supergaussian is inherently a poor description of the bunch density profiles or possibly because the overlap integrals must be calculated numerically which leads to some instabilities in the fitting routine.

Table 4.7 displays the set of model beam parameters that minimised the χ^2 value between data and model. The double supergaussian beam parameters comprise for each beam, and in addition to those used for the double Gaussian, the epsilon parameters in the x and y dimensions for supergaussians 'a' and 'b' ($\epsilon_{x,a}$, $\epsilon_{x,b}$, $\epsilon_{y,a}$, $\epsilon_{y,b}$).

A summary of the ratio R and of the χ^2 per degree of freedom obtained from the fit, for each scan and BCID analysed in November is given in Table 4.8. A plot of R as a function of scan number in November is shown in Figure 4.23 along with the associated statistical uncertainties (see Section 4.7.2).

Generally the value of R is much closer to one for the scans and BCIDs in the November scan session as compared to the April and July scan sessions indicating that the assumption of factorisation holds much better.

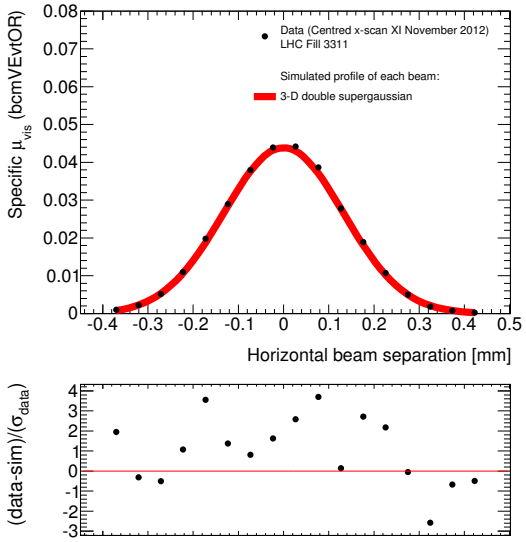

(a) Specific μ_{vis} as a function of horizontal separation

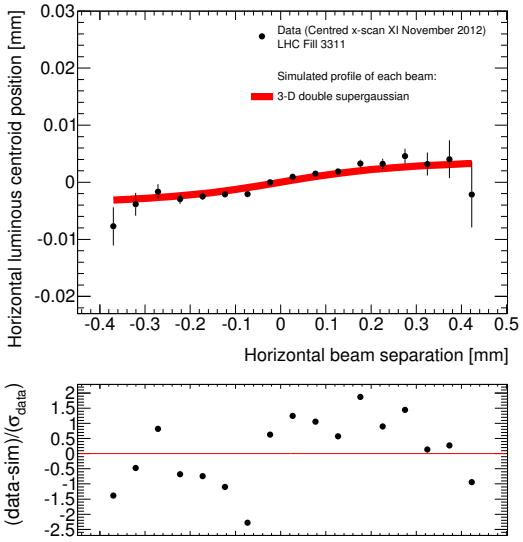

(b) Beam spot horizontal position as a function of horizontal separation

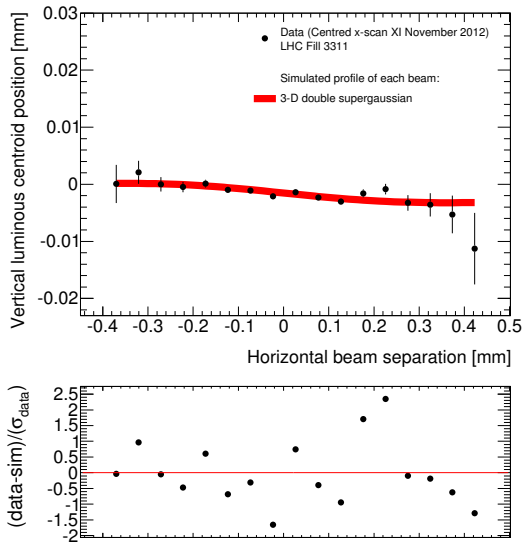

(c) Beam spot vertical position as a function of horizontal separation

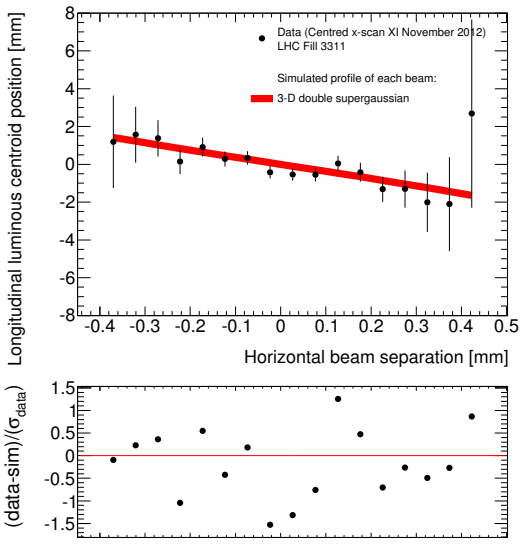

(d) Beam spot longitudinal position as a function of horizontal separation

Figure 4.21: Scan XI, BCID 1, x-scan

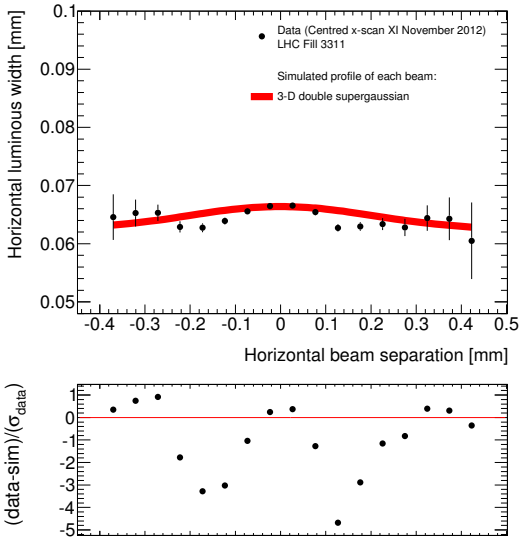

(e) Beam spot horizontal width as a function of horizontal separation

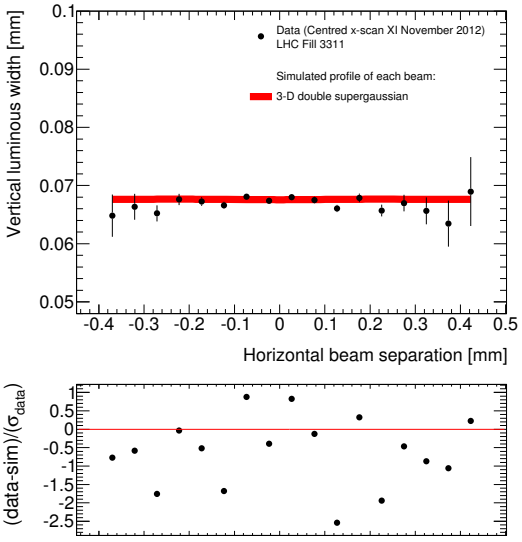

(f) Beam spot vertical width as a function of horizontal separation

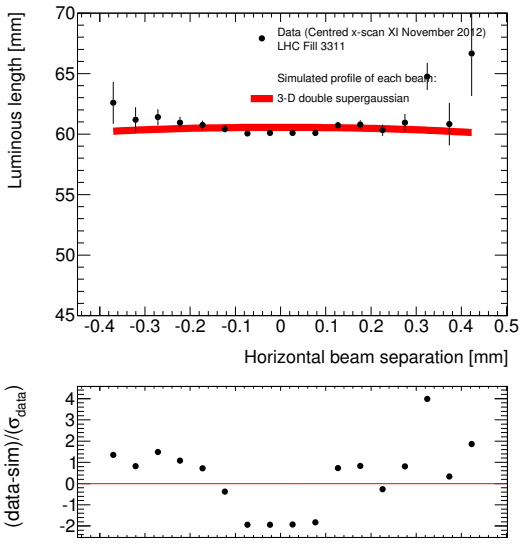

(g) Beam spot luminous length (z-width) as a function of horizontal separation

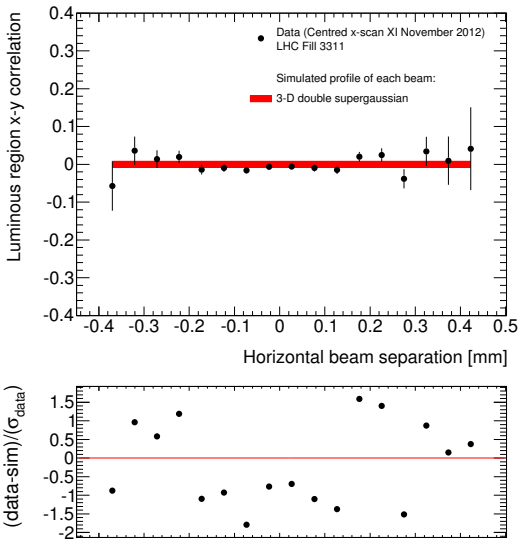

(h) Beam spot x-y correlation as a function of horizontal separation

Figure 4.21: Scan XI, BCID 1, x-scan

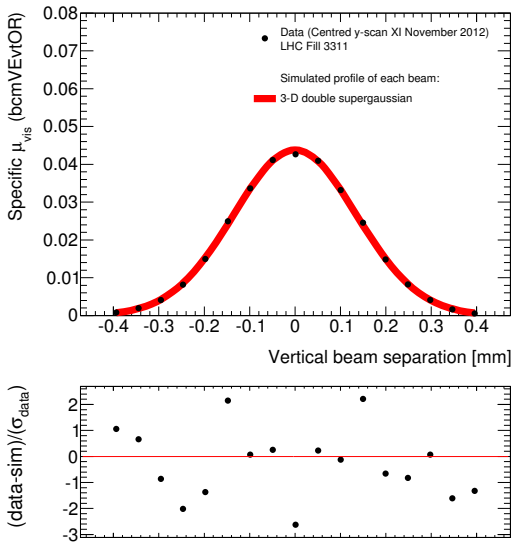

(a) Specific μ_{vis} as a function of vertical separation

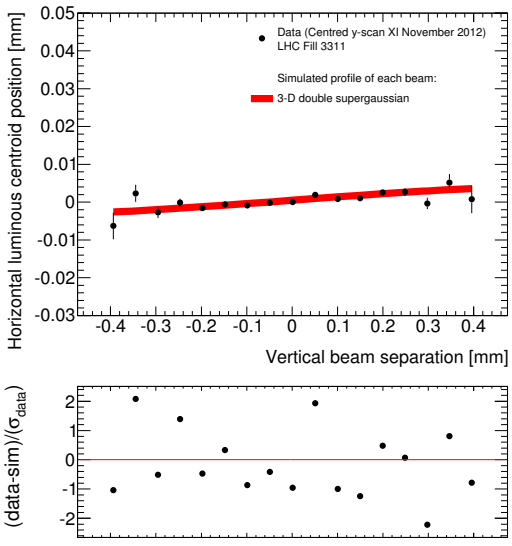

(b) Beam spot horizontal position as a function of vertical separation

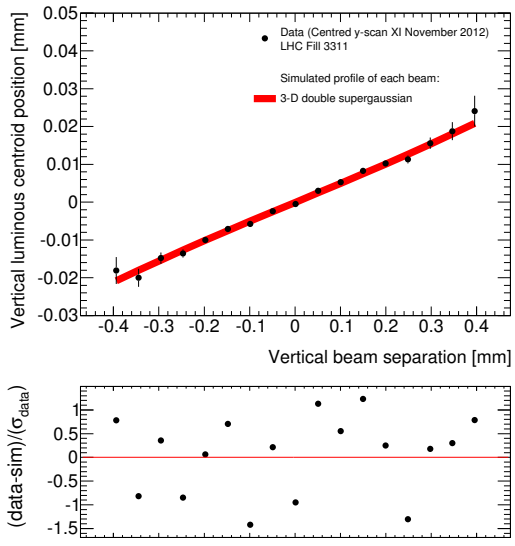

(c) Beam spot vertical position as a function of vertical separation

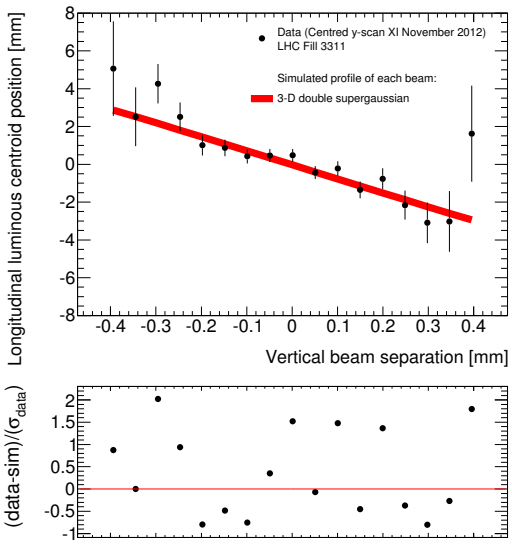

(d) Beam spot longitudinal position as a function of vertical separation

Figure 4.22: Scan XI, BCID 1, y-scan

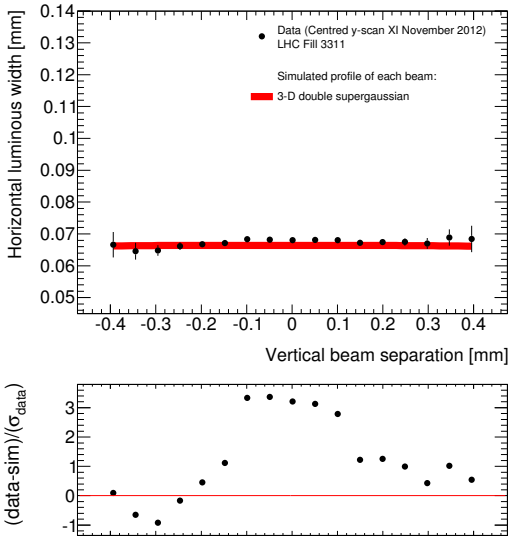

(e) Beam spot horizontal width as a function of vertical separation

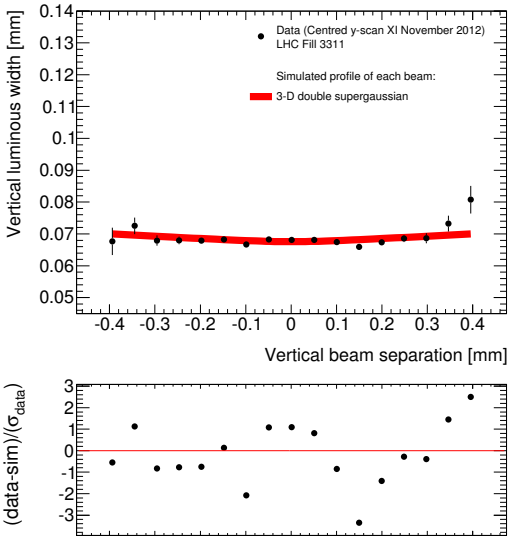

(f) Beam spot vertical width as a function of vertical separation

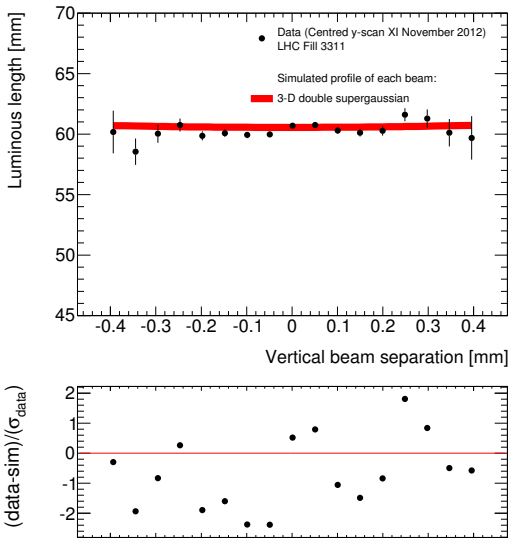

(g) Beam spot luminous length (z-width) as a function of vertical separation

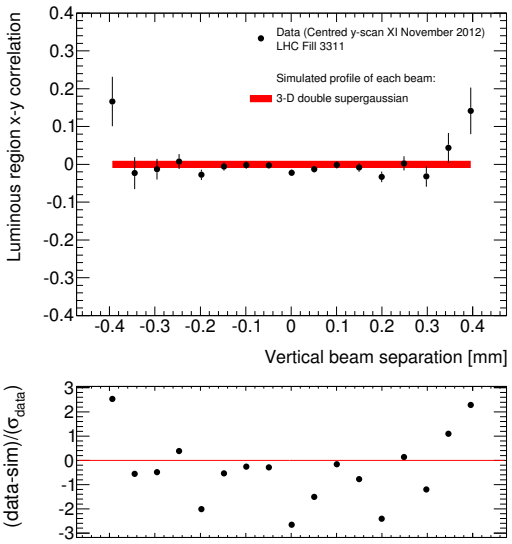

(h) Beam spot x-y correlation as a function of vertical separation

Figure 4.22: Scan XI, BCID 1, y-scan

Parameter	Beam 1	Beam 2
$\sigma_{x,a}$	0.0987	0.0976
$\sigma_{x,b}$	0.0972	0.0935
$\sigma_{y,a}$	0.0815	0.0919
$\sigma_{y,b}$	0.0935	0.104
$\sigma_{z,a}$	120	60
$\sigma_{z,b}$	60	105
κ_a	0.0501	-0.0501
κ_b	0.0163	-0.0163
$\epsilon_{x,a}$	0.14	0.119
$\epsilon_{y,a}$	0.0191	0.0346
w	0.146	0.206
α_{xz}	8.8 µrad	
α_{yz}	−19 µrad	
χ^2/NDF	496 / 244 = 2.03	
R	8.795 / 8.79 = 1.00	

Table 4.7: The beam parameter set which minimises the χ^2 for a 3D double super-gaussian beam density model in scan XI, BCID 1. The units of the beam widths are mm. R is the ratio of the true luminosity (not assuming factorisation) to the vdM luminosity (assuming factorisation) in which the vdM luminosity is calculated by numerically integrating a smooth luminosity curve and is the value by which σ_{vis} must be divided in order to correct for the factorisation assumption.

4.7 Systematic uncertainty evaluation

4.7.1 Introduction

Three sources of uncertainty on the value of the correction factor R are considered: the statistical uncertainties on the resulting fit parameters after the χ^2 minimisation, the uncertainty on the beam spot resolution and the uncertainty due to the choice of beam parameterisation. The uncertainties from each source for a particular scan and BCID are then added in quadrature to obtain the total uncertainty on the value

	Scan number			
	X	XI	XIV	XV
BCID 1	2.64 - 0.995	2.03 - 1.00	2.82 - 1.00	1.92 - 1.00
BCID 2361	2.93 - 0.996	2.07 - 0.998	2.21 - 0.997	3.15 - 1.00
BCID 2881	3.99 - 1.00	3.30 - 1.00	3.30 - 1.00	2.57 - 1.00

Table 4.8: The χ^2 per degree of freedom and the value of R for each scan and BCID studied in November.

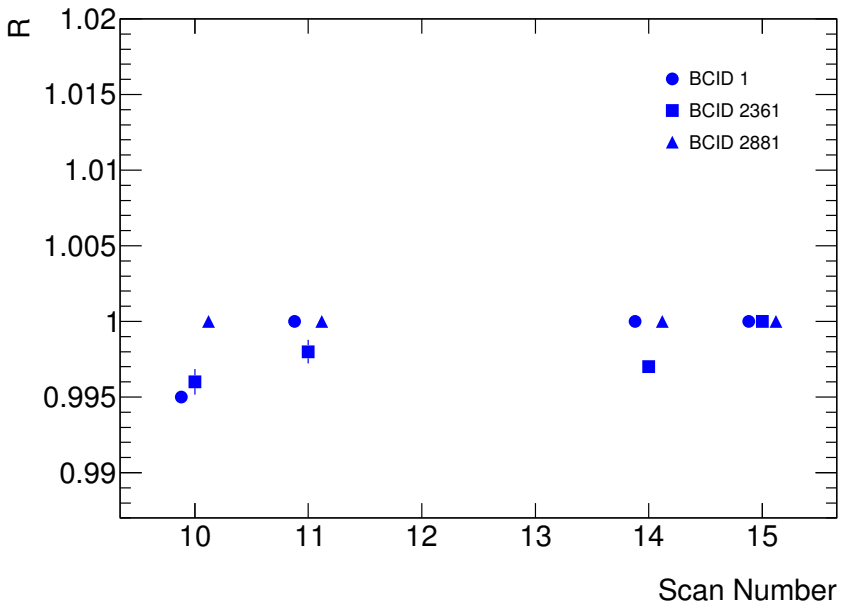

Figure 4.23: R as a function of scan number for each BCID considered during the November scan session.

of R.

There is no reason why the values of R from each of the BCIDs in a scan must be the same. However for those detectors that cannot distinguish separate BCIDs there needs to be some form of average correction factor per scan. This is chosen to be the mean of the R values from the individual BCIDs with the uncertainties on beam spot resolution and choice of beam parameterisation treated as correlated. The statistical uncertainty on the mean is obtained by either calculating the unbiased standard deviation of the set of R values and dividing by the square root of the number of BCIDs or by taking the mean of the statistical uncertainties on R for each BCID in the scan (and again dividing by the square root of the number of BCIDs), whichever is largest. The mean R value for each scan and the corresponding total uncertainty is provided in Tables 4.17, 4.18 and 4.19.

4.7.2 Statistical uncertainties on individual beam parameters

At the conclusion of a successful minimisation, Minuit 2 returns, along with the final set of beam parameters, a covariance matrix which details the statistical uncertainties on those parameters and the correlation between them. These uncertainties are propagated through to an uncertainty on R by sampling 2000 times from a multi-dimensional Gaussian distribution in which the mean in each dimension is

	Scan number		
	I	II	III
BCID 1	0.0012	0.0013	0.00057
BCID 241	0.00098	0.0013	0.00057
BCID 2881	0.00089	0.0014	0.0014
BCID 3121	0.00082	0.0014	0.0015
Statistical uncertainty on mean R value	0.0014	0.0011	0.0007

Table 4.9: The standard deviation of the histogram of R values for each scan and BCID in April is provided. The histograms were obtained by sampling 2000 times from a multi-dimensional Gaussian distribution in which the mean in each dimension is the minimised beam parameter and the covariance matrix is the same as returned by the minimisation routine. The bottom row gives the unbiased standard deviation of the central R values divided by the square root of the number of BCIDs in that scan.

the minimised beam parameter and the covariance matrix is the same as returned by the minimisation routine. One then has 2000 sets of parameter values, each of which corresponds to a slightly different value of R. The standard deviation of the set of 2000 R values obtained is taken to be the uncertainty on R corresponding to the statistical uncertainty on the individual beam parameters for a particular scan/BCID.

Figure 4.24 shows as an example a histogram of the 2000 R values for each BCID in scan I. A summary of the standard deviation of the histogram for each scan and BCID in April is given in Table 4.9, the summary in July is given in Table 4.10 and the summary in November (using the double Gaussian model for technical reasons described below) is given in Table 4.11.

For each scan considered, the unbiased standard deviation of the central R values divided by the square root of the number of BCIDs in that scan is shown in the bottom row of each table. This is one estimate of the statistical uncertainty on the mean R value.

The uncertainties are of a comparable magnitude in April (Table 4.9) and July (Table 4.10) with April generally having the slightly higher values. Double Gaussian beam profiles are used for evaluating the uncertainty in November as the double supergaussian beam profiles require numerical integration, which takes an unrealistically long time to evaluate. Although it is known that the double Gaussian model does not qualitatively describe some aspects of the data very well, the uncertainty on the choice of beam parameterisation (Section 4.7.4) is relatively small so the

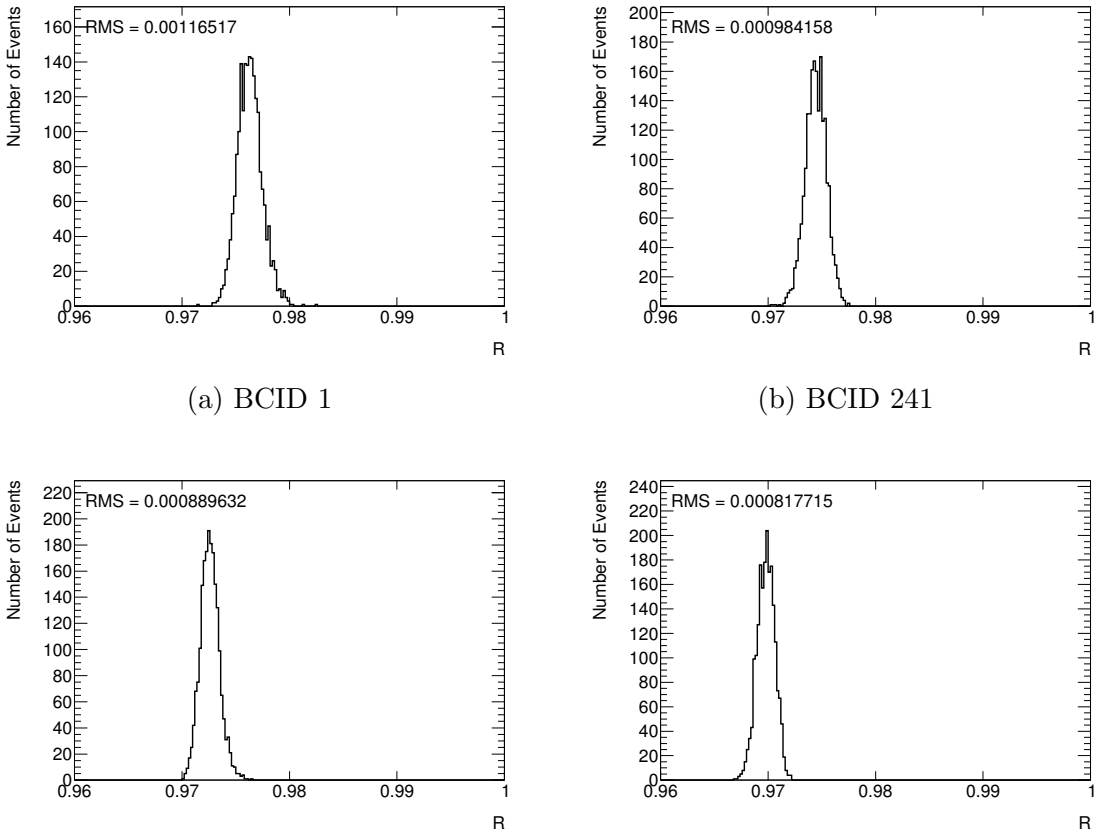

(a) BCID 1

(b) BCID 241

(c) BCID 2881

(d) BCID 3121

Figure 4.24: The distribution of R values for each BCID in scan I. The histograms were obtained by sampling 2000 times from a multi-dimensional Gaussian distribution in which the mean in each dimension is the minimised beam parameter and the covariance matrix is the same as returned by the minimisation routine.

	Scan number			
	IV	V	VI	VIII
BCID 1	0.00085	0.00072	0.00082	0.0010
BCID 721	0.00072	0.00080	0.00080	0.00098
BCID 1821	0.00091	0.00089	0.00070	0.0012
Statistical uncertainty on mean R value	0.0017	0.0013	0.0015	0.0025

Table 4.10: The standard deviation of the histogram of R values for each scan and BCID in July is provided. The histograms were obtained by sampling 2000 times from a multi-dimensional Gaussian distribution in which the mean in each dimension is the minimised beam parameter and the covariance matrix is the same as returned by the minimisation routine. The bottom row gives the unbiased standard deviation of the central R values divided by the square root of the number of BCIDs in that scan.

	Scan number			
	X	XI	XIV	XV
BCID 1	0.00034	0.00027	0.00026	0.00028
BCID 2361	0.00085	0.00078	0.00022	0.00022
BCID 2881	0.00004	0.00004	0.00004	0.00004
Statistical uncertainty on mean R value	0.0015	0.0007	0.0010	0

Table 4.11: The standard deviation of the histogram of R values for each scan and BCID in November is provided. The histograms were obtained by sampling 2000 times from a multi-dimensional Gaussian distribution in which the mean in each dimension is the minimised beam parameter and the covariance matrix is the same as returned by the minimisation routine. Note that the double Gaussian beam model was used to obtain the beam parameters used. The bottom row gives the unbiased standard deviation of the central R values divided by the square root of the number of BCIDs in that scan.

numbers in Table 4.11 are likely to be good approximations to the true statistical uncertainty.

4.7.3 Systematic uncertainty due to beam spot resolution

As outlined in Section 4.2 and expanded upon in [40], the beam spot is defined by performing an unbinned maximum-likelihood fit of a 3D Gaussian to the distribution of vertices (interaction points) collected over a certain time period. One of the fit parameters is named the k-factor, which takes into account the difference between the actual and expected tracking resolutions. The value of the k-factor obtained from the beam spot fit is generally within ten percent of one.

It is possible that the method of fitting the vertex distribution incorrectly estimates the tracking resolution. In order to examine how this might impact the value of R obtained the vertices in scans IV, V and VI (July) are refitted three times with the k-factor fixed to 1.0, 1.1 and 1.2.

The minimisation procedure of Section 4.5.1 is repeated for each scan and BCID analysed in July but using the beam spot data in which the k-factor is fixed to 1.0. A summary of the ratio R and of the χ^2 per degree of freedom obtained from each scan and BCID combination is provided in Table 4.12. Tables 4.13 and Table 4.14 provide the same values from the minimisation using beam spot data in which the k-factor has been fixed to 1.1 and 1.2 respectively.

With the exception of the analysis of BCID 721 in scans V and VI when the k-factor was fixed to 1.2, the greatest shift in R from the analysis in which the k-factor

	Scan number		
	IV	V	VI
BCID 1	2.27 - 0.964	2.19 - 0.975	2.46 - 0.978
BCID 721	2.77 - 0.962	2.61 - 0.976	2.74 - 0.980
BCID 1821	2.20 - 0.960	2.05 - 0.972	1.69 - 0.974

Table 4.12: The χ^2 per degree of freedom and the value of R for each BCID in scans IV, V and VI (July). The k-factor in the beam spot fit was fixed to 1.0.

	Scan number		
	IV	V	VI
BCID 1	1.92 - 0.962	1.79 - 0.974	1.80 - 0.976
BCID 721	2.22 - 0.960	1.97 - 0.975	2.11 - 0.979
BCID 1821	2.13 - 0.957	1.97 - 0.971	1.92 - 0.974

Table 4.13: The χ^2 per degree of freedom and the value of R for each BCID in scans IV, V and VI (July). The k-factor in the beam spot fit was fixed to 1.1.

	Scan number		
	IV	V	VI
BCID 1	4.86 - 0.960	4.47 - 0.973	3.93 - 0.976
BCID 721	6.79 - 0.958	6.09 - 0.988	5.56 - 0.992
BCID 1821	5.43 - 0.955	5.08 - 0.970	4.52 - 0.973

Table 4.14: The χ^2 per degree of freedom and the value of R for each BCID in scans IV, V and VI (July). The k-factor in the beam spot fit was fixed to 1.2.

	Scan number			
	X	XI	XIV	XV
BCID 1	2.67 - 0.999	2.17 - 1.00	2.61 - 1.00	2.28 - 1.00
BCID 2361	2.71 - 0.996	1.56 - 0.998	1.74 - 0.997	3.78 - 1.00
BCID 2881	3.68 - 1.00	3.40 - 1.00	2.82 - 1.00	2.54 - 0.999

Table 4.15: The χ^2 per degree of freedom and the value of R for each scan and BCID studied in November, in which the beam profiles are modelled as double Gaussian.

is not fixed (Table 4.6) is 0.004. This value is therefore chosen as the systematic uncertainty on R due to beam spot resolution for all scans and BCIDs in July. The rationale for neglecting the two outliers when choosing the systematic uncertainty is that fixing the k-factor to 1.2 causes an increase in the true luminosity for each scan and BCID of around 10%. There is then a large disagreement between the simulation and data for the curve of μ_{vis} versus separation and a large increase in the overall χ^2.

The procedure of refitting the beam spot whilst fixing the k-factor was not done for the April and November scan sessions. The uncertainty on R due to the beam spot resolution should depend on the size of the beam spot relative to the resolution. The beam spot width in the horizontal and vertical dimensions was much smaller in April than in July and November and therefore the uncertainty on R from this source would be expected to be larger. However, since the value of 0.004 chosen for July is already quite conservative, i.e., the χ^2 values increase markedly from Table 4.6 (k-factor not fixed) to Table 4.14 (k-factor fixed to 1.2), it is decided that the value of 0.004 should apply to the April and November scans as well.

4.7.4 Uncertainty on the choice of beam parameterisation

The defining feature of the November scan session is that modelling the beam profiles as double Gaussian is insufficient to describe the evolution of the in-plane beam spot width (with certain exceptions). However all other observed features in data can be easily reproduced using the double Gaussian profile. Therefore an estimate of the systematic uncertainty on R due to this choice of parameterisation can be made by observing the variation in R between the cases when the beams are modelled as double supergaussian and when they are modelled as double Gaussian. Table 4.15 gives the χ^2 per degree of freedom and the value of R for each scan and BCID considered in November when the beams are modelled as double Gaussian.

Comparing Tables 4.15 (double Gaussian profile) and 4.8 (double supergaussian

	Scan number		
	IV	V	VI
BCID 1	1.71 - 0.961	1.91 - 0.974	1.44 - 0.974
BCID 721	2.70 - 0.961	2.05 - 0.974	2.14 - 0.977
BCID 1821	1.95 - 0.957	2.12 - 0.970	1.92 - 0.972

Table 4.16: The χ^2 per degree of freedom and the value of R for each BCID in scans IV, V and VI (July) in which the beam profiles are modelled as double supergaussian. Note that the reason for the worse χ^2 compared to Table 4.6 is that the luminosity normalisation constant (as described in Section 4.5) was not a free variable in the double supergaussian minimisation.

profile) the largest change in the value of R is (with one exception) 0.001. This is considered to be the systematic uncertainty on R due to the choice of beam parameterisation for all scan/BCID pairs in November apart from scan X, BCID 1 which is assigned an uncertainty of 0.004. Although there are some scans in which the R value obtained is the same after using the two different beam parameterisations, an uncertainty of 0.001 is still assigned as a larger range of possible models has not been explored.

Such an uncertainty might be expected to be of similar magnitude or smaller in April and July as there are no qualitatively poorly described features in the horizontal or vertical beam spot positions and widths that the additional ϵ parameters of the double supergaussian are required to improve. To check this the minimisation for scans IV, V and VI was repeated modelling the beams as double supergaussian. Table 4.16 gives the χ^2 per degree of freedom and the value of R for each BCID in scans IV, V and VI when the beams are modelled as double supergaussian.

Comparing Tables 4.16 (double supergaussian profile) and 4.6 (double Gaussian profile) the differences in R value are (with one exception) 0.001 or 0. An uncertainty from this source of 0.001 is therefore assigned to all scans and BCIDs in April and July.

4.7.5 Conclusions

Tables 4.17, 4.18 and 4.19 give the value of R for each scan and BCID considered in 2012 along with the value averaged over the BCIDs. These are given together with the total systematic uncertainties on those values, calculated by adding in quadrature the uncertainties from the sources discussed in Sections 4.7.2, 4.7.3 and 4.7.4. The uncertainty on the averaged value treats the resolution and beam parameterisation uncertainties as correlated and the statistical component as uncorrelated.

	Scan number		
	I	II	III
BCID 1	0.976 ± 0.004	0.981 ± 0.004	0.992 ± 0.004
BCID 241	0.975 ± 0.004	0.980 ± 0.004	0.989 ± 0.004
BCID 2881	0.972 ± 0.004	0.976 ± 0.004	0.991 ± 0.004
BCID 3121	0.970 ± 0.004	0.979 ± 0.004	0.992 ± 0.004
Mean	0.974 ± 0.004	0.979 ± 0.004	0.991 ± 0.004

Table 4.17: The value of R and its associated total systematic uncertainty for each scan and BCID considered in April 2012. The value of R averaged over BCIDs is also provided.

	Scan number			
	IV	V	VI	VIII
BCID 1	0.962 ± 0.004	0.974 ± 0.004	0.975 ± 0.004	0.970 ± 0.004
BCID 721	0.959 ± 0.004	0.974 ± 0.004	0.977 ± 0.004	0.969 ± 0.004
BCID 1821	0.956 ± 0.004	0.970 ± 0.004	0.972 ± 0.004	0.962 ± 0.004
Mean	0.959 ± 0.004	0.973 ± 0.004	0.975 ± 0.004	0.967 ± 0.005

Table 4.18: The value of R and its associated total systematic uncertainty for each scan and BCID considered in July 2012. The value of R averaged over BCIDs is also provided.

Within each scan session the correlated sources dominate due to the large beam spot resolution uncertainty. The values of R as a function of scan number for individual BCIDs are plotted in Figure 4.25 and the mean values of R for each scan are plotted in Figure 4.26. Note that even for the November scans, where the R values are close to unity, symmetric uncertainties are assumed as it is physically possible for R to be greater than one.

The LHC is the first hadron collider in which it was recognised that beam non-factorisation effects could significantly bias the vdM calibration [31] and a precise estimation of the size of any correction to σ_{vis} is needed in order to achieve an uncertainty on the luminosity of 2% or better. Using the method described in this thesis one can obtain corrections to σ_{vis} of between 0 and 4% (Figure 4.26) depending on the vdM scan in question — without the understanding gained through this study a large systematic uncertainty would have to be applied to the luminosity and therefore also to total cross-section measurements (for which the luminosity can often already be the dominant source of uncertainty).

The default value of σ_{vis} in 2012 is ultimately taken from the November scan

	Scan number			
	X	XI	XIV	XV
BCID 1	0.995 ± 0.006	1.00 ± 0.004	1.00 ± 0.004	1.00 ± 0.004
BCID 2361	0.996 ± 0.004	0.998 ± 0.004	0.997 ± 0.004	1.00 ± 0.004
BCID 2881	1.00 ± 0.004	1.00 ± 0.004	1.00 ± 0.004	1.00 ± 0.004
Mean	0.997 ± 0.005	0.999 ± 0.004	0.999 ± 0.004	1.00 ± 0.004

Table 4.19: The value of R and its associated total systematic uncertainty for each scan and BCID considered in November 2012. The value of R averaged over BCIDs is also provided.

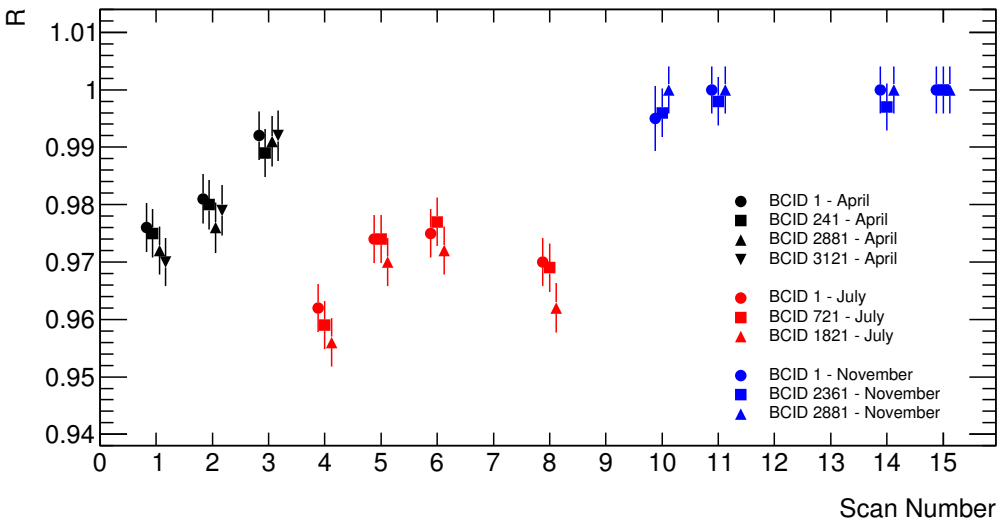

Figure 4.25: R as a function of scan number for each BCID considered in 2012. The error bars on each point are the quadratic sum of the correlated and uncorrelated uncertainties.

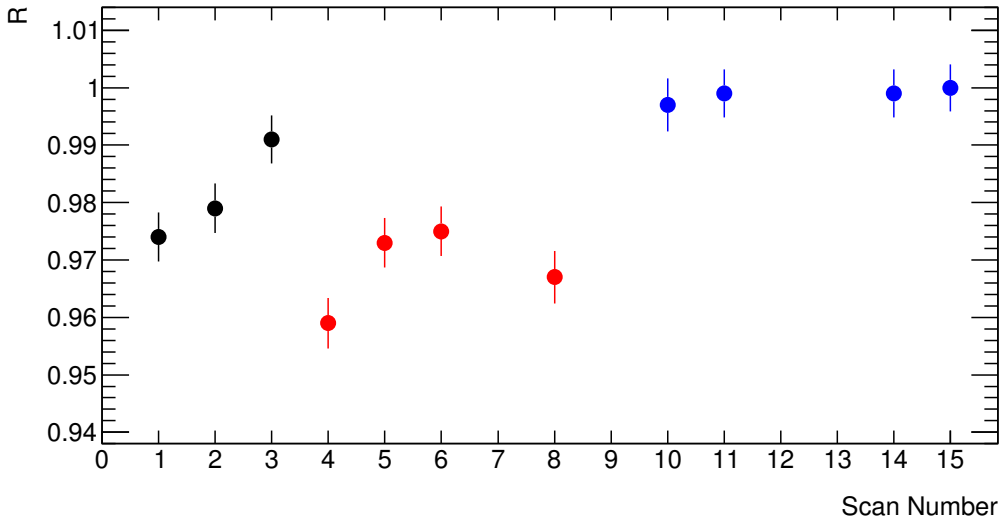

Figure 4.26: Mean R value as a function of scan number in 2012 averaged over BCIDs with beam spot data. The error bars on each point are the quadratic sum of the correlated and uncorrelated uncertainties.

session for the primary reason that the R values close to one allow for the avoidance of any non-factorisation correction and therefore possibly a smaller systematic uncertainty. However the analysis of the other scan sessions has still been critical, both in developing the method and in better understanding the long-term stability of the various detectors. The factorisable nature of the beams in the November scan session was a result of special preparation in the injector chain. After observation of large non-factorisation effects in both the April and July scan sessions an attempt was made to construct single Gaussian beams. Although this effort did lead to R values close to one, the beams could not eventually be described by a 3D Gaussian as demonstrated by the analysis of Section 4.6.4. The difficulty in qualitatively describing some of the observed effects (such as the decrease in beam horizontal width during a horizontal scan), even with the double supergaussian model, leads to concern over whether the level non-factorisation is being properly measured, for which further study and understanding will be required.

The dominant uncertainty on the value of R comes from the beam spot resolution and clearly this would need to be better understood in order to improve the precision of any future analysis. Because of this it would be beneficial to continue using the larger beam sizes used in July and November, rather than the smaller April beams. The crossing angle used in April also created additional problems, possibly due to drift of the longitudinal beam spot position, variation in the crossing angles during the run and/or poor description of the shape of the beams in the z-direction. It would therefore be recommended for future vdM scans to take place without any

beam crossing angle. Finally, the analysis procedure could be improved both by including all available information (i.e., measurements of μ_{vis} for which there is no beam spot data) and by using different beam parameterisations — specifically those which might be physically motivated from a more detailed study of the causes of non-factorisation effects.

Chapter 5

Probing soft QCD using the ϕ^*_η angular observable

5.1 Quantum Chromodynamics

Quantum Chromodynamics (QCD) is a quantum field theory which describes the interaction of particles with colour-charge, i.e., quarks and gluons [1]. The strength of the interaction can be parameterised by a coupling constant, α_s, the size of which depends on the energy scale of the process considered. For high-energy collisions α_s becomes small in a phenomenon known as asymptotic freedom, and interaction cross-sections can accurately be calculated using perturbation theory. At lower energies such as those typical inside a proton α_s becomes of order one and instead cross-sections are parameterised using form-factors which take their input from experiment. Figure 5.1 shows the value of α_s as a function of momentum transfer (Q) using data points from several experiments and methods [50].

5.2 The Drell-Yan process

5.2.1 Description

The Drell-Yan process involves the production of a lepton pair from hadron-hadron collisions via an intermediate boson — a photon, a Z boson or a W boson [51]. Although at high collision energies the partonic cross-sections can be calculated using perturbation theory, the partons are in fact confined to the structure of the hadron in a regime in which perturbation theory becomes invalid ($\alpha_s \approx 1$). However the QCD factorisation theorem states that these two parts can be separated when calculating interaction cross-sections with the non-perturbative piece obtained using

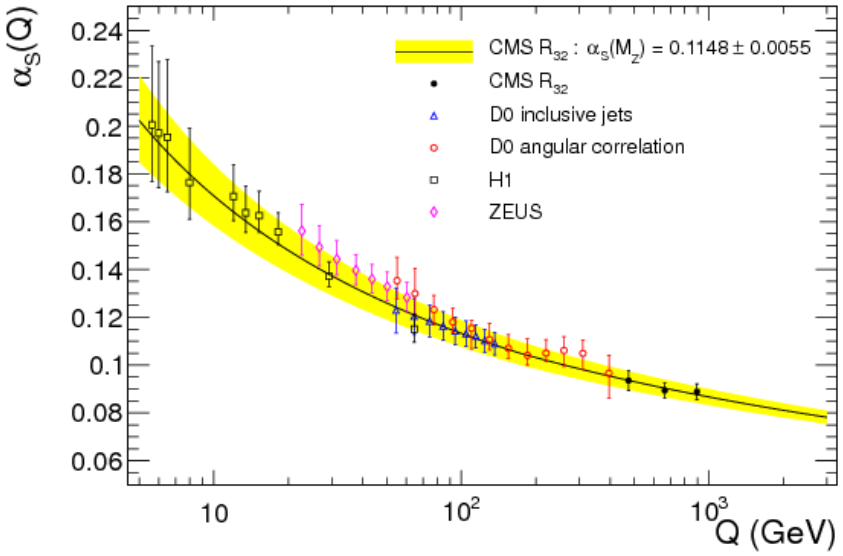

Figure 5.1: The strong coupling constant, α_s, is shown as a function of the momentum transfer, Q, using data points obtained from several different experiments and methods [50].

knowledge of the hadron parton distribution functions (PDFs), that is, the distribution of momentum of each parton species within a hadron which cannot currently be calculated from first principles and must be obtained from previous experimental data [52].

Equation 5.1 expresses this concept mathematically, where the Drell-Yan hadronic cross-section $\sigma_{h_A h_B \to l^+ l^-}$ is written as a convolution of the hadron PDFs, f_A and f_B, and the partonic cross-section $\sigma_{ab \to l^+ l^-}$, with a sum performed over all parton species, a and b, which contribute to the process [52]. The PDFs are functions of the parton longitudinal momentum fraction, x, and the factorisation scale, μ_F, which is a somewhat arbitrary energy scale generally chosen to be of the same order as the momentum transfer, Q.

$$\sigma_{h_A h_B \to l^+ l^-} = \sum_{a,b} \int_0^1 dx_a f_A\left(x_a, \mu_F^2\right) \int_0^1 dx_b f_B\left(x_b, \mu_F^2\right) \sigma_{ab \to l^+ l^-} \tag{5.1}$$

Corrections to Equation 5.1 must be made in order to better describe non-perturbative effects such as the transverse momentum of the parton within the hadron ('intrinsic k_T'). Note that the Drell-Yan process is one of only a few for which the QCD factorisation theorem has been analytically proven.

5.2.2 Boson transverse momentum distribution

The process under study in this thesis is that in which a photon or Z boson decays to an electron-positron pair[1]. Of particular interest is the boson transverse momentum distribution, firstly to test QCD predictions of initial state gluon radiation, but also in order to improve the measurement of the W boson mass. The detector signature used for such a measurement is an isolated high p_{T} lepton with missing transverse energy from the unobserved neutrino. The invariant mass of the W can therefore not be reconstructed and is instead obtained by simulating several kinematic variables (some of which depend on the W transverse momentum) for different W boson mass hypotheses and finding the best agreement with the data [53].

The tree-level diagram for the process of interest in this thesis is shown in Figure 5.2a, the Z boson in this case however does not receive any transverse momentum. Figure 5.2b is an example of a higher-order virtual correction to the tree-level process, also corresponding to zero boson transverse momentum. Figures 5.2c and 5.2d are examples of the lowest order Feynman diagrams in QCD which give a non-zero contribution to the Z transverse momentum. Such diagrams are referred to hereafter as 'leading-order in Z transverse momentum' or leading-order (LO).

For low p_{T} (soft) gluon emission and from emission collinear to the quark direction large logarithmic terms appear in the perturbative expansion when calculating the transverse momentum spectrum of this process. This is due to incomplete cancellation between diverging real and virtual diagrams. In order to obtain a finite prediction at low boson p_{T} it is possible to sum these logarithmic terms to all orders in a technique called 'resummation' [54]. Resummation of the dominant logarithmic terms at each order is referred to as 'leading-log' (LL) accuracy and resummation also including the sub-dominant terms is referred to as 'next to leading-log' (NLL) accuracy.

5.3 Monte Carlo event generators

Monte Carlo (MC) event generators are used to simulate the physical processes in order to obtain predictions for an observable of interest, for example, the Z boson transverse momentum or the ϕ^*_η distribution (see Section 5.4). There are several stages to the simulation procedure, which are briefly described now [1] [55].

The first step is the simulation of the hard (high momentum transfer) process. A probabilistic description of the process from which an event will have a particular

[1]Whenever reference to the Z boson is made in this thesis it is assumed that the contributions from the photon and its interference with the Z are also included.

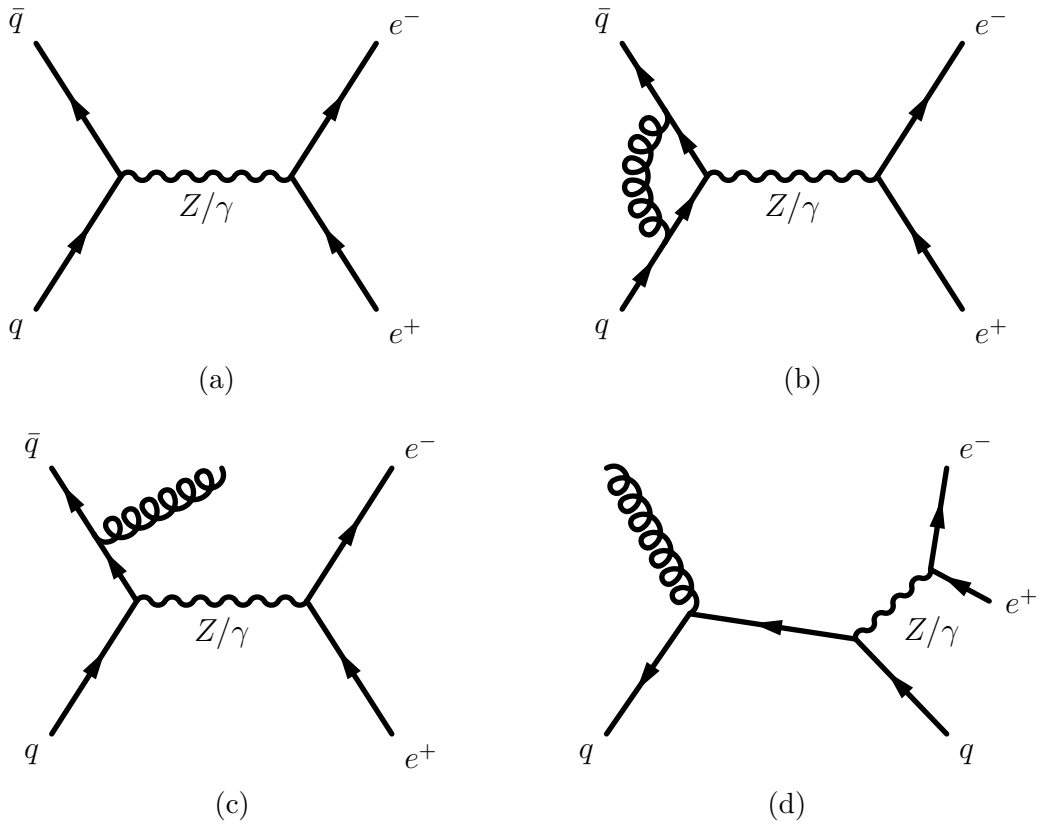

Figure 5.2: Four Feynman diagrams for the Drell-Yan process of interest. Figure 5.2a shows the tree-level process and Figure 5.2b shows an example of a higher-order virtual correction. Figures 5.2c and 5.2d are two examples of the lowest order diagrams in QCD which provide a non-zero contribution to the Z transverse momentum.

realisation is obtained by using PDFs (in the case of hadron collisions) to describe the incoming partons' momenta and then using perturbation theory to describe the outgoing partons.

The radiation of gluons from the incoming and outgoing partons, in addition to any from the hard process, is described by the MC parton shower. This is analogous to bremsstrahlung radiation of photons from a scattered electric charge. The parton shower is a step-by-step process which reduces the momentum transfer scale and increases α_s until using perturbation theory is no longer possible. The parton shower in an event generator performs a similar role to resummation in an analytical calculation, but as a phenomenological model the shower contains some free parameters which must be obtained from experimental data (tuned). This is one of the motivations for a measurement of the ϕ^*_η observable, which is described in Chapter 6.

The next stage of event generation is hadronisation, which also uses parameters which must be tuned from experiment. This models the non-perturbative process of the formation of hadrons from the partons in the event. Related to this is modelling of the underlying event, that is, the coloured remnants of the colliding protons which can also interact and form hadrons.

Finally various other processes can be simulated, depending on the requirements of the situation. These include modelling of the decay of the heavy, unstable hadrons, modelling of the final state photon radiation and modelling of additional simultaneous hadron-hadron interactions (pile-up). If the Monte Carlo is to be compared to data then modelling of the passage of the simulated particles through the detector must also be performed, typically using the Geant4 program [56].

5.4 The ϕ^*_η observable

5.4.1 Definition and motivation

The precision of a measurement of the boson p_{T} spectrum in Drell-Yan events is limited by the lepton momentum resolution, which is typically no better than one percent in ATLAS. This motivated the development of the ϕ^*_η variable, which is an angular observable that depends only on the better-measured lepton directions [57]. The ϕ^*_η variable is defined in Equation 5.2, where $\Delta\phi$ is the difference in azimuthal angle between the two leptons and θ^*_η is the polar angle of the negatively-charged lepton in the frame in which the two leptons have equal and opposite pseudorapidity. The variable θ^*_η is defined in Equation 5.3, where η^+ and η^- refer to the pseudorapidities, as measured in the lab-frame, of the positively-charged and negatively-charged

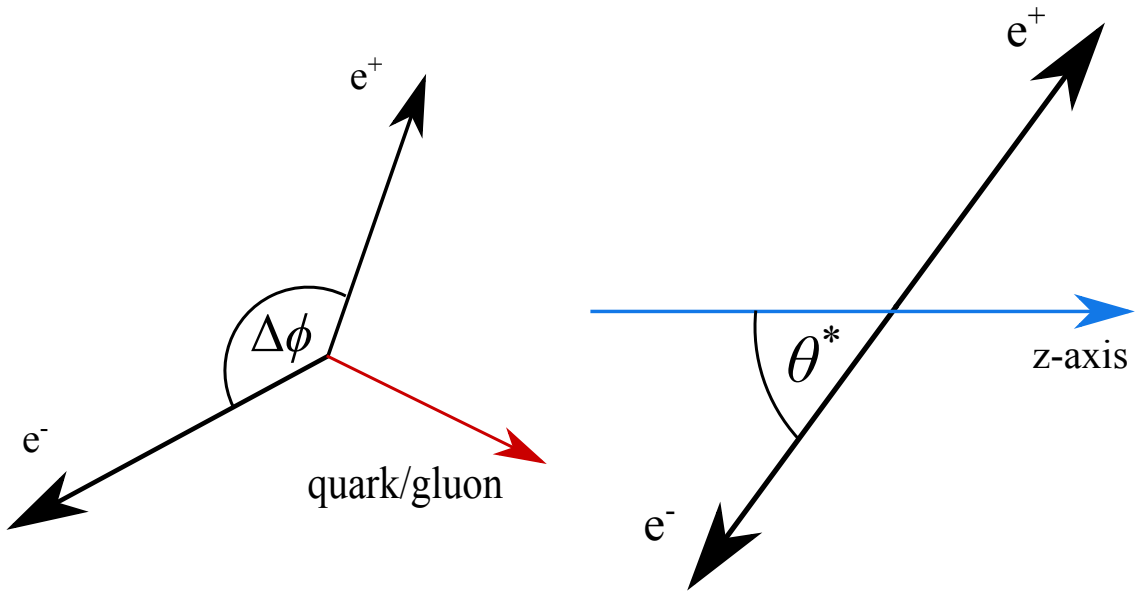

(a) Diagram of the process in the plane transverse to the beam axis.

(b) Diagram of the process in the r-θ plane in the frame in which the leptons have equal and opposite pseudorapidity. The system is shown for the limit in which there is zero initial state or final state radiation and therefore zero p_{T}.

Figure 5.3

leptons respectively. The frame in which θ^*_η is measured corresponds to the Lorentz boost, β, along the beam axis given in Equation 5.4.

$$\phi^*_\eta = \tan\left(\frac{\pi - \Delta\phi}{2}\right)\sin\theta^*_\eta \tag{5.2}$$

$$\theta^*_\eta = \arccos\left(\tanh\left(\frac{\eta^- - \eta^+}{2}\right)\right) \tag{5.3}$$

$$\beta = \tanh\left(\frac{\eta^- + \eta^-}{2}\right) \tag{5.4}$$

The relevant variables are shown diagrammatically in Figure 5.3. Figure 5.3a shows the plane transverse to the beam direction for the case in which the di-lepton system has non-zero transverse momentum due to some initial state quark or gluon radiation. Figure 5.3b shows the r-θ plane in the frame in which the leptons have equal and opposite pseudorapidity. The system is shown for the limit in which the di-lepton system has zero p_{T} and as such the frame corresponds to the di-lepton rest frame and the particles are emitted back-to-back.

The largest motivation for the definition of ϕ^*_η comes from a desire to more

precisely measure the properties of the low boson p_{T} regime (also corresponding to low ϕ^*_η), which is traditionally limited by the lepton momentum resolution. This regime is sensitive to both perturbative QCD dynamics (i.e., multiple soft and/or collinear radiation) as well as non-perturbative QCD effects such as the parton intrinsic k_T.

Zero boson p_{T} corresponds to the two leptons emitted back-to-back in the transverse plane, $\Delta\phi$ is equal to π and ϕ^*_η is equal to zero. Assuming approximately equal lepton p_{T}, an increase in the boson p_{T} causes a decrease in $\Delta\phi$, or decorrelation between the leptons. However for two events which both have the same di-lepton invariant mass and p_{T}, the $\Delta\phi$ can differ depending on the lepton scattering angle in the centre of mass frame, for which θ^*_η is a reasonable approximation at low boson p_{T}. At low ϕ^*_η therefore, there is very high correlation between the boson p_{T} and ϕ^*_η (for the same boson invariant mass). At high ϕ^*_η the definition becomes more arbitrary and the motivation is anyway reduced as the fractional resolution of the boson p_{T} improves.

5.4.2 Final state radiation

If there is final state photon radiation (FSR) from one or both leptons the ϕ^*_η measured will change. There are two main approaches that can be taken when considering this effect. The first is to correct the measured value back to that before FSR using a MC model of the process. This is called a 'Born level' measurement and is required if one wishes to perform a combination of electron and muon channels or to compare to theoretical predictions which do not simulate the effects of FSR (the majority). The disadvantage is that the systematic uncertainty due to the modelling of FSR in the MC can be large.

The second approach is to perform no correction (a 'bare level' measurement) or a partial correction for co-linear radiation (a 'dressed level' measurement). In these cases the MC modelling uncertainty is much reduced and the data remains relevant over longer periods of time as models of FSR improve. The measurements of ϕ^*_η in the di-electron channel detailed in Chapter 6 are made at both the Born and dressed levels. The exact details of the correction made along with the motivation for using the dressed level over the bare level is given in that chapter.

5.5 Measurements of ϕ^*_η at hadron colliders

Measurements of the ϕ^*_η distribution have previously been made at both the Tevatron and the LHC. The first was performed by the D0 collaboration, which presented the

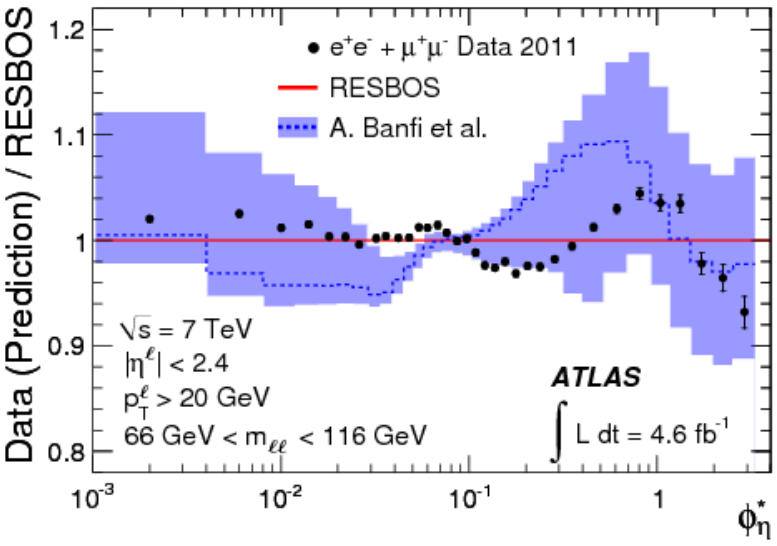

Figure 5.4: The ratio of the combined di-electron and di-muon differential cross-section from the 7 TeV ATLAS analysis to RESBOS [62]. Also shown is a prediction from Banfi et al. in which an NNLL resummation calculation is matched to NLO results from the MCFM MC generator [63].

normalised $Z \to l^+l^-$ cross-section, differential in ϕ^*_η for the di-electron and di-muon channels for events with an invariant mass close to the Z-peak [58]. The results have been used to tune parameters in the RESBOS program [59]. The D0 analysis was subsequently extended in the di-muon channel to make the measurement for events with a mass both above and below the Z-peak [60].

The absolute differential cross-section was measured by the LHCb collaboration in a wide invariant mass range at $\sqrt{s} = 7$ TeV [61]. The geometry of the LHCb detector allows observation of events highly boosted along the beam direction, which are inaccessible to D0 or ATLAS, and as such provides complementary information.

Finally the ATLAS collaboration measured the normalised differential cross-section for events with an invariant mass close to the Z-peak at $\sqrt{s} = 7$ TeV [62]. Figure 5.4 shows the ratio of the data (a combination of the di-electron and di-muon channels) to a prediction from RESBOS. The plot also shows a prediction from Banfi et al. in which an NNLL resummation calculation is matched to NLO results from the MCFM MC generator [63]. The ATLAS $\sqrt{s} = 7$ TeV data have been used to tune the PYTHIA and POWHEG+PYTHIA MC generators [64].

A measurement of the normalised differential cross-section in the di-electron channel at $\sqrt{s} = 8$ TeV with ATLAS data is presented in Chapter 6. This extends the ATLAS results at 7 TeV most prominently by performing the measurement for events with an invariant mass both above and below, in addition to at the Z-peak. The analysis also takes advantage of the larger data-set (an integrated luminosity

of $20.3\,\text{fb}^{-1}$ compared to $4.6\,\text{fb}^{-1}$ at 7 TeV) by adding two bins at high ϕ^*_η and by performing the measurement in finer divisions of boson rapidity.

Chapter 6

Measurements of the Z boson cross-section, differential in ϕ^*_η, in wide bins of boson mass and rapidity in the electron-positron channel with the ATLAS detector

6.1 Definition of the measurements

This chapter describes measurements of the quantity

$$\frac{1}{\sigma}\frac{d\sigma}{d\phi^*_\eta}$$

where σ is the Drell-Yan production cross-section multiplied by the branching-fraction into electron-positron pairs and ϕ^*_η is the angular observable introduced in Equation 5.2, Section 5.4.1. The quantity is henceforth referred to as the normalised differential cross-section and the electron and positron are generically referred to as electrons.

The analysis uses $20.3\,\text{fb}^{-1}$ of $\sqrt{s} = 8\,\text{TeV}$ proton-proton collision data recorded at the ATLAS detector in 2012. Measurements are made in twelve distinct kinematic regions defined by the invariant mass, M, and absolute rapidity, $|y|$, of the intermediate vector boson (Z boson or photon). The rapidity is defined in terms of the boson energy, E, and the longitudinal momentum, p_z, in Equation 6.1 and for massless particles is equivalent to the pseudorapidity. The twelve kinematic regions are defined in Table 6.1 where the three divisions in invariant mass are referred to

$46\,\text{GeV} < M < 66\,\text{GeV}$ 'low-mass region'	$66\,\text{GeV} < M < 116\,\text{GeV}$ 'peak-mass region'	$116\,\text{GeV} < M < 150\,\text{GeV}$ 'high-mass region'
$0.0 < \|y\| < 0.8$	$0.0 < \|y\| < 0.4$ $0.4 < \|y\| < 0.8$	$0.0 < \|y\| < 0.8$
$0.8 < \|y\| < 1.6$	$0.8 < \|y\| < 1.2$ $1.2 < \|y\| < 1.6$	$0.8 < \|y\| < 1.6$
$1.6 < \|y\| < 2.4$	$1.6 < \|y\| < 2.0$ $2.0 < \|y\| < 2.4$	$1.6 < \|y\| < 2.4$

Table 6.1: The twelve kinematic regions in which a measurement of the normalised differential cross-section was performed. The three divisions in invariant mass are referred to with respect to the position of the Z-peak.

with respect to the position of the Z-peak, that is, as the low-mass, peak-mass and high-mass regions.

$$y = \frac{1}{2} \ln \frac{E + p_z}{E - p_z} \tag{6.1}$$

As discussed in Section 5.4.2 any final state photon radiation (FSR) will change the value of ϕ^*_η measured. The motivation for this analysis is to improve understanding of non-perturbative QCD, which relates to the initial state quark or gluon radiation. Most theoretical predictions do not include or do not simulate very accurately the effects of FSR and therefore the results here are firstly provided at the Born level which corrects the measured electron direction to that before any FSR. The other main advantage is that assuming lepton-universality one can combine the di-electron and di-muon channels, which have different FSR signatures.

The other truth level definition for which the final results are provided is the dressed level. The electron four-vector at dressed level is defined by performing the sum of the bare level electron four-vector (electron after all FSR) and the four-vectors of photons within $\Delta R = 0.1$ of that bare electron. The quantity ΔR is a measure of solid angle and is defined in Equation 6.2 in terms of the pseudorapidity, η, and azimuthal angle, ϕ, of the two particles in question (here the bare electron and a photon).

$$\Delta R = \sqrt{(\eta_1 - \eta_2)^2 + (\phi_1 - \phi_2)^2} \tag{6.2}$$

The advantage of the dressed level definition is that an electron energy measurement at truth level more closely corresponds to that measured in the detector, that is, a cluster of energy in the EM calorimeter. However it must be noted that the direction of the track in the Inner Detector is better identified with the direction of

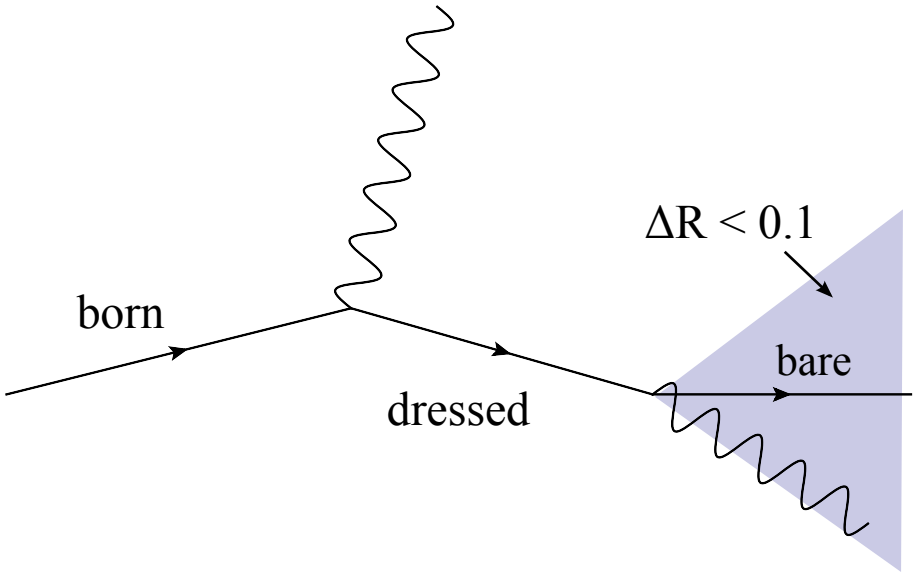

Figure 6.1: A diagram illustrating the different between the Born, dressed and bare level electron definitions. The Born level refers to the electron before any final state photon radiation, the bare level to the electron after all FSR and the dressed level to the four-vector sum of the bare electron and photons within $\Delta R = 0.1$ of the bare electron.

the bare level electron. The results at dressed level have a smaller systematic uncertainty due to theoretical modelling of FSR than those at Born level. This means that the results will remain relevant for longer periods of time, as better models of FSR are developed and integrated with theoretical predictions. A diagram illustrating the difference between the Born, bare and dressed electron is shown in Figure 6.1.

The reason for performing a normalised measurement is twofold. Firstly any overall scale uncertainty such as on the luminosity is fully correlated between bins of $d\sigma/d\phi^*_\eta$ and therefore cancels when dividing by the total cross-section, σ. Other uncertainties such as on the trigger scale factors (see Section 6.8.1) are partially correlated between bins, which means the uncertainty is much reduced after dividing by σ. The second reason for performing a normalised measurement is that most of the important information necessary to improve the theoretical calculations or parton shower modelling comes from the shape of the ϕ^*_η distribution, rather than from the absolute scale.

6.2 Outline of analysis method

In this section an outline of the analysis procedure is given, each step of which is expanded upon in subsequent sections. The first stage is to optimise the event selection criteria to reduce contamination from background processes, whilst keeping

a large number of signal events. This is described in more detail in Sections 6.3 to 6.5 and the motivation for the chosen binning in ϕ^*_η, mass and rapidity is discussed in Section 6.6. Section 6.7 then lists the background processes considered and explains how each one was estimated.

In order to be able to use Monte Carlo to estimate certain backgrounds, or to correct the measured data for detector resolution and inefficiency, one must be first convinced that the model describes the data reasonably well in the distributions of various basic variables, such as the electron η and ϕ distributions or the average number of interactions per bunch crossing. Certain corrections are applied to the data or model in order to improve the agreement and these are described in Section 6.8.1. The data-model comparison distributions or 'control plots', are then shown in Section 6.8.2.

The next stage of the analysis is to subtract the background estimation from the data and then obtain the normalised differential cross-section at both the Born and dressed levels using correction factors determined from Monte Carlo. This procedure is detailed in Section 6.9. Then systematic uncertainties from a number of sources are estimated by varying any experimental or theoretical parameters within their individual uncertainties and observing the change induced on the final distributions. The sources of uncertainty considered and the method used to estimate the size of each are described in Section 6.10.

The final dressed level distributions with total systematic and statistical uncertainties are displayed in Section 6.11.1. The Born level distributions are then combined with those from the di-muon channel and shown in Section 6.11.2. The combined results are compared to various theoretical predictions in Section 6.11.3.

6.3 Event selection

6.3.1 Overview

The selection of events for study was designed to have a high signal efficiency ($Z \to e^+e^-$) whilst rejecting a large fraction of background events. The basic cuts to select events with certain characteristics are applied to both the data and MC. These comprise a di-electron trigger and a requirement of two 'good' electrons, where the exact definition of a good electron is provided in Section 6.4. A second class of cuts is applied only to data and removes events in which sub-detectors were not functioning satisfactorily (application of a Good Runs List) or in which data are corrupted. A summary of the event selection is given in Table 6.2 and more detailed information is provided in Section 6.3.2.

Event characteristics (data and MC)
Pass trigger `EF_2e12Tvh_loose1` or `EF_2e12Tvh_loose1_L2StarB`
Number of 'good' electrons = 2
Detector quality (data)
Pass Good Runs List selection
Reject events with liquid argon noise bursts
Reject events with corrupted TileCal data
Remove incomplete events

Table 6.2: A summary of the event selection cuts. These are divided into two categories, those which distinguish event characteristics, which are applied to data and MC and those which define detector quality criteria and are only applied to data. More details on what constitutes a good electron are given in Section 6.4.

6.3.2 Additional details

Events must pass at least one of two di-electrons triggers: `EF_2e12Tvh_loose1` and `EF_2e12Tvh_loose1_L2StarB`. Both of these require that two electrons were identified at Event Filter level with a p_{T} greater than 12 GeV. It is additionally required that the ΔR between the selected analysis electron (see Section 6.4) and the electron object which caused the EF trigger to fire is less than 0.15.

Previously the two electrons must have passed the same p_{T} threshold at the L2 trigger stage and at L1 two electromagnetic clusters with p_{T} at least greater than 10 GeV must be identified. The actual threshold at L1 is optimised to correct for dead-material in the calorimeter (for example, cables and cooling systems) and is a function of pseudorapidity. The label 'v' in the trigger name refers to use of a variable threshold. The label 'loose1' refers to the electron identification criteria used at L1 and EF and corresponds to the 'loose++' identification at the offline analysis level (see Section 6.4.2).

The designation 'L2StarB' indicates the use of a particular software framework for the tracking trigger at L2 and the inclusion of this trigger provides a gain in efficiency for electrons in the end-cap regions. The label 'T' in each trigger name indicates a small gap (here a maximum of 2 GeV) between the L1 and L2 thresholds and the label 'h' indicates a cut on leakage of energy into the hadronic calorimeter, that is, a longitudinal isolation cut.

The requisite for exactly two electrons passing the electron selection criteria is made to reduce contamination from background processes with prompt high-p_{T} final state electrons, examples of which include Drell-Yan $W \to e\nu$ and di-boson decays into multiple electrons. The full list of backgrounds considered is given in

Medium++ identification
Electron author requirement
Object quality requirement
Relative isolation: $\sum p_{\mathrm{T,\,track}}(\Delta R < 0.4)/E_{\mathrm{T}} \leq 0.2$
$E_{\mathrm{T}} \geq 20\,\mathrm{GeV}$
$0 < \lvert\eta\rvert < 1.37$ or $1.52 < \lvert\eta\rvert < 2.40$

Table 6.3: A summary of the identification and selection criteria used to identify a 'good' electron. The $|\eta|$ cuts reject electrons which pass into the poorly instrumented region between the barrel and end-caps, known as the crack region. Both electrons are required to pass the isolation requirement in the low-mass and high-mass regions. This is loosened at peak-mass to require that at least one of the two electrons is isolated.

Section 6.7.

6.4 Electron selection

6.4.1 Overview

As discussed in Section 6.3 events are required to contain exactly two 'good' electrons. This section defines the properties of such electrons and details the cuts performed to select them. Electrons are identified using a variety of information including EM shower shape, hadronic leakage and isolation, and then cuts on p_{T} and pseudorapidity are made which define the kinematic and geometric acceptance. The p_{T} of an electron is defined using the energy of the electron cluster and the direction of the measured track (given that the track has at least four silicon hits) and is commonly referred to as the transverse energy, E_{T}, (Equation 6.3). The electron p_{T} can be defined using only track variables — this quantity is referred to as $p_{\mathrm{T,\,track}}$ and is used in this analysis only in the electron isolation requirement.

$$E_{\mathrm{T}} = E\sin\theta = \begin{cases} \frac{E}{\cosh\eta_{\mathrm{track}}} & \text{Number of silicon hits} \geq 4 \\ \frac{E}{\cosh\eta_{\mathrm{cluster}}} & \text{Number of silicon hits} < 4 \end{cases} \tag{6.3}$$

Table 6.3 summarises the cuts made and then Section 6.4.2 provides a more detailed description of each one.

6.4.2 Additional details

Reconstructed electromagnetic objects may originate from electrons, photons or other detector activity (for example, jets). Therefore a set of identification criteria is defined to select electrons with a particular efficiency and background. These include EM shower shape, leakage of cluster energy into the hadronic calorimeter and track quality. The two sets of criteria used in this analysis are named Medium++ (for the default electron selection, and is around 85% efficient) and Loose++ (for the multi-jet background selection — see Section 6.7). The Loose++ criteria are a less restrictive sub-set of the Medium++ criteria and the discriminating variables used for each are now listed [65].

w_{stot}: The shower width in the first layer (strip layer) of the EM calorimeter.

E_{ratio}: The ratio of the energy difference between the largest and smallest energy deposits of the cluster in the strip layer to the sum of those energies.

$W_{\eta 2}$: Lateral shower width in the middle layer of the EM calorimeter.

R_{η}: The ratio of energy in 3×3 cells to that in 3×7 cells, centred at the electron cluster position.

f_3: The ratio of energy in the back layer to the total energy in the EM accordion calorimeter (Medium++ identification only).

R_{had}(R_{had1}): Fraction of the cluster E_{T} deposited in the (first layer of) the hadronic calorimeter.

n_{Blayer}, n_{pix}, n_{Si}: Number of hits in the B-layer (first pixel layer), all pixel layers and all silicon (pixel + SCT) layers.

$\Delta\eta$: The difference between the η of the cluster and the η of the extrapolated track.

d_0: The transverse impact parameter (Medium++ identification only).

The electron author variable indicates which reconstruction algorithm identified the EM object from the raw data. Here it is required that the object was found by the standard cluster-seeded algorithm and was matched to at least one track in the Inner Detector [65]. Electrons are also required to pass the object quality requirement, which rejects clusters which pass through dead, noisy or otherwise problematic parts of the EM calorimeter.

The relative isolation variable I is defined in Equation 6.4, which is the sum of track p_{T} within a cone $\Delta R = 0.4$ around the electron divided by the electron E_{T}.

In the low-mass and high-mass regions both of the good electron candidates are required to have $I \leq 0.2$, whilst in the peak-mass region this requirement is relaxed such that only one electron need be isolated.

$$I = \frac{\sum p_{\mathrm{T,\,track}}(\Delta R < 0.4)}{E_{\mathrm{T}}} \tag{6.4}$$

The motivation for the isolation cut is to reduce contamination from multi-jet background. An example of such a process is a gluon splitting into two b-quarks, forming jets which contain or are reconstructed as an electron. A jet contains a lot of hadronic activity and as such the sum of the p_{T} of all tracks in a cone $\Delta R = 0.4$ surrounding the electron is likely to be larger than for a prompt electron from a Z decay. The cut is less strict at peak-mass to prevent a large systematic uncertainty at higher values of ϕ^*_η from the choice of MC used to correct the data to truth level. The multi-jet background contamination is nevertheless small in this mass region.

A cut on electron p_{T} is applied at 20 GeV. The value chosen is a compromise between a desire to have as wide a kinematic acceptance as possible (to fully utilise the data available) and the efficiency of the di-electron trigger, which is approximately constant above 20 GeV. A more detailed discussion on how the trigger inefficiency is treated using MC scale factors is given in Section 6.8.1.

The absolute pseudorapidity of both electrons is required to be less than 2.4 in order to be within the geometric acceptance of the tracker. Technically values up to $|\eta| = 2.47$ would be feasible but 2.4 was chosen for consistency with the di-muon channel for which the limitation is the Thin Gap Chamber trigger. The electrons are also required not to have an absolute pseudorapidity in the range 1.37 to 1.52 to avoid the poorly instrumented region between the barrel and end-cap calorimeters, known as the crack region. No such veto is required for the muon channel measurement, which means an extrapolation of the electron channel measurement must be performed in order to combine the two. Further details on this are provided in Section 6.11.2.

6.5 Truth event selection

The final normalised differential cross-section, at a particular truth level, is obtained by dividing the measured data by correction factors determined from Monte Carlo. The bin-by-bin correction factor, c_i, for a bin i is defined in Equation 6.5 as the number of events in that bin at reconstruction (detector) level divided by the number of events at truth level. Further and more precise details on the correction procedure are given in Section 6.9, but here it is discussed how MC events are selected in order

2 electrons (Born or dressed as required)
$p_{\mathrm{T}} \geq 20\,\mathrm{GeV}$
$0 < \lvert\eta\rvert < 1.37$ or $1.52 < \lvert\eta\rvert < 2.40$ (*fiducial* volume)
$0 < \lvert\eta\rvert < 2.40$ (*combination* volume)

Table 6.4: A summary of the truth level event selection criteria. The cuts on electron absolute pseudorapidity differ depending on whether the measurement is made in the fiducial volume (for the single channel measurement) or in the combination volume (for the combination with the muon channel).

to produce the necessary truth level ϕ^*_η distribution.

$$c_i = \frac{n_{i,\mathrm{reco}}}{n_{i,\mathrm{truth}}} \tag{6.5}$$

In addition to information on reconstructed objects at detector level, the MC event record includes details of many or all of the particles that existed during the different stages of event generation. The challenge is to select the (two) electrons which most closely correspond to the chosen truth level definition (here, Born or dressed). The event then passes the truth selection if the electrons are within the required geometric and kinematic acceptance.

The MC factors correct for detector inefficiencies, detector resolution and for FSR. In order to not use the Monte Carlo to correct for less well-understood effects an effort is made to require a similar set of selection criteria to that used at detector level (see Section 6.3). These are summarised in Table 6.4 and described in more detail below. Note that the selection is made using only signal MC ($Z \to e^+e^-$).

Three signal MC simulations are used in this analysis for the purposes of cross-checking results and estimating the size of certain uncertainties (see Section 6.10). The bin-by-bin correction factors obtained from each MC are averaged to obtain the central values of the final dressed and Born level distributions.

The first MC uses Powheg [66] to generate the hard process, Pythia [67] to simulate the parton shower, hadronisation and the underlying event, and Photos [68] to simulate the final state photon radiation. This MC is referred to as Powheg+Pythia in future discussions and is the signal sample used in the plots of this chapter, unless otherwise stated. The two other MC signal samples used are 'Powheg+Herwig', which again uses Powheg to generate the hard process and Photos for the FSR simulation, but uses Herwig [69] for the parton shower and underlying event, and a sample which uses Sherpa [70] to simulate all stages of the event generation. Details on the mass range over which events were generated and numbers of simulated events in each sample are provided in Table 6.5.

Generator	Mass range (GeV)	Channel number	Number of events
Powheg+Pythia	$20 < M < 60$	129502	10×10^6
	$M > 60$ (2e filter)	129680	50×10^6
	$M > 60$ (1e filter)	129685	20×10^6
Powheg+Herwig	$M > 60$ (2e filter)	185710	50×10^6
	$M > 60$ (1e filter)	185711	20×10^6
Sherpa	$M > 40$	147770	100×10^6

Table 6.5: A summary of the signal MC samples used in this analysis. The mass range refers to that in which the events were generated. Some samples are split according to the number of electrons with p_{T} greater than 15 GeV with $|\eta| < 2.7$ after FSR — these are described as di-electron (2e) filter and single-electron (1e) filter. The channel number is an ATLAS specific descriptor unique to a particular sample.

The formula for obtaining Born level electrons (or positrons) is generator specific, but in each case aims to select electrons before the effects of any final state photon radiation. The formula for obtaining bare level electrons is common to MC samples — one requires a final-state or 'stable' electron which has not been produced from the decay of a hadron or τ-lepton. The photons used for dressing the bare electrons must also pass the same requirements as well as be within a cone $\Delta R < 0.1$ of the bare electron. Only in a very small fraction of events are two pairs of oppositely-charged electrons found passing these criteria and also within the kinematic and geometric acceptance. For these events a random choice is made. Note that in all cases a veto is imposed on particles which originated from the Geant4 detector simulation.

6.6 Binning choices

Three main considerations were made when choosing the bin edges in ϕ^*_η, boson mass and rapidity for the normalised differential cross-section measurement. These are the number of data events ('statistics'), the angular resolution of the ATLAS detector and the bin purity, that is, the level of event migration between ϕ^*_η bins from truth level to detector or reconstruction level. Consistency with the ATLAS 7 TeV measurement was also important. Each of these considerations are now discussed.

The size of the 8 TeV data-set is several times larger than at 7 TeV (an integrated luminosity of 20.3 fb^{-1} compared to 4.6 fb^{-1} and in principle this could allow finer binning in ϕ^*_η, mass or rapidity. However due to the finite angular resolution and purity considerations (see below) and the desire to extend the set of measurements

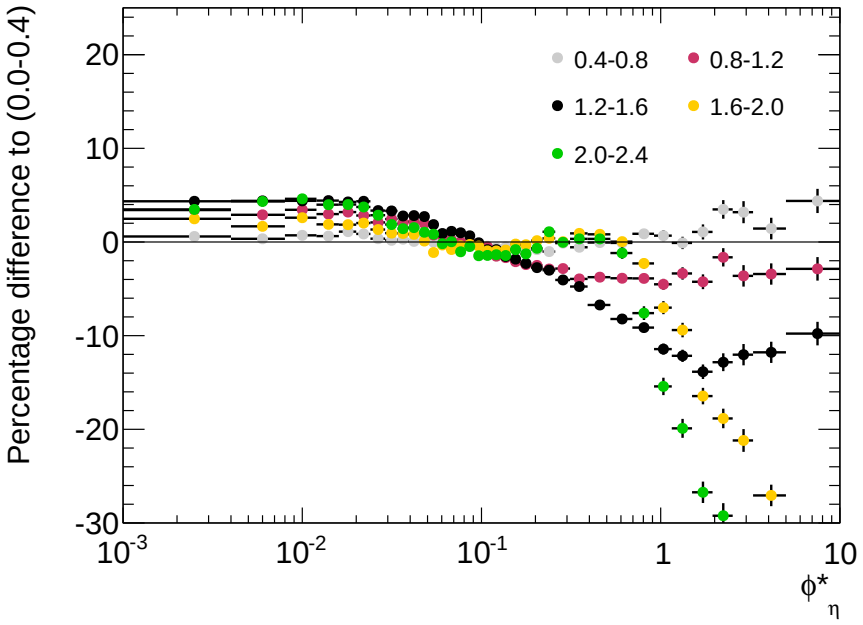

Figure 6.2: The percentage difference, as a function of ϕ^*_η at the Born level, between the value of $(1/\sigma)\, d\sigma/d\phi^*_\eta$ in each boson rapidity bin to the value in the central rapidity bin ($|y| < 0.4$). Events have an invariant mass between 46 GeV and 600 GeV and are simulated using Powheg+Pythia MC.

above and below the Z mass-peak it was decided to use the same binning in ϕ^*_η as at 7 TeV with the addition of two bins at the upper edge.

The number of boson rapidity regions in the peak-mass region was also increased from 3 to 6 because of the higher available statistics. From previous measurements and from theoretical predictions the shape of the ϕ^*_η distribution is known to change as a function of boson rapidity. This is illustrated using a Born level MC prediction in Figure 6.2, which shows the percentage difference between the value of $(1/\sigma)\, d\sigma/d\phi^*_\eta$ in each rapidity bin to the value in the central rapidity bin ($|y| < 0.4$), as a function of ϕ^*_η. The finer bins in rapidity give more detailed information which will constrain future MC tuning.

The finite detector angular resolution (very approximately 1 mrad [71]) puts a lower constraint on the size of the narrowest bins in ϕ^*_η. For low boson p_{T} and $|\eta| = 0$, ϕ^*_η can be approximated as $(\pi - \Delta\phi)/2$. The angular resolution in ϕ^*_η is therefore also of order 0.001. In this analysis the narrowest bins (the six lowest in ϕ^*_η) are given a width of 0.004. An uncertainty on the MC modelling of the angular resolution is discussed in Section 6.10.2.5.

A concept related to the angular resolution, but which also considers bin migration due to FSR is the purity. The purity, p_i, is defined in Equation 6.6, as the number of events reconstructed and generated in bin i, divided by the number

reconstructed in that bin. The label i can either be used to refer to a particular ϕ^*_η bin, a region in boson mass and rapidity or the union of all three.

$$p_i = \frac{n_{i,\text{reco \& truth}}}{n_{i,\text{reco}}} \tag{6.6}$$

The higher bin purity in ϕ^*_η compared to boson p_T is one of the primary motivations for the study of the observable. Although more sophisticated MC correction techniques (such as iterative Bayesian unfolding) can be used to compensate for lower bin purities, this nevertheless can bring additional uncertainties and therefore the ϕ^*_η observable allows study of non-perturbative physics (low p_T and ϕ^*_η) in finer detail. Any possible bias in using bin-by-bin correction factors is explored in Section 6.10.3.

Figure 6.3 shows the purity using the Born, bare and dressed truth level definitions as a function of ϕ^*_η for the three different mass regions. The curves are shown integrated over absolute boson rapidity from 0 to 2.4, but do not vary much as a function of rapidity. Events are required to be generated in the same ϕ^*_η bin as they are reconstructed, but no requirement is made on the truth boson mass or rapidity.

Two observations are made regarding the plots in Figure 6.3. In each mass region the Born level purity is lower than the bare and dressed levels and is particularly low in the low-mass region. The reason for this is that final state photon radiation may be emitted with large p_T and change the ϕ^*_η value quite considerably between truth and reconstruction level. The purity is further reduced in the low-mass plot because di-electron pairs generated with a Born mass around the Z-peak will also tend to be reconstructed with a lower invariant mass after FSR.

It is also observed that the dressed purity is nearly always higher than the bare purity, despite the track in the Inner Detector being better identified with the direction of the bare level electron. The reason is that the reconstruction level cut on E_T uses calorimeter energy cluster information and is therefore better identified with the dressed electron p_T. Events which are generated with a bare p_T just below 20 GeV may pass the reconstruction level E_T cut, which results in a lower purity.

The set of bin-edges in ϕ^*_η finally adopted are displayed in Table 6.6 along with the number of selected data events in each bin of ϕ^*_η, boson mass and boson rapidity. The same ϕ^*_η binning is used in each mass and rapidity region for convenience and easy comparison.

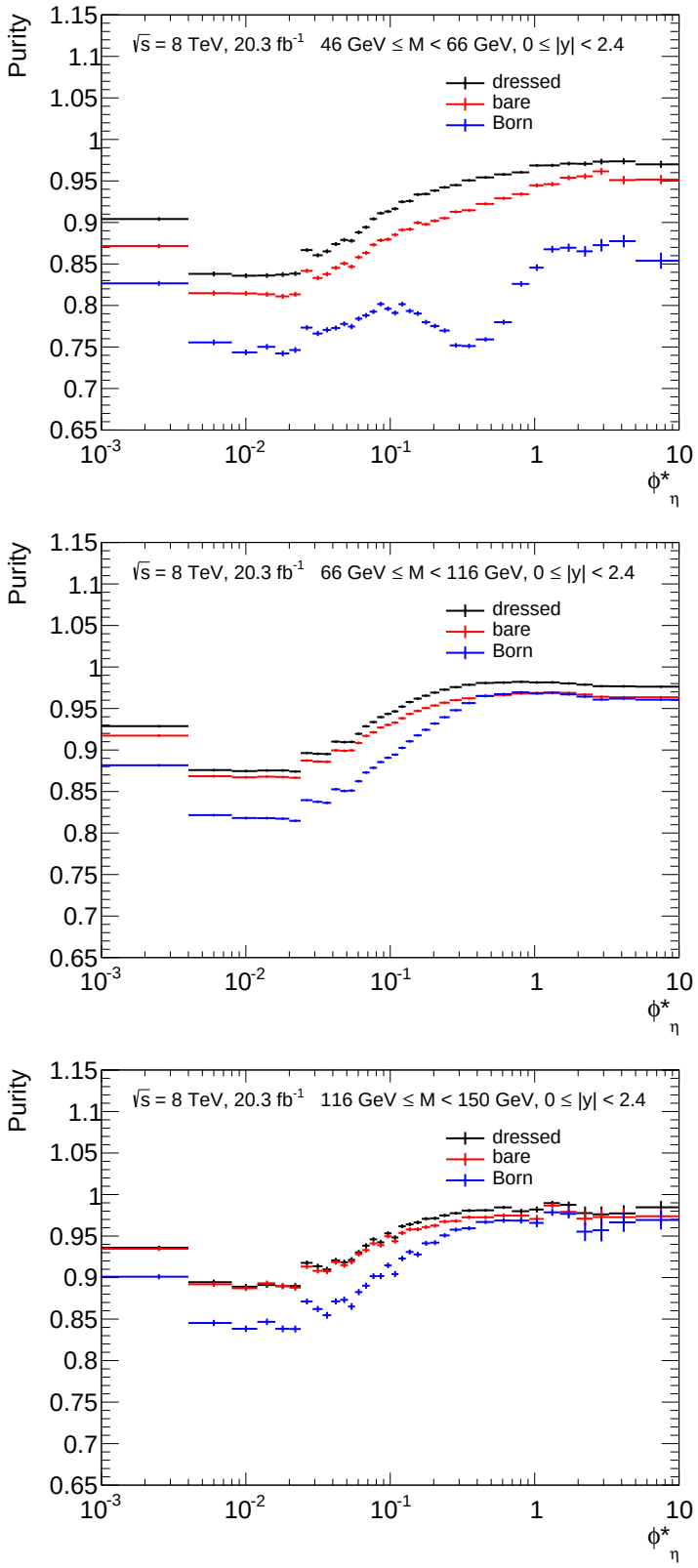

Figure 6.3: Bin purity as a function of ϕ^*_η in the low-mass (top plot), peak-mass (middle) and high-mass (bottom) regions, integrated over an absolute boson rapidity from 0 to 2.4. Events are required to be generated in the same ϕ^*_η bin as they are reconstructed, but no requirement is made on the truth boson mass or rapidity.

	46 GeV $< M <$ 66 GeV			66 GeV $< M <$ 116 GeV						116 GeV $< M <$ 150 GeV		
Bin	$0.0 < \|y\| < 0.8$	$0.8 < \|y\| < 1.6$	$1.6 < \|y\| < 2.4$	$0.0 < \|y\| < 0.4$	$0.4 < \|y\| < 0.8$	$0.8 < \|y\| < 1.2$	$1.2 < \|y\| < 1.6$	$1.6 < \|y\| < 2.0$	$2.0 < \|y\| < 2.4$	$0.0 < \|y\| < 0.8$	$0.8 < \|y\| < 1.6$	$1.6 < \|y\| < 2.4$
0 – 0.004	2793	2167	1094	61527	57053	51357	41470	25014	10164	1747	1214	437
0.004 – 0.008	2562	2017	1029	61222	55955	50508	41119	24677	9974	1655	1253	419
0.008 – 0.012	2533	1936	1015	59660	54921	50347	40174	24183	9907	1564	1129	417
0.012 – 0.016	2431	1812	1010	58347	53245	48509	39127	23572	9616	1523	1125	402
0.016 – 0.02	2393	1767	1000	57041	51701	47345	37723	22921	9176	1409	1039	351
0.02 – 0.024	2294	1741	1000	53689	49536	44974	36340	21903	8778	1334	1007	333
0.024 – 0.029	2771	2136	1192	64330	59436	53476	42993	25814	10763	1596	1114	413
0.029 – 0.034	2603	2078	1118	60835	55865	50095	40266	24761	9815	1472	985	341
0.034 – 0.039	2640	1917	1135	56995	52108	46975	38052	22589	9312	1207	980	341
0.039 – 0.045	2866	2157	1222	63341	58313	52415	42244	25527	10456	1419	1004	350
0.045 – 0.051	2731	2069	1173	58346	53314	48215	38700	23463	9366	1285	936	352
0.051 – 0.057	2562	1955	1113	54100	49347	44088	35447	21317	8796	1155	875	291
0.057 – 0.064	2782	2064	1226	57618	52476	47574	38254	22823	9382	1293	868	300
0.064 – 0.072	2938	2287	1274	60106	54716	48874	39536	23970	9765	1176	972	362
0.072 – 0.081	3062	2302	1252	60218	55176	49072	39840	24075	9699	1272	955	313
0.081 – 0.091	3090	2427	1338	59521	54602	48612	39149	23848	9501	1237	903	275
0.091 – 0.102	3127	2299	1291	57808	52904	46916	38342	23204	9380	1203	906	293
0.102 – 0.114	3018	2299	1252	55380	51216	44792	36044	22434	9017	1139	765	285
0.114 – 0.128	3144	2337	1335	56064	51097	45466	36554	22521	9090	1116	782	299
0.128 – 0.145	3334	2386	1266	57595	53081	46874	38040	23524	9309	1184	848	308
0.145 – 0.165	3285	2396	1349	56950	52148	46037	37151	23154	9330	1173	853	273
0.165 – 0.189	3296	2393	1386	56273	51687	45048	36372	22783	9302	1156	807	288
0.189 – 0.219	3355	2416	1466	56089	51765	45189	36171	22865	9380	1177	820	292
0.219 – 0.258	3557	2574	1467	56051	51699	45065	35810	22830	9278	1176	886	327
0.258 – 0.312	3739	2685	1482	56598	52099	45601	35996	23438	9450	1273	876	290
0.312 – 0.391	3933	2961	1587	55379	51126	44615	35159	22969	9213	1331	891	290
0.391 – 0.524	4107	2966	1741	54996	51060	44166	34182	22406	9068	1411	952	281
0.524 – 0.695	3304	2385	1280	37430	34308	29659	23156	14984	6020	1046	630	163
0.695 – 0.918	2453	1794	944	24879	23053	20239	15238	10010	3765	720	426	120
0.918 – 1.15	1721	1218	573	13928	12884	11208	8404	5350	1903	345	216	56
1.15 – 1.5	1525	1091	445	10760	9942	8491	6564	3858	1293	304	160	34
1.5 – 1.95	1120	785	315	6975	6328	5480	4141	2269	645	174	94	25
1.95 – 2.52	728	539	175	4458	4136	3606	2562	1260	318	95	54	10
2.52 – 3.28	493	411	103	3084	2757	2385	1666	800	130	64	44	6
3.28 – 5	538	361	91	2962	2715	2436	1776	730	73	82	43	4
5 – 10	347	288	54	2501	2342	2100	1494	595	36	76	42	3
Total	93175	69416	37793	1673056	1536111	1367809	1095256	672441	270470	38589	27454	9344

Table 6.6: The bin-edges in ϕ^*_η used to measure the normalised differential cross-section and the number of selected data events in each bin of ϕ^*_η, boson mass and boson rapidity.

Process	Generator	Channel number	Number of events
$Z \to \tau\tau$ Np0	Alpgen+Herwig+Jimmy	146930	5.5×10^6
$Z \to \tau\tau$ Np1	Alpgen+Herwig+Jimmy	146931	2.5×10^6
$Z \to \tau\tau$ Np2	Alpgen+Herwig+Jimmy	146932	5×10^5
$Z \to \tau\tau$ Np3	Alpgen+Herwig+Jimmy	146933	2×10^5
$Z \to \tau\tau$ Np4	Alpgen+Herwig+Jimmy	146934	3×10^4
$W \to e\nu$	Sherpa	147774	4×10^7
$W \to \tau\nu$	Sherpa	147776	7×10^6
WW	Herwig	105985	2.5×10^6
ZZ	Herwig	105986	2×10^5
WZ	Herwig	105987	1×10^6
$t\bar{t}$	McAtNLO+Jimmy	105200	1.5×10^7
single top, t-channel (e)	AcerMC+Pythia	117360	2×10^6
single top, t-channel (τ)	AcerMC+Pythia	117362	2×10^6
single top, s-channel (e)	McAtNLO+Jimmy	108343	1×10^6
single top, s-channel (τ)	McAtNLO+Jimmy	108345	1×10^6
single top, Wt-channel	McAtNLO+Jimmy	108346	5×10^6
$\gamma-$induced ($20\,\text{GeV} < M < 60\,\text{GeV}$)	Pythia8	129651	5×10^5
$\gamma-$induced ($60\,\text{GeV} < M < 200\,\text{GeV}$)	Pythia8	129652	5×10^5

Table 6.7: A summary of the background MC samples used in this analysis. The $Z \to \tau\tau$ samples are split according to how many additional partons are included in the hard-process matrix element and the single top samples are split according to the production channel. Further information on each of these processes is given in Section 6.7.1.

6.7 Background estimation

This section describes the methods used to obtain an estimate for the size and shape of the background contamination to the selected data distributions. These estimates are then subtracted from the data before the bin-by-bin correction factors are applied to obtain the final dressed or Born level distributions.

Backgrounds processes fall into two categories: irreducible background in which there are two real electrons in the final state within the kinematic and geometric acceptance and reducible or 'fake' backgrounds in which another detector object, such as a jet, is reconstructed as an electron. MC is used to describe the background processes which are reasonably well understood such as from Drell-Yan $Z \to \tau\tau$ and di-boson decays. These processes are described in more detail in Section 6.7.1 and are summarised in Table 6.7 along with information on which generator was used and the total number of events in each sample. The multi-jet background in which two jets are reconstructed as electrons is estimated using a data-driven technique, which is described in Section 6.7.2.

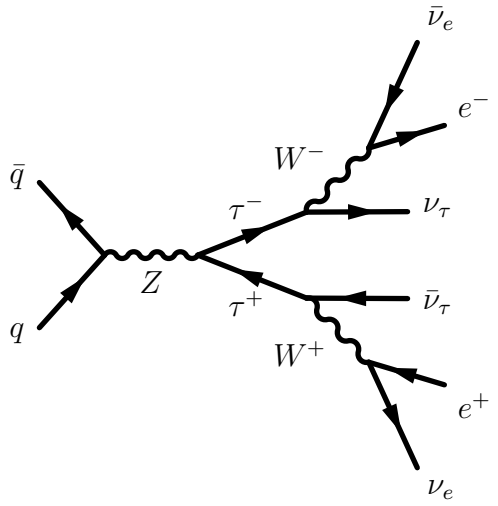

Figure 6.4: An example Feynman diagram for the $Z \to \tau\tau$ background process [72].

6.7.1 Monte Carlo backgrounds

6.7.1.1 $\mathbf{Z \to \tau\tau}$

Two real electrons can be produced from the decay of Drell-Yan $Z \to \tau\tau$ via Feynman diagrams such as the one displayed in Figure 6.4 [72]. This process is simulated using MC and is an important contribution to the total background in the low-mass regions and at lower ϕ^*_η. The background from the decay of $Z \to \mu\mu$ is negligible.

6.7.1.2 W+jets

The backgrounds due to the decay of a single W boson to either an electron or a τ (which subsequently decays to an electron) are collectively named 'W+jets'. One real electron is identified from the W decay with the other from a mis-identification of a jet. This background is very small in all regions of boson mass and rapidity.

6.7.1.3 Di-boson

Contribution from the decay of WW, WZ and ZZ is collectively called di-boson background. Example Feynman diagrams from each of these processes are shown in Figure 6.5. Events may pass the signal selection with one real electron and one mis-identified jet, two real electrons or multiple real electrons in which one or more fail to be reconstructed or fall outside the acceptance. These processes are important contributions to the total background in the peak-mass region at higher values of ϕ^*_η.

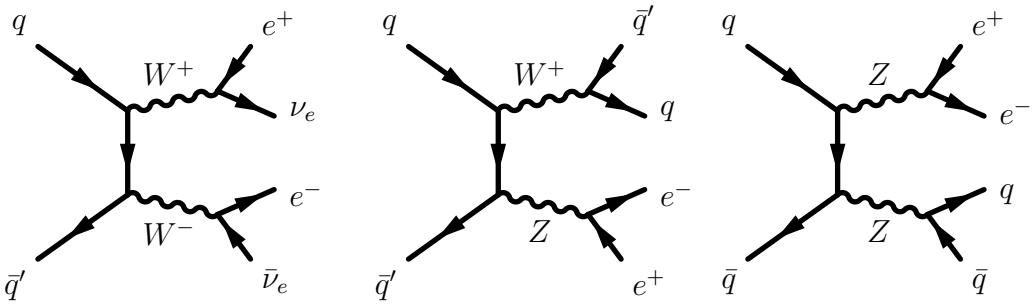

Figure 6.5: Example Feynman diagrams for di-boson production.

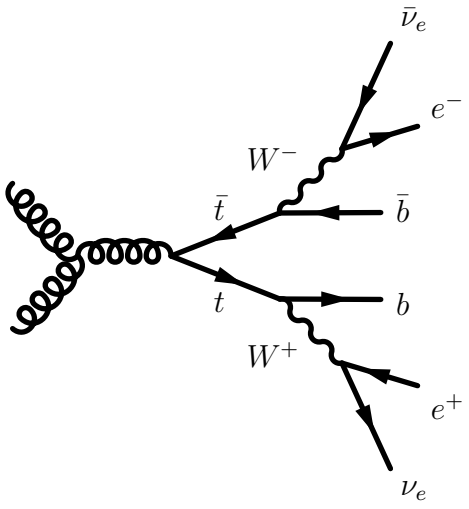

Figure 6.6: An example Feynman diagram for the $t\bar{t}$ background process [72].

6.7.1.4 $t\bar{t}$

The background due to $t\bar{t}$ decay is the dominant contribution to the total background at higher values of ϕ^*_η in all boson mass and rapidity regions. An example Feynman diagram for this process is shown in Figure 6.6 [72]. The event might have two real electrons, as in the example, or one of the jets originating from the b-quarks might be mis-identified.

6.7.1.5 Single top production

Three production channels for single top are considered as background. These are the s-channel, t-channel and Wt-channel. Example Feynman diagrams for each of these processes are shown in Figure 6.7. Real electrons may be identified from the decay of the top quark into an electron or τ or one of the several jets might be

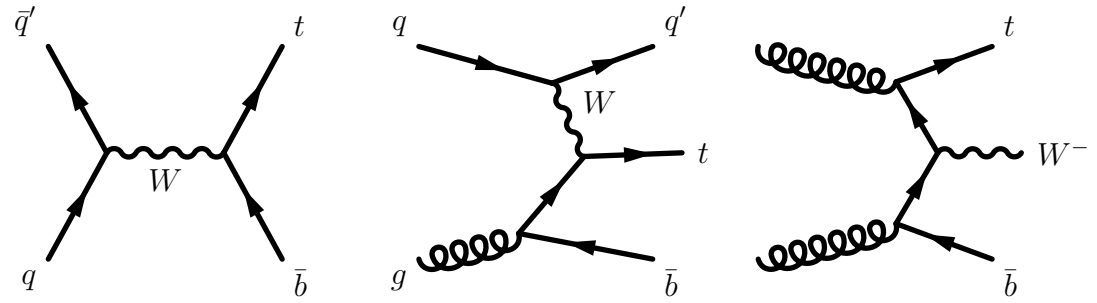

Figure 6.7: Example Feynman diagrams for single top production in the s-channel, t-channel and Wt-channel respectively [73].

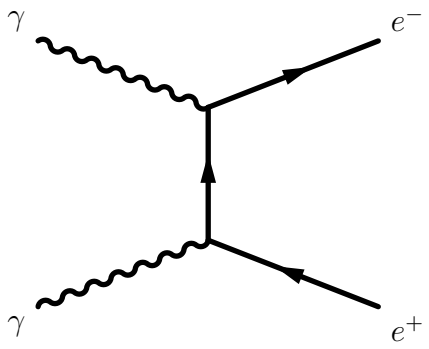

Figure 6.8: An example Feynman diagram of the photon-induced Drell-Yan sub-process.

mis-identified as an electron. Single top is not an important contribution to the total background.

6.7.1.6 Photon-induced

The process by which an electron-positron pair is produced from the interaction of photons in the proton collision is shown in Figure 6.8 and is referred to as photon-induced background. Such events are an important component of the total background at low to medium ϕ^*_η values, especially in the high-mass region. There also exist Drell-Yan sub-processes in which one of the initial state partons is a photon [74], but these are negligible for the boson mass range considered in this analysis [75].

6.7.2 Multi-jet background

The multi-jet or 'QCD' background describes a range of processes that produce several jets of which two are identified as electrons. One example process is a gluon

splitting into two b-quarks, which then hadronise, forming jets.

The multi-jet background contribution is not estimated using MC as there are large theoretical uncertainties on the behaviour of the constituent processes, which prevents a reliable estimate being made. A secondary reason (although not in itself insurmountable) is the large number of MC events for each sub-process that would be required to be simulated to produce enough which pass the signal selection criteria. This background is therefore estimated using a data-driven template-fit technique, which is now described.

The principle of the template-fit method is as follows: the shape of the background for a certain distribution (say ϕ^*_η) is obtained from data in a region of parameter space in which the multi-jet background is enhanced — this is the template. The assumption is made that the shape of the template is the same in the signal region as in the multi-jet enhanced region, but the normalisation differs. The scale of the template in the signal region is obtained by minimising the χ^2 variable defined in Equation 6.7 over a signal distribution which has sensitivity. The scale of the MC, A, and of the multi-jet template, B are free parameters in the fit and σ_i is the statistical uncertainty on the number of data events, N_i^{data} in a bin i. The resulting scale of the multi-jet background (B) is then used in all distributions and kinematic regions.

$$\chi^2 = \sum_i \left(\frac{N_i^{\text{data}} - A\, N_i^{\text{MC}} - B\, N_i^{\text{multi-jet}}}{\sigma_i} \right)^2 \tag{6.7}$$

Two different multi-jet template definitions are used for cross-check and consistency purposes. Both require that the event passes the standard selection as defined in Table 6.2 but with an alternative definition of a good electron. For the default template it is required that the electron passes Loose++ identification, fails Medium++, and that the two electrons selected must be of the same charge. The alternative template requires the same identification in addition to an inverse isolation requirement, $0.2 < I < 0.3$, where I is defined in Equation 6.4.

Any residual signal or MC background passing the multi-jet selection is subtracted from the template before the fitting procedure takes places. The first distribution in which an estimate of the multi-jet normalisation is obtained is the invariant mass spectrum. The fit using the same-sign template is performed over the range 46 GeV to 600 GeV and with absolute boson rapidity $|y| < 2.4$. To remove sensitivity to the exact description of the Z-peak by the signal MC, a single wide bin from 71 GeV to 111 GeV was used in this region. The minimum value of the χ^2 per degree of freedom obtained is 1.7 and the corresponding values for A and B are

1.025 ± 0.0004 and 0.036 ± 0.004 respectively, where the uncertainties are statistical in nature. The size of the background obtained using the inverse isolation template was consistent with that obtained with the same-sign template.

A second estimate of the normalisation was obtained by fitting the same-sign template in the distribution of a second isolation variable, J, which is defined in Equation 6.8 as the minimum value of $\sum E_{\mathrm{T}}(\Delta R < 0.2)/E_{\mathrm{T}}$ of the two electron candidates. Note that the standard isolation cut on I was not made when fitting in the related variable J and as such a further extrapolation to the full signal selection must also be performed [76].

$$J = \mathrm{Minimum}(\mathrm{e}_1, \mathrm{e}_2) \left\{ \frac{\sum E_{\mathrm{T}}(\Delta R < 0.2)}{E_{\mathrm{T}}} \right\} \tag{6.8}$$

As there is a priori no reason to select one estimate of the normalisation over the other and because the overall size of the background is small, the default value is arbitrarily taken from the fit in the isolation variable and the difference with respect to the fit in the invariant mass distribution is taken as an uncertainty.

6.7.3 Summary

The size of the individual backgrounds as percentage of total signal plus background is shown as a function of ϕ^*_η in Figure 6.9 for each of the twelve regions of boson mass and rapidity. The MC background estimates were verified with a data-driven cross-check [76].

6.8 Data and model comparison

In order to be confident that the background has been properly estimated and to be able to use MC to correct data for detector inefficiencies and resolution the data-model agreement is examined in various control distributions. It is understood that MC will not be able to properly model those variables which depend on poorly understood non-perturbative QCD, such as ϕ^*_η; indeed one of the primary motivations for this analysis is to provide information in this area for future MC tuning. However it is hoped that the MC will generally be able to describe other distributions such as the η and ϕ angles of each electron and the boson invariant mass for example.

The exact data-taking conditions are not necessarily known when the MC is simulated. Therefore some corrections must be applied to the MC (or to the data) at the analysis stage in order to improve the agreement in certain distributions, an example of which is the average number of interactions per bunch crossing, or

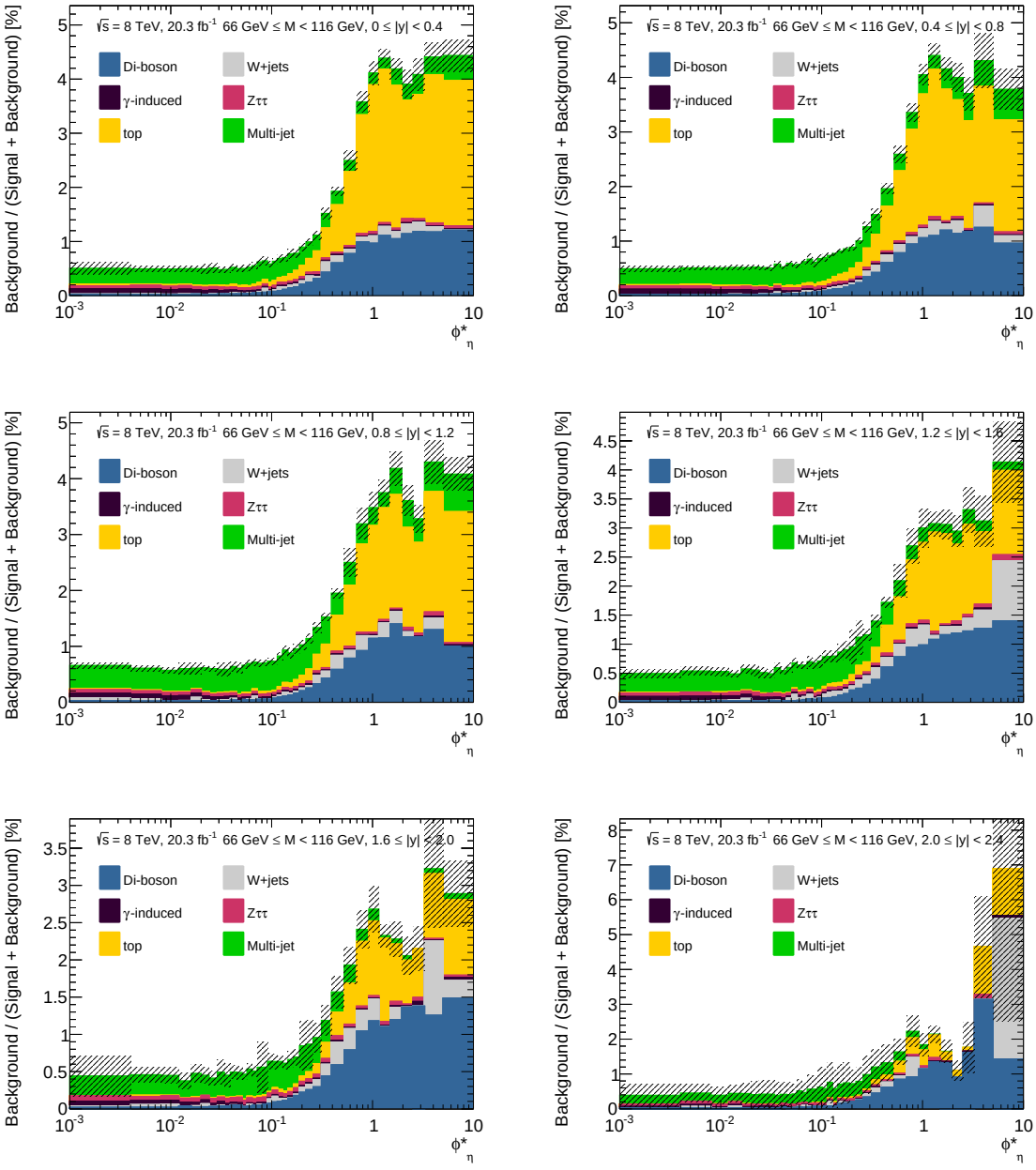

Figure 6.9: The size of the individual backgrounds as percentage of total signal plus background as a function of ϕ^*_η, for each boson rapidity bin in the peak-mass region. The di-boson and top backgrounds are merged. The statistical uncertainty on the total background is shown using hatched lines.

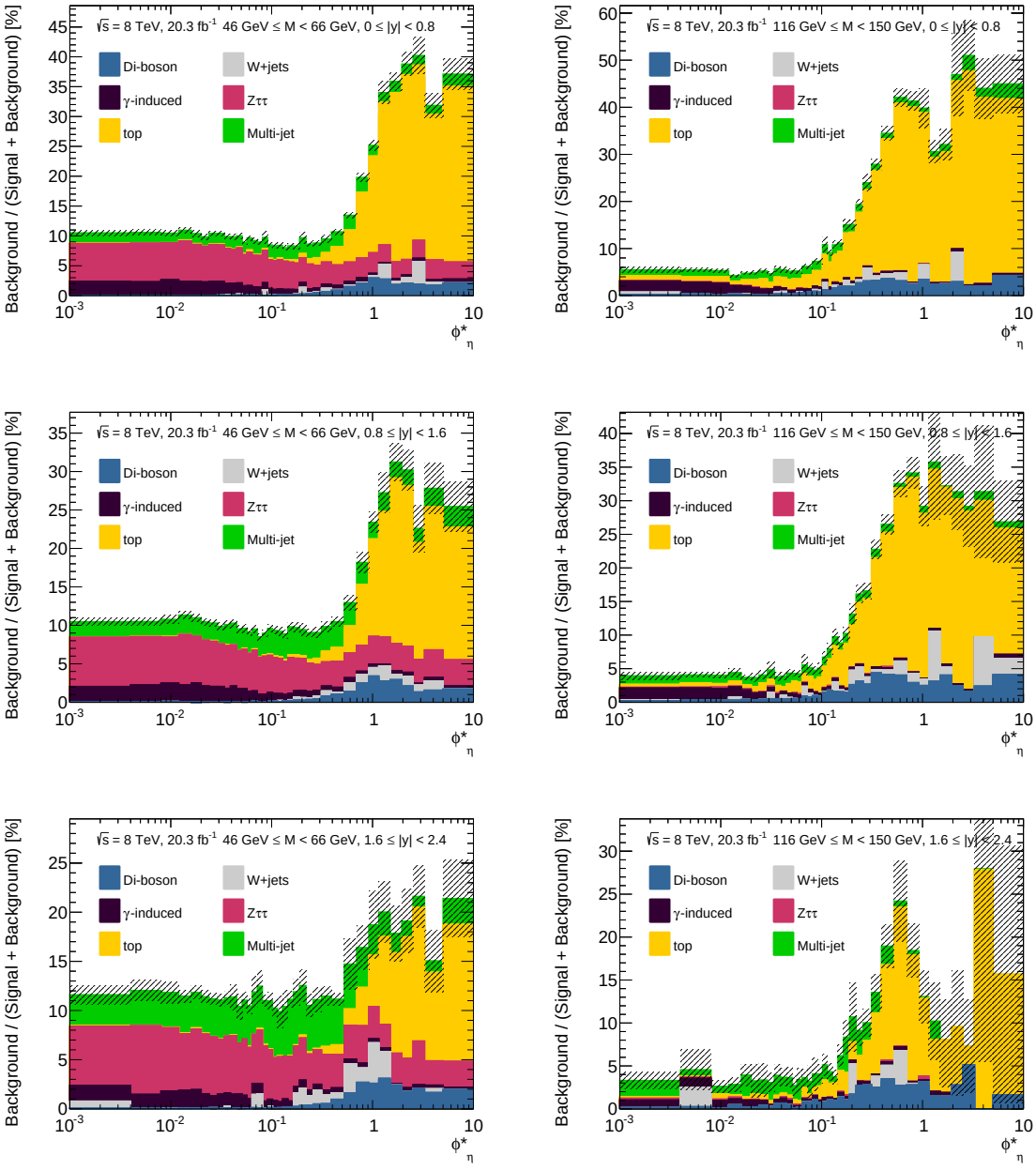

Figure 6.9: The size of the individual backgrounds as percentage of total signal plus background as a function of ϕ^*_η, for each boson rapidity bin in the low-mass and high-mass regions. The di-boson and top backgrounds are merged. The statistical uncertainty on the total background is shown using hatched lines.

pile-up. A description of each correction performed is given in Section 6.8.1 and a sub-set of the many data-model comparison distributions is shown in Section 6.8.2.

6.8.1 Corrections for known disagreement

The data and MC corrections can roughly be divided into two groups — those which affect the properties of the electron and therefore affect the electron selection decision (electron energy scale and resolution) and those which change the weight of an entire event (but may also depend on the properties of the two selected electrons). Note that even before any corrections each MC event has a weight which depends on the generator and simulation procedure and is not necessarily equal to one. The luminosity of the MC is also scaled such that it matches that of data and the MC cross-section is scaled by a k-factor to match that from a higher order prediction.

6.8.1.1 Electron energy scale and resolution

Any disagreement in energy response of the calorimeter ('energy scale') in data and in MC simulation can be parameterised as in Equation 6.9 [24], where E_{data} and E_{MC} are the electron energies in data and simulation respectively and α_i is the departure from optimal calibration in a bin of pseudorapidity, i.

$$E_{\text{data}} = (1 + \alpha_i)E_{\text{MC}} \tag{6.9}$$

The values of α_i are determined by finding the best agreement between data and MC in the position of the $Z \to e^+e^-$ resonance. The values of E_{data} are divided by $(1 + \alpha_i)$ in order to obtain the default values used in this analysis.

It is found that the energy resolution is slightly better in simulation than in data but it is assumed that it is well-modelled up to a Gaussian smearing term [24]. This is determined by finding the best agreement between data and MC in the width of the $Z \to e^+e^-$ resonance. Both the energy scale and energy resolution calibration are verified by comparing data and MC in the J/ψ invariant mass distribution for the process $J/\psi \to e^+e^-$.

6.8.1.2 Reconstruction, identification, trigger and isolation efficiency

The efficiency to detect an electron, ϵ_{total} can be written as a product of four terms (Equation 6.10): the efficiency to reconstruct and identify an electron, the efficiency for an electron to trigger the event and the efficiency for the electron to pass the

isolation requirements [65].

$$\epsilon_{\text{total}} = \epsilon_{\text{reconstruction}} \times \epsilon_{\text{identification}} \times \epsilon_{\text{trigger}} \times \epsilon_{\text{isolation}} \tag{6.10}$$

The tag-and-probe method, described below, is used to obtain these efficiencies both in data and MC in the order shown in Equation 6.10. Scale factors (SF), defined in Equation 6.11 as the ratio between an efficiency in data and MC are calculated in bins of η and E_{T} and applied as a weight to each MC event. There are two SF weights applied for each efficiency (one for each electron in the event) and these are generally close to unity.

$$SF_{\text{MC}} = \frac{\epsilon_{\text{data}}}{\epsilon_{\text{MC}}} \tag{6.11}$$

The tag-and-probe method requires a clean and unbiased sample of electrons [65] such as the well-understood resonances $Z \to e^+e^-$ and $J/\psi \to e^+e^-$. A *tag* electron is selected with strict quality and identification criteria and then a *probe* electron is sought passing a looser selection but with the requirement that the invariant mass of the tag-probe pair be in a window around the mass of the resonance. An opposite charge requirement is also made for some measurements. Each efficiency is then defined as the number of probe electrons passing the criterion in question (for example, to be reconstructed) divided by the total number of probe electrons. Note that the di-electron trigger efficiency is equal to the product of the two single-electron trigger efficiencies [77].

6.8.1.3 Pile-up

Pile-up events are simulated separately to the hard interaction and then merged at the stage before the conversion of energy deposits to detector signals [78]. The pile-up conditions simulated may not exactly match those in data, which could cause differences in the isolation or reconstruction efficiency for example. In order to correct for this an event weight is applied to MC, which is a function of the average number of interactions per bunch crossing, $\langle\mu\rangle$.

6.8.1.4 Longitudinal position of the primary vertex

The primary vertex is reconstructed using an iterative vertex finding algorithm [79] which utilises information on track position, curvature and p_{T}. The distribution of the longitudinal or z-position of the primary vertex is different in MC with respect to data, which could cause a difference in the fraction of events which pass the

geometric acceptance. This effect is corrected for by applying a weight to each MC event, which might be significantly different from unity.

6.8.1.5 Z boson line-shape

The Powheg+Pythia MC does not properly model the shape of the Z boson mass peak. The reasons for this, such as not including a running electroweak coupling, are understood and can be corrected for by applying a weight to each MC event. This 'line-shape re-weighting' has minimal effect on the shape of the ϕ^*_η distribution or on the sample of events selected.

6.8.1.6 ϕ^*_η shape modelling

In addition to the event weights described above a further weight is applied to MC to correct for any bias that the poor description of the ϕ^*_η distribution might bring when calculating the bin-by-bin correction factors, c_i. This effect is described in more detail in Section 6.9.

6.8.2 Control distributions

This section contains some example data-model comparison plots, which give an impression of the overall level of agreement. The model is normalised to the data using the scales A and B from the multi-jet background fit (Equation 6.7) and a re-weighting for the ϕ^*_η shape modelling is applied to the signal (Powheg+Pythia) and the $Z \to \tau\tau$ background. The distributions are shown integrated over events with an absolute boson rapidity less than 2.4 and the uncertainties on both the data and model are statistical in nature only.

Figure 6.10 shows the boson invariant mass distribution over a range from 46 GeV to 150 GeV. Figure 6.11 shows the boson rapidity and ϕ^*_η distributions in each mass region (low-mass, peak-mass and high-mass regions). Figure 6.12 then shows the η and ϕ distributions for the leading (larger p_{T}) and sub-leading (smaller p_{T}) electrons in the peak-mass region. An investigation into the agreement between the data and model in very fine bins of ϕ was performed and also found to be good. Figure 6.13 then shows the distributions of the average number of interactions per bunch crossing and the longitudinal position of the primary vertex in the peak-mass region, after the re-weighting described in Sections 6.8.1.3 and 6.8.1.4 respectively.

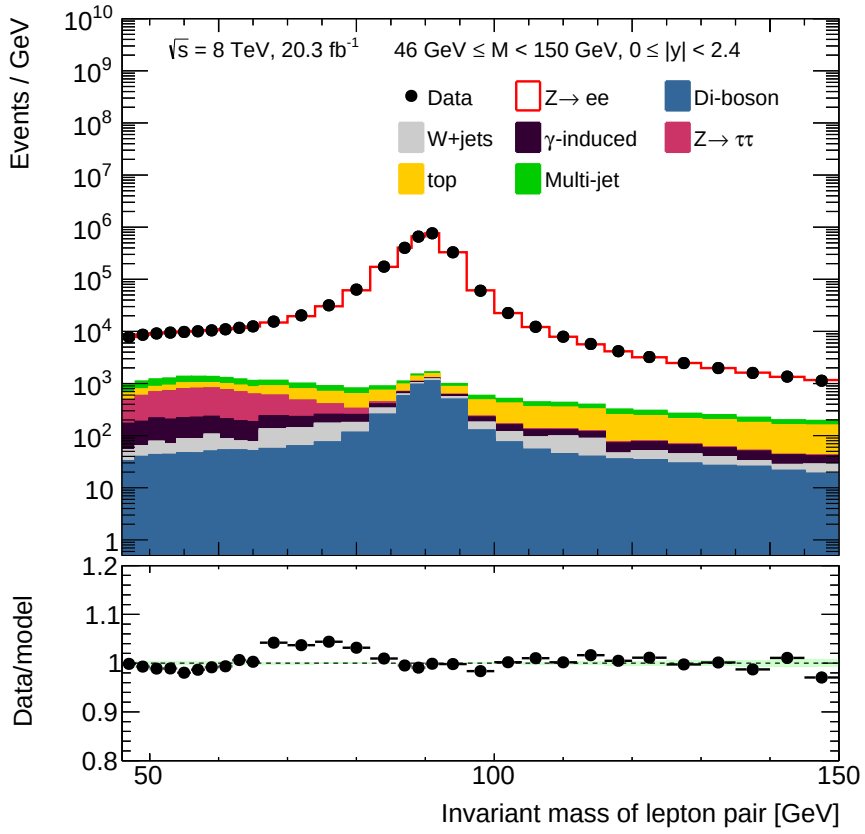

Figure 6.10: The boson invariant mass distribution over a range from 46 GeV to 150 GeV. Also shown is the ratio between data and model, where the light green band indicates the model statistical uncertainty.

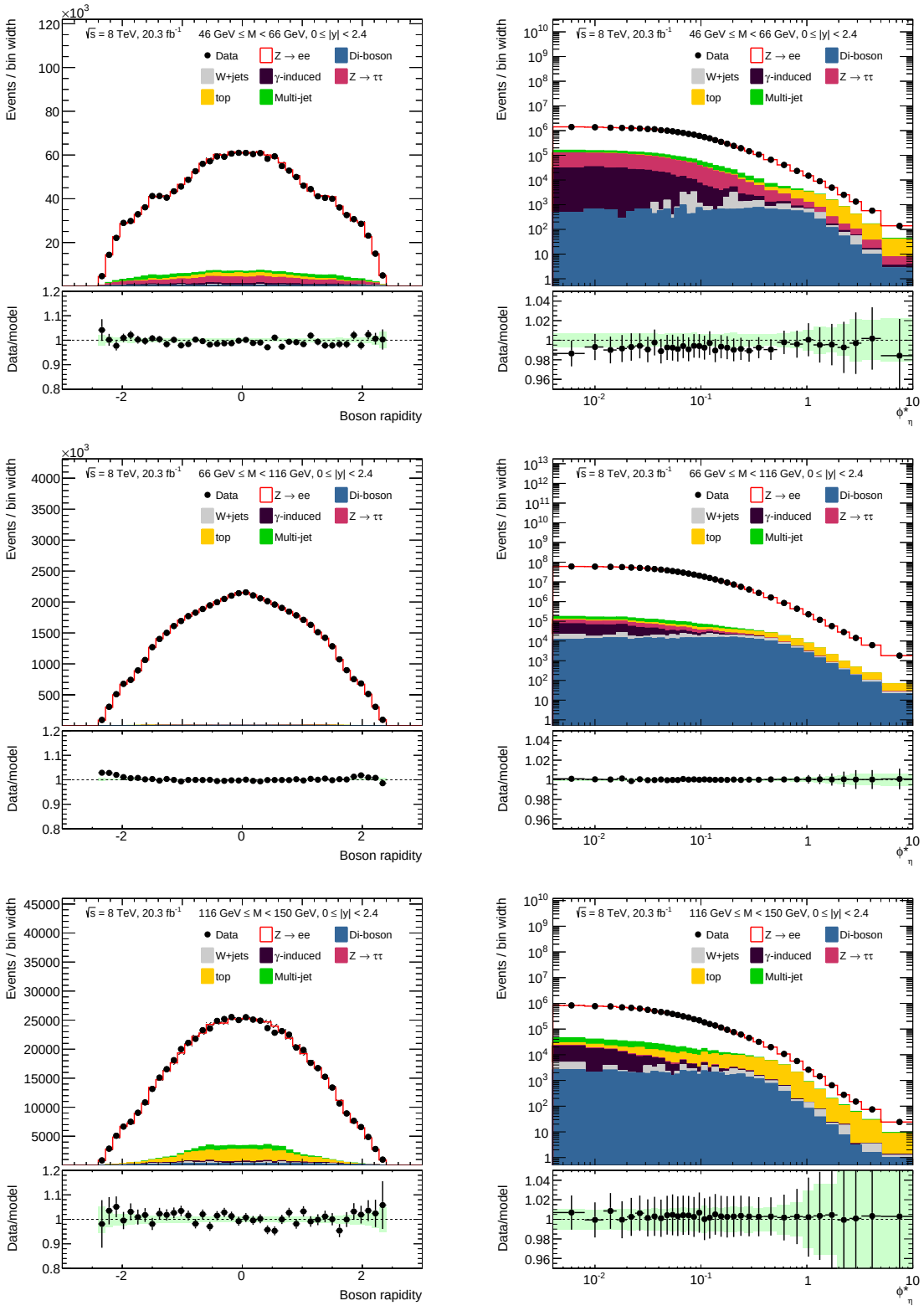

Figure 6.11: The boson rapidity distributions (left) and ϕ^*_η distributions (right) in the low-mass, peak-mass and high-mass regions (top to bottom). Also shown is the ratio between data and model, where the light green band indicates the model statistical uncertainty. The near perfect agreement between data and model in the ϕ^*_η distributions is due to the re-weighting of the signal MC at Born level (described in Section 6.9).

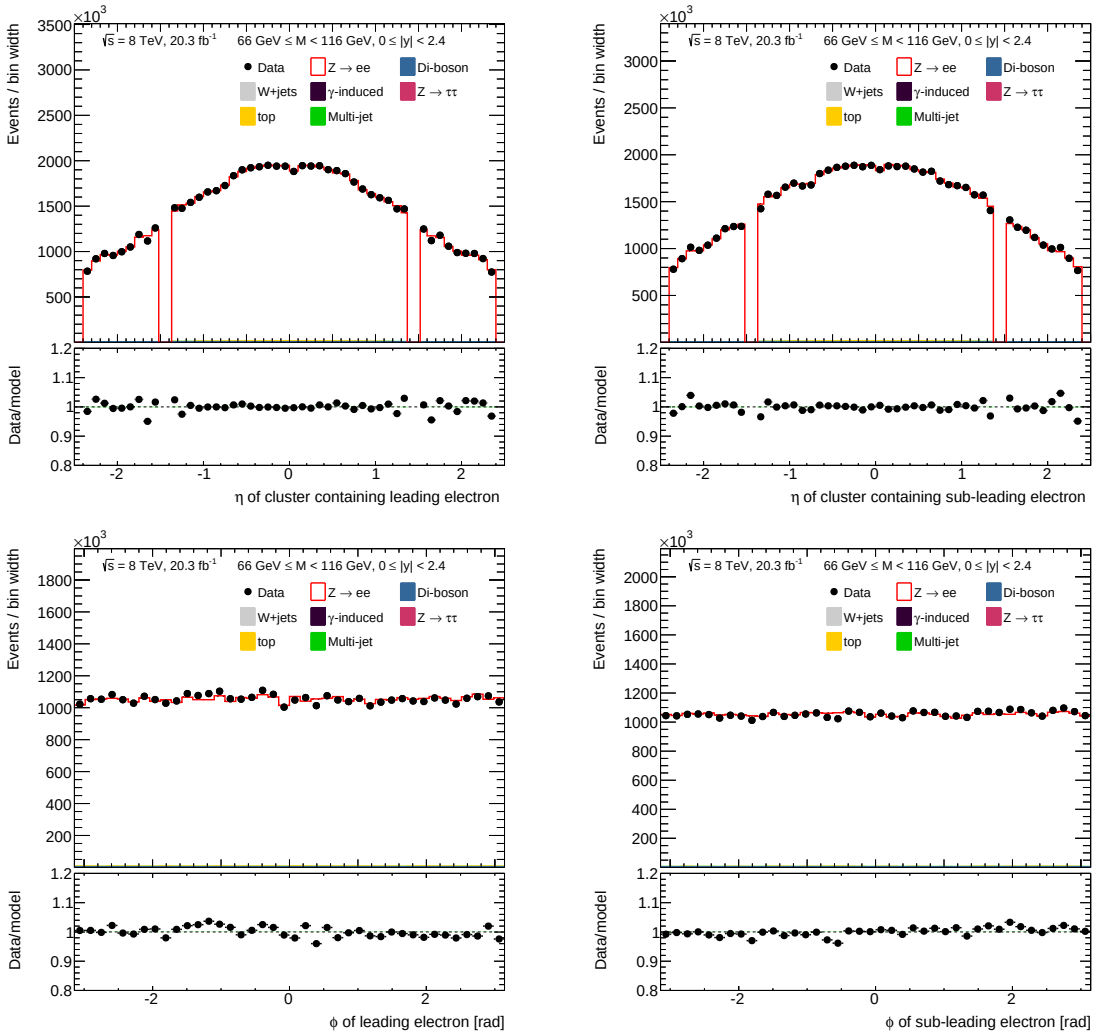

Figure 6.12: The distributions of the η of the calorimeter cluster (top) and of the azimuthal angle, ϕ, (bottom) for the leading and sub-leading electrons (left and right respectively). Plots are shown for the peak-mass region only, but the data-model agreement is representative of that in other mass and rapidity regions. Also shown is the ratio between data and model, where the light green band indicates the model statistical uncertainty.

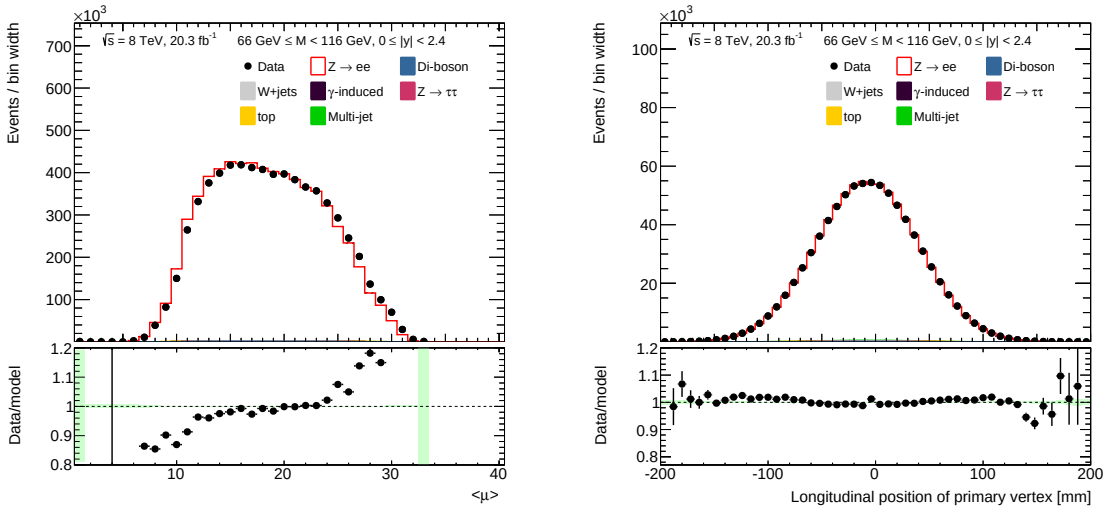

Figure 6.13: The distributions of the average number of interactions per bunch crossing (left) and the longitudinal position of the primary vertex (right) in the peak-mass region after the re-weighting described in Sections 6.8.1.3 and 6.8.1.4 respectively. Also shown is the ratio between data and model, where the light green band indicates the model statistical uncertainty.

6.9 Obtaining the normalised differential cross-section

The normalised ϕ^*_η differential cross-section in a given bin, i, is defined by the expression in Equation 6.12. $N_{i,\,\text{data}}$ and $N_{i,\,\text{background}}$ are the number of data and background events in bin i respectively, $\left(\Delta\phi^*_\eta\right)_i$ is the width of bin i, c_i is the bin-by-bin correction factor defined in Equation 6.5 and $\mathcal{N}$ is a normalisation constant. The ϕ^*_η differential cross-section is measured and normalised separately in each region of boson mass and rapidity and for each truth level definition used.

$$\frac{1}{\sigma}\left(\frac{d\sigma}{d\phi^*_\eta}\right)_i = \mathcal{N}\frac{N_{i,\,\text{data}} - N_{i,\,\text{background}}}{\left(\Delta\phi^*_\eta\right)_i c_i} \tag{6.12}$$

A description of the necessary steps required to obtain the normalised differential cross-section in a particular region of boson mass and rapidity is now provided.

Event selection The final weighted signal, background and data ϕ^*_η histograms are obtained.

Background subtraction The sum of all background ϕ^*_η histograms is subtracted from the data.

Correction to truth level The correction factors c_i are obtained by dividing the signal ϕ^*_η histogram at detector level by that at truth (Born or dressed) level.

The background subtracted data histogram is then divided by the correction factors.

Normalisation The resulting histogram is then normalised to one.

ϕ^*_η re-weighting A re-weighting histogram is obtained by dividing the normalised and corrected background-subtracted data by the normalised signal MC Born level distribution. The correction factors are re-derived by weighting each MC event by the entry in the re-weighting histogram corresponding to the event's Born ϕ^*_η value.

MC averaging The weighted average of the correction factors for each of the available signal MCs in a particular mass region is obtained (Powheg+Pythia and Sherpa at low-mass with the addition of Powheg+Herwig in other mass regions). The inverse of the square of the statistical uncertainty on each correction factor is used as the weight, although each MC contributes approximately equally to the average. The averaging step is performed as there is a priori no reason to choose one MC as the default over another (all three describe the control distributions equally well). Any difference in the truth level distributions obtained between using the correction factors from a particular MC or from the average is considered when determining the generator uncertainty, described in Section 6.10.4.4.

Final step The background-subtracted data are divided by the re-weighted and averaged correction factors and normalised to one.

Section 6.10 describes the sources of systematic uncertainty considered and how these are evaluated. The final results with total systematic and statistical uncertainties are then displayed in Section 6.11.

6.10 Systematic uncertainties

6.10.1 Introduction

Systematic uncertainties from a variety of sources are considered and can be roughly divided into three categories: modelling of the detector and of the beam-conditions (Section 6.10.2), the methodology of the correction to truth level (Section 6.10.3) and modelling of the signal and background processes at truth level (Section 6.10.4).

The general method in obtaining the contribution from a particular source to the total systematic uncertainty in a bin of ϕ^*_η is as follows. The quantity in question is

varied within its estimated uncertainty, whilst keeping all other quantities constant. Next, the procedure for obtaining the normalised differential cross-section (described in Section 6.9) is followed using the modified data or MC. Then for each bin in ϕ^*_η the deviation in $(1/\sigma)\, d\sigma/d\phi^*_\eta$ from the central value (i.e., the value obtained with no variation) is taken as the systematic uncertainty from that source. For sources which have both upwards and downwards variations (such the electron energy scale) the largest deviation in $(1/\sigma)\, d\sigma/d\phi^*_\eta$ of the two from the central value is taken as the systematic uncertainty.

The total systematic uncertainty in a bin of ϕ^*_η is then defined as the quadrature sum of all of individual uncertainties in that bin. The uncertainty due to the number of available MC signal and background events (MC statistics) is included as a source of systematic uncertainty and kept separate from the data statistical uncertainty.

6.10.2 Modelling of the detector and beam-conditions

6.10.2.1 Electron energy scale and resolution

After applying the default energy scale correction to the data (Section 6.8.1.1) the systematic uncertainty is found by scaling the electron energy in MC. Sources of uncertainty sources considered include modelling of detector material and details of the $Z \to e^+e^-$ calibration [24]. Similarly the Gaussian smearing term is varied in MC to obtain the systematic uncertainty on the electron energy resolution. The contribution to the total uncertainty from these two sources is small in most bins.

6.10.2.2 Reconstruction, identification, trigger and isolation efficiency

Each of the SFs described in Section 6.8.1.2 has an associated uncertainty due to effects such as the tag-electron definition or background modelling. The contribution of SF uncertainties to the total uncertainty on $(1/\sigma)\, d\sigma/d\phi^*_\eta$ is generally small, other than at high ϕ^*_η.

6.10.2.3 Pile-up

After applying the MC weight described in Section 6.8.1.3, the agreement between data and the model in the $\langle\mu\rangle$ distribution (Figure 6.13) is reasonably good. A conservative estimate of the uncertainty due to the re-weighting procedure is obtained by setting the weight to unity and observing the change in $(1/\sigma)\, d\sigma/d\phi^*_\eta$, which is found to be small.

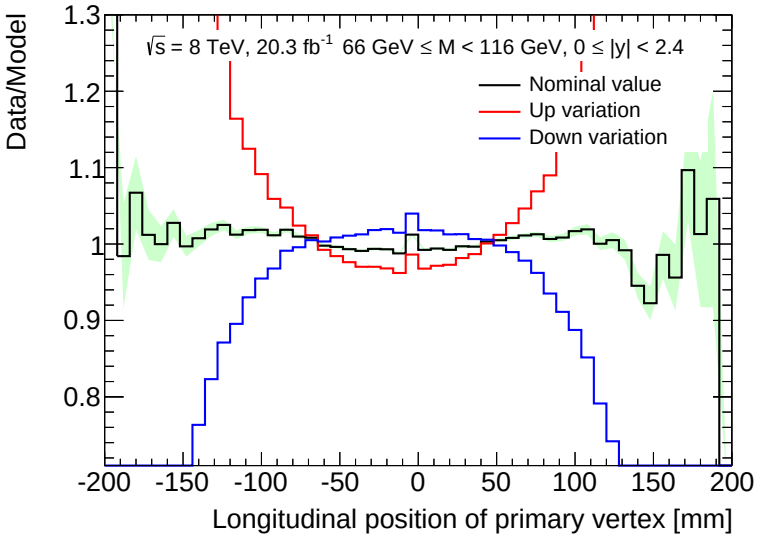

Figure 6.14: The ratio between data and model as a function of the longitudinal position of the primary vertex in the peak-mass region. The black curve is obtained using the nominal weights and the red and blue curves are obtained using the w_{up} and w_{down} weights defined in Equations 6.13 and 6.14 respectively. The light green band indicates the model statistical uncertainty.

6.10.2.4 Longitudinal position of the primary vertex

The agreement between the data and model in the longitudinal position of the primary vertex is improved after re-weighting the MC (Figure 6.13). The uncertainty due to the re-weighting procedure is estimated by varying the nominal weight, w, up and down on an event-by-event basis according to the prescription in Equations 6.13 and 6.14.

$$w_{\text{up}} = 1 + 1.1 \times (w - 1) \tag{6.13}$$

$$w_{\text{down}} = 1 + 0.9 \times (w - 1) \tag{6.14}$$

Figure 6.14 shows the ratio between the data and model as a function of the longitudinal position of the primary vertex in the peak-mass region. The black curve is obtained using the nominal weights, the red curve using w_{up} and the blue curve using w_{down}. Any disagreement between the data and model using the nominal weights is approximately covered by the systematic variations. A similar conclusion is drawn in the other regions of boson mass and rapidity.

The contribution from this source to the total uncertainty on $(1/\sigma)\, d\sigma/d\phi^*_\eta$ is generally small.

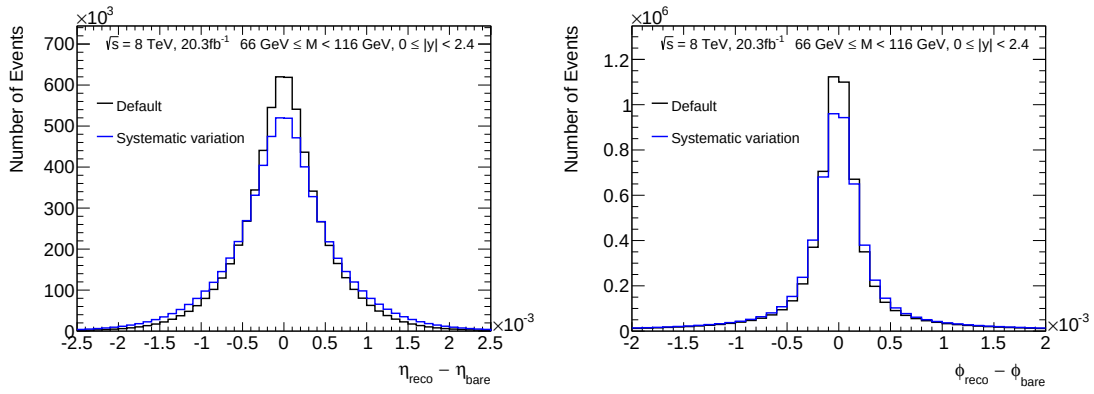

Figure 6.15: The distributions of $\eta_{\text{reco}} - \eta_{\text{bare}}$ (left) and $\phi_{\text{reco}} - \phi_{\text{bare}}$ (right) for the default MC (black curve) and the systematic variation (blue curve) for events in the peak-mass region.

6.10.2.5 Angular resolution

Poor modelling of the detector angular resolution by the MC could result in bin purities and correction factors being under or over estimated. In order to examine the dependence of this modelling on the final normalised distributions the difference between the reconstructed and bare values of the η and ϕ of the track was increased by a factor of 1.2. This method is expressed by Equation 6.15, where a is either η or ϕ and the subscript differentiates between the reconstructed and bare track values. The value of 1.2 is motivated by cosmic-ray studies during Inner Detector commissioning [71].

$$a_{\text{track,reco}} \rightarrow a_{\text{track,bare}} + 1.2 \times (a_{\text{track,reco}} - a_{\text{track,bare}}) \tag{6.15}$$

Figure 6.15 shows the distributions of $\eta_{\text{reco}} - \eta_{\text{bare}}$ (left) and $\phi_{\text{reco}} - \phi_{\text{bare}}$ (right) for the default MC (black curve) and the systematic variation (blue curve) in the peak-mass region. The contribution to the total uncertainty on $(1/\sigma)\, d\sigma/d\phi^*_\eta$ from the MC mis-modelling of the angular resolution is found to be small.

6.10.3 Methodology of correction to truth level

Figure 6.16 shows the dressed level bin-by-bin correction factors, c_i, as a function of ϕ^*_η for each of the three mass regions (for events with an absolute boson rapidity less than 2.4). One observes that the correction factors do have a dependence on ϕ^*_η and mass (and also on rapidity) and therefore could be biased by the imperfect MC modelling of the ϕ^*_η distribution.

The ϕ^*_η re-weighting described in Section 6.9 mitigates some of the error introduced by this effect. A further iteration of this procedure is used to estimate a

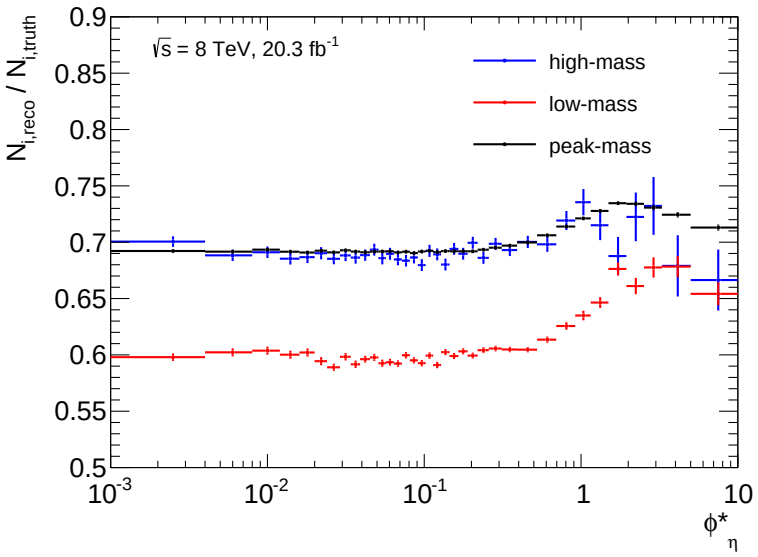

Figure 6.16: The dressed level bin-by-bin correction factors, c_i, as a function of ϕ^*_η in the low-mass region (red curve), peak-mass region (black curve) and high-mass region (blue curve) for events with $|y| < 2.4$. Only the uncertainties due to the limited MC statistics are displayed.

contribution to the systematic uncertainty on the MC modelling and is found to be very small. An additional uncertainty on the MC modelling is found by comparing the results using different MC generators and is described in more detail in Section 6.10.4.4.

The results obtained using the bin-by-bin correction factors were cross-checked with results obtained using an alternative method — Iterative Bayesian Unfolding, as implemented in the RooUnfold package [80]. The two sets of results were found to be consistent and therefore no additional systematic is applied.

6.10.4 Modelling of the signal and background processes

6.10.4.1 Monte Carlo background

Aside from the statistical uncertainty on the MC background there is also an uncertainty on the normalisation of each component due to imperfect knowledge of the process cross-section and of the data luminosity. The cross-section for each background is varied independently upwards and downwards by the percentages indicated in Table 6.8, which are slightly larger than the true cross-section uncertainties in order to cover any residual mis-modelling of the shape of the ϕ^*_η distribution.

The change induced in the final values of $(1/\sigma)\, d\sigma/d\phi^*_\eta$ is small in the peak-mass regions, where the background contamination is also small. In the low-mass and high-mass regions this uncertainty becomes larger, yet still much smaller than the

Background process	Uncertainty [%]
$Z \to \tau\tau$	10
W+jets	25
Di-boson	7
$t\bar{t}$	7
Single top	12
Photon-induced	40

Table 6.8: The percentages by which the normalisation of each MC background process was scaled upwards and downwards in order to estimate the contribution to the uncertainty on $(1/\sigma)\, d\sigma/d\phi^*_\eta$ from imperfect knowledge of the MC cross-section and from mis-modelling of the shape of the ϕ^*_η distribution.

data statistical uncertainty.

6.10.4.2 Multi-jet background

As described in Section 6.7.2, two estimates of the multi-jet background normalisation are obtained using the template fit method. The nominal value is obtained by fitting a same-sign data template in an isolation variable, J, and the difference with respect to the value obtained by fitting the same template in the invariant mass distribution is regarded as a systematic uncertainty. The contribution from this source to the total systematic uncertainty is generally small in all boson mass and rapidity regions.

6.10.4.3 *Z* boson line-shape

A weight is applied to Powheg+Pythia events to correct for deficiencies in modelling the shape of the Z boson mass peak (Section 6.8.1.5). The uncertainty on this reweighting procedure is conservatively estimated by setting the weights to unity and observing the change in $(1/\sigma)\, d\sigma/d\phi^*_\eta$, which is found to be negligible.

6.10.4.4 Choice of signal Monte Carlo generator

The different stages of Monte Carlo event generation, as described in Section 5.3 may not be modelled in the same way by different generators. This could affect the values of the bin-by-bin correction factors for both the Born and dressed levels by introducing biases in the electron reconstruction, identification, triggering or isolation efficiencies.

One specific example of a difference between the signal generators studied is in the modelling of final state photon radiation. Both Powheg+Pythia and Pow-

heg+Herwig use Photos to simulate FSR, whilst the Sherpa program has its own implementation [81]. Neither Photos nor Sherpa include the second order Quantum Electrodynamic (QED) matrix element but Photos has been shown to simulate its dominant contribution [81]. However Photos does not include corrections for QED lepton pair emission or interference with initial state radiation [82]. One would expect any modelling differences to be largest at Born level as corrections are needed for both wide and narrow-angle FSR, whilst the dressed level results are only corrected for the latter.

The dashed lines, labelled x (MC) on the plots in Figure 6.17 show the ratio (minus one) between the final normalised distributions (for a particular truth level and kinematic region) as obtained using the average (default) correction factors and as obtained using those from an individual MC (Equation 6.16). The quantity is calculated using a reduced number of bins to smooth statistical fluctuations.

$$\mathrm{x\,(MC)} = \left(\frac{1}{\sigma}\frac{d\sigma}{d\phi^*_\eta}\right)_{\text{average}} \Bigg/ \left(\frac{1}{\sigma}\frac{d\sigma}{d\phi^*_\eta}\right)_{\text{MC}} - 1 \tag{6.16}$$

The size of the uncertainty due to the choice of MC generator is displayed as a yellow shaded band on the plots. This is set by hand and chosen to roughly encompass the spread of the dashed lines. The uncertainty for a particular mass region and truth level is determined using the integrated rapidity distributions ($|y| < 2.4$) in Figure 6.17 to reduce variations from the limited MC statistics. However after checking the band also covers the variation of x (MC) as a function of boson rapidity (to within statistical fluctuations), the same uncertainty is used in each rapidity region.

Several observations can be made about Figure 6.17. Firstly the generator uncertainty is largest at Born level, in the low-mass region. This is indicative of a difference in FSR modelling as wide-angle FSR can cause large event migration down in invariant mass from the Z-peak. In the peak-mass region, at both Born and dressed levels, the generator uncertainty is large compared to all other sources (Section 6.10.5), however it is smaller than the data statistical uncertainty. For the low-mass region at dressed level and for both truth levels at high-mass the generator uncertainty is small compared to the other uncertainty sources and much smaller than the data statistical uncertainty.

6.10.5 Summary

The size of various systematic uncertainties as a percentage of the dressed level normalised differential cross-section is shown for each of the twelve regions of boson

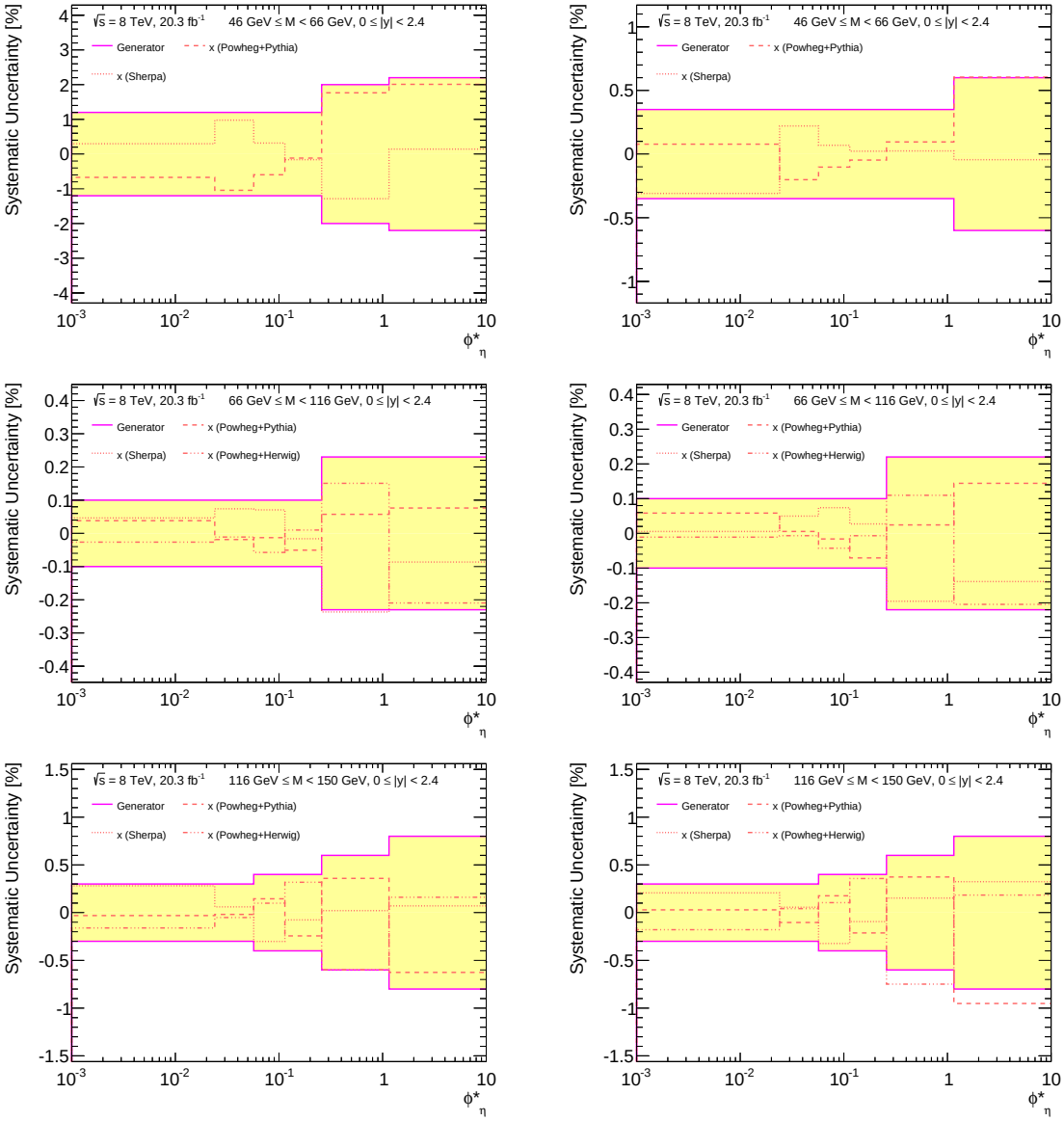

(a) Born level (b) Dressed level

Figure 6.17: (a) shows the size of the Born level generator choice systematic (yellow shaded band) as a function of ϕ^*_η in the low-mass region (top), peak-mass region (centre) and high-mass region (bottom). Also plotted, and labelled as x (MC), is the ratio (minus one) between the final normalised distributions as obtained using the average (default) correction factors and as obtained using those from an individual MC. (b) then shows the corresponding plots for the dressed level.

mass and rapidity in Figure 6.18. The curves labelled 'Detector / beam-conditions' are the quadrature sum of the uncertainties on the electron energy scale, electron energy resolution, scale factors, pile-up, longitudinal position of the primary vertex and angular resolution. The curves labelled 'Background' are quadrature sum of MC and multi-jet background uncertainties. Also shown is the total systematic uncertainty (black-dashed curve) and the data statistical uncertainty (blue-dashed curve). Figure 6.19 shows the same information for the Born level uncertainties. In all regions the data statistical uncertainty is of the same order or larger than the total systematic uncertainty.

6.11 Results

6.11.1 Dressed level, di-electron channel

Figure 6.20 shows the final dressed level normalised differential cross-section as a function of ϕ^*_η in each region of boson mass and rapidity and obtained using the average MC correction factors. The data are shown with statistical uncertainties (dark-blue) and the quadrature sum of the statistical and systematic uncertainties (light-blue), and the ratio with respect to the prediction from Powheg+Pythia (without the ϕ^*_η re-weighting) is also displayed.

Table 6.9 provides the values of $(1/\sigma)\, d\sigma/d\phi^*_\eta$ for each ϕ^*_η bin in each of the boson rapidity regions at peak-mass. Also given are the associated total statistical and systematic uncertainties in percent. A blue-red colour scale is used to indicate the relative contribution of each uncertainty to the total. For example, if the systematic uncertainty is coloured blue it has a small contribution with respect to the statistical uncertainty, one coloured purple has an equal contribution and one coloured red has a large contribution. Table 6.10 provides the same information for each boson rapidity region in the low-mass and high-mass regions.

6.11.2 Born level, combination with di-muon channel

Under the assumption that the coupling of electrons and muons to the intermediate boson Z/γ is identical one can perform a combination of the two channels in order to benefit from a larger sample of events and possibly a reduction in the systematic uncertainty if certain sources were uncorrelated or anticorrelated. Due to their relative mass difference, electrons and muons radiate differently as they pass through the detector and therefore the combination must be performed at the Born level, before any FSR.

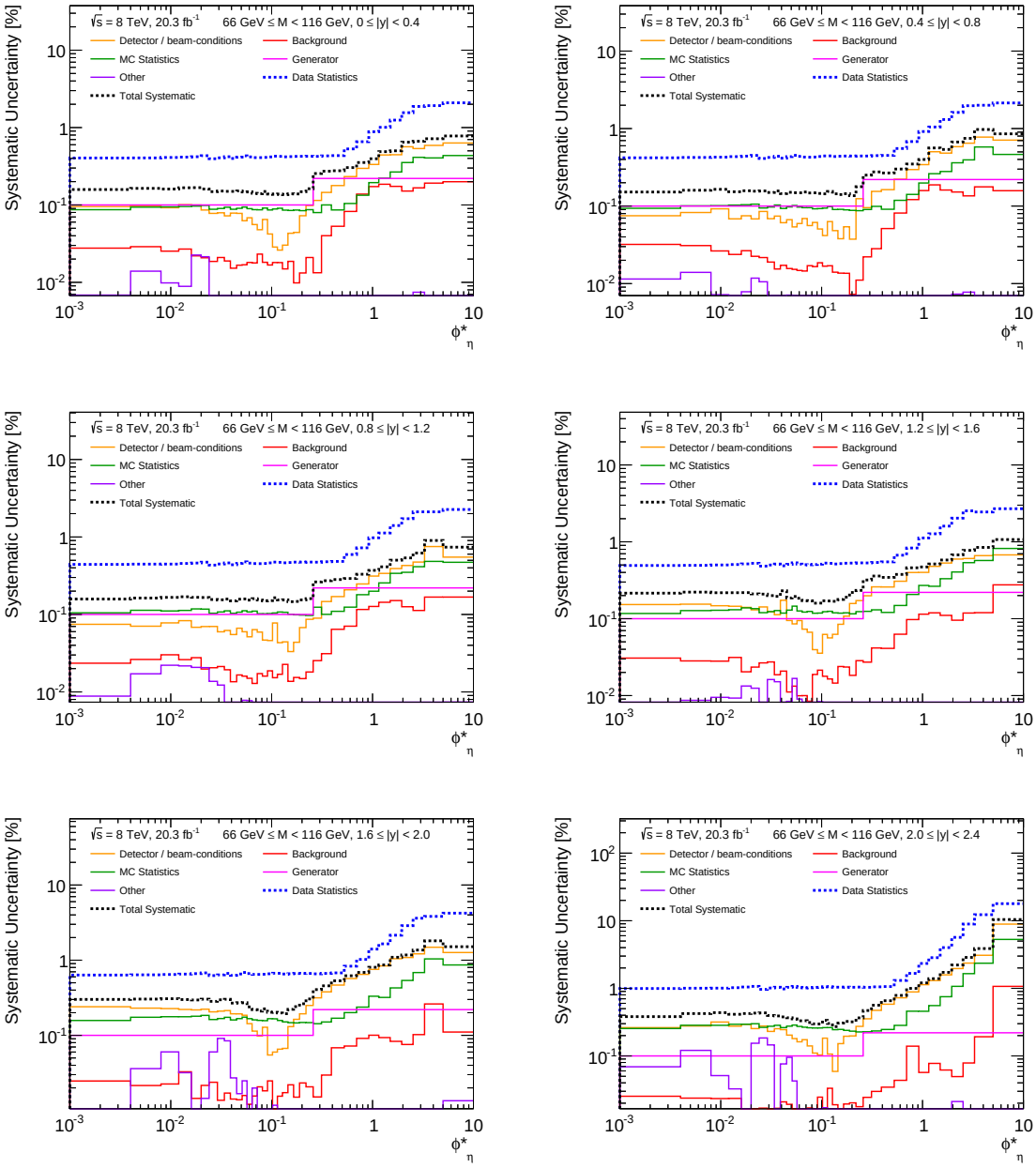

Figure 6.18: The size of various systematic uncertainties as a percentage of the dressed level normalised differential cross-section for each boson rapidity region in the peak-mass region. The total systematic uncertainty is shown as a black-dashed line and the data statistical uncertainty as a blue-dashed line.

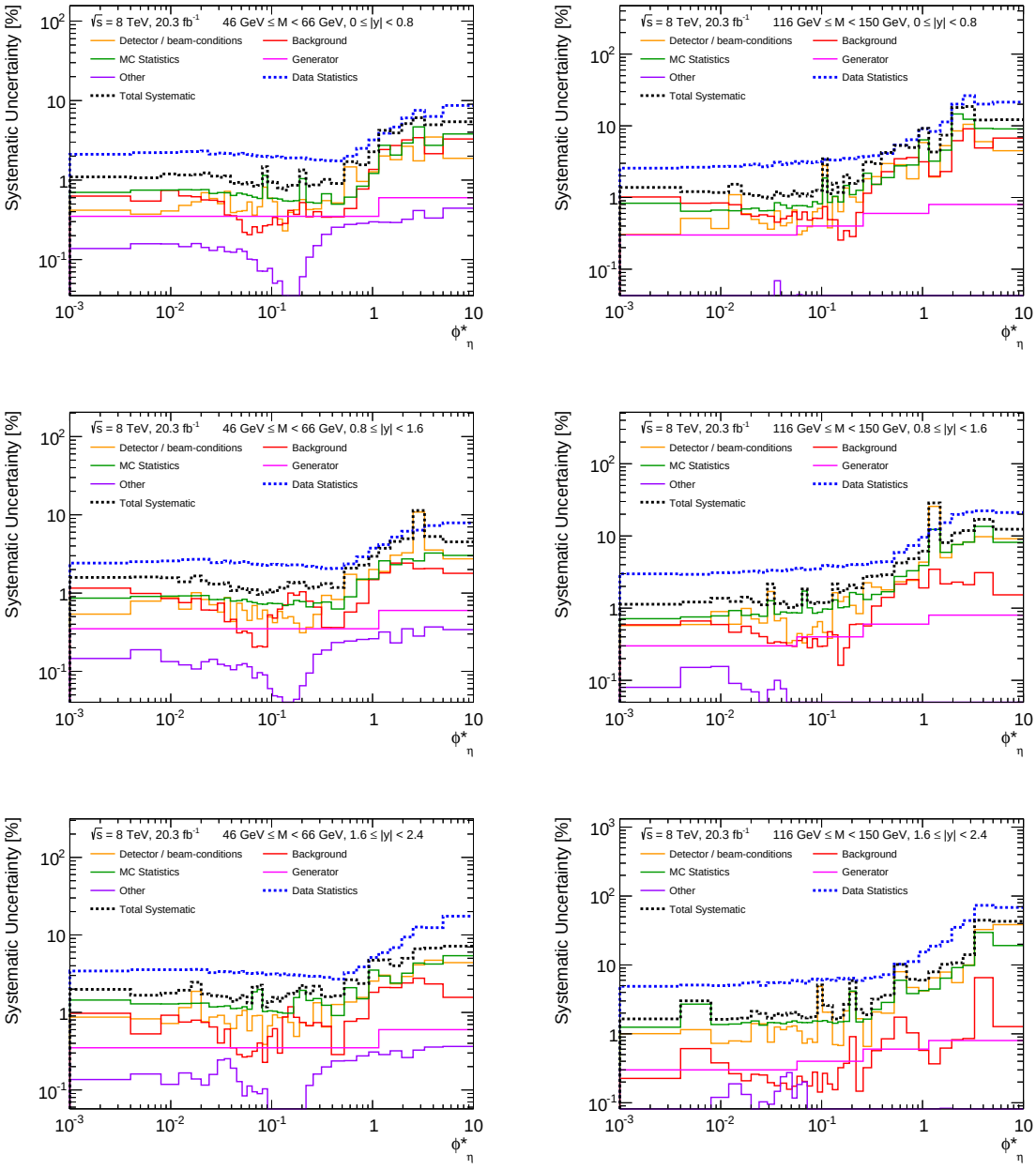

Figure 6.18: The size of various systematic uncertainties as a percentage of the dressed level normalised differential cross-section for each boson rapidity region in the low-mass and high-mass regions. The total systematic uncertainty is shown as a black-dashed line and the data statistical uncertainty as a blue-dashed line.

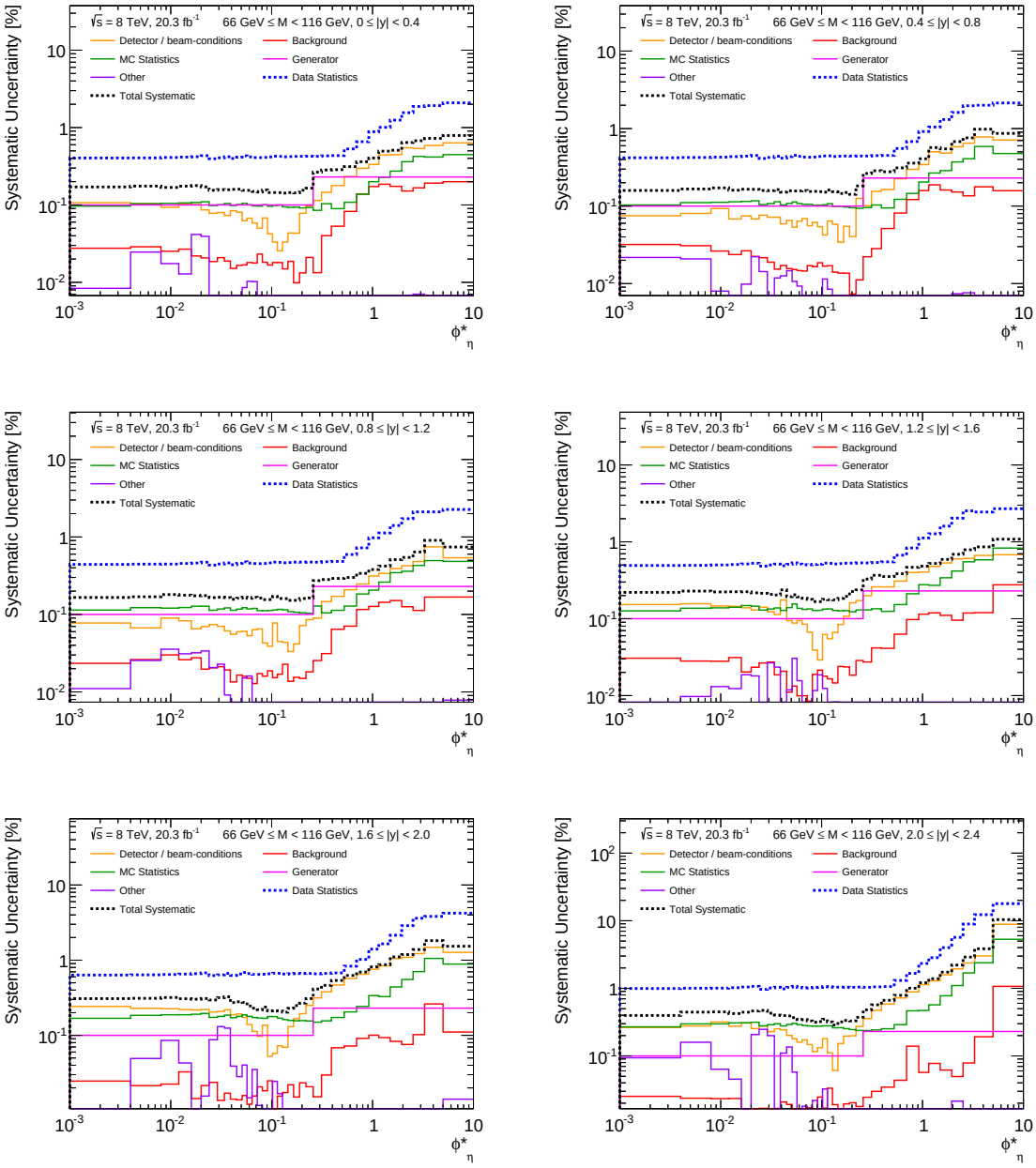

Figure 6.19: The size of various systematic uncertainties as a percentage of the Born level normalised differential cross-section for each boson rapidity region in the peak-mass region. The total systematic uncertainty is shown as a black-dashed line and the data statistical uncertainty as a blue-dashed line.

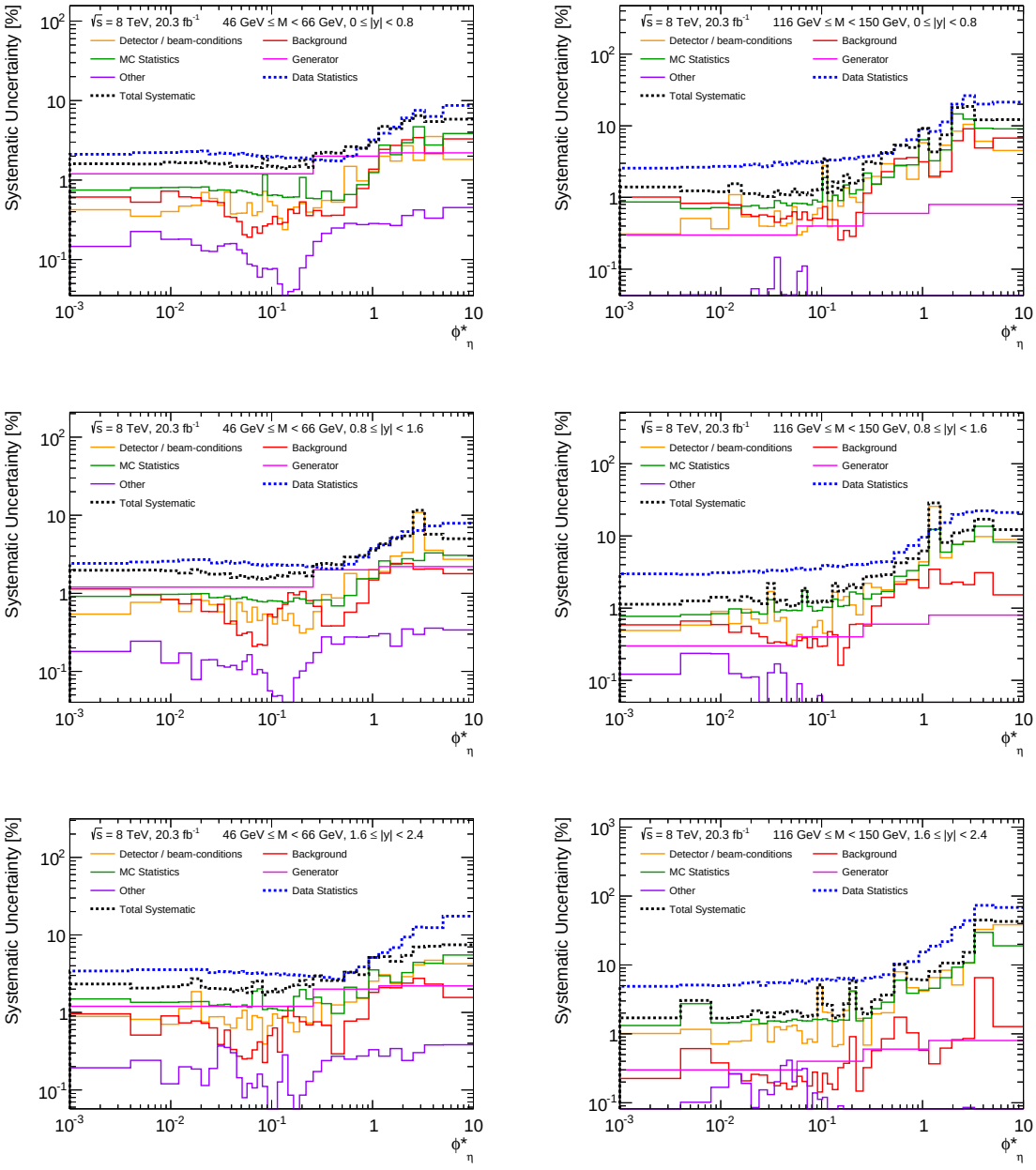

Figure 6.19: The size of various systematic uncertainties as a percentage of the Born level normalised differential cross-section for each boson rapidity region in the low-mass and high-mass regions. The total systematic uncertainty is shown as a black-dashed line and the data statistical uncertainty as a blue-dashed line.

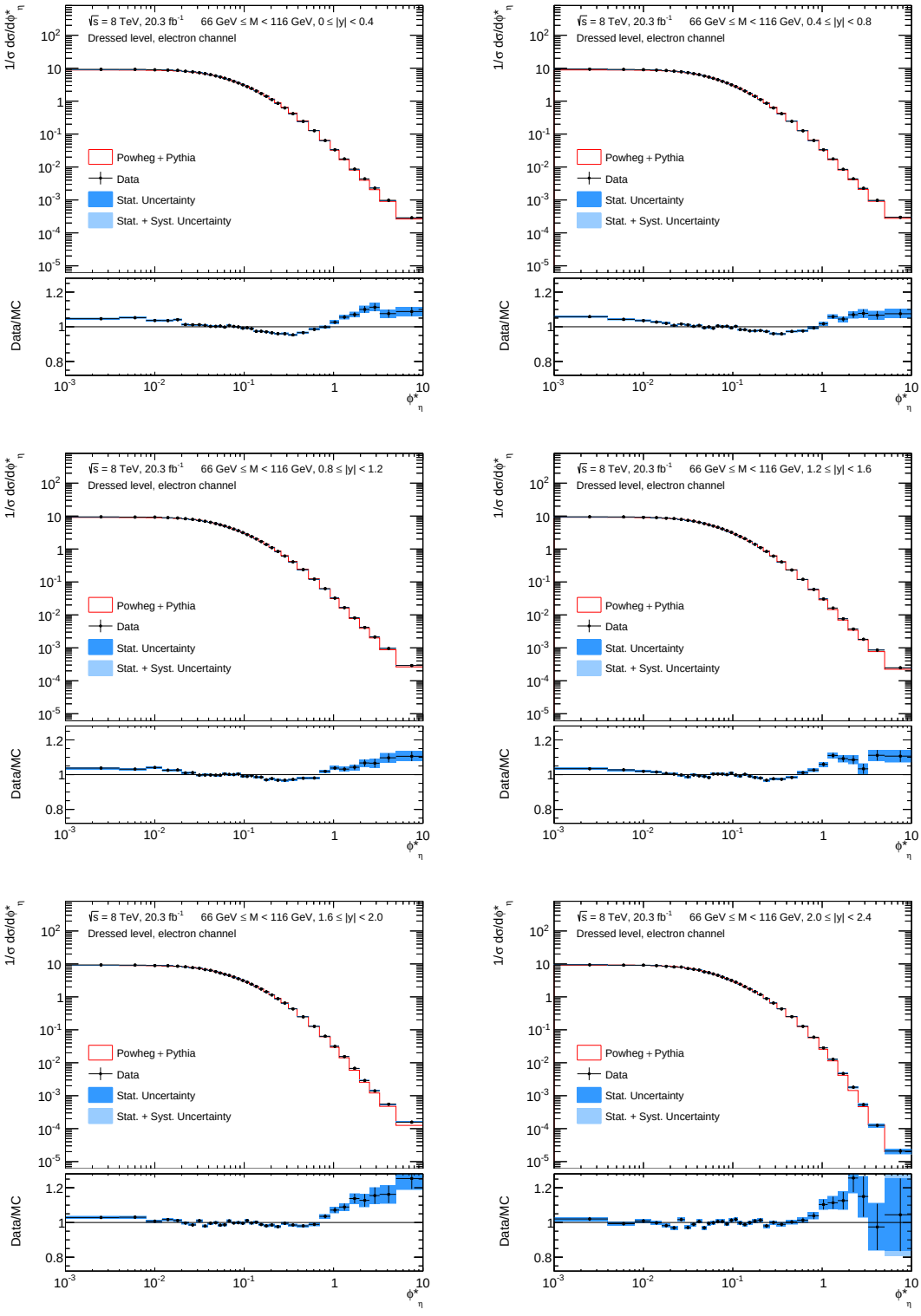

Figure 6.20: The final dressed level normalised differential cross-section as a function of ϕ^*_η for each boson rapidity region in the peak-mass region. The data are shown with statistical uncertainties (dark-blue) and the quadrature sum of the statistical and systematic uncertainties (light-blue), and the ratio with respect to the prediction from Powheg+Pythia (without the ϕ^*_η re-weighting) is also displayed.

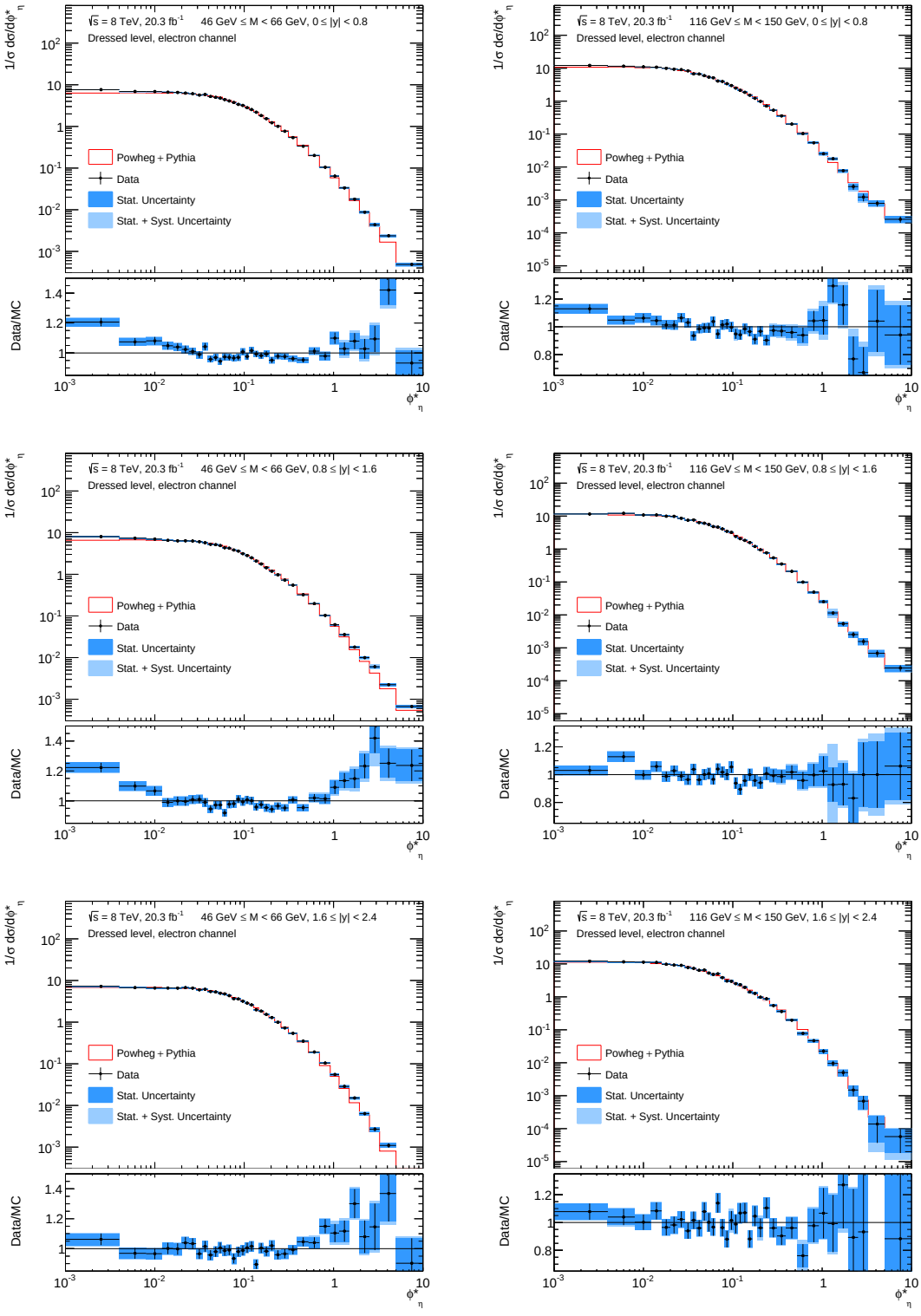

Figure 6.20: The final dressed level normalised differential cross-section as a function of ϕ^*_η for each boson rapidity region in the low-mass and high-mass regions. The data are shown with statistical uncertainties (dark-blue) and the quadrature sum of the statistical and systematic uncertainties (light-blue), and the ratio with respect to the prediction from Powheg+Pythia (without the ϕ^*_η re-weighting) is also displayed.

	66 GeV $< M <$ 116 GeV																	
	$\lvert y\rvert < 0.4$			$0.4 < \lvert y\rvert < 0.8$			$0.8 < \lvert y\rvert < 1.2$			$1.2 < \lvert y\rvert < 1.6$			$1.6 < \lvert y\rvert < 2.0$			$2.0 < \lvert y\rvert < 2.4$		
Bin	$(1/\sigma)\, d\sigma/d\phi^*$	$\delta\phi^*_{\text{sys}}$[%]	$\delta\phi^*_{\text{stat}}$[%]	$(1/\sigma)\, d\sigma/d\phi^*$	$\delta\phi^*_{\text{sys}}$[%]	$\delta\phi^*_{\text{stat}}$[%]	$(1/\sigma)\, d\sigma/d\phi^*$	$\delta\phi^*_{\text{sys}}$[%]	$\delta\phi^*_{\text{stat}}$[%]	$(1/\sigma)\, d\sigma/d\phi^*$	$\delta\phi^*_{\text{sys}}$[%]	$\delta\phi^*_{\text{stat}}$[%]	$(1/\sigma)\, d\sigma/d\phi^*$	$\delta\phi^*_{\text{sys}}$[%]	$\delta\phi^*_{\text{stat}}$[%]	$(1/\sigma)\, d\sigma/d\phi^*$	$\delta\phi^*_{\text{sys}}$[%]	$\delta\phi^*_{\text{stat}}$[%]
0.000 - 0.004	9.229	0.16	0.40	9.372	0.15	0.42	9.450	0.16	0.44	9.507	0.21	0.49	9.320	0.30	0.63	9.399	0.38	0.99
0.004 - 0.008	9.219	0.16	0.41	9.176	0.16	0.42	9.312	0.16	0.45	9.418	0.22	0.49	9.201	0.30	0.64	9.160	0.42	1.0
0.008 - 0.012	8.952	0.16	0.41	9.003	0.16	0.43	9.289	0.17	0.45	9.190	0.22	0.50	8.948	0.31	0.64	9.144	0.44	1.0
0.012 - 0.016	8.765	0.17	0.42	8.763	0.15	0.43	8.935	0.17	0.46	8.968	0.22	0.51	8.814	0.30	0.65	8.878	0.41	1.0
0.016 - 0.020	8.584	0.17	0.42	8.486	0.16	0.44	8.725	0.17	0.46	8.645	0.22	0.52	8.534	0.30	0.66	8.458	0.42	1.0
0.020 - 0.024	8.066	0.16	0.43	8.124	0.16	0.45	8.286	0.17	0.47	8.340	0.21	0.53	8.153	0.30	0.68	8.095	0.43	1.1
0.024 - 0.029	7.740	0.15	0.40	7.795	0.16	0.41	7.894	0.16	0.43	7.883	0.21	0.48	7.673	0.28	0.62	8.035	0.43	0.97
0.029 - 0.034	7.311	0.15	0.41	7.342	0.15	0.42	7.381	0.15	0.45	7.380	0.20	0.50	7.395	0.30	0.64	7.211	0.40	1.0
0.034 - 0.039	6.850	0.15	0.42	6.840	0.16	0.44	6.928	0.16	0.46	6.988	0.20	0.51	6.718	0.30	0.67	6.873	0.39	1.0
0.039 - 0.045	6.345	0.15	0.40	6.374	0.14	0.42	6.448	0.15	0.44	6.455	0.23	0.49	6.359	0.27	0.63	6.502	0.38	0.98
0.045 - 0.051	5.849	0.15	0.42	5.824	0.15	0.43	5.931	0.16	0.46	5.923	0.19	0.51	5.843	0.27	0.65	5.742	0.37	1.0
0.051 - 0.057	5.423	0.15	0.43	5.399	0.15	0.45	5.414	0.16	0.48	5.409	0.19	0.53	5.278	0.27	0.69	5.439	0.35	1.1
0.057 - 0.064	4.944	0.15	0.42	4.913	0.15	0.44	5.018	0.15	0.46	5.016	0.18	0.51	4.880	0.24	0.66	4.957	0.33	1.0
0.064 - 0.072	4.517	0.14	0.41	4.486	0.15	0.43	4.496	0.16	0.45	4.548	0.17	0.50	4.480	0.22	0.65	4.517	0.33	1.0
0.072 - 0.081	4.024	0.14	0.41	4.008	0.15	0.43	4.017	0.15	0.45	4.068	0.17	0.50	3.996	0.21	0.65	4.010	0.31	1.0
0.081 - 0.091	3.575	0.15	0.41	3.577	0.15	0.43	3.585	0.15	0.45	3.604	0.16	0.51	3.565	0.23	0.65	3.529	0.30	1.0
0.091 - 0.102	3.151	0.14	0.42	3.141	0.15	0.44	3.137	0.15	0.46	3.204	0.16	0.51	3.151	0.20	0.66	3.169	0.30	1.0
0.102 - 0.114	2.773	0.14	0.43	2.786	0.14	0.44	2.748	0.16	0.47	2.761	0.17	0.53	2.802	0.20	0.67	2.797	0.34	1.1
0.114 - 0.128	2.403	0.14	0.42	2.381	0.15	0.44	2.384	0.15	0.47	2.397	0.17	0.53	2.406	0.20	0.67	2.408	0.30	1.1
0.128 - 0.145	2.032	0.14	0.42	2.037	0.14	0.44	2.023	0.15	0.46	2.057	0.17	0.52	2.073	0.19	0.65	2.035	0.27	1.0
0.145 - 0.165	1.707	0.14	0.42	1.699	0.14	0.44	1.689	0.15	0.47	1.704	0.18	0.52	1.734	0.22	0.66	1.740	0.31	1.0
0.165 - 0.189	1.404	0.14	0.42	1.404	0.14	0.44	1.371	0.15	0.47	1.393	0.19	0.53	1.420	0.24	0.67	1.443	0.32	1.0
0.189 - 0.219	1.119	0.15	0.43	1.122	0.14	0.44	1.101	0.15	0.47	1.104	0.22	0.53	1.144	0.26	0.67	1.170	0.32	1.0
0.219 - 0.258	0.858	0.16	0.43	0.860	0.18	0.44	0.841	0.16	0.47	0.838	0.23	0.53	0.877	0.30	0.67	0.888	0.37	1.0
0.258 - 0.312	0.624	0.25	0.42	0.623	0.25	0.44	0.610	0.26	0.47	0.608	0.32	0.53	0.648	0.41	0.66	0.650	0.47	1.0
0.312 - 0.391	0.415	0.27	0.43	0.415	0.28	0.45	0.407	0.27	0.48	0.404	0.36	0.54	0.432	0.46	0.67	0.432	0.56	1.1
0.391 - 0.524	0.243	0.28	0.43	0.244	0.27	0.45	0.237	0.28	0.48	0.230	0.34	0.55	0.248	0.53	0.68	0.251	0.66	1.1
0.524 - 0.695	0.127	0.30	0.53	0.126	0.30	0.55	0.122	0.29	0.59	0.120	0.38	0.67	0.127	0.62	0.83	0.128	0.79	1.3
0.695 - 0.918	0.0636	0.35	0.66	0.0639	0.35	0.68	0.0625	0.33	0.72	0.0593	0.46	0.83	0.0637	0.69	1.0	0.0596	1.00	1.7
0.918 - 1.153	0.0334	0.40	0.88	0.0335	0.40	0.92	0.0323	0.37	0.98	0.0304	0.47	1.1	0.0315	0.80	1.4	0.0283	1.2	2.3
1.153 - 1.496	0.0176	0.49	1.0	0.0176	0.56	1.0	0.0166	0.41	1.1	0.0161	0.52	1.3	0.0154	0.86	1.6	0.0127	1.4	2.8
1.496 - 1.947	0.00866	0.50	1.2	0.00851	0.54	1.3	0.00811	0.50	1.4	0.00761	0.58	1.6	0.00675	1.1	2.1	0.00469	1.7	4.0
1.947 - 2.522	0.00437	0.65	1.6	0.00438	0.67	1.6	0.00418	0.54	1.7	0.00372	0.68	2.0	0.00288	1.2	2.9	0.00180	2.2	5.7
2.522 - 3.277	0.00229	0.67	1.9	0.00226	0.75	2.0	0.00213	0.62	2.1	0.00182	0.77	2.5	0.00140	1.4	3.6	0.000533	2.9	8.9
3.277 - 5.000	0.000976	0.72	1.9	0.000973	0.97	2.0	0.000959	0.90	2.1	0.000855	0.85	2.4	0.000552	1.8	3.8	0.000126	3.9	12
5.000 - 10.000	0.000287	0.78	2.1	0.000298	0.86	2.1	0.000291	0.74	2.3	0.000247	1.1	2.7	0.000157	1.5	4.2	0.0000208	10	18

Table 6.9: The values of the dressed level normalised differential cross-section in bins of ϕ^*_η for the di-electron channel, for each boson rapidity region in the peak-mass region. Also given are the associated statistical and systematic uncertainties in percent, where the colour on the blue-red scale indicates the relative contribution to the total uncertainty.

	46 GeV $< M <$ 66 GeV									116 GeV $< M <$ 150 GeV								
	$\|y\| < 0.8$			$0.8 < \|y\| < 1.6$			$1.6 < \|y\| < 2.4$			$\|y\| < 0.8$			$0.8 < \|y\| < 1.6$			$1.6 < \|y\| < 2.4$		
Bin	$(1/\sigma)\, d\sigma/d\phi^*$	$\delta\phi^*_{\text{sys}}$[%]	$\delta\phi^*_{\text{stat}}$[%]	$(1/\sigma)\, d\sigma/d\phi^*$	$\delta\phi^*_{\text{sys}}$[%]	$\delta\phi^*_{\text{stat}}$[%]	$(1/\sigma)\, d\sigma/d\phi^*$	$\delta\phi^*_{\text{sys}}$[%]	$\delta\phi^*_{\text{stat}}$[%]	$(1/\sigma)\, d\sigma/d\phi^*$	$\delta\phi^*_{\text{sys}}$[%]	$\delta\phi^*_{\text{stat}}$[%]	$(1/\sigma)\, d\sigma/d\phi^*$	$\delta\phi^*_{\text{sys}}$[%]	$\delta\phi^*_{\text{stat}}$[%]	$(1/\sigma)\, d\sigma/d\phi^*$	$\delta\phi^*_{\text{sys}}$[%]	$\delta\phi^*_{\text{stat}}$[%]
0.000 - 0.004	7.631	1.1	2.1	8.024	1.6	2.4	7.259	2.0	3.4	12.120	1.4	2.6	11.544	1.1	3.0	12.146	1.6	4.9
0.004 - 0.008	6.906	1.1	2.2	7.365	1.6	2.5	6.727	1.7	3.6	11.482	1.2	2.6	12.102	1.2	2.9	11.553	3.0	5.1
0.008 - 0.012	6.889	1.2	2.2	6.988	1.6	2.6	6.617	1.8	3.6	11.008	1.2	2.7	10.785	1.4	3.1	11.330	1.6	5.0
0.012 - 0.016	6.627	1.2	2.3	6.526	1.4	2.7	6.602	1.9	3.6	10.731	1.5	2.7	10.808	1.2	3.1	11.068	1.7	5.1
0.016 - 0.020	6.565	1.2	2.3	6.356	1.7	2.7	6.573	2.4	3.6	9.963	1.1	2.9	9.899	1.4	3.2	9.738	1.7	5.5
0.020 - 0.024	6.303	1.2	2.3	6.372	1.4	2.7	6.730	1.7	3.6	9.338	1.1	2.9	9.821	1.2	3.3	9.236	2.1	5.6
0.024 - 0.029	6.089	1.1	2.1	6.290	1.3	2.4	6.567	1.6	3.3	9.029	1.0	2.7	8.581	1.1	3.1	9.055	2.0	5.0
0.029 - 0.034	5.679	1.1	2.2	6.061	1.3	2.5	5.988	1.6	3.4	8.335	0.98	2.8	7.478	2.2	3.4	7.773	1.7	5.5
0.034 - 0.039	5.843	1.1	2.2	5.725	1.4	2.6	6.140	1.6	3.3	6.727	1.2	3.1	7.635	1.2	3.3	7.311	2.0	5.5
0.039 - 0.045	5.227	0.91	2.1	5.248	1.1	2.4	5.450	1.4	3.2	6.649	1.1	2.9	6.369	1.2	3.3	6.387	1.9	5.5
0.045 - 0.051	4.984	0.94	2.1	5.128	1.2	2.5	5.312	1.5	3.3	5.921	1.0	3.0	6.075	1.0	3.4	6.516	2.0	5.5
0.051 - 0.057	4.771	0.89	2.2	4.882	1.1	2.5	4.959	1.7	3.4	5.367	1.2	3.2	5.553	1.0	3.5	5.277	2.1	6.0
0.057 - 0.064	4.417	0.93	2.1	4.345	1.0	2.5	4.756	1.3	3.2	5.128	1.0	3.0	4.788	1.1	3.6	4.805	1.9	5.9
0.064 - 0.072	4.090	0.84	2.0	4.228	1.1	2.3	4.329	2.1	3.2	4.080	1.1	3.2	4.628	1.8	3.4	4.994	1.7	5.4
0.072 - 0.081	3.752	0.86	2.0	3.828	0.96	2.3	3.666	2.2	3.2	3.964	1.0	3.0	4.070	1.2	3.4	3.852	1.7	5.8
0.081 - 0.091	3.379	1.5	2.0	3.614	1.0	2.3	3.596	1.2	3.1	3.391	1.3	3.1	3.453	1.2	3.5	3.034	1.8	6.3
0.091 - 0.102	3.199	0.95	2.0	3.134	1.1	2.3	3.192	1.4	3.1	2.988	1.3	3.2	3.198	1.2	3.5	2.968	5.1	6.1
0.102 - 0.114	2.808	0.94	2.0	2.838	1.0	2.3	2.865	1.6	3.1	2.498	3.5	3.4	2.419	1.2	3.9	2.525	2.6	6.2
0.114 - 0.128	2.537	0.80	1.9	2.485	1.2	2.3	2.595	1.4	3.0	2.130	1.1	3.4	2.053	1.2	3.9	2.335	2.6	6.0
0.128 - 0.145	2.193	0.75	1.9	2.078	1.2	2.3	1.985	1.6	3.1	1.855	1.6	3.3	1.819	2.2	3.8	1.954	1.6	5.9
0.145 - 0.165	1.820	0.86	1.9	1.771	1.4	2.3	1.837	1.7	3.1	1.517	1.2	3.3	1.578	1.7	3.8	1.408	1.7	6.4
0.165 - 0.189	1.538	0.86	1.9	1.441	1.4	2.3	1.531	1.9	3.0	1.220	2.1	3.5	1.193	1.8	3.9	1.276	2.7	6.2
0.189 - 0.219	1.229	1.3	1.9	1.188	1.4	2.3	1.294	2.2	3.0	0.985	1.6	3.5	0.941	2.1	4.0	0.974	5.9	6.4
0.219 - 0.258	1.010	0.84	1.8	0.972	1.2	2.2	0.993	1.8	2.9	0.711	1.7	3.7	0.768	1.9	4.0	0.874	2.3	6.0
0.258 - 0.312	0.766	0.87	1.8	0.727	1.2	2.2	0.728	2.2	2.9	0.531	3.1	3.7	0.538	2.7	4.1	0.544	1.9	6.5
0.312 - 0.391	0.542	1.0	1.8	0.549	1.3	2.1	0.540	1.6	2.8	0.358	3.0	3.8	0.351	2.8	4.3	0.360	3.2	6.7
0.391 - 0.524	0.336	0.91	1.7	0.323	1.2	2.1	0.350	1.6	2.7	0.201	4.3	4.1	0.210	2.9	4.4	0.197	3.6	7.2
0.524 - 0.695	0.201	1.7	2.0	0.197	2.1	2.4	0.192	2.6	3.3	0.103	5.3	5.4	0.0988	4.2	5.9	0.0777	10	10
0.695 - 0.918	0.105	1.6	2.5	0.103	2.3	2.9	0.104	2.4	3.9	0.0546	5.0	6.4	0.0490	4.8	7.4	0.0466	6.2	11
0.918 - 1.153	0.0641	2.3	3.2	0.0617	3.0	3.8	0.0553	4.7	5.1	0.0253	9.2	9.1	0.0251	6.2	9.6	0.0225	6.0	15
1.153 - 1.496	0.0335	4.2	3.9	0.0357	3.7	4.2	0.0286	4.8	5.9	0.0178	4.3	8.3	0.0114	29	12	0.00956	7.9	19
1.496 - 1.947	0.0179	3.9	4.6	0.0178	4.6	5.2	0.0151	4.0	6.9	0.00774	7.4	11	0.00540	8.1	15	0.00503	10	22
1.947 - 2.522	0.00876	5.1	6.0	0.00999	4.9	6.2	0.00636	5.0	9.4	0.00255	18	20	0.00254	11	20	0.00149	11	35
2.522 - 3.277	0.00435	6.1	7.5	0.00603	11	6.4	0.00269	6.6	13	0.00123	19	26	0.00155	12	21	0.000684	14	44
3.277 - 5.000	0.00237	5.0	6.3	0.00224	5.3	7.3	0.00110	6.8	12	0.000791	12	20	0.000685	17	22	0.000138	45	73
5.000 - 10.000	0.000486	5.4	8.7	0.000671	4.5	7.9	0.000213	7.2	17	0.000259	12	21	0.000245	12	21	0.0000573	43	68

Table 6.10: The values of the dressed level normalised differential cross-section in bins of ϕ^*_η for the di-electron channel, for each boson rapidity region in the low and high-mass regions. Also given are the associated statistical and systematic uncertainties in percent, where the colour on the blue-red scale indicates the relative contribution to the total uncertainty.

Uncorrelated between channels
Electron energy scale and resolution
Muon momentum scale and resolution
Scale factors
Angular resolution
Correction method
Multi-jet background
Correlated between channels
Pile-up
Longitudinal position of the primary vertex
MC background normalisation
Z boson line-shape
Generator choice

Table 6.11: A list of the electron channel and muon channel uncertainties which are considered to be correlated between bins of ϕ^*_η when performing the Born level combination of the two channels. Uncertainties are divided into those which are assumed to be correlated between the two channels and those assumed to be uncorrelated. The data and MC statistical uncertainties are taken as uncorrelated between both ϕ^*_η bins and channels.

The di-electron (as described in this thesis) and di-muon [72] Born level results are combined using a generalised χ^2 fit, which takes into account correlations between ϕ^*_η bins and between channels [83]. Table 6.11 provides a list of the electron channel and muon channel uncertainties which are considered to be correlated between ϕ^*_η bins and indicates which of those are considered to be correlated between channels. The data and MC statistical uncertainties are taken as uncorrelated between both ϕ^*_η bins and channels. Note that uncertainties are assumed to be either fully correlated or fully uncorrelated.

In order to combine the two channels a common geometric and kinematic acceptance is defined, known as the combination volume (see Table 6.4). This is equal to the muon channel fiducial volume, but differs from the electron channel fiducial volume in that it contains the crack-region from which no data events are selected. This amounts to modifying the selection criteria for the denominator of the correction factors (Equation 6.5) in order to perform an extrapolation of the background-subtracted data over the crack-region, as well as correcting for the effects of detector inefficiencies, resolution and FSR.

The combined results are not necessarily normalised to unity, and so a renormalisation is performed. In practice this is a negligible effect with respect to the data statistical uncertainty.

Figure 6.21 shows the final electron channel, muon channel and combined Born level distributions in each region of boson mass and rapidity. The error bars on the data points represent the uncertainties uncorrelated between the two channels (the quadrature sum of statistical and systematic). Also displayed is the χ^2 per degree of freedom from the fit, the ratio of each channel to the combined result and the pull between channels. The green band in the ratio plot represents the uncertainty on the combination from sources uncorrelated between channels. Uncertainty from correlated sources is negligible. The pull is defined in Equation 6.17 in terms of the electron and muon Born level values, e and μ, and their uncorrelated uncertainties, σ_e and σ_μ.

$$\text{pull} = \frac{e - \mu}{\sqrt{\sigma_e^2 + \sigma_\mu^2}} \tag{6.17}$$

Table 6.12 provides the combined Born level values of $(1/\sigma)\, d\sigma/d\phi^*_\eta$ for each ϕ^*_η bin in each of the boson rapidity regions at peak-mass. Also given are the associated correlated and uncorrelated (including statistical) uncertainties in percent. As in Section 6.11.1, a blue-red colour scale is used to indicate the relative contribution of each to the total. Table 6.13 provides the same information for each boson rapidity region in the low-mass and high-mass regions.

6.11.3 Comparison with theoretical predictions

One of the aims of this analysis is to provide data which can improve future analytical calculations and tune MC event generators in the non-perturbative regime of QCD. This section shows comparisons between the combined Born level results of Section 6.11.2 and two of the current generation of theoretical predictions, namely RESBOS [84] and a NNLL+NLO calculation from Banfi et al. [63].

The RESBOS program takes as input tables (or 'grids') of boson production cross-section values evaluated at different values of boson invariant mass, transverse momentum and rapidity. Separate grids exist for the fixed-order perturbative calculation and the re-summed non-perturbative calculation, which are then combined ('matched') appropriately by RESBOS. MC events are produced by sampling the grids and decaying the vector boson, and the ϕ^*_η variable is computed for each event using the directions of the decay products.

The Banfi et al. prediction matches an NNLL re-summed analytical calculation of the ϕ^*_η distribution with an NLO fixed-order description obtained using the MCFM MC event generator. Predictions exist only for boson invariant mass greater than 66 GeV due to issues with the matching procedure, which are as yet unresolved [72].

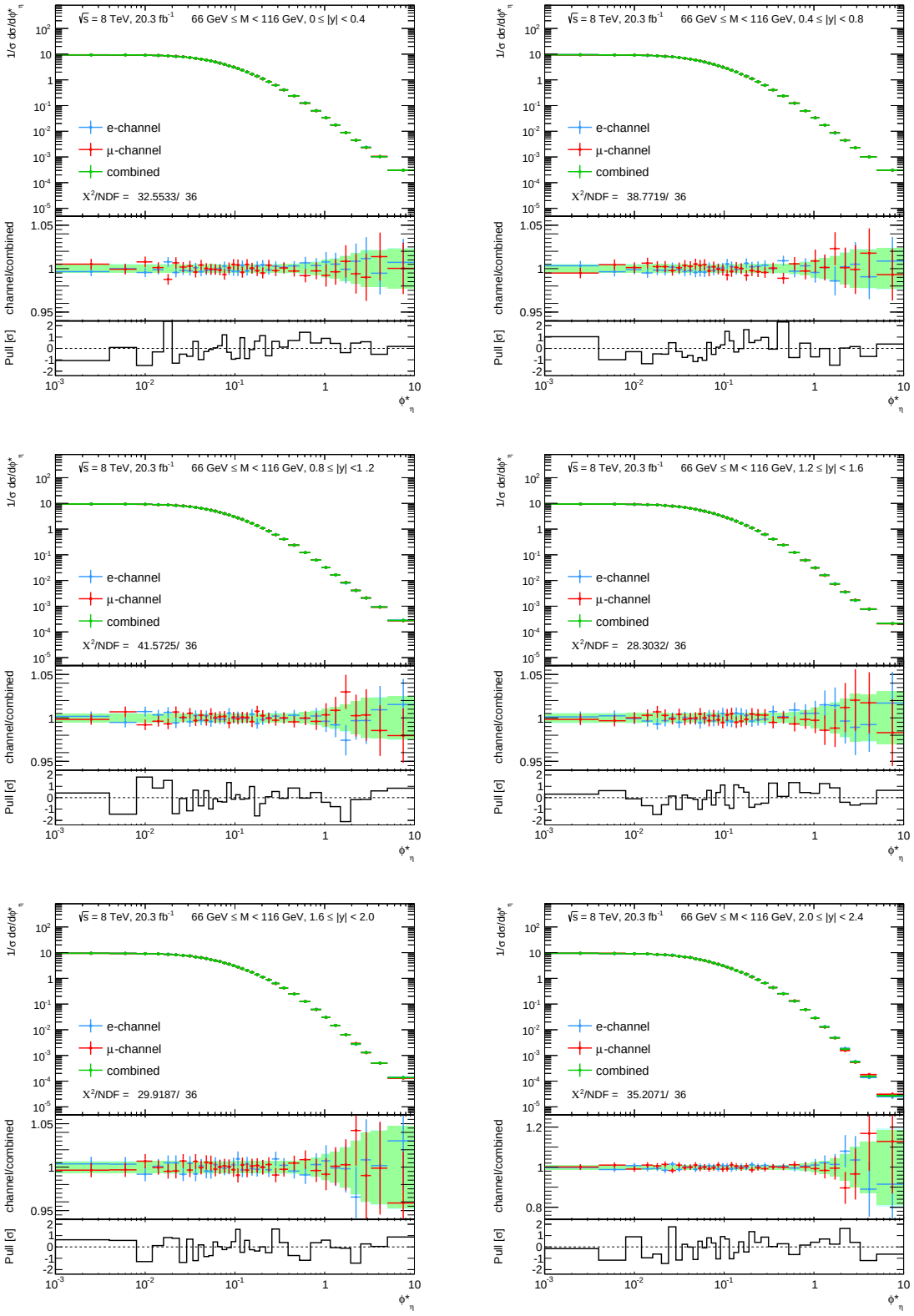

Figure 6.21: The final electron channel (blue), muon channel (red) and combined (green) Born level distributions for each region of boson rapidity in the peak-mass region. Also displayed is the χ^2 per degree of freedom from the fit, the ratio of each channel to the combined result and the pull between channels (Equation 6.17).

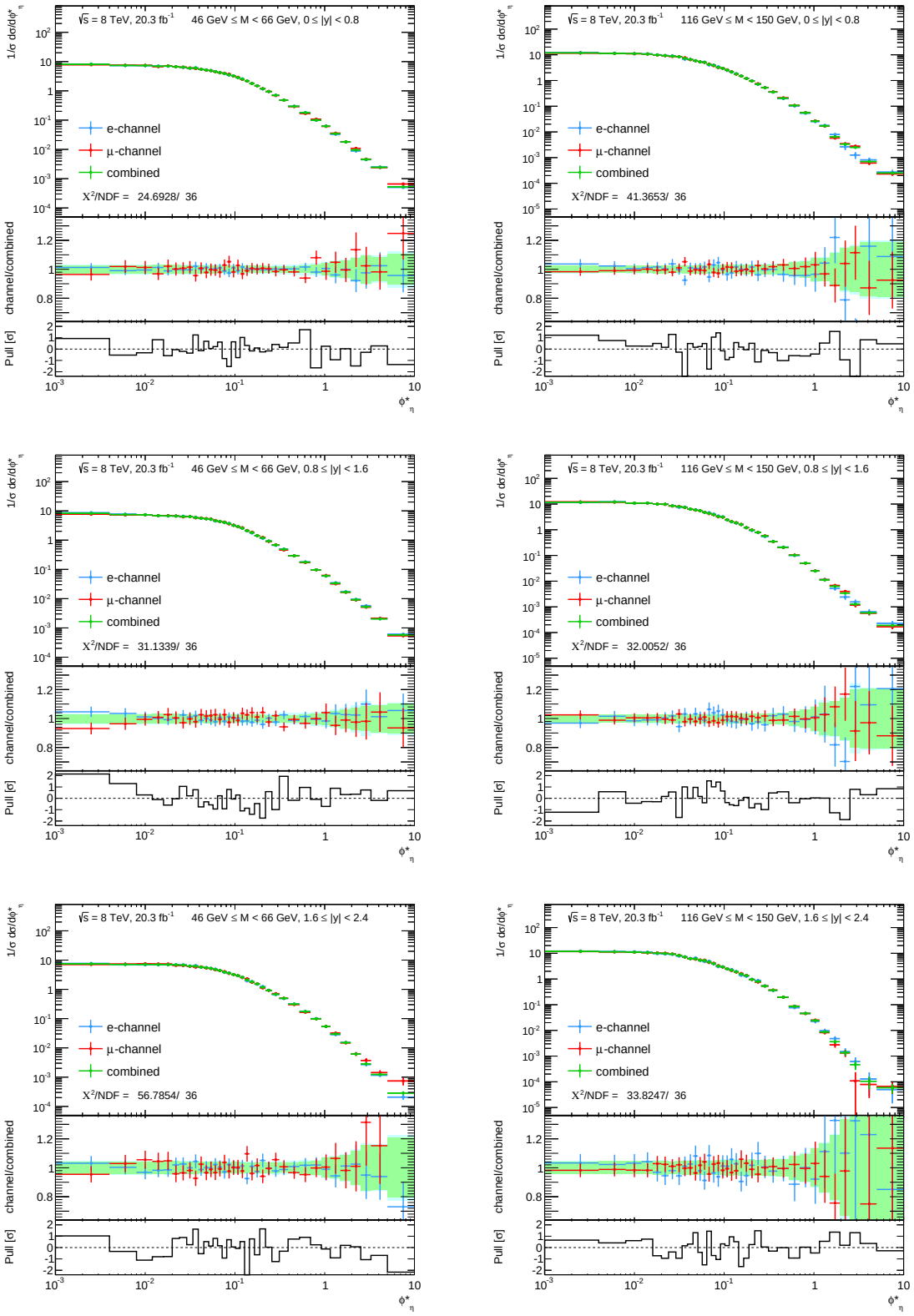

Figure 6.21: The final electron channel (blue), muon channel (red) and combined (green) Born level distributions for each region of boson rapidity in the low-mass and high-mass regions. Also displayed is the χ^2 per degree of freedom from the fit, the ratio of each channel to the combined result and the pull between channels (Equation 6.17).

	66 GeV $< M <$ 116 GeV																	
	$\lvert y\rvert < 0.4$			$0.4 < \lvert y\rvert < 0.8$			$0.8 < \lvert y\rvert < 1.2$			$1.2 < \lvert y\rvert < 1.6$			$1.6 < \lvert y\rvert < 2.0$			$2.0 < \lvert y\rvert < 2.4$		
Bin	$(1/\sigma)\, d\sigma/d\phi^*$	$\delta\phi^*_{\text{corr.}}$[%]	$\delta\phi^*_{\text{uncorr.}}$[%]	$(1/\sigma)\, d\sigma/d\phi^*$	$\delta\phi^*_{\text{corr.}}$[%]	$\delta\phi^*_{\text{uncorr.}}$[%]	$(1/\sigma)\, d\sigma/d\phi^*$	$\delta\phi^*_{\text{corr.}}$[%]	$\delta\phi^*_{\text{uncorr.}}$[%]	$(1/\sigma)\, d\sigma/d\phi^*$	$\delta\phi^*_{\text{corr.}}$[%]	$\delta\phi^*_{\text{uncorr.}}$[%]	$(1/\sigma)\, d\sigma/d\phi^*$	$\delta\phi^*_{\text{corr.}}$[%]	$\delta\phi^*_{\text{uncorr.}}$[%]	$(1/\sigma)\, d\sigma/d\phi^*$	$\delta\phi^*_{\text{corr.}}$[%]	$\delta\phi^*_{\text{uncorr.}}$[%]
0.000 - 0.004	9.385	0.14	0.32	9.498	0.12	0.33	9.488	0.13	0.34	9.477	0.19	0.37	9.454	0.18	0.47	9.449	0.26	0.77
0.004 - 0.008	9.352	0.14	0.32	9.338	0.16	0.33	9.405	0.19	0.34	9.381	0.16	0.37	9.344	0.16	0.47	9.294	0.24	0.77
0.008 - 0.012	9.103	0.16	0.33	9.154	0.13	0.33	9.262	0.12	0.34	9.176	0.17	0.38	9.154	0.18	0.47	9.115	0.24	0.78
0.012 - 0.016	8.889	0.13	0.33	8.920	0.16	0.34	8.961	0.13	0.35	8.973	0.14	0.38	8.942	0.16	0.48	8.965	0.22	0.79
0.016 - 0.020	8.625	0.13	0.34	8.610	0.13	0.34	8.713	0.13	0.35	8.675	0.18	0.39	8.621	0.21	0.49	8.521	0.30	0.80
0.020 - 0.024	8.190	0.14	0.34	8.227	0.13	0.35	8.358	0.11	0.36	8.322	0.17	0.39	8.224	0.14	0.50	8.221	0.27	0.82
0.024 - 0.029	7.827	0.10	0.31	7.880	0.12	0.32	7.920	0.15	0.33	7.838	0.12	0.36	7.820	0.21	0.46	7.948	0.28	0.75
0.029 - 0.034	7.395	0.12	0.32	7.419	0.09	0.33	7.425	0.09	0.34	7.374	0.10	0.37	7.456	0.20	0.47	7.261	0.18	0.78
0.034 - 0.039	6.893	0.11	0.33	6.916	0.10	0.34	6.926	0.09	0.35	6.936	0.11	0.38	6.822	0.14	0.49	6.848	0.17	0.80
0.039 - 0.045	6.393	0.10	0.32	6.435	0.10	0.32	6.471	0.08	0.33	6.416	0.14	0.36	6.410	0.10	0.46	6.491	0.18	0.75
0.045 - 0.051	5.878	0.09	0.33	5.881	0.08	0.34	5.908	0.09	0.35	5.895	0.08	0.38	5.908	0.13	0.48	5.780	0.18	0.79
0.051 - 0.057	5.441	0.07	0.34	5.445	0.06	0.35	5.432	0.08	0.36	5.394	0.08	0.40	5.329	0.13	0.50	5.386	0.12	0.82
0.057 - 0.064	4.951	0.09	0.33	4.950	0.07	0.34	5.013	0.07	0.35	4.990	0.08	0.38	4.886	0.13	0.49	4.943	0.11	0.80
0.064 - 0.072	4.508	0.09	0.32	4.492	0.08	0.33	4.490	0.08	0.34	4.503	0.13	0.38	4.503	0.12	0.47	4.460	0.15	0.78
0.072 - 0.081	3.996	0.09	0.32	4.019	0.07	0.33	4.016	0.08	0.34	4.051	0.09	0.37	4.006	0.10	0.47	3.971	0.13	0.78
0.081 - 0.091	3.560	0.09	0.33	3.572	0.09	0.33	3.556	0.12	0.35	3.569	0.12	0.38	3.564	0.11	0.47	3.534	0.14	0.79
0.091 - 0.102	3.139	0.11	0.33	3.129	0.10	0.34	3.131	0.08	0.35	3.167	0.10	0.38	3.137	0.19	0.48	3.129	0.21	0.79
0.102 - 0.114	2.758	0.10	0.34	2.758	0.12	0.35	2.738	0.12	0.36	2.751	0.12	0.39	2.769	0.13	0.49	2.770	0.18	0.81
0.114 - 0.128	2.371	0.14	0.34	2.359	0.12	0.35	2.382	0.09	0.36	2.398	0.12	0.39	2.400	0.13	0.49	2.412	0.13	0.80
0.128 - 0.145	2.012	0.11	0.33	2.024	0.12	0.34	2.018	0.11	0.35	2.041	0.12	0.38	2.053	0.15	0.48	2.034	0.25	0.79
0.145 - 0.165	1.685	0.11	0.33	1.683	0.13	0.34	1.678	0.13	0.35	1.698	0.14	0.39	1.721	0.14	0.48	1.727	0.17	0.79
0.165 - 0.189	1.382	0.12	0.34	1.379	0.11	0.34	1.378	0.13	0.36	1.392	0.14	0.39	1.412	0.17	0.48	1.446	0.14	0.79
0.189 - 0.219	1.098	0.11	0.34	1.105	0.11	0.34	1.102	0.12	0.36	1.115	0.11	0.39	1.132	0.14	0.48	1.155	0.25	0.79
0.219 - 0.258	0.847	0.10	0.34	0.846	0.12	0.34	0.840	0.12	0.36	0.848	0.11	0.39	0.870	0.10	0.48	0.886	0.16	0.79
0.258 - 0.312	0.613	0.15	0.34	0.611	0.16	0.34	0.610	0.15	0.36	0.619	0.15	0.39	0.635	0.18	0.48	0.649	0.21	0.79
0.312 - 0.391	0.409	0.16	0.34	0.408	0.15	0.35	0.407	0.14	0.36	0.411	0.15	0.40	0.426	0.17	0.49	0.437	0.24	0.80
0.391 - 0.524	0.239	0.14	0.34	0.238	0.14	0.35	0.236	0.14	0.37	0.237	0.14	0.40	0.245	0.17	0.49	0.255	0.28	0.81
0.524 - 0.695	0.125	0.15	0.42	0.124	0.16	0.43	0.122	0.15	0.45	0.123	0.15	0.50	0.126	0.21	0.61	0.131	0.33	0.99
0.695 - 0.918	0.0631	0.18	0.52	0.0625	0.19	0.53	0.0621	0.18	0.55	0.0612	0.20	0.62	0.0619	0.25	0.76	0.0609	0.39	1.3
0.918 - 1.153	0.0332	0.22	0.70	0.0331	0.21	0.71	0.0322	0.19	0.74	0.0311	0.22	0.84	0.0302	0.28	1.1	0.0289	0.57	1.8
1.153 - 1.496	0.0176	0.24	0.80	0.0174	0.28	0.82	0.0166	0.21	0.86	0.0160	0.27	0.97	0.0148	0.32	1.2	0.0129	0.58	2.2
1.496 - 1.947	0.00881	0.29	0.99	0.00860	0.27	1.0	0.00820	0.26	1.1	0.00739	0.30	1.2	0.00643	0.43	1.6	0.00486	0.73	3.1
1.947 - 2.522	0.00445	0.29	1.2	0.00438	0.34	1.3	0.00411	0.27	1.3	0.00356	0.31	1.6	0.00282	0.52	2.2	0.00175	0.99	4.6
2.522 - 3.277	0.00236	0.29	1.5	0.00228	0.39	1.5	0.00209	0.28	1.6	0.00170	0.31	1.9	0.00129	0.50	2.8	0.000562	1.2	7.1
3.277 - 5.000	0.00103	0.31	1.5	0.00100	0.42	1.6	0.000930	0.43	1.6	0.000773	0.33	1.9	0.000508	0.73	3.0	0.000155	1.5	9.0
5.000 - 10.000	0.000304	0.35	1.6	0.000306	0.36	1.7	0.000279	0.33	1.8	0.000212	0.37	2.1	0.000137	0.58	3.3	0.0000272	4.0	13

Table 6.12: The values of the combined Born level normalised differential cross-section in bins of ϕ^*_η, for each boson rapidity region in the peak-mass region. Also given are the associated correlated and uncorrelated (including statistical) uncertainties in percent, where the colour on the blue-red scale indicates the relative contribution to the total uncertainty.

	46 GeV $< M <$ 66 GeV									116 GeV $< M <$ 150 GeV								
	$\|y\| < 0.8$			$0.8 < \|y\| < 1.6$			$1.6 < \|y\| < 2.4$			$\|y\| < 0.8$			$0.8 < \|y\| < 1.6$			$1.6 < \|y\| < 2.4$		
Bin	$(1/\sigma)\, d\sigma/d\phi^*$	$\delta\phi^*_{\text{corr.}}$[%]	$\delta\phi^*_{\text{uncorr.}}$[%]	$(1/\sigma)\, d\sigma/d\phi^*$	$\delta\phi^*_{\text{corr.}}$[%]	$\delta\phi^*_{\text{uncorr.}}$[%]	$(1/\sigma)\, d\sigma/d\phi^*$	$\delta\phi^*_{\text{corr.}}$[%]	$\delta\phi^*_{\text{uncorr.}}$[%]	$(1/\sigma)\, d\sigma/d\phi^*$	$\delta\phi^*_{\text{corr.}}$[%]	$\delta\phi^*_{\text{uncorr.}}$[%]	$(1/\sigma)\, d\sigma/d\phi^*$	$\delta\phi^*_{\text{corr.}}$[%]	$\delta\phi^*_{\text{uncorr.}}$[%]	$(1/\sigma)\, d\sigma/d\phi^*$	$\delta\phi^*_{\text{corr.}}$[%]	$\delta\phi^*_{\text{uncorr.}}$[%]
0.000 - 0.004	8.102	1.2	2.0	8.319	1.3	2.2	7.341	1.4	3.0	11.842	0.64	1.7	11.855	0.79	1.9	11.882	0.84	3.0
0.004 - 0.008	7.397	1.1	2.0	7.538	1.2	2.2	7.006	1.3	3.0	11.355	0.41	1.7	12.014	0.58	1.9	11.473	0.72	3.1
0.008 - 0.012	7.345	1.3	2.0	7.403	1.2	2.2	7.021	1.5	3.0	11.069	0.87	1.8	10.841	0.98	1.9	11.141	0.80	3.1
0.012 - 0.016	6.950	1.0	2.1	6.917	1.3	2.3	6.970	1.2	3.0	10.777	0.53	1.8	10.934	0.87	2.0	10.664	0.84	3.1
0.016 - 0.020	7.025	1.2	2.1	6.769	1.1	2.3	6.926	2.0	3.1	9.917	0.56	1.9	9.905	0.56	2.0	10.080	1.3	3.3
0.020 - 0.024	6.698	1.2	2.1	6.700	1.3	2.3	6.769	1.3	3.1	9.323	0.48	1.9	9.761	0.47	2.1	9.884	1.1	3.3
0.024 - 0.029	6.422	1.2	1.9	6.461	1.2	2.1	6.648	1.3	2.8	8.815	0.76	1.8	8.413	0.64	1.9	9.298	1.0	3.1
0.029 - 0.034	5.983	1.2	2.0	6.383	1.3	2.1	6.187	1.1	2.9	8.403	0.50	1.8	7.881	0.91	2.1	8.269	1.1	3.2
0.034 - 0.039	6.042	1.1	2.0	5.960	1.1	2.2	6.124	1.4	2.9	7.305	0.68	1.9	7.402	0.54	2.1	7.268	1.0	3.4
0.039 - 0.045	5.434	1.1	1.9	5.631	1.2	2.0	5.655	1.3	2.7	6.571	0.79	1.9	6.362	0.84	2.0	6.183	1.2	3.3
0.045 - 0.051	5.166	1.1	1.9	5.395	1.2	2.1	5.435	1.2	2.8	5.915	0.40	1.9	5.871	0.63	2.1	6.108	0.76	3.4
0.051 - 0.057	4.934	1.1	2.0	5.200	1.1	2.1	5.132	1.2	2.9	5.305	0.93	2.0	5.505	0.41	2.2	5.405	0.84	3.6
0.057 - 0.064	4.547	1.0	1.9	4.633	0.99	2.1	4.740	0.99	2.8	5.093	0.45	2.0	4.762	0.56	2.2	5.208	1.1	3.4
0.064 - 0.072	4.220	1.0	1.8	4.404	1.1	2.0	4.353	1.1	2.8	4.243	0.35	2.0	4.332	0.67	2.2	4.585	1.1	3.4
0.072 - 0.081	3.909	1.0	1.8	4.063	0.97	1.9	3.842	1.2	2.8	3.874	0.44	2.0	3.888	0.91	2.2	4.001	0.88	3.4
0.081 - 0.091	3.548	1.2	1.9	3.715	1.0	1.9	3.532	1.1	2.6	3.273	0.42	2.0	3.265	0.56	2.2	3.212	0.82	3.6
0.091 - 0.102	3.241	0.88	1.8	3.235	1.1	2.0	3.167	1.1	2.7	2.981	0.42	2.0	3.119	0.66	2.2	2.962	1.8	3.6
0.102 - 0.114	2.844	0.93	1.8	2.928	0.85	2.0	2.888	1.1	2.7	2.566	0.98	2.2	2.431	1.0	2.3	2.487	1.2	3.7
0.114 - 0.128	2.537	0.86	1.8	2.583	1.1	1.9	2.535	1.2	2.6	2.170	0.43	2.1	2.067	1.1	2.4	2.218	0.75	3.7
0.128 - 0.145	2.175	1.00	1.7	2.111	0.91	1.9	2.078	1.1	2.6	1.806	0.48	2.1	1.854	0.59	2.3	1.907	1.4	3.7
0.145 - 0.165	1.787	1.0	1.7	1.819	1.0	1.9	1.788	1.3	2.6	1.504	1.2	2.1	1.601	0.52	2.3	1.548	1.3	3.7
0.165 - 0.189	1.494	0.86	1.7	1.437	1.0	1.9	1.514	1.1	2.6	1.204	0.66	2.3	1.201	0.48	2.4	1.351	1.6	3.7
0.189 - 0.219	1.178	1.1	1.8	1.205	1.1	1.9	1.170	1.3	2.7	0.963	0.42	2.2	0.973	0.68	2.4	0.964	1.4	4.0
0.219 - 0.258	0.952	1.1	1.6	0.933	1.1	1.8	0.918	1.3	2.6	0.730	1.2	2.3	0.788	0.79	2.4	0.795	0.93	3.7
0.258 - 0.312	0.704	1.7	1.6	0.686	1.7	1.8	0.670	2.2	2.5	0.526	0.91	2.4	0.568	0.97	2.4	0.535	0.79	3.8
0.312 - 0.391	0.482	1.7	1.6	0.489	2.0	1.7	0.486	1.9	2.4	0.355	1.1	2.4	0.346	0.85	2.6	0.369	1.2	4.0
0.391 - 0.524	0.297	1.9	1.5	0.295	2.0	1.7	0.309	2.1	2.3	0.206	1.1	2.6	0.206	1.1	2.7	0.196	1.6	4.2
0.524 - 0.695	0.179	2.1	1.8	0.179	2.0	2.0	0.171	2.1	3.0	0.107	2.0	3.3	0.102	1.5	3.5	0.0865	2.6	5.7
0.695 - 0.918	0.100	1.9	2.2	0.0979	2.2	2.5	0.0971	1.8	3.3	0.0558	1.6	4.0	0.0502	1.6	4.3	0.0459	2.7	6.7
0.918 - 1.153	0.0620	1.7	2.9	0.0604	1.9	3.2	0.0533	1.9	4.7	0.0261	2.0	5.7	0.0246	2.0	5.8	0.0245	2.8	9.2
1.153 - 1.496	0.0342	2.0	3.7	0.0340	2.2	3.8	0.0297	2.2	5.2	0.0172	1.9	5.6	0.0112	4.4	7.8	0.00873	2.6	12
1.496 - 1.947	0.0181	1.9	4.2	0.0169	2.7	4.5	0.0149	2.7	6.1	0.00649	2.0	8.0	0.00629	1.6	8.4	0.00363	4.7	16
1.947 - 2.522	0.00961	2.7	5.3	0.00933	3.7	5.4	0.00608	2.7	8.3	0.00334	3.8	10	0.00341	3.6	10	0.00136	9.5	24
2.522 - 3.277	0.00456	2.2	6.8	0.00527	5.9	6.1	0.00280	3.7	11	0.00250	4.6	11	0.00127	9.3	14	0.000467	17	38
3.277 - 5.000	0.00245	3.0	5.9	0.00206	2.7	6.6	0.00122	3.3	11	0.000705	5.3	13	0.000583	4.6	14	0.000105	15	51
5.000 - 10.000	0.000527	4.8	7.5	0.000583	3.5	7.1	0.000281	6.4	15	0.000250	4.8	13	0.000189	3.2	14	0.0000589	15	40

Table 6.13: The values of the combined Born level normalised differential cross-section in bins of ϕ^*_η, for each boson rapidity region in the low and high-mass regions. Also given are the associated correlated and uncorrelated (including statistical) uncertainties in percent, where the colour on the blue-red scale indicates the relative contribution to the total uncertainty.

Figure 6.22 shows the ratio between the two theoretical predictions and the combined Born level data as function of ϕ^*_η for each region of boson mass and rapidity studied. The Banfi et al. prediction is shown with an associated uncertainty band obtained by varying the three perturbative scales in the calculation [72]. The uncertainties on the prediction from RESBOS have not been calculated and are not shown. The agreement between the data and theory is good, but not perfect.

Despite the inability of the theory to precisely describe the ϕ^*_η distribution, RESBOS is able to describe the evolution of the distribution with increasing absolute boson rapidity. This is illustrated in Figure 6.23 which shows the ratio of the ϕ^*_η distribution of theory or data in each rapidity region at peak-mass to the distribution in the central rapidity region ($|y| < 0.4$). Figure 6.24 show the same thing for the off-peak mass regions. The prediction from Banfi et al. is also displayed, where available, but does not describe the data as well as RESBOS at peak-mass.

It is also interesting to examine the evolution of the ϕ^*_η distribution with invariant mass, for a given region of boson rapidity. Figure 6.25 shows the ratio of the ϕ^*_η distribution of data or RESBOS at high-mass to that at low-mass for each region of boson rapidity. The ratio to peak-mass is not included due to the different (narrower) binning in rapidity. The data are described reasonably well by the theoretical prediction.

6.12 Conclusions

Measurements of the normalised Drell-Yan Z/γ cross-section, differential in ϕ^*_η in the electron-positron channel have been presented in twelve regions of boson invariant mass and absolute rapidity. The analysis uses $20.3\,\text{fb}^{-1}$ of $\sqrt{s} = 8\,\text{TeV}$ proton-proton collision data recorded at the ATLAS detector in 2012. The results, corrected to the Born truth level definition were combined with those in the di-muon channel and compared to theoretical predictions from RESBOS and an NNLL+NLO calculation from Banfi et al. Neither prediction can perfectly describe the basic data distributions, but RESBOS is able to describe the evolution of the ϕ^*_η distribution with absolute boson rapidity and with boson invariant mass.

The analysis presented features significant improvements over the corresponding ATLAS measurement at $\sqrt{s} = 7\,\text{TeV}$. The boson invariant mass regions above and below the Z-peak have been explored and finer bins in boson rapidity in the peak-mass region have been used. This has allowed the predictions of QCD to be tested in more extreme regions of phase-space. A better understanding of the sources of systematic uncertainty at $\sqrt{s} = 8\,\text{TeV}$ has led to a reduction of the total uncer-

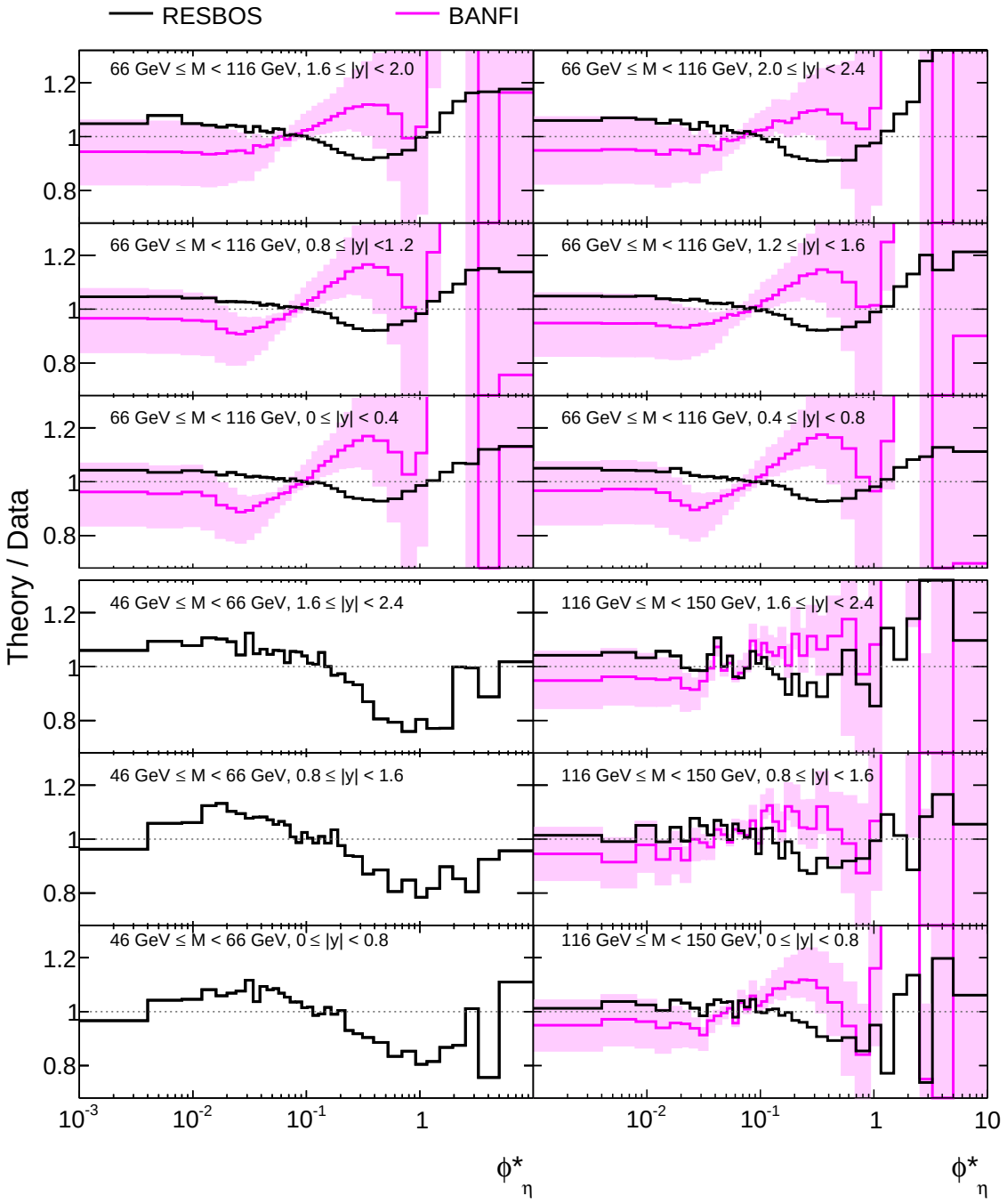

Figure 6.22: The ratio between two theoretical predictions and the combined Born level data, as a function of ϕ^*_η and for each region of boson mass and rapidity studied. The Banfi et al. prediction is shown with an associated uncertainty band which is obtained by varying the three perturbative scales in the calculation [72]. The uncertainties on the prediction from RESBOS have not been calculated and are not shown.

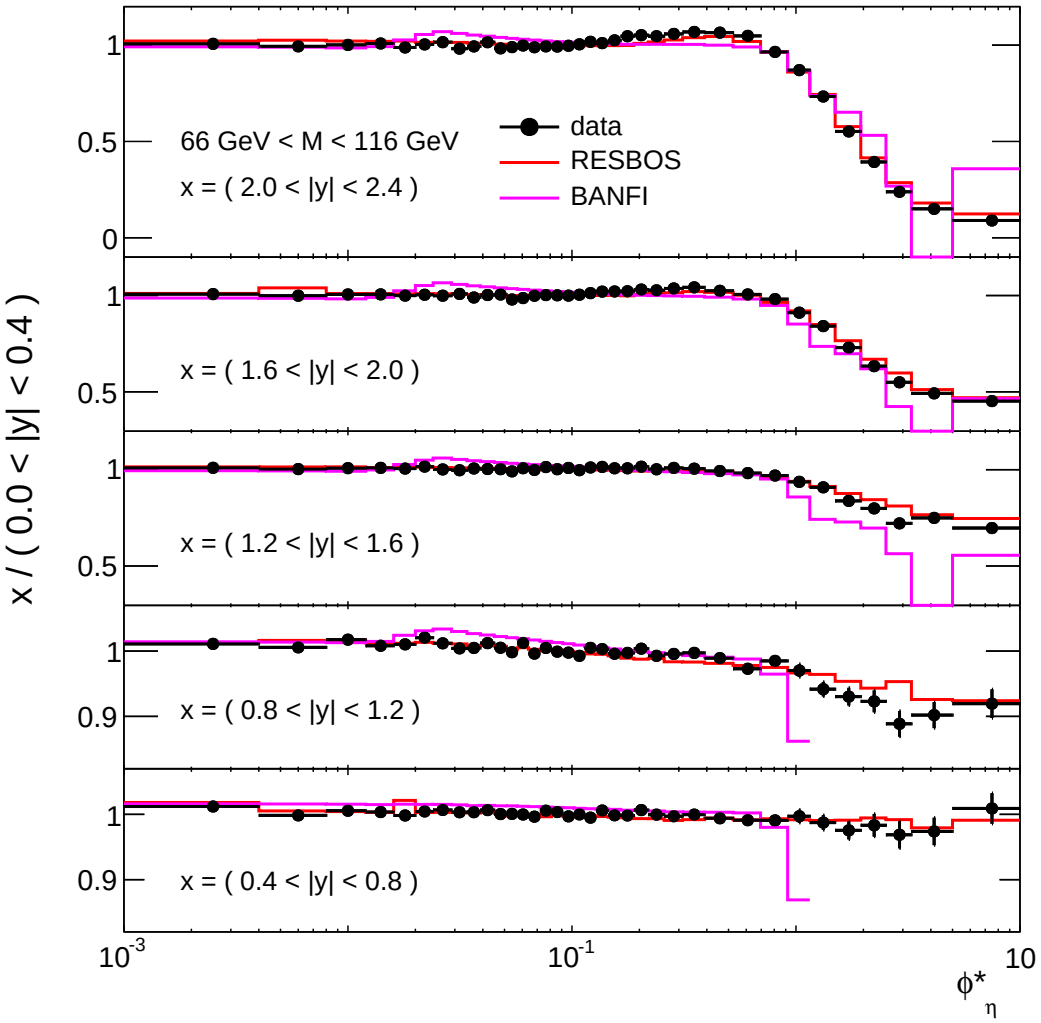

Figure 6.23: The ratio of the ϕ^*_η distribution of theory or data in a particular rapidity region at peak-mass to the distribution in the central rapidity region ($|y| < 0.4$). The same y-axis scale is used for the top three distributions and a different scale for the bottom two distributions. The RESBOS prediction provides a good description of the evolution of ϕ^*_η with boson rapidity, whilst the Banfi et al. prediction is not as good. The uncertainty band on Banfi et al. is not plotted but is much smaller than the discrepancy with data at low to medium values of ϕ^*_η.

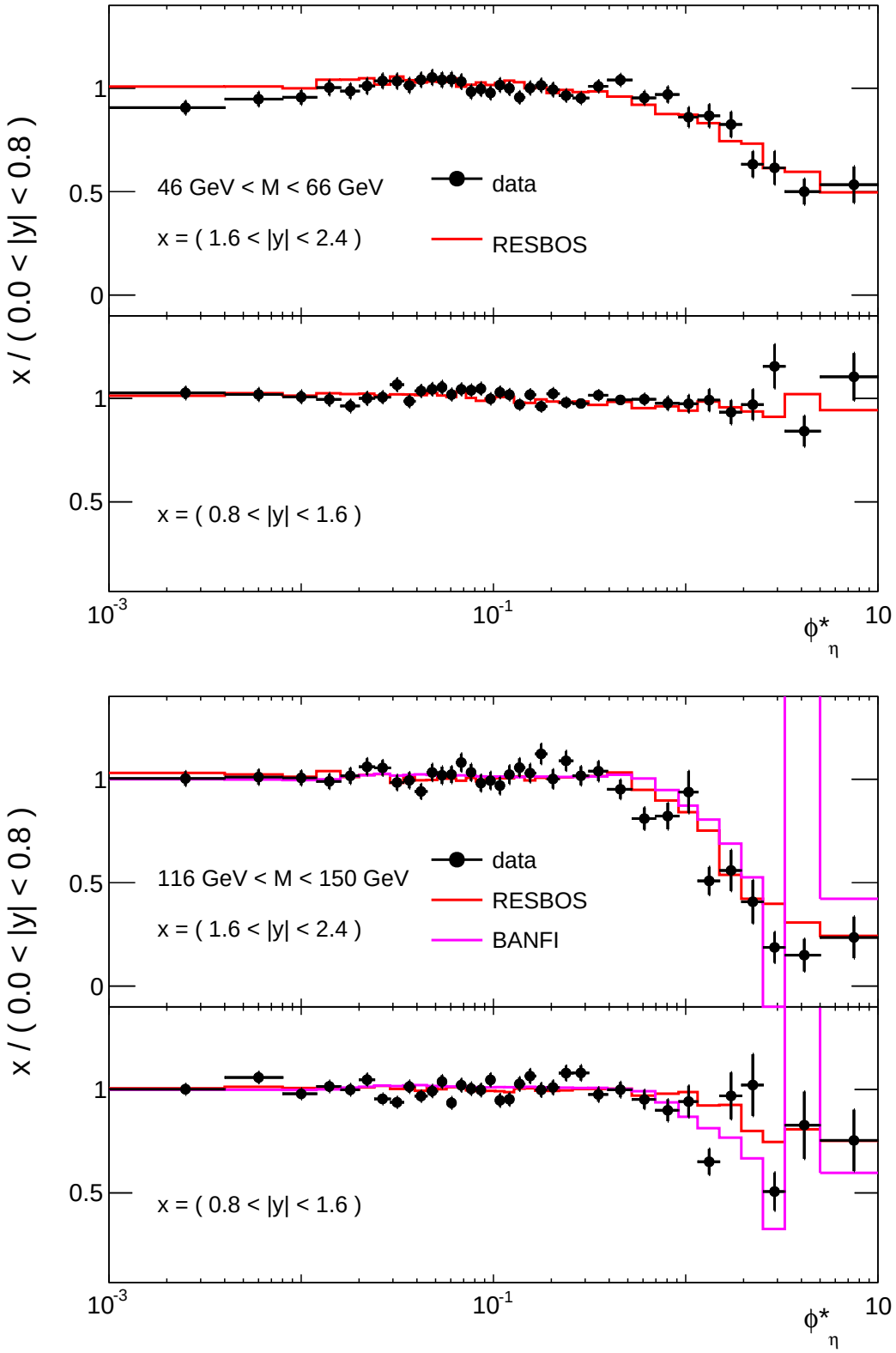

Figure 6.24: The ratio of the ϕ^*_η distribution of theory or data in a particular rapidity region at low-mass (top plot) or high-mass (bottom plot) to the distribution in the central rapidity region ($|y| < 0.8$). The same y-axis scale is used for each distribution.

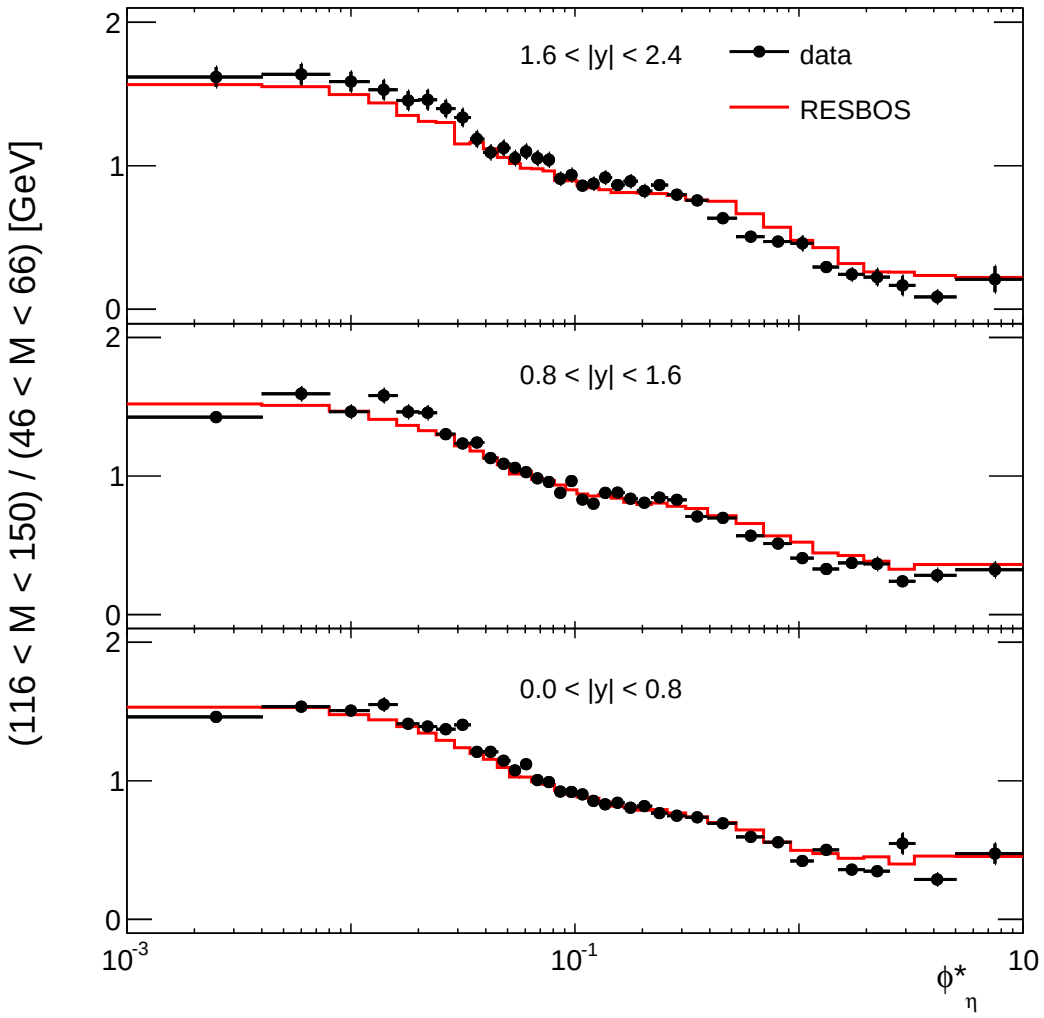

Figure 6.25: The ratio of the ϕ^*_η distribution of data or RESBOS at high-mass to that at low-mass for each region of boson rapidity. The data are described reasonably well by the theoretical prediction.

tainty in the peak-mass region as compared to $\sqrt{s} = 7\,\text{TeV}$. In particular, separate uncertainties are provided for the dressed level and Born level measurements, as the dressed level results have reduced dependence on the model used to estimate FSR.

The ϕ^*_η observable is a probe of initial state gluon radiation and is correlated with the p_T of the boson. Unlike p_T, which is limited at low values by the lepton momentum resolution, the definition of ϕ^*_η relies only upon the better-measured lepton directions and as such provides an avenue to probe the regimes of QCD in which large perturbative logarithms must be re-summed and non-perturbative effects become important. The results presented will be used to improve (tune) future Monte Carlo generators as well as providing input to new analytical calculations. The understanding and insight gained in the study of initial state radiation in the Drell-Yan process can be directly applied to other processes such as Higgs production and therefore the analysis in this thesis will play a critical role in searches for evidence of new physics beyond the Standard Model.

The proton-proton centre of mass energy in the LHC has been increased to 13 TeV for operations in 2015. Future measurements of the ϕ^*_η distribution at this energy will allow the very low x (parton longitudinal momentum fraction) domain of the parton distribution functions to be tested. Measurements of ϕ^*_η could also be made for processes other than Drell-Yan, for example the Higgs boson decaying to two photons.

Bibliography

[1] Particle Data Group Collaboration, K. Olive et al., *Review of Particle Physics*, Chin.Phys. **C38** (2014) 090001.

[2] D. Wark, *Particle physics: The hunt for Majorana neutrinos hots up*, Nature **510** (2014) 224–225.

[3] NEMO Collaboration, K. Lang, *Latest results from the NEMO-3 experiment and status of SuperNEMO*, PoS **ICHEP2012** (2013) 376.

[4] C. Sivaram, *What is special about the Planck mass?*, arXiv:0707.0058 [gr-qc].

[5] P. Singh, *A Glance at the Earliest Universe*, Physics **5** (2012) 142.

[6] W.-S. Hou, *Source of CP Violation for the Baryon Asymmetry of the Universe*, Chin.J.Phys. **47** (2009) 134, arXiv:0803.1234 [hep-ph].

[7] NA62 Collaboration, *NA62: Technical Design Document*, NA62-10-07 (2010), https://cds.cern.ch/record/1404985.

[8] L. Evans and P. Bryant, *LHC Machine*, Journal of Instrumentation **3** no. 08, (2008) S08001.

[9] D. Bandurin et al., *Review of physics results from the Tevatron*, International Journal of Modern Physics A **30** no. 06, (2015) 1541001, arXiv:1409.4861 [hep-ex].

[10] D. Brandt, H. Burkhardt, M. Lamont, S. Myers, and J. Wenninger, *Accelerator physics at LEP*, Rept.Prog.Phys. **63** (2000) 939–1000.

[11] M. Klein and R. Yoshida, *Collider Physics at HERA*, Prog.Part.Nucl.Phys. **61** (2008) 343–393, arXiv:0805.3334 [hep-ex].

[12] ATLAS Collaboration, *The ATLAS Experiment at the CERN Large Hadron Collider*, Journal of Instrumentation **3** no. 08, (2008) S08003.

[13] ALICE Collaboration, *The ALICE experiment at the CERN LHC*, Journal of Instrumentation **3** no. 08, (2008) S08002.

[14] CMS Collaboration, *The CMS experiment at the CERN LHC*, Journal of Instrumentation **3** no. 08, (2008) S08004.

[15] LHCb Collaboration, *The LHCb Detector at the LHC*, Journal of Instrumentation **3** no. 08, (2008) S08005.

[16] LHCf Collaboration, *The LHCf detector at the CERN Large Hadron Collider*, Journal of Instrumentation **3** no. 08, (2008) S08006.

[17] TOTEM Collaboration, *The TOTEM Experiment at the CERN Large Hadron Collider*, Journal of Instrumentation **3** no. 08, (2008) S08007.

[18] MoEDAL Collaboration, *Technical Design Report of the MoEDAL Experiment*, CERN-LHCC-2009-006. MoEDAL-TDR-001 (2009), https://cds.cern.ch/record/1181486.

[19] CERN bigscience.web.cern.ch/bigscience/Objects/LHC/accelerator.jpg, Accessed: 2014-12-08.

[20] A. Ahmad et al., *The Silicon microstrip sensors of the ATLAS semiconductor tracker*, Nucl.Instrum.Meth. **A578** (2007) 98–118.

[21] ATLAS Collaboration, *Simulation of Transition Radiation and Electron Identification Ability of the ATLAS TRT*, Nucl.Instrum.Meth. **A706** (2013) 79–82.

[22] ATLAS Collaboration, *The ATLAS Liquid Argon calorimeter: An overview*, Journal of Physics: Conference Series **160** no. 1, (2009) 012043.

[23] F. Djama, *Performance of the ATLAS Liquid Argon electromagnetic calorimeter modules under test beam*, Advanced Technology and Particle Physics (2002) 401–408.

[24] ATLAS Collaboration, *Electron and photon energy calibration with the ATLAS detector using LHC Run 1 data*, Eur.Phys.J. **C74** no. 10, (2014) 3071, arXiv:1407.5063 [hep-ex].

[25] A. Dudarev et al., *First full-size ATLAS barrel toroid coil successfully tested up to 22 kA at 4 T*, IEEE Transactions on Applied Superconductivity **15** no. 2, (2005) 1271–1274.

[26] ATLAS Collaboration, *ATLAS muon spectrometer: Technical design report*, CERN-LHCC-97-022, ATLAS-TDR-10 (1997), https://cds.cern.ch/record/331068.

[27] J. Wenninger, *Integrated performance of the LHC at 25 ns without and with LINAC4*, Review of LHC and Injector Upgrade Plans (2013), https://cds.cern.ch/record/1977351.

[28] ATLAS, *Pile-up subtraction and suppression for jets in ATLAS*, ATLAS-CONF-2013-083 (2013), https://cds.cern.ch/record/1570994.

[29] ATLAS Collaboration, *Improved luminosity determination in pp collisions at $\sqrt{s}$ = 7 TeV using the ATLAS detector at the LHC*, Eur.Phys.J. **C73** no. 8, (2013) 2518.

[30] S. van der Meer, *Calibration of the effective beam height in the ISR*, Tech. Rep. CERN-ISR-PO-68-31. ISR-PO-68-31, CERN, Geneva, 1968. https://cds.cern.ch/record/296752.

[31] P. Grafström and W. Kozanecki, *Luminosity determination at proton colliders*, Prog.Part.Nucl.Phys. **81** (2015) 97–148.

[32] ATLAS Collaboration https://twiki.cern.ch/twiki/bin/view/AtlasPublic/LuminosityPublicResults, Accessed: 2014-12-05.

[33] J. Goodson, *Search for Supersymmetry in States with Large Missing Transverse Momentum and Three Leptons including a Z-Boson*, PhD thesis, Stony Brook University, Presented 17 Apr 2012, https://cds.cern.ch/record/1449722.

[34] V. Cindro et al., *The ATLAS Beam Conditions Monitor*, Journal of Instrumentation **3** no. 02, (2008) P02004.

[35] ATLAS Collaboration, *Luminosity determination in pp collisions at $\sqrt{s}$ = 7 TeV using the ATLAS detector at the LHC*, Eur.Phys.J. **C71** no. 4, (2011).

[36] D. Caforio, *The ATLAS Forward Detectors - LUCID, ALFA and AFP: Past, Present and Future*, ATL-LUM-SLIDE-2013-054 (2013), https://cds.cern.ch/record/1514203.

[37] The Luminosity Group, *Preliminary Luminosity Determination in pp Collisions at $\sqrt{s}$ = 8 TeV using the ATLAS Detector in 2012*, ATL-COM-LUM-2012-013 (2012), https://cds.cern.ch/record/1494059.

[38] A. Sopczak, *Luminosity monitoring in ATLAS with MPX detectors*, Journal of Instrumentation **9** no. 01, (2014) C01027.

[39] S. M. White, *Determination of the Absolute Luminosity at the LHC*, CERN-THESIS-2010-139 (2010), https://cds.cern.ch/record/1308187.

[40] ATLAS Collaboration, *Characterization of Interaction-Point Beam Parameters Using the pp Event-Vertex Distribution Reconstructed in the ATLAS Detector at the LHC*, ATLAS-CONF-2010-027 (2010), https://cds.cern.ch/record/1277659.

[41] L. Tomlinson, *The effect of linear transverse coupling on the luminosity calibration by the van der Meer method*, ATL-COM-LUM-2012-011 (2012), https://cds.cern.ch/record/1470360.

[42] L. Tomlinson, *An analytical determination of the parameters of the single-Gaussian model of bunch densities and their impact on the luminosity calibration by the van der Meer method*, ATL-COM-LUM-2013-009 (2013), https://cds.cern.ch/record/1523278.

[43] F. J. Decker, *Beam Distributions Beyond RMS*, SLAC-PUB–95-6684 (1994), http://inspirehep.net/record/384364.

[44] F. James and M. Winkler, *Minuit2 minimization package*, http://seal.web.cern.ch/seal/MathLibs/Minuit2/html/index.html.

[45] W. Kozanecki, T. Pieloni, and J. Wenninger, *Observation of Beam-beam Deflections with LHC Orbit Data*, CERN-ACC-NOTE-2013-0006 (2013), https://cds.cern.ch/record/1581723.

[46] M. Bassetti and G. A. Erskine, *Closed expression for the electrical field of a two-dimensional Gaussian charge*, Tech. Rep. CERN-ISR-TH-80-06. ISR-TH-80-06, CERN, Geneva, 1980. https://cds.cern.ch/record/122227.

[47] W. Herr, *Beam-beam effects and dynamic β^**, LHC Lumi Days 2012 https://indico.cern.ch/event/162948 (2012).

[48] W. Kozanecki, *Updated prescription for dynamic-beta correction*, ATLAS Luminosity Taskforce https://indico.cern.ch/event/228910 (2013).

[49] W. Herr and F. Schmidt, *A MAD-X primer*, CERN-AB-2004-027-ABP (2004) 32 p, https://cds.cern.ch/record/744163.

[50] CMS Collaboration, *Measurement of the ratio of the inclusive 3-jet cross section to the inclusive 2-jet cross section in pp collisions at $\sqrt{s} = 7$ TeV and first determination of the strong coupling constant in the TeV range*, Eur.Phys.J. **C73** no. 10, (2013) 2604, arXiv:1304.7498 [hep-ex].

[51] S. Drell and T.-M. Yan, *Massive Lepton Pair Production in Hadron-Hadron Collisions at High-Energies*, Phys.Rev.Lett. **25** (1970) 316–320.

[52] J. C. Collins, D. E. Soper, and G. F. Sterman, *Factorization of Hard Processes in QCD*, Adv.Ser.Direct.High Energy Phys. **5** (1988) 1–91, arXiv:hep-ph/0409313 [hep-ph].

[53] D0 Collaboration, *Measurement of the W Boson Mass with the D0 Detector*, Phys.Rev.Lett. **108** (2012) 151804, arXiv:1203.0293 [hep-ex].

[54] S. Catani, *Soft gluon resummation: A Short review*, arXiv:hep-ph/9709503 [hep-ph].

[55] M. H. Seymour and M. Marx, *Monte Carlo Event Generators*, arXiv:1304.6677 [hep-ph].

[56] GEANT4 Collaboration, S. Agostinelli et al., *GEANT4: A Simulation toolkit*, Nucl.Instrum.Meth. **A506** (2003) 250–303.

[57] A. Banfi, S. Redford, M. Vesterinen, P. Waller, and T. Wyatt, *Optimisation of variables for studying dilepton transverse momentum distributions at hadron colliders*, Eur.Phys.J. **C71** (2011) 1600, arXiv:1009.1580 [hep-ex].

[58] D0 Collaboration, *Precise study of the Z/γ^* boson transverse momentum distribution in $p\bar{p}$ collisions using a novel technique*, Phys.Rev.Lett. **106** (2011) 122001, arXiv:1010.0262 [hep-ex].

[59] M. Guzzi, P. M. Nadolsky, and B. Wang, *Nonperturbative contributions to a resummed leptonic angular distribution in inclusive neutral vector boson production*, Phys.Rev. **D90** (2014) 014030, arXiv:1309.1393 [hep-ph].

[60] D0 Collaboration, *Measurement of the ϕ^*_η distribution of muon pairs with masses between 30 and 500 GeV in 10.4 fb^{-1} of $p\bar{p}$ collisions*, arXiv:1410.8052 [hep-ex].

[61] LHCb Collaboration, *Measurement of the cross-section for $Z \to e^+e^-$ production in pp collisions at $\sqrt{s} = 7$ TeV*, JHEP **1302** (2013) 106, arXiv:1212.4620 [hep-ex].

[62] ATLAS Collaboration, *Measurement of angular correlations in Drell-Yan lepton pairs to probe Z/γ^* boson transverse momentum at $\sqrt{s} = 7$ TeV with the ATLAS detector*, Phys.Lett. **B720** (2013) 32–51, arXiv:1211.6899 [hep-ex].

[63] A. Banfi, M. Dasgupta, S. Marzani, and L. Tomlinson, *Predictions for Drell-Yan and observables at the LHC*, Physics Letters B **715** no. 13, (2012) 152 – 156.

[64] ATLAS Collaboration, *Example ATLAS tunes of Pythia8, Pythia6 and Powheg to an observable sensitive to Z boson transverse momentum*, ATL-PHYS-PUB-2013-017 (2013).

[65] ATLAS Collaboration, *Electron efficiency measurements with the ATLAS detector using the 2012 LHC proton-proton collision data*, ATLAS-CONF-2014-032 (2014), https://cds.cern.ch/record/1706245.

[66] P. Nason, *A New method for combining NLO QCD with shower Monte Carlo algorithms*, JHEP **0411** (2004) 040, arXiv:hep-ph/0409146 [hep-ph].

[67] T. Sjostrand, S. Mrenna, and P. Z. Skands, *PYTHIA 6.4 Physics and Manual*, JHEP **0605** (2006) 026, arXiv:hep-ph/0603175 [hep-ph].

[68] E. Barberio, B. van Eijk, and Z. Was, *PHOTOS: A Universal Monte Carlo for QED radiative corrections in decays*, Comput.Phys.Commun. **66** (1991) 115–128.

[69] G. Corcella, I. Knowles, G. Marchesini, S. Moretti, K. Odagiri, et al., *HERWIG 6: An Event generator for hadron emission reactions with interfering gluons (including supersymmetric processes)*, JHEP **0101** (2001) 010, arXiv:hep-ph/0011363 [hep-ph].

[70] T. Gleisberg, S. Hoeche, F. Krauss, M. Schonherr, S. Schumann, et al., *Event generation with SHERPA 1.1*, JHEP **0902** (2009) 007, arXiv:0811.4622 [hep-ph].

[71] ATLAS Collaboration, *The ATLAS Inner Detector commissioning and calibration*, Eur.Phys.J. **C70** (2010) 787–821, arXiv:1004.5293 [physics.ins-det].

[72] L. Tomlinson, *Azimuthal decorrelation between leptons in the Drell-Yan process as a probe of infrared QCD: Phenomenology, predictions and*

measurement of a novel collider observable using perturbative resummation techniques, PhD thesis, University of Manchester, Presented 2014.

[73] K. Lannon, F. Margaroli, and C. Neu, *Measurements of the Production, Decay and Properties of the Top Quark: A Review*, Eur.Phys.J. **C72** (2012) 2120, arXiv:1201.5873 [hep-ex].

[74] A. Arbuzov and R. Sadykov, *Inverse bremsstrahlung contributions to Drell-Yan like processes*, J.Exp.Theor.Phys. **106** (2008) 488–494, arXiv:0707.0423 [hep-ph].

[75] S. Dittmaier and M. Huber, *Radiative corrections to the neutral-current Drell-Yan process in the Standard Model and its minimal supersymmetric extension*, JHEP **1001** (2010) 060, arXiv:0911.2329 [hep-ph].

[76] M. Karnevskiy, T.-H. Lin, M. Lisovyi, M. Schott, L. Tomlinson, S. Webb, T. Wyatt, and C. Zimmermann, *Measurement of the transverse momentum and azimuthal decorrelation of leptons in Drell-Yan events at* $\sqrt{s} = 8$ *TeV with ATLAS*, ATL-COM-PHYS-2014-281 (2014), https://cds.cern.ch/record/1694674.

[77] ATLAS Collaboration, *Performance of the ATLAS Electron and Photon Trigger in p-p Collisions at* $\sqrt{s} = 7$ *TeV in 2011*, ATLAS-CONF-2012-048, ATLAS-COM-CONF-2012-071 (2012), https://cds.cern.ch/record/1450089.

[78] Z. Marshall, *Simulation of Pile-up in the ATLAS Experiment*, ATL-SOFT-PROC-2013-030 (2013), https://cds.cern.ch/record/1616394.

[79] V. Lacuesta, *Track and vertex reconstruction in the ATLAS experiment*, Journal of Instrumentation **8** no. 02, (2013) C02035, http://stacks.iop.org/1748-0221/8/i=02/a=C02035.

[80] T. Adye, *Unfolding algorithms and tests using RooUnfold*, Proceedings of the PHYSTAT 2011 Workshop (2011) 313–318, arXiv:1105.1160 [physics.data-an].

[81] T. K. O. Doan, W. Placzek, and Z. Was, *Observable* ϕ^*_η *at LHC and second-order QED matrix element in* $Z/\gamma \to l^+l^-$ *decays*, Phys.Lett. **B725** (2013) 92–96, arXiv:1303.2220 [hep-ph].

[82] A. Arbuzov, R. Sadykov, and Z. Was, *QED Bremsstrahlung in decays of electroweak bosons*, Eur.Phys.J. **C73** no. 11, (2013) 2625, arXiv:1212.6783 [hep-ph].

[83] A. Glazov, *Averaging of DIS cross section data*, AIP Conf.Proc. **792** (2005) 237–240.

[84] C. Balazs and C. Yuan, *Soft gluon effects on lepton pairs at hadron colliders*, Phys.Rev. **D56** (1997) 5558–5583, arXiv:hep-ph/9704258 [hep-ph].

[85] A. Webb. Private communication, 2013.

[86] M. Furman, *The Moller luminosity factor*, LBNL-53553/CBP Note-543 (2003).

Appendix A

Luminosity

A.1 Overlap integral of two moving beams modelled by the sum of multiple Gaussian distributions

This appendix provides the formulae describing the luminosity, beam spot position and beam spot width given two moving beams each modelled by the sum of multiple single Gaussian distributions [85]. The effects of a beam crossing angle are also included.

The single Gaussian distribution, G (in 3 dimensions), is defined in Equation A.1 as a function of coordinate $\mathbf{x}$, with a mean denoted by the vector $\boldsymbol{\mu}$ and with a covariance matrix denoted by $\boldsymbol{\sigma}$.

$$G(\mathbf{x}, \boldsymbol{\mu}, \boldsymbol{\sigma}) = \frac{1}{(2\pi)^{\frac{3}{2}}|\boldsymbol{\sigma}|^{\frac{1}{2}}} \exp\left(-\frac{1}{2}(\mathbf{x}-\boldsymbol{\mu})^{\mathsf{T}}\boldsymbol{\sigma}^{-1}(\mathbf{x}-\boldsymbol{\mu})\right) \tag{A.1}$$

The mean is a function of time and this is made explicit by defining $\boldsymbol{\mu} = \boldsymbol{\mu}_0 + c\boldsymbol{a}t$. The symbol $\boldsymbol{\mu}_0$ equals $(\delta_x/2, \delta_y/2, 0)$ where δ_x and δ_y are the separations of the two beams in the vdM scan. The quantity c is the speed of the two beams (here the speed of light), t is time and $\boldsymbol{a}$ is a unit vector in the direction of the beam's motion.

The covariance matrix $\boldsymbol{\sigma}$ and the mean, $\boldsymbol{\mu}$, are both defined in the detector frame of reference. However the convention is to present the covariance matrix of a beam in the frame in which the beam moves in the z-direction ($\boldsymbol{a}_B = (0, 0, 1)$) which is also the frame in which there is assumed to be no x-z or y-z correlation; this frame is labelled the beam frame and the covariance matrix is denoted as $\boldsymbol{\sigma}_B$. The detector frame and the beam frame coincide if there is no beam crossing angle. The quantities defined above are used for the Gaussian distributions which comprise

beam 1. For beam 2 the covariance matrix is labelled $\mathbf{s}$ and the mean is $\boldsymbol{\nu} = \boldsymbol{\nu}_0 + c\boldsymbol{b}t$.

To obtain $\boldsymbol{\sigma}$, $\boldsymbol{\sigma}^{-1}$, $\mathbf{s}$ and $\mathbf{s}^{-1}$, a set of similarity transformations are applied to the corresponding matrices in the beam frame (subscript B) using the rotation matrix $R(\theta_{xz}, \theta_{yz})$ (Equation A.2). R is defined in Equation A.3.

$$\begin{aligned}
\boldsymbol{\sigma} &= R^{-1}(\theta_{xz}, \theta_{yz})\boldsymbol{\sigma}_B R(\theta_{xz}, \theta_{yz}) \\
\boldsymbol{\sigma}^{-1} &= R^{-1}(\theta_{xz}, \theta_{yz})\boldsymbol{\sigma}_B^{-1} R(\theta_{xz}, \theta_{yz}) \\
\mathbf{s} &= R^{-1}(-\theta_{xz}, -\theta_{yz})\mathbf{s}_B R(-\theta_{xz}, -\theta_{yz}) \\
\mathbf{s}^{-1} &= R^{-1}(-\theta_{xz}, -\theta_{yz})\mathbf{s}_B^{-1} R(-\theta_{xz}, -\theta_{yz})
\end{aligned} \tag{A.2}$$

$$R(\theta_{xz}, \theta_{yz}) = \begin{pmatrix} \cos\theta_{xz} & \sin\theta_{xz}\sin\theta_{yz} & \sin\theta_{xz}\cos\theta_{yz} \\ 0 & \cos\theta_{yz} & -\sin\theta_{yz} \\ -\sin\theta_{xz} & \sin\theta_{yz}\cos\theta_{xz} & \cos\theta_{xz}\cos\theta_{yz} \end{pmatrix} \tag{A.3}$$

The quantities $\boldsymbol{a}$ and $\boldsymbol{b}$ are obtained from $\boldsymbol{a}_B$ and $\boldsymbol{b}_B$ by the relations in Equation A.4.

$$\begin{aligned}
\boldsymbol{a} &= R^{-1}(\theta_{xz}, \theta_{yz})\boldsymbol{a}_B = (-\sin\theta_{xz}, \cos\theta_{xz}\sin\theta_{yz}, \cos\theta_{xz}\cos\theta_{yz}) \\
\boldsymbol{b} &= -R^{-1}(-\theta_{xz}, -\theta_{yz})\boldsymbol{b}_B = (-\sin\theta_{xz}, \cos\theta_{xz}\sin\theta_{yz}, -\cos\theta_{xz}\cos\theta_{yz})
\end{aligned} \tag{A.4}$$

The rotation matrix R corresponds to a rotation of the beam direction firstly around the y-axis and then around the x-axis. The term crossing angle sometimes refers to the angles made between the beam and the detector frame when projected onto either the x-z (α_{xz}) or y-z (α_{yz}) planes. The relationship between θ and α is given in Equation A.5. For small angles they are equivalent (up to a sign).

$$\begin{aligned}
\alpha_{xz} &= \theta_{xz} \\
\alpha_{yz} &= \arctan\left(-\frac{\tan\theta_{yz}}{\cos\theta_{xz}}\right)
\end{aligned} \tag{A.5}$$

The two moving beams with density profiles ρ_1 and ρ_2 collide with a luminosity, $\mathscr{L}$, given in Equation A.6 [86], where K_F is the Møller luminosity factor (or kinematic factor) and is defined in Equation A.7.

$$\mathscr{L} = \int dt\, d^3\mathbf{x}\, \rho_1\, \rho_2\, K_F \tag{A.6}$$

$$K_F = \sqrt{(\mathbf{v}_1 - \mathbf{v}_2)^2 - \frac{(\mathbf{v}_1 \times \mathbf{v}_2)^2}{c^2}} \tag{A.7}$$

The variables $\mathbf{v}_1$ and $\mathbf{v}_2$ are the velocity vectors of the two beams. For beams colliding head on at the speed of light the kinematic factor becomes $2c$. In fact the crossing angles must be around 250 times larger than those used in the April scan (of order 100 µrad) to create a 0.1% deviation from $2c$ in the kinematic factor.

The product of two Gaussian distributions, one from each beam, $G(\mathbf{x}, \boldsymbol{\mu}, \boldsymbol{\sigma})$ and $G(\mathbf{x}, \boldsymbol{\nu}, \mathbf{s})$ is also a Gaussian distribution, $A \times G(\mathbf{x}, \boldsymbol{\alpha}, K)$. The following equations show how this can be derived and give the values of A, $\boldsymbol{\alpha}$ and K. Equation A.8 shows the product of the two Gaussian distributions with all terms written explicitly.

$$\begin{aligned} G(\mathbf{x}, \boldsymbol{\mu}, \boldsymbol{\sigma})G(\mathbf{x}, \boldsymbol{\nu}, \mathbf{s}) = \frac{1}{(2\pi^3)|\boldsymbol{\sigma}|^{\frac{1}{2}}|\mathbf{s}|^{\frac{1}{2}}} \exp\Bigg(& -\frac{1}{2}(\mathbf{x} - \boldsymbol{\mu}_0 - c\mathbf{a}t)^\mathsf{T}\boldsymbol{\sigma}^{-1}(\mathbf{x} - \boldsymbol{\mu}_0 - c\mathbf{a}t) \\ & -\frac{1}{2}(\mathbf{x} - \boldsymbol{\nu}_0 - c\mathbf{b}t)^\mathsf{T}\mathbf{s}^{-1}(\mathbf{x} - \boldsymbol{\nu}_0 - c\mathbf{b}t)\Bigg) \end{aligned} \tag{A.8}$$

One can factorise the time dependent part of Equation A.8 by completing the square. This gives Equation A.9, where σ_t is defined in Equation A.10 and t_0 in Equation A.11.

$$\begin{aligned} G(\mathbf{x}, \boldsymbol{\mu}, \boldsymbol{\sigma})G(\mathbf{x}, \boldsymbol{\nu}, \mathbf{s}) = & \frac{\sqrt{2\pi}\sigma_t}{(2\pi^3)|\boldsymbol{\sigma}|^{\frac{1}{2}}|\mathbf{s}|^{\frac{1}{2}}} \frac{1}{\sqrt{2\pi}\sigma_t} \exp\left(-\frac{1}{2\sigma_t^2}(t - t_0)^2\right) \\ & \exp\left(-\frac{1}{2}(\mathbf{x} - \boldsymbol{\mu}_0)^\mathsf{T}\boldsymbol{\sigma}^{-1}(\mathbf{x} - \boldsymbol{\mu}_0) - \frac{1}{2}(\mathbf{x} - \boldsymbol{\nu}_0)^\mathsf{T}\mathbf{s}^{-1}(\mathbf{x} - \boldsymbol{\nu}_0) + \frac{t_0^2}{2\sigma_t^2}\right) \end{aligned} \tag{A.9}$$

$$\frac{1}{\sigma_t^2} = c^2\left(\mathbf{a}^\mathsf{T}\boldsymbol{\sigma}^{-1}\mathbf{a} + \mathbf{b}^\mathsf{T}\mathbf{s}^{-1}\mathbf{b}\right) \tag{A.10}$$

$$t_0 = \frac{c\,(\mathbf{x} - \boldsymbol{\mu}_0)^\mathsf{T}\,\boldsymbol{\sigma}^{-1}\mathbf{a} + c\,(\mathbf{x} - \boldsymbol{\nu}_0)^\mathsf{T}\,\mathbf{s}^{-1}\mathbf{b}}{c^2\,(\mathbf{a}^\mathsf{T}\boldsymbol{\sigma}^{-1}\mathbf{a} + \mathbf{b}^\mathsf{T}\mathbf{s}^{-1}\mathbf{b})} \tag{A.11}$$

It is now easy to integrate Equation A.9 with respect to time as the only term which depends on time is a one-dimensional normalised Gaussian which integrates

to one. Therefore one now has Equation A.12.

$$\frac{\sqrt{2\pi}\sigma_t}{(2\pi^3)|\boldsymbol{\sigma}|^{\frac{1}{2}}|\mathbf{s}|^{\frac{1}{2}}}\exp\left(-\frac{1}{2}(\mathbf{x}-\boldsymbol{\mu}_0)^{\mathsf{T}}\boldsymbol{\sigma}^{-1}(\mathbf{x}-\boldsymbol{\mu}_0)-\frac{1}{2}(\mathbf{x}-\boldsymbol{\nu}_0)^{\mathsf{T}}\mathbf{s}^{-1}(\mathbf{x}-\boldsymbol{\nu}_0)+\frac{t_0^2}{2\sigma_t^2}\right) \tag{A.12}$$

Again by completing the square one can write Equation A.12 in the form $A \times G(\mathbf{x}, \boldsymbol{\alpha}, K)$ where K is defined in Equation A.13 and $\boldsymbol{\alpha}$ in Equation A.14.

$$K^{-1} = \boldsymbol{\sigma}^{-1} + \mathbf{s}^{-1} - \left(\frac{\boldsymbol{\sigma}^{-1}\mathbf{a}\mathbf{a}^{\mathsf{T}}\boldsymbol{\sigma}^{-1} + \mathbf{s}^{-1}\mathbf{b}\mathbf{b}^{\mathsf{T}}\mathbf{s}^{-1} + \boldsymbol{\sigma}^{-1}\mathbf{a}\mathbf{b}^{\mathsf{T}}\mathbf{s}^{-1} + \mathbf{s}^{-1}\mathbf{b}\mathbf{a}^{\mathsf{T}}\boldsymbol{\sigma}^{-1}}{\mathbf{a}^{\mathsf{T}}\boldsymbol{\sigma}^{-1}\mathbf{a} + \mathbf{b}^{\mathsf{T}}\mathbf{s}^{-1}\mathbf{b}}\right) \tag{A.13}$$

$$\begin{aligned}\boldsymbol{\alpha} =& K\left(\boldsymbol{\sigma}^{-1}\boldsymbol{\mu}_0 + \mathbf{s}^{-1}\boldsymbol{\nu}_0\right) - \\ & K\left(\frac{\boldsymbol{\sigma}^{-1}\mathbf{a}\mathbf{a}^{\mathsf{T}}\boldsymbol{\sigma}^{-1}\boldsymbol{\mu}_0 + \mathbf{s}^{-1}\mathbf{b}\mathbf{b}^{\mathsf{T}}\mathbf{s}^{-1}\boldsymbol{\nu}_0 + \boldsymbol{\sigma}^{-1}\mathbf{a}\mathbf{b}^{\mathsf{T}}\mathbf{s}^{-1}\boldsymbol{\nu}_0 + \mathbf{s}^{-1}\mathbf{b}\mathbf{a}^{\mathsf{T}}\boldsymbol{\sigma}^{-1}\boldsymbol{\mu}_0}{\mathbf{a}^{\mathsf{T}}\boldsymbol{\sigma}^{-1}\mathbf{a} + \mathbf{b}^{\mathsf{T}}\mathbf{s}^{-1}\mathbf{b}}\right)\end{aligned} \tag{A.14}$$

The parameter A is defined in Equation A.15, where β is defined in Equation A.16.

$$A = \frac{\exp(\beta)}{2\pi}\frac{\sigma_t|K|^{\frac{1}{2}}}{|\boldsymbol{\sigma}|^{\frac{1}{2}}|\mathbf{s}|^{\frac{1}{2}}} \tag{A.15}$$

$$\begin{aligned}\beta = & -\frac{1}{2}(\boldsymbol{\mu}_0^{\mathsf{T}}\boldsymbol{\sigma}^{-1}\boldsymbol{\mu}_0 + \boldsymbol{\nu}_0^{\mathsf{T}}\mathbf{s}^{-1}\boldsymbol{\nu}_0) + \\ & \frac{1}{2}\left(\frac{\boldsymbol{\mu}_0^{\mathsf{T}}\boldsymbol{\sigma}^{-1}\mathbf{a}\mathbf{a}^{\mathsf{T}}\boldsymbol{\sigma}^{-1}\boldsymbol{\mu}_0 + \boldsymbol{\nu}_0^{\mathsf{T}}\mathbf{s}^{-1}\mathbf{b}\mathbf{b}^{\mathsf{T}}\mathbf{s}^{-1}\boldsymbol{\nu}_0 + -2\boldsymbol{\nu}_0^{\mathsf{T}}\mathbf{s}^{-1}\mathbf{b}\mathbf{a}^{\mathsf{T}}\boldsymbol{\sigma}^{-1}\boldsymbol{\mu}_0}{\mathbf{a}^{\mathsf{T}}\boldsymbol{\sigma}^{-1}\mathbf{a} + \mathbf{b}^{\mathsf{T}}\mathbf{s}^{-1}\mathbf{b}}\right) + \\ & \frac{1}{2}\boldsymbol{\alpha}_0^{\mathsf{T}}K^{-1}\boldsymbol{\alpha}_0\end{aligned} \tag{A.16}$$

The procedure for calculating the luminosity, beam spot position and beam spot width is then similar to that described in Section 4.4.2. The luminosity of 3D single Gaussian colliding beams is given by the integral over space of the time integrated beam product, Equation A.17.

$$\mathscr{L} = K_F \int A \times G(\mathbf{x}, \boldsymbol{\alpha}, K) d\mathbf{x} = K_F\, A \tag{A.17}$$

For beams described by the sum of N single Gaussian distributions the time

integrated product will contain N^2 terms, each of which is a single Gaussian. Each Gaussian in a beam has a weight defined such that the sum of all weights is equal to one. Each of the Gaussians in the time integrated product therefore also has an associated weight equal to the product of the weight of the component Gaussians from beams 1 and 2. This weight is now absorbed into the definition of A. The total luminosity for such beams is given by Equation A.18.

$$\mathscr{L} = \sum_{i=1}^{N} K_F \int A_i \times G(\mathbf{x}, \boldsymbol{\alpha}_i, K_i) d\mathbf{x} = \sum_{i=1}^{N} K_F \, A_i \tag{A.18}$$

The beam spot position (using the definition in Equation 4.2) is given by Equation A.19.

$$\langle \mathbf{x} \rangle = \frac{\sum_{i=1}^{N} A_i \boldsymbol{\alpha}_i}{\sum_{i=1}^{N} A_i} \tag{A.19}$$

Then the beam spot covariance matrix, $\boldsymbol{\Sigma}$, (in order to determine the beam spot width in each dimension using the definition in Equation 4.3) is given by Equation A.20.

$$\boldsymbol{\Sigma} = \frac{\sum_{i=1}^{N} A_i \left(K_i + \boldsymbol{\alpha}_i \boldsymbol{\alpha}_i^{\mathsf{T}} \right)}{\sum_{i=1}^{N} A_i} - \frac{\left(\sum_{i=1}^{N} A_i \boldsymbol{\alpha}_i \right) \left(\sum_{i=1}^{N} A_i \boldsymbol{\alpha}_i \right)^{\mathsf{T}}}{\left(\sum_{i=1}^{N} A_i \right)^2} \tag{A.20}$$